Daniel Rieser, Dipl.-Ing.

GOCE gravity gradients for geoid and Moho determination applying the Least Squares Collocation approach

Doctoral Thesis

to achieve the university degree of
Doktor der technischen Wissenschaften
submitted to

Graz University of Technology

Supervisor

Univ.-Prof. Dr.techn. Mag.rer.nat. Roland Pail
Institute of Astronomical and Physical Geodesy, TU Munich

Co-supervisor

Univ.-Prof. Dr.-Ing. Torsten Mayer-Gürr
Institute of Geodesy, TU Graz

Graz, May 2015

Affidavit

I declare that I have authored this thesis independently, that I have not used other than the declared sources/resources, and that I have explicitly indicated all material which has been quoted either literally or by content from the sources used. The text document uploaded to TUGRAZonline is identical to the present doctoral thesis.

Date	Signature

Acknowledgements

At this place I want to express my gratitude to several people who have been involved in the evolution of this thesis in one way or the other:

- Roland Pail, my supervisor, who motivated me to tackle the PhD, proposed the field of investigations and was supporting and guiding me with his expertise despite the spatial distance;
- Torsten Mayer-Gürr, who gave me the freedom to pursue my research ambitions and was helping me with his tremendous knowledge whenever a question arose;
- my colleagues from the Institute of Geodesy, in particular Christian Pock and Norbert Kühtreiber, for their fruitful discussions and help;
- my friends, who arranged the necessary distractions from writing a dissertation from time to time;
- my parents and family, who were unconditionally supporting me and my goals;
- and finally, my gratitude goes to Petra, who was by my side all the long way until the completion of this work and who knows what I want to tell her without putting it into words.

Thank you!

Abstract

The Gravity field and steady-state Ocean Circulation Explorer (GOCE) satellite mission, which was operational from spring 2009 to autumn 2013, was dedicated to determine the static Earth gravity field on global scale in particular in the medium-wavelength range of the gravity signal spectrum. The key component of the GOCE mission was the gradiometer instrument, which enabled the measurement of the gravity gradient tensor, i.e. the second order derivatives of the Earth's gravitational potential. This thesis is dedicated to investigate the applicability of the GOCE gradients for regional and local applications in geodesy and geophysics.

The Least Squares Collocation method was chosen for gravity field computations. Its main advantage is the capability to handle all types of quantities related to the gravity field, either representing input observations or signals to be estimated. With the implemented approach the corresponding covariances can be rotated to an arbitrary reference frame, which is of great importance when dealing with GOCE gradients. The calculations in this work are based on a consistent Remove-Compute-Restore concept, in which the systematic effects of a global gravity potential model, topography, isostasy and the atmosphere are considered by appropriate modeling.

Due to the specific mission and instrument design, the GOCE gravity gradients cannot be used directly as observations. On the one hand, the measurements were taken in the gradiometer instrument frame and are only accurate enough for further use in a particular frequency range. On the other hand, not all components of the gravity gradient tensor could be determined with the same accuracy. In order to cope with these problems, appropriate processing strategies have been developed, which include a combination of Wiener and high-pass filters to reduce the colored noise of the GOCE observations. Besides the filtered observations, also information on the remaining measurement errors are an important result of this preprocessing step.

In a first application, the GOCE gradients are used in combination with terrestrial gravity data for the determination of a geoid solution within the Austrian region. The comparison with a gravity-only solution highlights the beneficial impact of including GOCE gradient observations in particular in the medium-wavelength part of the gravity signal. A validation with independent GPS/levelling observations from the Austrian Bundesamt für Eich- und Vermessungswesen shows that the root mean square of the differences can be decreased from 5.5 cm to 4.6 cm by including GOCE gradient observations.

Moreover, an approach for the determination of the Moho surface with GOCE gradients based on the Airy-Heiskanen isostatic concept has been developed as a second field of application. Since the gradiometer instrument is not able to resolve the long-wavelength structures of the gravity field, the residual Moho surface in the spectral range of spherical harmonic degrees and orders 50 to approximately 250 has been estimated. Based on empirical values for a mean Moho depth of 30 km and a constant crust-mantle density contrast of $350\,\mathrm{kg\,m^{-3}}$, residual

Moho variations between $-19.9\,\mathrm{km}$ and $13.5\,\mathrm{km}$ have been derived within the investigated central European area. The results are validated with external regional and global Moho models, which have been derived from seismic and gravimetric measurements. It can be shown that the Moho model derived in this thesis is resolving more detailed structures in terms of spatial resolution due to the dense and homogeneous data coverage of the GOCE mission. Further comparisons with several local seismic studies reveal that the resulting Moho features can be directly linked to geophysical and tectonic units.

Kurzfassung

Die Gravity field and steady-state Ocean Circulation Explorer (GOCE) Satellitenmission war von Frühling 2009 bis Herbst 2013 operationell und wurde für die Bestimmung der statischen Komponente des globalen Erdschwerefeldes, insbesondere im Bereich der mittleren Wellenlängen des Gravitationssignalspektrums, konzipiert. Das Herzstück von GOCE war das Gradiometerinstrument, das die Messung der zweiten Ableitungen des Gravitationspotentials und somit des Schweregradiententensors ermöglichte. In dieser Arbeit wird die Verwendbarkeit der GOCE Gradienten für regionale und lokale Anwendungen in der Geodäsie und Geophysik untersucht.

Für die Schwerefeldberechnungen wurde die Methode der Kollokation nach kleinsten Quadraten verwendet. Deren großer Vorteil ist die Möglichkeit, verschiedenste Schwerefeldgrößen zu verarbeiten, sei es als Beobachtungen oder als zu schätzende Signale. Mit dem implementierten Ansatz können die entsprechenden Kovarianzen in ein beliebiges Referenzsystem rotiert werden, was im Fall von GOCE Gradienten vorteilhaft ist. Die Berechnungen in dieser Arbeit basieren auf einem konsistenten Remove-Compute-Restore Konzept, in dem die systematischen Einflüsse eines globalen Schwerefeldmodells, der Topographie, der Isostasie und der Atmosphäre durch eine adäquate Modellierung berücksichtigt werden.

Aufgrund der Konzeption der Mission können die GOCE Schweregradienten nicht direkt als Beobachtungen eingeführt werden. Zum einen wurden die Messungen im instrumentenspezifischen Koordinatensystem aufgezeichnet und sind nur in einem eingeschränkten Frequenzbereich mit ausreichender Genauigkeit verfügbar. Zum anderen wurden nicht alle Komponenten des Gradiententensors mit derselben Genauigkeit gemessen. Aus diesen Gründen wurden entsprechende Strategien zur Lösung dieser Problematiken entwickelt, wobei eine Kombination aus Wiener- und Hochpassfiltern zur Reduktion des farbigen Rauschens der GOCE Beobachtungen angewendet wurde. Neben den gefilterten Beobachtungen selbst sind auch die Informationen über die verbleibenden Messfehler wichtige Ergebnisse dieser Vorprozessierung.

In einer ersten Anwendung wurden die GOCE Gradienten in Kombination mit terrestrischen Schweremessungen zur Bestimmung einer Geoidlösung im österreichischen Gebiet verwendet. Der Vergleich einer rein terrestrischen Lösung mit der Kombinationslösung zeigt den Mehrwert der Hinzunahme von GOCE Gradienten im Speziellen im mittelwelligen Bereich des Schweresignals. Eine Validierung mit unabhängigen GPS/Nivellement Beobachtungen des Bundesamts für Eich- und Vermessungswesen zeigt, dass das quadratische Mittel der Differenzen durch die zusätzlichen GOCE Beobachtungen von 5.5 cm auf 4.6 cm gesenkt werden kann.

Als zweite Anwendung der GOCE Gradienten auf regionaler Ebene wurde ein Ansatz zur Bestimmung der Moho Grenzfläche basierend auf dem Konzept der Isostasie nach Airy-Heiskanen entwickelt. Da das Gradiometer die langwelligen Anteile des Schwerefeldes nicht

auflösen kann, wurde eine residuale Moho geschätzt, die dem spektralen Bereich einer sphärisch-harmonischen Reihenentwicklung von Grad und Ordnung 50 bis etwa 250 entspricht. Auf Basis von empirischen Werten für eine mittlere Moho Tiefe von 30 km und einem konstanten Dichtekontrast zwischen Erdkruste und -mantel von $350\,\mathrm{kg\,m^{-3}}$, welche im zentraleuropäischen Untersuchungsgebiet gelten, wurden Variationen in der Moho zwischen -19.9 km und 13.5 km bestimmt. Die Ergebnisse wurden mit externen globalen und lokalen Moho Modellen validiert, die aus seismischen und gravimetrischen Messungen abgeleitet wurden. Die Untersuchungen zeigen, dass das berechnete Moho Modell detailliertere räumliche Strukturen abbildet, was auf die dichte und homogene Datenüberdeckung der GOCE Mission zurückzuführen ist. Weitere Vergleiche mit mehreren lokalen seismischen Studien zeigen, dass die resultierenden Moho Strukturen direkt mit geophysikalischen und tektonischen Einheiten in Verbindung gebracht werden können.

Contents

Abbreviations

ADM	Atmospheric Density Model
BEV	Bundesamt für Eich- und Vermessungswesen
CHAMP	CHAllenging Minisatellite Payload
COM	Center Of Mass
cpr	cycle per revolution
D/O	Degree and Order
DEM	Digital Elevation Model
DFACS	Drag-Free and Attitude Control System
DIR	DIRect approach
ECF	Empirical Covariance Function
EGG	Electrostatic Gravity Gradiometer
EGM	Earth Gravity field Model
ERF	Earth-fixed Reference Frame
ESA	European Space Agency
ESC	European Seismological Comission
GEMMA	GOCE Exploitation for Moho Modeling and Applications
GGT	Gravity Gradient Tensor
GOCE	Gravity field and steady-state Ocean Circulation Explorer
GOCO	Gravity Observation COmbination
GPS	Global Positioning System
GRACE	Gravity Recovery and Climate Experiment
GRF	Gradiometer Reference Frame
HPF	High-level Processing Facility
ICGEM	International Center for Global Earth Models
IERS	International Earth Rotation and Reference System Service
IRF	Inertial Reference Frame
LNOF	Local North-Oriented reference Frame
LORF	Local Orbital Reference Frame
LSC	Least Squares Collocation
LTI	Linear Time-Invariant
MBW	Measurement Bandwidth
MCF	Model Covariance Function
PSD	Power Spectral Density
RCR	Remove-Compute-Restore
RMS	Root Mean Square
SGG	Satellite Gravity Gradiometry
SPW	SPace-Wise approach
SST-hl	Satellite-to-Satellite Tracking in high-low mode
SSTI	Satellite-to-Satellite Tracking Instrument
TIM	TIMe-wise approach
w.r.t.	with respect to

1 Introduction

The determination of the Earth's gravity field is one of the main objectives in the field of geodesy. Nowadays, a wide range of techniques for observing the gravity and related quantities exists. However, the observables considerably differ in their information content at different spectral scales of the gravity signal. Space techniques like satellite laser ranging (SLR) are primarily used to determine the very long wavelength components of the gravity signal, and the Gravity Recovery and Climate Experiment (GRACE) satellite mission in particular contributes to the long wavelengths. On the other hand, the high frequency gravity constituents can be covered with terrestrial gravity observations and the ultra-high frequency signals are commonly accounted for by accurate topographic models. However, the spectral coverage at the transition from long to short wavelengths has been underrepresented for a long time.

With the advent of the Gravity field and steady-state Ocean Circulation Explorer (GOCE) satellite mission, launched on the 17$^{\text{th}}$ of March 2009 by the European Space Agency (ESA), a new gravity field observable has become available to the scientific user community. For the first time, gravity gradients, representing the tensor of second order derivatives of the gravity potential, could be measured in space by an exclusively designed gradiometer instrument. These observations are superior to other gravity field measurements in particular in the medium wavelengths of the gravity signal spectrum and thus have the ability to close the existing gap. The scientific goal of the mission was the determination of the static component of the Earth's gravity field with an accuracy level of 1 to 2 cm in terms of geoid heights on global scale with a spatial resolution of 100 km. This was achieved by estimating globally best fitting gravity field solutions, which are parametrized as a series of spherical harmonics coefficients, with complex workflows and methods.

This thesis is triggered by the initial question, if these measurements could also be exploited for the purpose of gravity field determination on regional or local scale. Due to the dense spatial coverage of GOCE gradients and the outstanding performance in the medium wavelengths, the use of gradients as in-situ observations poses an interesting field for corresponding investigations. For such regional scale applications, Least Squares Collocation (LSC) is a standard method for the computation of the Earth's gravity field which, for instance, is applied for the determination of the current official Austrian geoid solution. The major advantage of LSC is its ability to combine various kinds of complementary gravity field signals, e.g. geoid undulations, gravity anomalies or also gravity gradients from GOCE and will therefore also be the computation method applied in this thesis. However, the use of GOCE gradients as direct observations in LSC is not straightforward due to several mission-specific characteristics, which will be reviewed in detail in this work. This thesis proposes a set of necessary tools and strategies to handle these difficulties. In this way, the range of applications for GOCE gradients observations can be extended to regional scales.

In the beginning of this thesis, the necessary theoretical foundations are reviewed in chapter 2. After an overview on the various reference frames and coordinate systems appearing within this thesis, the basics of the potential theory are reflected with a focus on the expansion of the Earth's gravitational potential into a spherical harmonics series. The chapter ends with the description of the Earth's disturbing gravity field and the manifold gravity field quantities that can be used for its representation.

In chapter 3, the concept of the LSC approach for the estimation of disturbing gravity field quantities is introduced. The required steps for the application to GOCE gravity gradients are shown. In particular, the necessary covariance propagations for second order derivatives of the disturbing potential are derived. The implemented approach is independent of the reference frame, which is of great importance when dealing with GOCE gradients.

Chapter 4 deals with the elements for a consistent Remove-Compute-Restore (RCR) method within gravity field processing. The systematic influences of global Earth Gravity field Models (EGMs), the atmospheric and topographic masses and the isostatic compensation are discussed and their proper consideration is proposed. Concerning the atmospheric effects, an independent Atmospheric Density Model (ADM) has been developed within this chapter.

The details of the GOCE mission are summarized in chapter 5. Besides a general overview on the mission concept, the available observations and official data products which are of interest for this thesis are introduced.

Using GOCE gravity gradients as in-situ observations requires appropriate preprocessing steps and methodological developments, which are treated in chapter 6. At first, the signal characteristics of the gradient time series are investigated. Afterwards, the applied filter procedure for noise reduction is discussed, which is followed by some investigations on the possible strategies for introducing the GOCE observations into the LSC approach.

Two different fields of applications are described in chapter 7 and chapter 8. Within the former, GOCE gradients are used in combination with terrestrial gravity data to determine a new geoid solution for Austria. After a discussion of the current geoid solution, the used data sets and preprocessing steps are described. The results of the geoid computations are validated with independent GPS/levelling observations.

Furthermore, an approach for the determination of the Moho surface with GOCE gradients is introduced in chapter 8. First, the Moho and its role within the Earth's structure is defined. Then, a concept for the derivation of the Moho depth using GOCE gradients in an LSC procedure is proposed. Afterwards, the data and preprocessing is described and the results of the Moho computations are shown. The estimated Moho depths are compared to external models and their geophysical plausibility is investigated by a detailed validation with other local Moho studies. The results and possible improvements are summarized at the end of this chapter.

Finally, chapter 9 gives a summary of the investigations and results achieved within this study, and the thesis is closed with an outlook on possible improvements and further developments.

2 Theoretical background

This chapter has the purpose to provide the basic theoretical background for this thesis. As there are various reference frames and systems involved, this will be the first issue to be treated. Afterwards, a general overview on potential theory and the Earth's gravity field is given, leading to the definition of gravity field quantities used in these studies. In order to keep the body of this work concise, selected topics may also be found in the appendices, which will be referred to when required.

2.1 Reference frames and coordinate systems

This section gives an overview of the coordinate systems and reference frames as well as of the transformations between the systems which are of relevance in this thesis. Following the conventions, e.g. given in Seeber (1993), one should distinguish between the terms reference system and reference frame. While the first term should be understood as the fundamental theoretical definition including standards and models for its implementation, its actual realization based on observations is commonly denoted as reference frame.

2.1.1 Global Cartesian coordinate systems and frames

Inertial Reference Frame (IRF) The Celestial Reference System (CRS) is a three-dimensional space-fixed reference system with its origin coinciding with the solar barycenter. By convention, the Z-axis of the Cartesian system is defined as the mean rotation axis of the Earth at the standard epoch J2000.0, the X-axis is the intersection between the Earth's equatorial plane and the ecliptic plane pointing towards the vernal equinox, while the Y-axis is complementing a right-handed coordinate system. Neglecting the minor accelerations of the Earth while orbiting the sun, this system can be considered as an inertial reference system and is therefore also denoted as Conventional Inertial System (CIS).

The International Earth Rotation and Reference System Service (IERS) establishes the International Celestial Reference Frame (ICRF) as a realization, which is also used as a standard for the GOCE mission as outlined in Gruber et al. (2010a). To be consistent with the nomenclature of the GOCE standards, this type of reference frame will be abbreviated as IRF throughout the thesis.

Earth-fixed Reference Frame (ERF) The Conventional Terrestrial System (CTS) has its origin in the Earth's Center Of Mass (COM) with the Z-axis associated with the mean rotation axis, which is defined by the Conventional Terrestrial Pole (CTP). The X-axis is pointing towards the Greenwich meridian, thus the CTS is co-rotating with the Earth.

A corresponding reference frame called International Terrestrial Reference Frame (ITRF) is again provided by the IERS. GOCE data and products refer to the definitions given in Gruber et al. (2010a) or in the IERS Conventions (2003) published by McCarthy and Petit (2004). In the naming conventions of the GOCE products a data type EGG_TRF_2 can be found (see section 5.4.1), which actually does not refer to the kind of reference frame introduced at this place. In order to avoid confusion, the notation for this Earth-fixed terrestrial reference frame will be ERF in the sequel.

The transformation between the space-fixed IRF and the Earth-fixed ERF is described in detail again in Gruber et al. (2010a), McCarthy and Petit (2004) or in standard literature like Seeber (1993). The transformation of an arbitrary vector $\boldsymbol{x}$ between the two frames can be summarized by the consecutive rotations

$$\boldsymbol{x}_{ERF} = R^M R^S R^N R^P R^B \boldsymbol{x}_{IRF} \tag{2.1}$$

where

R^M ... rotation matrix for polar motion,
R^S ... rotation matrix for Earth rotation (Greenwich apparent sidereal time GAST),
R^N ... rotation matrix for nutation,
R^P ... rotation matrix for precession,
R^B ... rotation matrix for frame bias.

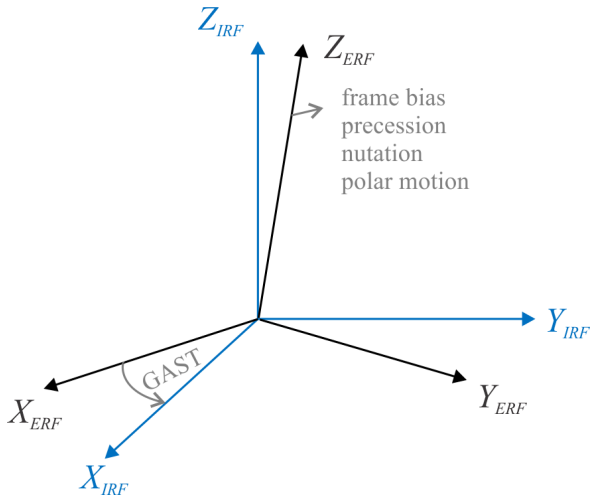

Figure 2.1: Sketch of the global Cartesian reference frames IRF and ERF

During the GOCE mission lifetime an updated version of IERS Conventions (2010) was published by Petit and Luzum (2010) with modified definitions for the computation of the

rotation matrices. Since GOCE standards still refer to the IERS Conventions (2003), this older version is also used in this thesis.

2.1.2 Global ellipsoidal and spherical coordinates

For several reasons in geodesy it can be advantageous to represent a vector $\boldsymbol{x} = (x, y, z)^T$ to a distinct point P given in a Cartesian reference frame in terms of ellipsoidal coordinates latitude φ, longitude λ and height above a reference ellipsoid h. The reference ellipsoid is centered at the same origin as the Cartesian frame with the 0° longitude defined by the Greenwich meridian and the semi-minor axis of the ellipsoid coinciding with the Z-axis of the Cartesian frame. The geometry of the ellipsoid is determined by the semi-major and semi-minor axis a, b, as indicated on the left of Figure 2.2.

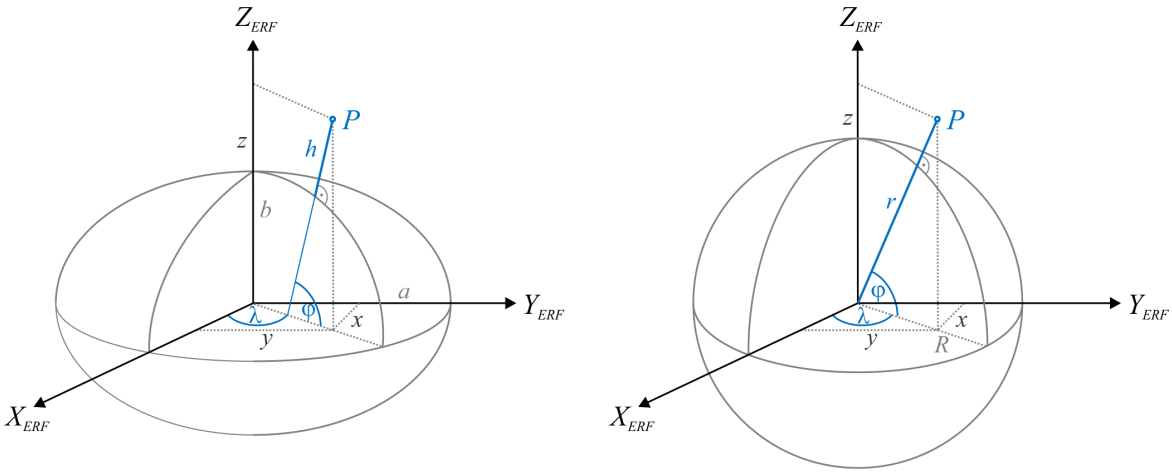

Figure 2.2: Global ellipsoidal (left) and spherical (right) coordinate systems

The transformations between the two systems are given for instance in Hofmann-Wellenhof and Moritz (2005) by

$$\begin{pmatrix} x \\ y \\ z \end{pmatrix} = \begin{pmatrix} (N+h)\cos\varphi\cos\lambda \\ (N+h)\cos\varphi\sin\lambda \\ \left(\frac{b^2}{a^2}N+h\right)\sin\varphi \end{pmatrix} \Leftrightarrow \begin{pmatrix} \varphi \\ \lambda \\ h \end{pmatrix} = \begin{pmatrix} \arctan\frac{z+e'^2 b\sin^3\theta}{p-e^2 a\cos^3\theta} \\ \arctan y/x \\ \frac{p}{\cos\varphi} - N \end{pmatrix}, \tag{2.2}$$

with

$$\begin{aligned} N &= \frac{a^2}{\sqrt{a^2\cos^2\varphi + b^2\sin^2\varphi}}, \\ p &= \sqrt{x^2+y^2}, \\ e^2 &= (a^2-b^2)/a^2, \\ e'^2 &= (a^2-b^2)/b^2, \\ \theta &= \frac{za}{pb}. \end{aligned} \tag{2.3}$$

Using a reference sphere instead of a reference ellipsoid simplifies the equations to

$$\begin{pmatrix} x \\ y \\ z \end{pmatrix} = \begin{pmatrix} r\cos\varphi\cos\lambda \\ r\cos\varphi\sin\lambda \\ r\sin\varphi \end{pmatrix} \Leftrightarrow \begin{pmatrix} \varphi \\ \lambda \\ r \end{pmatrix} = \begin{pmatrix} \arctan\frac{\sqrt{x^2+y^2}}{z} \\ \arctan y/x \\ \sqrt{x^2+y^2+z^2} \end{pmatrix}, \tag{2.4}$$

where r is the geocentric radius, see Figure 2.2, right.

2.1.3 Local level systems

As a third type of coordinate system which is used in this thesis a local Cartesian system is introduced. Its origin is defined by an arbitrary point O in space. For terrestrial applications and measurements, local astronomical or local ellipsoidal systems are common. In the first case, the Z-axis of the local system is defined by the tangent to the plumb line, that is the direction of the gravity vector $\boldsymbol{g}$, at the point where the system is centered (i.e. where the measurements are taken). The X-axis is pointing North and Y to the East as shown on the left of Figure 2.3. This choice of the triad defines a left-handed Cartesian system, which is also commonly denoted as North-East-Up system.

The local ellipsoidal system only differs in the definition of the Z-axis, which is corresponding to the ellipsoid normal in this case, which is sketched on the right of Figure 2.3. In case of satellite applications, the origin of such a system is often defined by the satellite's COM and the Z-axis is parallel to the direction to the Earth's center, radially pointing outwards. Due to the orientation to the North direction, such systems will be denoted as Local North-Oriented reference Frame (LNOF).

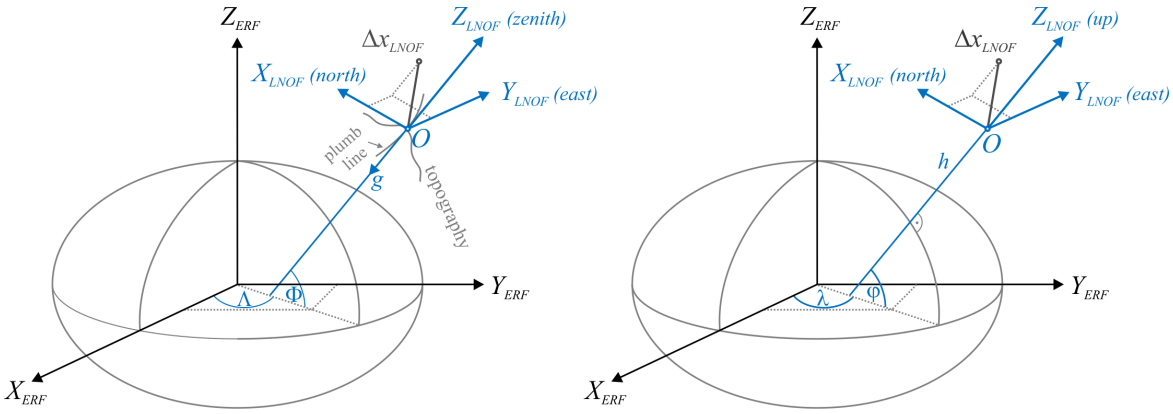

Figure 2.3: Astronomical (left) and ellipsoidal (right) local frames

A vector $\Delta\boldsymbol{x} = (x, y, z)^T$ of coordinate differences observed in the ellipsoidal LNOF can be transformed to the global ERF by

$$\Delta\boldsymbol{x}_{ERF} = R^{ERF}_{LNOF}\,\Delta\boldsymbol{x}_{LNOF}\,. \tag{2.5}$$

The rotation matrix R^{ERF}_{LNOF} can be derived by the projection of the axes of the LNOF onto

those of the ERF, which results in

$$R_{LNOF}^{ERF} = \begin{pmatrix} -\sin\varphi\cos\lambda & -\sin\lambda & \cos\varphi\cos\lambda \\ -\sin\varphi\sin\lambda & \cos\lambda & \cos\varphi\sin\lambda \\ \cos\varphi & 0 & \sin\varphi \end{pmatrix} , \tag{2.6}$$

where φ is in this case defined by the angle between the local Z-axis and the global XY-plane, and λ is the angle between the meridian through the origin of the local system and the Greenwich meridian. For the transformation of a vector given in an astronomical frame, the astronomical coordinates Φ and Λ have to be used accordingly.

2.2 Potential theory

This section summarizes the fundamentals of potential theory which are of interest for this thesis. For an extensive treatment of the theoretical background the reader is referred to, e.g., Heiskanen and Moritz (1967) or Torge (1989) and references therein.

Starting with Newton's law of gravitation, the attracting force between two point masses m_1 and m_2, located at the positions $\boldsymbol{r_1}$ and $\boldsymbol{r_2}$ with respect to an arbitrary origin, reads

$$\boldsymbol{F} = G\, m_1\, m_2\, \frac{(\boldsymbol{r_2} - \boldsymbol{r_1})}{|\boldsymbol{r_2} - \boldsymbol{r_1}|^3} , \tag{2.7}$$

where $G = 6.673\,84 \times 10^{-11}\,\mathrm{m^3/kg\,s^2}$ is the gravitational constant (Mohr et al., 2012). Each attracting mass m_1 defines a force field with the field strength $\boldsymbol{f}$, the gravitational acceleration, acting on another mass m_2 at an arbitrary distance $(\boldsymbol{r_2} - \boldsymbol{r_1})$ with

$$\boldsymbol{f} = G\, m_1\, \frac{(\boldsymbol{r_2} - \boldsymbol{r_1})}{|\boldsymbol{r_2} - \boldsymbol{r_1}|^3} , \tag{2.8}$$

with the resulting force

$$\boldsymbol{F} = \boldsymbol{f}\, m_2 . \tag{2.9}$$

Since gravity is a conservative force field, there exists a scalar function called gravitational potential V, which is related to the gravitational acceleration vector by

$$\boldsymbol{f} = \nabla V = \left(\frac{\partial V}{\partial x}, \frac{\partial V}{\partial y}, \frac{\partial V}{\partial z} \right)^T . \tag{2.10}$$

The gravitational potential of a solid body can be expressed with the Newtonian volume integral formula by

$$V = G \iiint_{\Omega} \frac{1}{l}\, \rho \, \mathrm{d}\Omega , \tag{2.11}$$

where ρ is the density of the body and $l = |\boldsymbol{r_2} - \boldsymbol{r_1}|$ is again the distance between a point P, at which the potential is evaluated, and the integration point Q associated with the body. The integration is performed for the entire body volume Ω in a three-dimensional coordinate

system. If the Laplace operator $\triangle$ is applied to the potential, it can be shown that V satisfies the Poisson's equation

$$\triangle V(x,y,z) = \left(\frac{\partial^2}{\partial x^2} + \frac{\partial^2}{\partial y^2} + \frac{\partial^2}{\partial z^2}\right) V = -4\pi G\rho\,. \tag{2.12}$$

If considered outside the attracting masses where the density ρ becomes zero, the Poisson's equation turns into the Laplace's equation

$$\triangle V = 0\,, \tag{2.13}$$

which is a fundamental property in particular in geodesy, since it implies that the gravitational potential can be represented by harmonic functions.

2.2.1 Spherical harmonics

Due to the Earth's, in first approximation, spherical shape, the spherical harmonic functions are the most used harmonic functions to solve the Laplace equation of the Earth's gravitational field. For the derivation of spherical harmonics, the spherical coordinates radius r, co-latitude $\theta = 90° - \varphi$ and geocentric longitude λ are introduced instead of Cartesian coordinates. The conversion between the two systems is given by Eq. (2.4). The Laplace equation (2.13) can then be formulated in spherical coordinates as

$$r^2\frac{\partial^2 V}{\partial r^2} + 2r\frac{\partial V}{\partial r} + \frac{\partial^2 V}{\partial \theta^2} + \cot\theta\frac{\partial V}{\partial \theta} + \frac{1}{\sin^2\theta}\frac{\partial^2 V}{\partial \lambda^2} = 0\,, \tag{2.14}$$

and it can be shown that this differential equation is solved by two possible series expansions, denoted as solid spherical harmonics

$$V(r,\theta,\lambda) = \sum_{n=0}^{\infty} r^n Y_n(\theta,\lambda) \qquad \text{or} \qquad V(r,\theta,\lambda) = \sum_{n=0}^{\infty} \frac{1}{r^{n+1}} Y_n(\theta,\lambda)\,, \tag{2.15}$$

with the so-called Laplace's surface spherical harmonics Y_n which are defined as homogeneous harmonic polynomials of degree n (integer numbers $0, 1, \ldots, \infty$) on the surface of a unit sphere with radius $r = 1$. Once again, $Y_n(\theta,\lambda)$ can be reformulated as a harmonic differential equation in θ and λ, for which the solutions exist if

$$Y_n(\theta,\lambda) = P_{nm}(\cos\theta)\cos m\lambda \qquad \text{or} \qquad Y_n(\theta,\lambda) = P_{nm}(\cos\theta)\sin m\lambda\,. \tag{2.16}$$

Here, $P_{nm}(\cos\theta)$ is the Legendre function (cf. Appendix A.1) and m is defining the order of the series expansion again in integer numbers $0, 1, \ldots, \leq n$. Apart from the Legendre function $P_{nm}(\cos\theta)$, there exists another solution for Laplace's differential equation, denoted as Legendre function of the second kind $Q_{nm}(\cos\theta)$. For spherical harmonics expansions this function is not practicable, since it produces singularities at the poles (co-latitudes $\theta = 0$ or π). However, they play an important role in ellipsoidal harmonics, which will not be treated in this thesis. For more information on this subject, the reader is referred to Heiskanen and Moritz (1967).

The general solution for the Laplace surface spherical harmonics is the linear combination of all possible solutions

$$Y_n(\theta,\lambda) = \sum_{m=0}^{n} \left[c_{nm} P_{nm}(\cos\theta)\cos m\lambda + s_{nm} P_{nm}(\cos\theta)\sin m\lambda\right] , \tag{2.17}$$

where c_{nm} and s_{nm} are arbitrary constants commonly denoted as spherical harmonics coefficients. Another common convention for the Laplace surface harmonics is to combine

$$C_{nm}(\theta,\lambda) = P_{nm}(\cos\theta)\cos m\lambda \qquad \text{and} \qquad S_{nm}(\theta,\lambda) = P_{nm}(\cos\theta)\sin m\lambda , \tag{2.18}$$

so Eq. (2.17) simplifies to

$$Y_n(\theta,\lambda) = \sum_{m=0}^{n} \left[c_{nm}\, C_{nm}(\theta,\lambda) + s_{nm}\, S_{nm}(\theta,\lambda)\right] . \tag{2.19}$$

In an alternative way, each harmonic polynomial $Y_n(\theta,\lambda)$ itself can be represented by a linear combination of $2n+1$ linearly independent basis polynomials $Y_{nm}(\theta,\lambda)$ and arbitrary coefficients a_{nm}

$$Y_n(\theta,\lambda) = \sum_{m=0}^{2n} a_{nm}\, Y_{nm}(\theta,\lambda) = \sum_{m=-n}^{n} a_{nm}\, Y_{nm}(\theta,\lambda) , \tag{2.20}$$

which are related to Eq. (2.17) and Eq. (2.19) by

$$Y_{nm}(\theta,\lambda) = \begin{cases} C_{nm}(\theta,\lambda) & = P_{nm}(\cos\theta)\cos m\lambda \\ S_{n|m|}(\theta,\lambda) & = P_{n|m|}(\cos\theta)\sin |m|\lambda \end{cases} , \; a_{nm} = \begin{cases} c_{nm} & \ldots\; m = 0,\ldots,n \\ s_{n|m|} & \ldots\; m = -n,\ldots,-1 \end{cases} . \tag{2.21}$$

An essential property of the basis polynomials $Y_{nm}(\theta,\lambda)$ is their orthogonality which implies that integrating the product of two different kinds of $Y_{nm}(\theta,\lambda)$ over the unit sphere σ is

$$\iint\limits_{\sigma} Y_{nm}(\theta,\lambda) Y_{n'm'}(\theta,\lambda)\mathrm{d}\sigma = \begin{cases} \dfrac{4\pi}{(2-\delta_{0m})(2n+1)} \dfrac{(n+|m|)!}{(n-|m|)!} & \ldots\; n = n' \wedge m = m' \\ 0 & \ldots \text{ otherwise} \end{cases} , \tag{2.22}$$

with

$$\iint\limits_{\sigma} \mathrm{d}\sigma = \int\limits_{\lambda=0}^{2\pi} \int\limits_{\theta=0}^{\pi} \sin\theta \,\mathrm{d}\theta \,\mathrm{d}\lambda = 4\pi . \tag{2.23}$$

Using these orthogonality relations, one can easily derive the unknown spherical harmonics coefficients a_{nm} by multiplication of Eq. (2.20) with $Y_{nm}(\theta,\lambda)$ and integrating the product

over the unit sphere σ, which leads to

$$a_{nm} = \frac{(2-\delta_{0m})(2n+1)}{4\pi}\frac{(n-|m|)!}{(n+|m|)!}\iint\limits_{\sigma} Y_n(\theta,\lambda)Y_{nm}(\theta,\lambda)\mathrm{d}\sigma\,. \tag{2.24}$$

For reasons of convenience, in geodesy the spherical harmonics are commonly normalized in such a way that the average square of the so-called fully normalized surface spherical harmonics basis functions $\bar{Y}_{nm}(\theta,\lambda)$ over the unit sphere is

$$\frac{1}{4\pi}\iint\limits_{\sigma} \bar{Y}^2_{nm}(\theta,\lambda)\mathrm{d}\sigma = 1\,, \tag{2.25}$$

with

$$\bar{Y}_{nm}(\theta,\lambda) = \begin{cases} \bar{C}_{nm}(\theta,\lambda) & = \bar{P}_{nm}(\cos\theta)\cos m\lambda \\ \bar{S}_{n|m|}(\theta,\lambda) & = \bar{P}_{n|m|}(\cos\theta)\sin|m|\lambda \end{cases}\,, \tag{2.26}$$

using the fully normalized Legendre functions $\bar{P}_{nm}$ (cf. Appendix A.1). This normalization is also advantageous from a numerical perspective, since otherwise the unnormalized values would soon become very large. The simple relation between the conventional spherical harmonics coefficients a_{nm} of Eq. (2.24) and their corresponding fully normalized version $\bar{a}_{nm}$ is

$$\bar{a}_{nm} = \sqrt{\frac{1}{(2-\delta_{0m})(2n+1)}\frac{(n+|m|)!}{(n-|m|)!}}\,a_{nm}\,. \tag{2.27}$$

Combining the Laplace surface spherical harmonics of Eq. (2.17) and the solid spherical harmonics of Eq. (2.15) we obtain the general solutions of the gravitational potential as fully normalized spherical harmonics series

$$\begin{aligned} V_i(r,\theta,\lambda) &= \sum_{n=0}^{\infty} r^n \sum_{m=0}^{n} \left(\bar{c}_{nm}\cos m\lambda + \bar{s}_{nm}\sin m\lambda\right)\bar{P}_{nm}(\cos\theta)\,, \\ V_e(r,\theta,\lambda) &= \sum_{n=0}^{\infty} \frac{1}{r^{n+1}} \sum_{m=0}^{n} \left(\bar{c}_{nm}\cos m\lambda + \bar{s}_{nm}\sin m\lambda\right)\bar{P}_{nm}(\cos\theta)\,, \end{aligned} \tag{2.28}$$

or in a more compact notation using the Laplace spherical harmonics of Eq. (2.20)

$$\begin{aligned} V_i(r,\theta,\lambda) &= \sum_{n=0}^{\infty} r^n \sum_{m=-n}^{n} \bar{a}_{nm}\,\bar{Y}_{nm}(\theta,\lambda)\,, \\ V_e(r,\theta,\lambda) &= \sum_{n=0}^{\infty} \frac{1}{r^{n+1}} \sum_{m=-n}^{n} \bar{a}_{nm}\,\bar{Y}_{nm}(\theta,\lambda)\,. \end{aligned} \tag{2.29}$$

The remarkable differences between V_i and V_e in the equations (2.28) or (2.29) are related to the radial distance r of the position at which the potential is considered. If we again adopt the simple case of a unit sphere with radius $r = 1$, we can instantly see that the series V_i converges if $r \leq 1$, thus the Laplace equation is satisfied inside the unit sphere. On the other

hand, we obtain a convergent series for V_e if $r \geq 1$, so V_e is harmonic in the exterior of the unit sphere. In case of an arbitrary sphere with radius $r = R$ the same differentiation of internal potential V_i for $r \leq R$ and external potential V_e for $r \geq R$ can be made if we write

$$\begin{aligned} V_i(r,\theta,\lambda) &= \sum_{n=0}^{\infty} \left(\frac{r}{R}\right)^n \sum_{m=-n}^{n} \bar{a}_{nm}\, \bar{Y}_{nm}(\theta,\lambda)\,, \\ V_e(r,\theta,\lambda) &= \sum_{n=0}^{\infty} \left(\frac{R}{r}\right)^{n+1} \sum_{m=-n}^{n} \bar{a}_{nm}\, \bar{Y}_{nm}(\theta,\lambda)\,. \end{aligned} \tag{2.30}$$

2.2.2 The Earth's gravitational potential in spherical harmonics

The gravitational potential of the Earth is defined by the Newtonian volume integral Eq. (2.11) for which the integration has to be performed for the entire Earth

$$V = G \iiint_{\Omega} \frac{1}{l}\, \rho \, \mathrm{d}\Omega\,.$$

In order to obtain a more convenient expression for the gravitational potential, one can expand the reciprocal distance $1/l$ between evaluation point $P(r,\theta,\lambda)$ and integration point $Q(r',\theta',\lambda')$ in spherical coordinates into a series of Legendre polynomials

$$\frac{1}{l} = \frac{1}{r} \sum_{n=0}^{\infty} \left(\frac{r'}{r}\right)^n P_n(\cos\psi) \tag{2.31}$$

where ψ is the angle between the radial vectors of P and Q, also given by the spherical distance on the unit sphere

$$\cos\psi = \cos\theta\, \cos\theta' + \sin\theta\, \sin\theta'\, \cos\left(\lambda' - \lambda\right). \tag{2.32}$$

Next, we can use the addition theorem of spherical harmonics (Hobson, 1931), which is

$$P_n(\cos\psi) = \frac{1}{2\,n+1} \sum_{m=-n}^{n} \bar{Y}_{nm}(P)\, \bar{Y}_{nm}(Q)\,, \tag{2.33}$$

and insert this in combination with Eq. (2.31) into Eq. (2.11) to obtain the integral formula for the entire body volume Ω in dependence of the integration point Q

$$V(P) = G \iiint_{\Omega(Q)} \frac{1}{r} \sum_{n=0}^{\infty} \left(\frac{r'}{r}\right)^n \frac{1}{2\,n+1} \sum_{m=-n}^{n} \bar{Y}_{nm}(P)\, \bar{Y}_{nm}(Q)\, \rho(Q)\, \mathrm{d}\Omega(Q)\,. \tag{2.34}$$

Expanding with RM/RM, where R represents the mean Earth's equatorial radius and M is the Earth's mass, and changing the order of summations and integrations leads to the

definition of the gravitational potential for the exterior space

$$V_e(P) = \frac{GM}{R} \sum_{n=0}^{\infty} \left(\frac{R}{r}\right)^{n+1} \sum_{m=-n}^{n} \left(\frac{1}{M(2\,n+1)} \iiint\limits_{\Omega(Q)} \left(\frac{r'}{R}\right)^{n} \bar{Y}_{nm}(Q)\, \rho(Q)\, \mathrm{d}\Omega(Q) \right) \bar{Y}_{nm}(P). \tag{2.35}$$

Defining the spherical harmonics coefficients for the exterior

$$\bar{a}^{e}_{nm} = \frac{1}{M(2\,n+1)} \iiint\limits_{\Omega(Q)} \left(\frac{r'}{R}\right)^{n} \bar{Y}_{nm}(Q)\, \rho(Q)\, \mathrm{d}\Omega(Q)\,, \tag{2.36}$$

we arrive at the fully normalized spherical harmonics expansion of the gravitational potential for the exterior space

$$V_e(P) = \frac{GM}{R} \sum_{n=0}^{\infty} \left(\frac{R}{r}\right)^{n+1} \sum_{m=-n}^{n} \bar{a}^{e}_{nm} \bar{Y}_{nm}(P)\,. \tag{2.37}$$

In the same manner, we can derive the gravitational potential for the interior space by

$$V_i(P) = \frac{GM}{R} \sum_{n=0}^{\infty} \left(\frac{r}{R}\right)^{n} \sum_{m=-n}^{n} \bar{a}^{i}_{nm} \bar{Y}_{nm}(P)\,, \tag{2.38}$$

with the spherical harmonics coefficients for the inner space

$$\bar{a}^{i}_{nm} = \frac{1}{M(2\,n+1)} \iiint\limits_{\Omega(Q)} \left(\frac{R}{r'}\right)^{n+1} \bar{Y}_{nm}(Q)\, \rho(Q)\, \mathrm{d}\Omega(Q)\,. \tag{2.39}$$

2.3 The gravity field of the Earth

The gravitational acceleration is the fundamental force which is acting on a unit mass located on the Earth's surface due to the gravitational attraction from the Earth's mass. Since the Earth is rotating, there exists also a centrifugal acceleration $\boldsymbol{z}$ which is influencing the point mass, with its norm given by

$$z = \omega^2 \, d \, , \tag{2.40}$$

where d denotes the radius of the circle of latitude given in an ERF by $d = \sqrt{x^2 + y^2}$ and ω is the mean angular velocity of the Earth's rotation. The associated centrifugal potential Φ is then given by the analytic function

$$\Phi = \frac{1}{2}\omega^2(x^2 + y^2) \, . \tag{2.41}$$

The Earth's gravity potential W is the sum of the gravitational potential V generated by the Earth's masses and the centrifugal potential Φ

$$W = V + \Phi \, . \tag{2.42}$$

The geometry of the gravity field can be described by surfaces which are defined by a uniform gravity potential W, the so-called equipotential or level surfaces. One of these surfaces is the geoid, which is the equipotential surface $W = W_0 = \textit{constant}$ that coincides with the physical surface of the mean ocean at rest and is virtually continued beneath the continents. In geodetic sense, this is the most important level surface, as it serves as reference for the definition of height systems. The gravity vector $\boldsymbol{g}$ is, analogously to the gravitational vector in Eq. (2.10), the gradient of the gravity potential

$$\boldsymbol{g} = \nabla W = \left(\frac{\partial W}{\partial x}, \frac{\partial W}{\partial y}, \frac{\partial W}{\partial z} \right)^T \, . \tag{2.43}$$

The direction of $\boldsymbol{g}$ is perpendicular to the equipotential surface at a specific point and defines also the direction of the plumb line, i.e. the vertical direction, at this point.

For this thesis, the Gravity Gradient Tensor (GGT) W_{ij}, also called Eötvös tensor, is a central gravity field quantity. It contains the second order derivatives of the gravity potential W, which are measured by the GOCE satellite mission (actually, the provided satellite observation is not the gravity gradient tensor but the gravitational gradient tensor without any centrifugal constituents, see section 5.2). The symmetric gravity gradient tensor is the gradient of the gravity vector $\nabla \boldsymbol{g} = \nabla\nabla W$ given in the Cartesian coordinate system by

$$W_{ij} = \begin{pmatrix} \frac{\partial^2 W}{\partial x^2} & \frac{\partial^2 W}{\partial x \partial y} & \frac{\partial^2 W}{\partial x \partial z} \\ \frac{\partial^2 W}{\partial y \partial x} & \frac{\partial^2 W}{\partial y^2} & \frac{\partial^2 W}{\partial y \partial z} \\ \frac{\partial^2 W}{\partial z \partial x} & \frac{\partial^2 W}{\partial z \partial y} & \frac{\partial^2 W}{\partial z^2} \end{pmatrix} = \begin{pmatrix} W_{xx} & W_{xy} & W_{xz} \\ W_{xy} & W_{yy} & W_{yz} \\ W_{xz} & W_{yz} & V_{zz} \end{pmatrix} , \tag{2.44}$$

2.3.1 The normal gravity field

The gravity at two different points with the same geometrical distance to the Earth's center is varying due to the inhomogeneous mass distributions in the Earth's interior. Consequently, equipotential surfaces are not necessarily parallel and do not have a regular and smooth geometrical shape. To overcome this, a level ellipsoid is introduced, which approximates the geoid. This level ellipsoid represents a body which is associated with the so-called normal potential

$$U = V_{ell} + \Phi \,, \tag{2.45}$$

the sum of the gravitational potential V_{ell} of the ellipsoid and the centrifugal potential Φ. The normal potential is defined in such way that $U_0 = W_0 = constant$, i.e. the potential at the ellipsoid surface equals the gravity potential of the geoid. The normal potential can be expressed by closed formulas if described in ellipsoidal coordinates as shown in Heiskanen and Moritz (1967). A more convenient representation is given as spherical harmonics expansion of the normal gravitational potential for the exterior space

$$V_{ell} = \frac{GM}{R} \sum_{n=0}^{\infty} \left(\frac{R}{r}\right)^{n+1} c_{2n} P_{2n}(\cos\theta) \,, \tag{2.46}$$

which contains only even zonal terms c_{2n} ($m = 0$) due to the rotational symmetry of the ellipsoid and the symmetry with respect to the equator

$$c_{2n} = (-1)^n \frac{3e^{2n}}{(2n+1)(2n+3)} \left[1 + \frac{2n}{3}\left(1 - \frac{me'}{3q_0}\right)\right] \,, \tag{2.47}$$

with e, e' given in Eq. (2.3) and the auxiliary terms

$$\begin{aligned} q_0 &= \frac{1}{2}\left[\left(1 + \frac{3}{e'^2}\right)\arctan e' - \frac{3}{e'}\right] \,, \\ m &= \frac{\omega^2 a^2 b}{GM} \,. \end{aligned} \tag{2.48}$$

The centrifugal potential Φ, which is an integral part of the normal potential U, is not quoted at this place for practical reasons, as we may see in the following section.

In analogy to the actual gravity g on the geoid, the normal gravity γ_0 on the ellipsoid surface can be defined as the gradient of the normal potential $\boldsymbol{\gamma_0} = \nabla U_0$. A rigorous determination of the magnitude of γ_0 is possible by evaluating the well known formula of Somigliana

$$\gamma_0 = \frac{a\,\gamma_a \cos^2\varphi + b\,\gamma_b \sin^2\varphi}{\sqrt{a^2\cos^2\varphi + b^2\sin^2\varphi}} \,, \tag{2.49}$$

with the normal gravity at the equator γ_a

$$\gamma_a = \frac{GM}{ab}\left(1 - m - \frac{m\,e'\,q_0'}{6\,q_0}\right) \tag{2.50}$$

and the normal gravity at the poles γ_b

$$\gamma_b = \frac{GM}{a^2}\left(1 + \frac{m\, e'\, q'_0}{3\, q_0}\right) , \tag{2.51}$$

where

$$q'_0 = 3\left(1 + \frac{1}{e'^2}\right)\left(1 - \frac{\arctan e'}{e'}\right) - 1 . \tag{2.52}$$

For a specific height h above the ellipsoid, one can obtain the normal gravity γ_h from a series expansion of $\partial\gamma/\partial h$ leading to

$$\gamma_h = \gamma_0\left[1 - \frac{2}{a}\left(1 + f + m - 2f\sin^2\varphi\right)h + \frac{3}{a^2}h^2\right] , \tag{2.53}$$

with the ellipsoid flattening

$$f = \frac{a-b}{a} .$$

The reference ellipsoid and physical parameters for the derivation of the normal potential in this work are those corresponding to the Geodetic Reference System (GRS) 1980. The parameters and computational formulas can be found for instance in Moritz (1980b).

2.3.2 The disturbing potential and derived gravity field quantities

With the introduction of the level ellipsoid and its physical parametrization, the actual gravity field is linearized and split up into a first approximation represented by the normal gravity field and a remaining and comparably small residual part. In terms of potential, these deviations are denoted as the disturbing potential or anomalous potential T, indicating the difference between the normal potential U and the actual gravity potential W

$$T = W - U . \tag{2.54}$$

By building this difference we can see that the centrifugal part, which is the same in W and U (see Eqs. 2.42 and 2.45), cancels and thus does not have to be considered. Therefore, the disturbing potential T still satisfies the Laplace equation $\triangle T = 0$ outside the Earth's masses, so that it can also be expanded into a spherical harmonics series

$$T(r,\theta,\lambda) = \sum_{n=0}^{\infty}\left(\frac{R}{r}\right)^{n+1}\sum_{m=-n}^{n}\Delta\bar{a}_{nm}\,\bar{Y}_{nm}(\theta,\lambda) = \sum_{n=0}^{\infty}\left(\frac{R}{r}\right)^{n+1}T_n(\theta,\lambda), \tag{2.55}$$

with the fully normalized residual coefficients $\Delta\bar{a}_{nm}$, which are obtained by subtracting the normal gravitational potential coefficients from those of the actual gravitational potential.

If the mass of the reference ellipsoid is defined equally to the mass of the Earth, then the zero degree term of the series vanishes. Furthermore, if the origin of the ellipsoid is coinciding with the Earth's COM, also the first degree terms of the series are zero, so that

$$T(r,\theta,\lambda) = \sum_{n=2}^{\infty} \left(\frac{R}{r}\right)^{n+1} T_n(\theta,\lambda). \tag{2.56}$$

Looking at a specific point P_0 on the equipotential surface geoid and its equivalent point Q_0 projected along the ellipsoid normal onto the level ellipsoid so that $W_0(P_0) = U_0(Q_0)$, the geometrical discrepancy between P_0 and Q_0 is denoted as the geoid height or geoid undulation N, see Figure 2.4. It can be related to the disturbing potential $T(P_0)$ by the formula of Bruns

$$N = \frac{T(P_0)}{\gamma_0}\,. \tag{2.57}$$

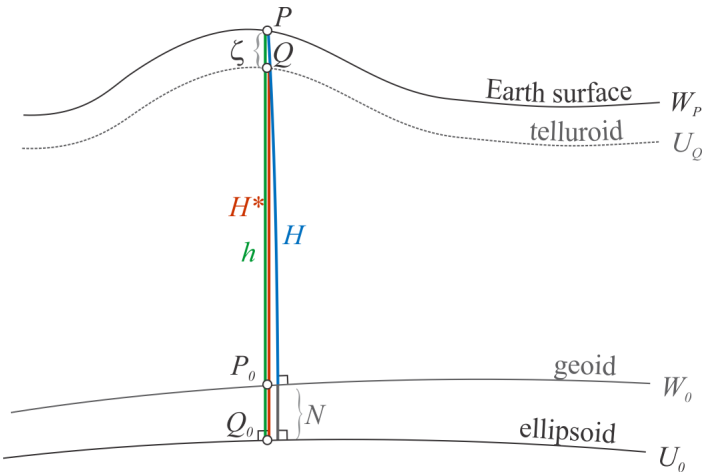

Figure 2.4: Interrelation between potential surfaces and heights

The same relation can be defined for a point P which is located at the ellipsoidal height h on the Earth's surface. According to the theory of Molodensky (Hofmann-Wellenhof and Moritz, 2005), for every surface point P with its gravity potential $W(P)$ one can find a corresponding point Q at the ellipsoidal height $h = H^*$, also denoted as normal height, at which the potential of the surface point equals the normal potential $W(P) = U(Q)$. This imaginary surface is called the telluroid, and the distance between P and Q is denoted as the height anomaly ζ. Hence, we can reconsider Bruns' formula at the surface point P and obtain

$$\zeta = \frac{T(P)}{\gamma_Q}\,. \tag{2.58}$$

In this way, the interrelation between normal heights H^*, orthometric heights H and ellipsoidal heights h can be found by

$$h = N + H = \zeta + H^*\,. \tag{2.59}$$

If we compare the gravity vector and the normal gravity vector at the same point P, we obtain the gravity disturbance vector

$$\boldsymbol{\delta g} = \boldsymbol{g}(P) - \boldsymbol{\gamma}(P) \,. \tag{2.60}$$

Its magnitude is also found by the derivative of the disturbing potential with respect to the height h along the ellipsoid normal

$$\delta g = -\frac{\partial T}{\partial h} \,. \tag{2.61}$$

The difference between the gravity vector $\boldsymbol{g}(P)$ at point P and the vector of normal gravity $\boldsymbol{\gamma}(Q)$ at point Q is defined as the gravity anomaly vector

$$\boldsymbol{\Delta g} = \boldsymbol{g}(P) - \boldsymbol{\gamma}(Q) \,. \tag{2.62}$$

Taking Bruns formula and the expression for the gravity disturbance in Eq. (2.61) into account and assuming that the vertical derivatives $\partial/\partial h$ are more or less identical at P and Q, one can derive the relation of disturbing potential and gravity anomaly

$$\Delta g = -\frac{\partial T}{\partial h} + \frac{1}{\gamma_0}\frac{\partial \gamma}{\partial h} T \,, \tag{2.63}$$

which is called the fundamental equation of physical geodesy.

The difference in the directions of the vectors are denoted as the deflections of the vertical, i.e. the deflections of the plumb line defined by $\boldsymbol{g}(P)$ from the ellipsoid normal defined by $\boldsymbol{\gamma}(Q)$. Conventionally, the deflections of the vertical are represented by a North-South component ξ and an East-West component η with

$$\begin{aligned} \xi &= \Phi - \varphi \,, \\ \eta &= (\Lambda - \lambda)\cos\varphi \,, \end{aligned} \tag{2.64}$$

the difference between astronomical coordinates Φ, Λ and ellipsoidal coordinates φ, λ. Likewise, the deflections can also be derived from the disturbing potential in a LNOF by

$$\begin{aligned} \xi &= -\frac{1}{\gamma_0}\frac{\partial T}{\partial x} \,, \\ \eta &= -\frac{1}{\gamma_0}\frac{\partial T}{\partial y} \,. \end{aligned} \tag{2.65}$$

Furthermore, we can also derive the gradient tensor of the anomalous potential T_{ij} in analogy to Eq. (2.44) by

$$T_{ij} = \begin{pmatrix} T_{xx} & T_{xy} & T_{xz} \\ T_{xy} & T_{yy} & T_{yz} \\ T_{xz} & T_{yz} & T_{zz} \end{pmatrix} \,. \tag{2.66}$$

2.3.3 Derivatives of the disturbing potential

From Eq. (2.65) and Eq. (2.66) we can see that for certain derived quantities of the disturbing potential we need the first and second order derivatives of the disturbing potential T in a LNOF with respect the local Cartesian coordinates x, y, z. For the later use in the LSC approach, it will be necessary to represent these derivatives with respect to geocentric (spherical) coordinates φ, λ, r, too. The corresponding relationships were derived by Tscherning (1976) and are summarized here. For a more compact notation, the partial derivatives are denoted as

$$\begin{aligned} T_n &= \frac{\partial T}{\partial n}, \\ T_{nn} &= \frac{\partial^2 T}{\partial n^2}, \qquad \text{with} \quad n = \{x, y, z\} \quad \text{or} \quad n = \{\varphi, \lambda, r\}\,. \end{aligned} \tag{2.67}$$

For the first order derivatives of T with respect to the Cartesian coordinates expressed in spherical coordinates we can write

$$T_x = \frac{1}{r}\, T_\varphi\,, \tag{2.68}$$

$$T_y = \frac{1}{r\,\cos\varphi}\, T_\lambda\,, \tag{2.69}$$

and

$$T_z = T_r\,. \tag{2.70}$$

The second order derivatives of the disturbing potential T, i.e. the components of the gradient tensor, are given by

$$T_{xx} = \frac{1}{r}\, T_r + \frac{1}{r^2} T_{\varphi\varphi}\,, \tag{2.71}$$

$$T_{xy} = \frac{1}{r^2\,\cos\varphi}\, T_{\varphi\lambda} + \frac{\tan\varphi}{r^2\,\cos\varphi}\, T_\lambda\,, \tag{2.72}$$

$$T_{xz} = \frac{1}{r}\, T_{r\varphi} - \frac{1}{r^2}\, T_\varphi\,, \tag{2.73}$$

$$T_{yy} = \frac{1}{r} T_r - \frac{\tan\varphi}{r^2}\, T_\varphi + \frac{1}{r^2\,\cos^2\varphi}\, T_{\lambda\lambda}\,, \tag{2.74}$$

$$T_{yz} = \frac{1}{r\,\cos\varphi} T_{r\lambda} - \frac{1}{r^2\,\cos\varphi}\, T_\lambda\,, \tag{2.75}$$

and

$$T_{zz} = T_{rr} \,. \tag{2.76}$$

2.3.4 Spherical approximation and linearization issues

The considerations made above assume that the reference surface for the normal gravity field is an ellipsoid. In geodetic practice it is common to treat the reference ellipsoid as if it was a sphere with a mean Earth radius $R = \sqrt[3]{a^2 b}$ which has the same volume as the ellipsoid in order to facilitate the equations for quantities of the disturbing gravity field. In this way, we can introduce the spherical approximation

$$\frac{\partial}{\partial h} = \frac{\partial}{\partial r} \quad \text{and} \quad \gamma = \frac{GM}{R^2} \,, \tag{2.77}$$

so that

$$\frac{1}{\gamma}\frac{\partial \gamma}{\partial h} = -\frac{2}{R} \,, \tag{2.78}$$

which results in the formula of the fundamental equation of physical geodesy in spherical approximation

$$\Delta g = -\frac{\partial T}{\partial r} - \frac{2}{R} T \,. \tag{2.79}$$

Using Eq. (2.79), also Δg can then be expanded into a spherical harmonics series

$$\Delta g(r, \theta, \lambda) = \frac{1}{R} \sum_{n=0}^{\infty} (n-1) \left(\frac{R}{r}\right)^{n+1} T_n(\theta, \lambda). \tag{2.80}$$

With this approximation, an error in the order of the Earth's flattening of 0.3% is accepted in the formulas, which are then formally spherical expressions. However, the actual geometric reference surface is still the ellipsoid Moritz (1980a). In the case of the geoid, which has a global Root Mean Square (RMS) of approximately ±30 m, this would lead to a corresponding error of 0.09 m. This is considerably higher than the nowadays desired geoid accuracy in the order of a few centimeters or even less. From Bruns' formula given in Eq. (2.57) we know that the geoid height is a function of the disturbing potential T and the normal gravity γ_0, which is only depending on the latitude. The disturbing potential in turn represents the second order element of the linearized gravity field, which is in first approximation described by the normal potential of the reference ellipsoid according to the conventional gravity field theory as shown in section 2.3.2.

With the advent of global Earth Gravity field Model (EGM) in the last decades, which were substantially improved due to satellite based observations in particular in the last few years, the first order approximation of the gravity field using the normal potential may be considered as a deprecated approach. According to several validation studies, e.g. Gruber (2009), Gruber et al. (2011) or Ferreira et al. (2013), the differences between EGM-derived geoid heights and GPS/levelling heights in different regions of the world show a RMS of 0.3 m for the long wavelength structures of the gravity field. We could now replace the normal

potential by such an EGM, which then leads to an improved first order approximation of the actual gravity field. Assuming that the results of the validation studies are correct and valid for the whole Earth and the entire spectrum, the remaining linearization error due to the spherical approximation can be assessed with a RMS of roughly 1 mm. Especially in the context of geoid determination these considerations will be important, since they allow us to work with spherical approximation without introducing a significant loss of accuracy.

3 Least Squares Collocation

Least squares methods for the prediction and interpolation of gravity were introduced in geodesy in the early 1960's, with the one of the first appearances in literature given by Moritz (1962). An overview on the least squares prediction method can also be found in Heiskanen and Moritz (1967). The approach was enhanced and extended to the LSC method by Krarup (1969). A fundamental treatment of these methods is summarized by Moritz (1980a). This chapter gives an excerpt of this book reviewing the basics of the LSC approach.

3.1 Least squares prediction and Least Squares Collocation

Let l be a vector of observations $l = (l_1, l_2, \ldots, l_q)^T$ and s be a vector of signals $s = (s_1, s_2, \ldots, s_p)^T$ of the same quantities as in l so that s is approximated by a linear combination of the elements of l

$$\hat{s} = Hl\,. \tag{3.1}$$

We assume that l and s are random quantities which have, in probabilistic sense, an expectation value (or mean value) $\mathrm{E}\{l\} = \mathrm{E}\{s\} = 0$, i.e. they are centered. Furthermore, we can define the auto-covariance matrices for l and s and their cross-covariance matrix by

$$\begin{aligned} C_{ll} &= \mathrm{cov}(l,l) &&= \mathrm{E}\{l\, l^T\} \\ C_{ss} &= \mathrm{cov}(s,s) &&= \mathrm{E}\{s\, s^T\} \\ C_{sl} &= \mathrm{cov}(s,l) &&= \mathrm{E}\{s\, l^T\}\,. \end{aligned} \tag{3.2}$$

The discrepancy between the approximated $\hat{s}$ and true values of s is then the error vector ϵ

$$\epsilon = \hat{s} - s \tag{3.3}$$

with the corresponding error covariance matrix

$$C_{\epsilon\epsilon} = \mathrm{cov}(\epsilon,\epsilon) = \mathrm{E}\{\epsilon\, \epsilon^T\} = \mathrm{E}\{(\hat{s}-s)\,(\hat{s}-s)^T\}\,. \tag{3.4}$$

We want to find the minimum error variances σ_i^2 of each of the estimated signals $\hat{s}_i$, which are the trace values of the error covariance matrix $C_{\epsilon\epsilon}$. Therefore, we use Eq. (3.1) in Eq. (3.4)

and obtain after some reordering and using the fact that $C_{sl} = C_{ls}^T$

$$C_{\epsilon\epsilon} = \underbrace{C_{ss} - C_{sl}\ C_{ll}^{-1}\, C_{ls}}_{A} + \underbrace{\left(H - C_{sl}\ C_{ll}^{-1}\right)\, C_{ll}\, \left(H - C_{sl}\ C_{ll}^{-1}\right)^T}_{B} . \tag{3.5}$$

In this way we have expressed $C_{\epsilon\epsilon}$ in such way that the left terms of Eq. (3.5), indicated by the letter A, are independent of the choice of H and are thus the same for all linear estimates, whereas the right term, summarized by the letter B, is varying with H. We now can minimize $C_{\epsilon\epsilon}$ if this right term is zero, which can be achieved by setting

$$H = C_{sl}\ C_{ll}^{-1} , \tag{3.6}$$

and relying on the fact that we consider regular and positive definite covariance matrices. Consequently, the best, in terms of minimum variance, linear estimate for s from a set of quantities l is given by

$$\hat{s} = C_{sl}\ C_{ll}^{-1}\, l , \tag{3.7}$$

which is purely based on the statistical correlation between the quantities in l and s, given by the cross- and auto-covariances in C_{sl} and C_{ll}. The definition of such a covariance function, which is able to represent these correlations, will be the issue of the following section 3.2. The corresponding error covariance matrix of the prediction is then given by

$$C_{\epsilon\epsilon} = C_{ss} - C_{sl}\ C_{ll}^{-1}\, C_{ls} . \tag{3.8}$$

This is the basic principle of *least squares prediction*.

In physical geodesy we have now the case that we want to predict quantities that are linear functionals of the disturbing potential T from measurements which are themselves linear functionals of T. This generalization of the least squares prediction problem is called *Least Squares Collocation*. We define l_i as an observation at a distinct point Q, which represents a functional of the disturbing potential

$$l_i = L_i\, T(Q) , \tag{3.9}$$

with the linear operator L_i applied to $T(Q)$. In vector notation we can summarize all observations and functionals to $l = (l_1, l_2, \ldots, l_q)^T$ and $L = (L_1, L_2, \ldots, L_q)^T$ and write

$$l = L\, T . \tag{3.10}$$

Furthermore, we define an averaging operator $\mathrm{M}\{\cdot\}$ instead of the expectation $\mathrm{E}\{T\}$. In case of the disturbing potential, M is homogeneous and isotropic and $\mathrm{M}\{T\} = 0$ by requirement (see section 3.2). We still have the expectation $\mathrm{E}\{l_i\} = \mathrm{M}\{l_i\} = 0$ and it is justified, due to the commutative property of M and L_i, to write $\mathrm{M}\{l_i\} = L_i \mathrm{M}\{T\} = 0$. Therefore, we have the same preconditions as for least squares prediction with the difference, that we have to consider the application of the linear operators L in the derivation of the covariances in C_{ll}. Using the aforementioned properties, we get the covariance between the measurements l_i at point P and l_j at point Q $(i, j = 1 \ldots q)$ by

$$C_{ij} = \mathrm{cov}(l_i, l_j) = \mathrm{M}\{L_i^P\, T(P)\, L_j^Q\, T(Q)\} = L_i^P\, L_j^Q\, \mathrm{M}\{T(P)\, T(Q)\} , \tag{3.11}$$

with the covariance function of the disturbing potential, which is depending on the location of the points P and Q

$$K(P,Q) = \mathrm{M}\{T(P)\,T(Q)\}\,, \tag{3.12}$$

so that we obtain the single entries for the covariance matrix C_{ll}

$$C_{ij} = L_i^P\, L_j^Q\, K(P,Q)\,, \tag{3.13}$$

which is equivalent to covariance propagation in classical sense. Note that L_i^P and L_j^Q indicate that the linear operators are evaluated at the corresponding points P and Q, where the measurements took place. In analogy to the measurements, also the signals s to be estimated can be linear functionals of the disturbing potential T at some point P and thus, as in Eq. (3.10)

$$s = S\,T, \quad \text{with} \quad s = (s_1, s_2, \ldots, s_p)^T\,, \quad \text{and} \quad S = (S_1, S_2, \ldots, S_p)^T\,. \tag{3.14}$$

Again, the covariances of C_{sl} between the signals s_k at a point P and the measurements l_i at a point Q have to be derived. This is achieved once more by covariance propagation

$$C_{ki} = \mathrm{cov}(s_k, l_i) = S_k^P\, L_i^Q\, K(P,Q), \quad k = 1, \ldots p, \quad i = 1, \ldots q\,. \tag{3.15}$$

Hence, we can use the least squares prediction formula of Eq. (3.7)

$$\hat{s} = C_{sl}\;\; C_{ll}^{-1}\, l\,, \tag{3.16}$$

also for predicting an arbitrary gravity field quantity that is a linear functional of the disturbing potential T, from whatever other gravity field quantities of the same field, if the covariances are derived via a correct and consistent covariance propagation from a suitable covariance function, which is describing the analytical structure of the anomalous field. There are some remarkable properties of LSC:

- The data is reproducible, which means if the signals s to be estimated are the same as the input observations l, then $C_{sl} = C_{ll}$ and thus $\hat{l} = C_{ll}C_{ll}^{-1}l = l$.
- It is invariant with respect to (w.r.t.) linear transformation of the estimated signals. It does not matter whether one estimates a distinct quantity and then transforms it to another linear functional of T, or the linear functional is estimated directly.
- It is invariant w.r.t. linear transformation of the input data. If the input data l is transformed to $l' = Al$, then $\hat{s} = C_{sl'}\, C_{l'l'}^{-1} l' = C_{sl}C_{ll}^{-1}l$.

Until now, only the case of error-free observations was considered. However, real measurements will always be deteriorated by noise. We will assume that the measurements l_i are composed of a true signal part $t_i = L_i\, T$ which is affected by the random errors or white noise n_i

$$l_i = t_i + n_i\,. \tag{3.17}$$

Under these circumstances, we have to reconsider the covariance matrices C_{sl} and C_{ll} once

again. For C_{ll} we can write

$$C_{ll} = C_{tt} + C_{tn} + C_{nt} + C_{nn} \,, \tag{3.18}$$

and it can be shown that $C_{tn} = C_{nt} = 0$ under the assumption that the noise n and the signal component t are uncorrelated. Equivalently, the cross-covariance matrix C_{sl} is given by

$$C_{sl} = C_{st} + C_{sn} \,, \tag{3.19}$$

and again s and n are uncorrelated, so that $C_{sn} = 0$. Consequently, we obtain the basis formula of LSC with noise

$$\hat{s} = C_{st} \ (C_{tt} + C_{nn})^{-1} \ l \,, \tag{3.20}$$

with the error-covariance matrix of the estimate

$$C_{\epsilon\epsilon} \ = C_{ss} - C_{st} \, (C_{tt} + C_{nn})^{-1} \, C_{ts} \,. \tag{3.21}$$

We can use Eq. (3.20) in a further step to estimate the signal part t of the observations l by

$$\hat{t} = C_{tt} \ (C_{tt} + C_{nn})^{-1} \ l \,, \tag{3.22}$$

which is nothing else than filtering out the noise from the observations. If we solve for l and insert into Eq. (3.20) we arrive at

$$\hat{s} = C_{st} \ \ C_{tt}^{-1} \, \hat{t} \,, \tag{3.23}$$

which is the solution of the error-free collocation based on the filtered $\hat{t}$. Hence, LSC is able to filter the measurements l and predict the signals s based on the minimum variance principle at once.

The most generalized form of this approach is LSC with parameters, which is given by

$$l = Ax + s + n \tag{3.24}$$

and combines the methods of least squares adjustment, filtering and prediction in one unified approach. It splits up the measurement l into a (linearized) systematic part Ax with the parameters x and the design matrix A relating x and l, and the random parts s, the signal, and n, the noise. A detailed treatment of the general LSC approach can be found in Moritz (1972) and Moritz (1980a). In this thesis, the systematic constituents Ax are not estimated specifically but are assumed to be known (for instance by an a-priori global gravity field model). The Least Squares Collocation approach is used here to predict gravity field quantities from gravity measurements in the presence of noise according to the equations (3.20) and (3.21) with special focus on the application of the gradient observation type of the GOCE mission.

3.2 Covariance functions and degree variances

In order to describe the statistical behaviour of the anomalous gravity field, covariance functions of the gravity field quantities are introduced. In case of LSC, where quantities that are linear functionals of the disturbing potential are estimated or serve as input data, the covariance function of the disturbing potential T is essential, since all necessary covariances between the functionals are derived from this covariance function by covariance propagation, see section 3.1.

To obtain the covariance function of the disturbing potential, first a measure for the expectation value of T has to be defined (the consideration of the disturbing potential as a stochastic process is extensively discussed in Moritz (1980a)). Hence, an average operator $\mathrm{M}\{\cdot\}$ is defined to give the expectation value in such way that $\mathrm{M}\{T\} = 0$ on global scale with

$$\mathrm{M}\{T\} = \frac{1}{8\pi^2} \iint_{\sigma} \int_{\alpha=0}^{2\pi} T(\theta,\lambda)\, \mathrm{d}\sigma\, \mathrm{d}\alpha = \frac{1}{4\pi} \iint_{\sigma} T(\theta,\lambda)\, \mathrm{d}\sigma\,, \tag{3.25}$$

where the integration is performed over the unit sphere σ as in Eq. (2.23) with θ and λ denoting the spherical co-latitude and longitude, so this average is homogeneous. The integration with respect to the azimuth α is introduced in order to obtain a covariance function of the disturbing potential $K(P,Q)$ between two points $P(\theta,\lambda)$ and $Q(\theta',\lambda')$

$$\mathrm{M}\{T(P)\,T(Q)\} = K(P,Q) = K(\psi) = \frac{1}{8\pi^2} \iint_{\sigma} \int_{\alpha=0}^{2\pi} T(\theta,\lambda)\, T(\theta',\lambda')\, \mathrm{d}\sigma\, \mathrm{d}\alpha\,, \tag{3.26}$$

which is only depending on the spherical distance ψ between P and Q

$$\cos\psi = \sin\varphi\, \sin\varphi' + \cos\varphi\, \cos\varphi'\, \cos(\lambda' - \lambda) \tag{3.27}$$

and not on the direction. Therefore, the average operator can be considered as isotropic. According to Heiskanen and Moritz (1967), the covariance function $K(\psi)$ can be expanded into a spherical harmonics series of the form

$$K(\psi) = \sum_{n=2}^{\infty} k_n P_n(\cos\psi)\,. \tag{3.28}$$

The coefficients k_n can be obtained by

$$k_n = \frac{2n+1}{2} \int_{\psi=0}^{\pi} K(\psi) P_n(\cos\psi)\, \sin\psi\, \mathrm{d}\psi\,. \tag{3.29}$$

We can now insert Eq. (3.26) into Eq. (3.29) and, after some reordering, performing integrations as outlined in Heiskanen and Moritz (1967) we get

$$k_n = \frac{1}{4\pi} \iint_{\sigma} T(\theta,\lambda)\, T_n(\theta,\lambda)\, \mathrm{d}\sigma\,, \tag{3.30}$$

where $T_n(\theta, \lambda)$ are the Laplace's surface spherical harmonics (refer to section 2.2.1 or compare with Eq. (2.56)) of the disturbing potential. In analogy to Eq. (3.25) and inserting Eq. (2.56) for $T(\theta, \lambda)$ into Eq. (3.30) , we arrive at

$$k_n = \mathrm{M}\{\sum_{n=2}^{\infty} T_n(\theta, \lambda)\, T_n(\theta, \lambda)\} = \mathrm{M}\{T_n(\theta, \lambda)^2\}\,. \tag{3.31}$$

Recalling from Eq. (2.22) that the basis polynomials of the Laplace's surface spherical harmonics $T_n(\theta, \lambda)$ are orthogonal, we finally obtain for the coefficients k_n

$$k_n = \sum_{m=0}^{n} \left(\bar{c}_{nm}^2 + \bar{s}_{nm}^2\right)\,, \tag{3.32}$$

which are called degree variances. They represent the variances of the Laplace's surface spherical harmonics of degree n. The degree variances can be interpreted as the power spectral density of a function, in this case of the disturbing potential, and indicate the energy content of the signal per frequency n. Note that the spherical harmonics coefficients in Eq. (3.32) are fully normalized as given in Eq. (2.27), while the Legendre polynomials in Eq. (3.28) are the conventional polynomials, see section A.1.

Until now, we have always considered a covariance function for points P and Q located on the unit sphere σ. To derive a covariance function which is also valid outside the sphere, we use the knowledge that the spherical harmonics expansion of the disturbing potential is harmonic outside a sphere with radius R with $(R/r)^{n+1}$ as given in Eq. (2.56). In the context of LSC, this radius R is commonly also denoted as Bjerhammar radius R_B of a sphere completely enclosed by the Earth's surface, which is a requirement to obtain a convergent covariance function (Moritz, 1980a). Applying this information gives the spatial covariance function of the disturbing potential for points $P(r, \theta, \lambda)$, $Q(r', \theta', \lambda')$ outside the sphere

$$K(r, r', \psi) = \sum_{n=2}^{\infty} \left(\frac{R^2}{rr'}\right)^{n+1} k_n\, P_n(\cos\psi)\,. \tag{3.33}$$

In practice, the disturbing potential can not be determined by direct measurements. Hence, the respective coefficients k_n of the covariance function have to be determined from other sources. One option is to use a global EGM, which implicitly provides the (in most cases fully normalized) spherical harmonics coefficients $\bar{c}_{nm}$, $\bar{s}_{nm}$, from which the degree variances can be computed according to Eq. (3.32). For more localized applications, it is common to derive the coefficients from the covariance function of gravity anomalies Δg, which are deduced from terrestrial gravity measurements. In Eq. (2.79) we already found the linear operator that transforms the disturbing potential into gravity anomalies, which is given by the factor $(n-1)/r$. From Eq. (3.13) we know that we can derive the covariance of any gravity quantity by covariance propagation applied to the covariance function of the disturbing potential. Consequently, the covariance function for gravity anomalies $C(P, Q)$ can be computed by

$$C(P, Q) = \sum_{n=2}^{\infty} \frac{(n-1)^2}{rr'} \left(\frac{R^2}{rr'}\right)^{n+1} k_n\, P_n(\cos\psi)\,. \tag{3.34}$$

With some reformulation, we can introduce the degree variances of the gravity anomalies c_n by

$$c_n = \left(\frac{n-1}{R}\right)^2 k_n \,, \tag{3.35}$$

so we finally have related the covariance function for gravity anomalies to the degree variances of the disturbing potential k_n and obtain

$$C(P,Q) = \sum_{n=2}^{\infty} \left(\frac{R^2}{rr'}\right)^{n+2} c_n \, P_n(\cos\psi) \,. \tag{3.36}$$

3.3 Covariance propagation for anomalous gravity quantities

As shown in section 3.1 the LSC approach is based on the statistical correlations among the signals s to be estimated and the observations l, which are assembled in the cross-covariance matrix C_{sl}, as well as on the correlations among the observations themselves represented by the covariance matrix C_{ll}. To retrieve the single entries of these matrices, a consistent covariance propagation of the covariance function of the disturbing potential $K(r, r', \psi)$ (see section 3.2) according to Eq. (3.13) has to be performed.

To illustrate the derivation of the covariances between functionals of the disturbing potential, the covariance propagation for geoid heights, gravity anomalies and gravity gradients given at points P and Q is shown. The coordinates with respect to P are denoted as x, y, z in a LNOF with its Z-axis defined radially outwards, and φ, λ, r in their spherical representation. For Q, they are denoted as x', y', z' and φ', λ', r'. The linear operators L_i^P or L_j^Q relating the gravity quantities to the disturbing potential are already introduced in section 2.3.2 and have to be applied to the covariance function accordingly following the rule of covariance propagation. Hence, the covariance between two geoid heights $N(P)$ and $N'(Q)$ is given by

$$cov(N, N') = \frac{1}{\gamma_0} \left(\frac{1}{\gamma_0'} K\right) = \frac{1}{\gamma_0 \gamma_0'} K \,. \tag{3.37}$$

In the same way, the covariance between two gravity anomalies $\Delta g(P)$ and $\Delta g'(Q)$ can be derived with

$$cov(\Delta g, \Delta g') = \left(-\frac{\partial}{\partial r} - \frac{2}{r}\right)\left(-\frac{\partial K}{\partial r'} - \frac{2}{r'} K\right) = \frac{\partial^2 K}{\partial r \partial r'} + \frac{2}{r}\frac{\partial K}{\partial r'} + \frac{2}{r'}\frac{\partial K}{\partial r} + \frac{4}{rr'} K \,. \tag{3.38}$$

The covariance between a gravity anomaly Δg at P and a geoid height N at Q is calculated by

$$cov(\Delta g, N') = \left(-\frac{\partial}{\partial r} - \frac{2}{r}\right)\left(\frac{1}{\gamma_0'} K\right) = \frac{1}{\gamma_0'}\left(-\frac{\partial K}{\partial r} - \frac{2}{r} K\right) \,. \tag{3.39}$$

The linear operators for anomalous gravity gradients were already shown in section 2.3.3. Hence, the covariance between a geoid height N and a vertical gradient $T_{z'z'}$ is given by

$$cov(N, T_{z'z'}) = \frac{1}{\gamma_0} \frac{\partial^2 K}{\partial r'^2} , \tag{3.40}$$

or between a geoid height N and a $T_{x'x'}$ gradient by

$$cov(N, T_{x'x'}) = \frac{1}{\gamma_0} \left(\frac{1}{r'} \frac{\partial K}{\partial r'} + \frac{1}{r'^2} \frac{\partial^2 K}{\partial \varphi'^2} \right) . \tag{3.41}$$

In the same way, for gravity anomalies and gradients we have for instance

$$cov(\Delta g, T_{z'z'}) = \left(-\frac{\partial}{\partial r} - \frac{2}{r} \right) \frac{\partial^2 K}{\partial r'^2} = -\frac{\partial^3 K}{\partial r \partial r'^2} - \frac{2}{r} \frac{\partial^2 K}{\partial r'^2} , \tag{3.42}$$

and

$$\begin{aligned} cov(\Delta g, T_{x'x'}) &= \left(-\frac{\partial}{\partial r} - \frac{2}{r} \right) \left(\frac{1}{r'} \frac{\partial K}{\partial r'} + \frac{1}{r'^2} \frac{\partial^2 K}{\partial \varphi'^2} \right) = \\ &= -\frac{1}{r'} \frac{\partial^2 K}{\partial r \partial r'} - \frac{1}{r'^2} \frac{\partial^3 K}{\partial r \partial \varphi'^2} - \frac{2}{r r'} \frac{\partial K}{\partial r'} - \frac{2}{r r'^2} \frac{\partial^2 K}{\partial \varphi'^2} . \end{aligned} \tag{3.43}$$

If the covariance between two vertical gradients T_{zz} and $T_{z'z'}$ has to be derived, the covariance expression is still rather simple

$$cov(T_{zz}, T_{z'z'}) = \left(\frac{\partial^2}{\partial r^2} \right) \left(\frac{\partial^2 K}{\partial r'^2} \right) = \frac{\partial^4 K}{\partial r^2 \partial r'^2} . \tag{3.44}$$

The covariance between T_{xx} and $T_{x'x'}$ is

$$\begin{aligned} cov(T_{xx}, T_{x'x'}) &= \left(\frac{1}{r} \frac{\partial}{\partial r} + \frac{1}{r^2} \frac{\partial^2}{\partial \varphi^2} \right) \left(\frac{1}{r'} \frac{\partial K}{\partial r'} + \frac{1}{r'^2} \frac{\partial^2 K}{\partial \varphi'^2} \right) = \\ &= \frac{1}{r r'} \frac{\partial^2 K}{\partial r \partial r'} + \frac{1}{r^2 r'} \frac{\partial^3 K}{\partial \varphi^2 \partial r'} + \frac{1}{r r'^2} \frac{\partial^3 K}{\partial r \partial \varphi'^2} + \frac{1}{r^2 r'^2} \frac{\partial^4 K}{\partial \varphi^2 \partial \varphi'^2} . \end{aligned} \tag{3.45}$$

This derivation of covariance expressions can be performed for any other gravity gradient and also other quantities in the same manner as shown above. For the sake of completeness, the covariance expressions for quantities up to second order derivatives of the anomalous potential are derived in Appendix A.3. Note that a change of quantities in P and Q implies that the corresponding linear operators L_i^P and L_j^Q have to be evaluated at the respective other point L_i^Q and L_j^P. This does not change composition of the covariance expressions, but is simply obtained by changing all the corresponding variables from $\gamma_0, x, y, z, \varphi, \lambda, r$ to $\gamma_0', x', y', z', \varphi', \lambda', r'$ and vice versa.

3.4 Derivatives of the covariance function

As we have seen in the preceding section, the covariance propagation leads to expressions that incorporate derivatives of the covariance function up to the order four. Starting with the general three-dimensional case of the covariance function from Eq. (3.33)

$$K(P,Q) = K(r,r',\cos\psi) = \sum_{n=0}^{\infty} \left(\frac{R^2}{rr'}\right)^{n+1} k_n \, P_n(\cos\psi) \,,$$

the radial derivatives with respect to r and r' up to order four can be computed by (for simplification we denote $K(r,r',\cos\psi)$ as K)

$$\frac{\partial K}{\partial r} = \sum_{n=0}^{\infty} -\frac{n+1}{r} \left(\frac{R^2}{rr'}\right)^{n+1} k_n \, P_n(\cos\psi) \,, \tag{3.46}$$

$$\frac{\partial^2 K}{\partial r \partial r'} = \sum_{n=0}^{\infty} \frac{(n+1)^2}{rr'} \left(\frac{R^2}{rr'}\right)^{n+1} k_n \, P_n(\cos\psi) \,, \tag{3.47}$$

$$\frac{\partial^2 K}{\partial r^2} = \sum_{n=0}^{\infty} \frac{(n+1)(n+2)}{r^2} \left(\frac{R^2}{rr'}\right)^{n+1} k_n \, P_n(\cos\psi) \,, \tag{3.48}$$

$$\frac{\partial^3 K}{\partial r^2 \partial r'} = \sum_{n=0}^{\infty} -\frac{(n+1)^2(n+2)}{r^2 r'} \left(\frac{R^2}{rr'}\right)^{n+1} k_n \, P_n(\cos\psi) \,, \tag{3.49}$$

and

$$\frac{\partial^4 K}{\partial r^2 \partial r'^2} = \sum_{n=0}^{\infty} \frac{(n+1)^2(n+2)^2}{r^2 r'^2} \left(\frac{R^2}{rr'}\right)^{n+1} k_n \, P_n(\cos\psi) \,. \tag{3.50}$$

Basically, the radial derivatives are obtained by including an additional factor in the summation, which is depending on the degree of the expansion and the radii, for which the derivatives are performed. Note that interchanging r and r' in the differentiation only changes the division of the factor from r to r' and vice versa.

The derivatives with respect to the spherical coordinates φ, λ and φ', λ' are not that straightforward. They imply that we have to find the derivatives of the Legendre polynomials $P_n(\cos\psi)$, which are themselves a function of the cosine of the spherical distance ψ, as we know from Eqs. (3.27) and (3.28). To solve this problem, we can apply the chain rule of differentiation, which for example leads to a derivative with respect to φ

$$\frac{\partial K}{\partial \varphi} = \frac{\partial K}{\partial t}\frac{\partial t}{\partial \varphi} = \sum_{n=0}^{\infty} \left(\frac{R^2}{rr'}\right)^{n+1} k_n \, \frac{\partial P_n(t)}{\partial t}\frac{\partial t}{\partial \varphi} \,, \tag{3.51}$$

by introducing the substitution

$$t = \cos\psi \, . \tag{3.52}$$

For higher order derivatives with respect to a horizontal coordinate, the product rule has to be considered. Hence, a second order derivative has the form

$$\begin{aligned} \frac{\partial^2 K}{\partial\varphi^2} &= \frac{\partial^2 K}{\partial t^2}\left(\frac{\partial t}{\partial\varphi}\right)^2 + \frac{\partial K}{\partial t}\frac{\partial^2 t}{\partial\varphi^2} = \\ &= \sum_{n=0}^{\infty}\left(\frac{R^2}{rr'}\right)^{n+1} k_n \left[\frac{\partial^2 P_n(t)}{\partial t^2}\left(\frac{\partial t}{\partial\varphi}\right)^2 + \frac{\partial P_n(t)}{\partial t}\frac{\partial^2 t}{\partial\varphi^2}\right] . \end{aligned} \tag{3.53}$$

The further differentiations of the covariance function up to the fourth order are shown in Appendix A.2. Essentially, what is needed to derive the higher order derivatives of $K(r, r', \cos\psi)$ are the linear combinations of derivatives of K with respect to r, r' and $t = \cos\psi$ and the derivatives of $t = \cos\psi$ with respect to the spherical coordinates φ, λ and φ', λ'.

3.5 Analytic covariance models

In the previous section 3.2 it was already mentioned that the degree variances k_n for the covariance function of the disturbing potential T given in Eq. (3.33) can for instance be obtained from the spherical harmonics coefficients of a global EGM. Although the EGM represents the best fit of the gravity field on global scale, this is not necessarily true for local or regional applications, where the statistics of the anomalous potential or of derived quantities may be considerably different from the global average. Thus, on local scale it is common to fit a Model Covariance Function (MCF) to an Empirical Covariance Function (ECF) of actual measurements, e.g. terrestrial gravity anomalies, given in the area of interest. In order to derive an ECF of a set of given discrete observations $l(\varphi, \lambda)$ within a restricted area, the observation pairs l_i, l_j can be arranged in predefined distance classes k, so that the spherical distance $\psi_{k-1} < \psi_{ij} < \psi_k$, see Knudsen (1987). The ECF can then be found by

$$ECF(k) = \frac{1}{N_k}\sum_{i,j}^{N_k} l_i l_j \, , \tag{3.54}$$

where N_k denotes the number of observation pairs in the respective distance class k.

In practice, a local covariance function model is commonly represented by a Tscherning-Rapp degree variance model, which was developed in a closed analytical form in Tscherning and Rapp (1974). Within this thesis, the model of the form

$$K(r, r', \psi) = \sum_{n=2}^{\infty}\left(\frac{R_B^2}{rr'}\right)^{n+1} \frac{A}{(n-1)(n-2)(n+B)} P_n(\cos\psi) \, , \tag{3.55}$$

is used, which describes the degree variances k_n of the disturbing potential T by

$$k_n = \frac{A}{(n-1)(n-2)(n+B)} \,. \tag{3.56}$$

In this relation A is a constant value of the units $[(\mathrm{m/s})^4]$ in order to obtain the degree variances in the corresponding potential units, while B is another constant integer variable. These constants, A, B, and also the Bjerhammar radius R_B can be estimated within a least squares adjustment procedure, see again Knudsen (1987). If the purpose is to fit a covariance model to an ECF based on gravity anomalies, we have consider the relation defined Eq. (3.34) and obtain the respective MCF as

$$cov(\Delta g, \Delta g') = \sum_{n=2}^{\infty} \frac{{R_B}^{2n+2}}{(rr')^{n+2}} \, \frac{A(n-1)}{(n-2)(n+B)} \, P_n(\cos\psi) \,, \tag{3.57}$$

which represents the fundamental relationship between the covariances of gravity anomalies and the parameters we are looking for.

In this study we will not only use terrestrial observations but also gravity gradient measurements from the GOCE mission. Hence, a combined adjustment of the parameters to fit both empirical covariance functions in a best possible way can be advantageous. For this reason, the MCF for vertical gradients T_{zz} can be derived by considering Eq. (3.50)

$$cov(T_{zz}, T_{z'z'}) = \sum_{n=2}^{\infty} \left(\frac{R_B^2}{rr'}\right)^{n+1} \, \frac{(n+1)^2(n+2)^2}{r^2 r'^2} \, \frac{A}{(n-1)(n-2)(n+B)} \, P_n(\cos\psi) \,. \tag{3.58}$$

By linearization of Eqs. (3.57) and (3.58) with respect to A, B and R_B it is then possible to solve for these unknown parameters within a least squares adjustment. This will be applied and further investigated in chapter 7.

In this thesis, we only consider stationary and isotropic covariance functions, see section 3.2. This means, that we assume the gravity field to have a constant mean (globally, the expectation of the anomalous potential $\mathrm{M}\{T\} = 0$), and furthermore that the covariance is independent of the spatial position and direction. However, these assumptions are quite often violated in reality. For instance, let us consider only a subset of the Earth's surface, which has regions of rough topography on the one hand, as well as regions of rather flat terrain on the other hand. It is very likely that the covariance in the mountainous area is not equal to the one in the flat terrain, so it is not stationary. Furthermore, the covariance may be depending on the outline of the spatial characteristics, e.g. the direction of mountain ridges or trenches, and thus it is not isotropic.

A review of various methods that deal with the non-stationarity problem in spatial data is for instance given in Darbeheshti and Featherstone (2010). They suggest to use an approach proposed in Darbeheshti and Featherstone (2009) for a non-stationary covariance modeling in LSC, and show some first results and benefits when applied to a 2D-LSC prediction problem. In the frame of the official GOCE processing using the so-called space-wise approach (see section 5.4.3), strategies for anisotropic covariance modeling within this particular application have successfully been developed (Migliaccio et al. (2011), Gatti et al. (2013)). In this thesis, such a non-stationary and anisotropic covariance modeling is not considered. Instead, it is

aimed at reducing the irregularities of the gravity field to the best possible extent within a consistent RCR procedure, see chapter 4. In this way, homogeneous anomalous gravity quantities should be obtained, which justify the use of covariance models as explained in the beginning of this section.

3.6 The sum of a series of Legendre polynomials and its derivatives

The covariance functions treated in this thesis can be understood as sums of a series of Legendre polynomials with specific factors applied. There exists a recursive algorithm for the computation of such Legendre polynomials sums which is also capable of calculating their derivatives up to an arbitrary high order. It is proposed by Tscherning and Rapp (1974) for the computation of a covariance function and uses the Clenshaw summation based on Clenshaw (1955). Let

$$f(x) = \sum_{n=0}^{N} c_n F_n(x) \,, \tag{3.59}$$

be a function in which $F_n(x)$ satisfies a recurrence condition

$$F_{n+1}(x) + \alpha(n,x) F_n(x) + \beta(n,x) F_{n-1}(x) = 0 \,, \tag{3.60}$$

with $\alpha(n,x)$ and $\beta(n,x)$ being arbitrary functions depending on n and (not necessarily) x. By defining a recurrence quantity

$$b_n(x) = c_n - \alpha(n,x) b_{n+1}(x) - \beta(n,x) b_{n+2}(x) \,, \tag{3.61}$$

with $b_{N+1} = b_{N+2} = 0$, the sum can be derived by

$$f(x) = \sum_{n=0}^{N} c_n F_n(x) = b_0(x) F_0(x) + b_1(x) \left[F_1(x) + \alpha_0(x) F_0(x) \right] \,. \tag{3.62}$$

For LSC we have to consider a covariance function, which is, as shown previously, a sum of Legendre polynomials of the form given in Eq. (3.33)

$$K(r, r', \cos\psi) = \sum_{n=0}^{N} \left(\frac{R^2}{r r'} \right)^{n+1} k_n \, P_n(\cos\psi) \,.$$

We can substitute $\cos\psi = t$ and combine the first two terms in the sum to a new factor

$$c_n = \left(\frac{R^2}{r r'} \right)^{n+1} k_n \,, \tag{3.63}$$

to get the notation

$$K(t) = \sum_{n=0}^{N} c_n \, P_n(t) \, , \tag{3.64}$$

which is of the same form as Eq. (3.59). Note that c_n in this case should not be mistaken for the degree variances of gravity anomalies as given in Eq. (3.35).

The Legendre polynomials can be recursively determined, e.g. by Bonnet's recursion formula (see Appendix A.3)

$$P_{n+1}(t) - \frac{2n+1}{n+1} \, t \, P_n(t) + \frac{n}{n+1} P_{n-1}(t) = 0 \, . \tag{3.65}$$

Hence, using the analogy to Eq. (3.60), the Clenshaw algorithm can also be applied for evaluating the covariance function by defining

$$\begin{aligned} e_n &= -\frac{2n+1}{n+1} \\ f_n &= \quad \frac{n}{n+1} \end{aligned} \, . \tag{3.66}$$

Note that e_n does not contain the variable t, which is intentionally excluded of this term for the derivatives explained later in this section. So, the recurrence quantity b_n is in this case given as

$$b_n = c_n - e_n \, t \, b_{n+1} - f_{n+1} \, b_{n+2} = c_n + \frac{2n+1}{n+1} \, t \, b_{n+1} - \frac{n+1}{n+2} \, b_{n+2} \, , \tag{3.67}$$

and the sum in Eq. (3.62) is represented by

$$K(t) = b_0(t) P_0(t) + b_1(t) \left[P_1(t) + e_0 \, t \, P_0(t) \right] \, . \tag{3.68}$$

Recalling that the Legendre Polynomials $P_0(t) = 1$ and $P_1(t) = t$, and inserting $e_0 = -1$ in Eq. (3.62), the sum of Legendre Polynomials for the covariance function finally simplifies to

$$K(t) = \sum_{n=0}^{N} c_n \, P_n(t) = b_0 \, . \tag{3.69}$$

Most applications require the evaluation of the covariance function in a specific range between degrees N_{min} and N_{max}

$$K = \sum_{n=N_{min}}^{N_{max}} \left(\frac{R^2}{rr'} \right)^{n+1} k_n \, P_n(\cos\psi) \, . \tag{3.70}$$

As the recursion in Eq. (3.67) must be performed fully down to $n = 0$ to get the correct sum,

the recursive algorithm has to be applied twice

$$\begin{aligned} b_n^{N_{max}} \quad & \ldots n = N_{max} : -1 : 0 \,, \\ b_n^{N_{min}-1} \quad & \ldots n = N_{min} - 1 : -1 : 0 \,, \end{aligned} \tag{3.71}$$

and the sum is then defined as

$$K = b_0^{N_{max}} - b_0^{N_{min}-1} \,. \tag{3.72}$$

Derivatives of the Legendre series covariance function

In this work the derivatives of the covariance function with respect to $t = \cos\psi$ up to order four are required. Using the Clenshaw algorithm, these derivatives can be computed quite comfortably. The derivatives with respect to t according to Eq. (3.69) are

$$\frac{\partial^k K}{\partial t^k} = \frac{\partial^k b_0}{\partial t^k} = {b_0}^k \,. \tag{3.73}$$

Starting with Eq. (3.67)

$$b_n = c_n - e_n \, t \, b_{n+1} - f_{n+1} \, b_{n+2} \,,$$

the derivatives are

$$\begin{aligned} b'_n \quad & = - e_n \, b_{n+1} - e_n \, t \, b'_{n+1} - f_{n+1} \, b'_{n+2} && = - e_n \left(\; b_{n+1} + t \, b'_{n+1} \right) - f_{n+1} \, b'_{n+2} \,, \\ b''_n \quad & = - e_n \left(b'_{n+1} + b'_{n+1} + t \, b''_{n+1} \right) - f_{n+1} \, b''_{n+2} && = - e_n \left(2b'_{n+1} + t \, b''_{n+1} \right) - f_{n+1} \, b''_{n+2} \,, \\ b'''_n \quad & = - e_n \left(2b''_{n+1} + b''_{n+1} + t \, b'''_{n+1} \right) - f_{n+1} \, b'''_{n+2} && = - e_n \left(3b''_{n+1} + t \, b'''_{n+1} \right) - f_{n+1} \, b'''_{n+2} \,, \\ & \vdots && \vdots \end{aligned}$$

ending up with the general formula for the k^{th} derivative

$$b_n^k = -e_n \left(k \, b_{n+1}^{k-1} + t \, b_{n+1}^k \right) - f_{n+1} \, b_{n+2}^k \,. \tag{3.74}$$

For radial derivatives of the covariance function the Legendre series is expanded by an additional factor, which is depending on the order of differentiation corresponding to Eqs. (3.46) to (3.50). Hence, in the Clenshaw algorithm it is only necessary to introduce these factors accordingly in Eq. (3.63) and the recursion to obtain the Legendre series and its derivatives can be performed as explained above.

3.7 Computation of covariances for second and lower order derivatives of the disturbing potential

In this thesis, a very convenient approach is chosen to compute the covariances of derivatives of the disturbing potential. Its methodology is introduced in this section. The approach is based on the developments published by Tscherning (1993) and has two remarkable advantages. The first one is that all derivatives of the covariance function can be calculated by simple combinations of basis functions, which will be introduced below. The second advantage is that all the derivatives are then given in a LNOF but can be easily rotated to an arbitrary other Cartesian system, which will be necessary in case of gravity gradients as observed by GOCE.

The derivatives of the covariance function $K(r, r', t = \cos\psi)$ in the most compact notation are given by

$$C_{ij}^{k} = r^n r'^m \frac{\partial^i}{\partial t^i} \frac{\partial^j K(r, r', t)}{\partial r^n r'^m} \quad \dots n+m=j,\ i+j \leq 4,\ k = \begin{cases} 1 & \text{if} \quad n=m=1 \\ 0 & \text{else} \end{cases}, \tag{3.75}$$

where i is the index describing the number of derivatives of the covariance function with respect to t. The radial derivatives in r are indicated with n, while those in r' are numerated by m. Together, they describe the sum $n+m=j$ of the radial derivatives with respect to r and r'. In case of $n=m=1$, i.e. one radial derivative in r and r' an thus $j=2$ according to Eq. (3.47), this has to be treated differently from the conventional second order derivatives in either r or r', which also lead to $j=2$ but have different factors in the derivation, see Eq. (3.48). This is indicated by the additional index k. In case of dealing with gravity gradients, the highest order of derivatives we need is four (maximum two at each point), so the total sum of derivatives of the covariance function with respect to t and/or to r and r' is $i+j \leq 4$.

The derivatives of $t = \cos\psi$ are also summarized in a compact variable t_{ij}. In this case, the subscript i is denoting a derivative with respect to the local coordinates y, x at point P, while the derivatives with respect to y', x' at point Q are indicated with subscript j. Hence, $i=1$ or $j=1$ means a derivative with respect to y or y', while $i=2$ or $j=2$ means a derivative with respect to x or x' (note that $t_{00} = t = \cos\psi$)

$$\begin{aligned} t_{i0} &= r \frac{\partial t}{\partial \boldsymbol{x}_i}, \\ t_{0j} &= r' \frac{\partial t}{\partial \boldsymbol{x'}_j}, \\ t_{ij} &= r r' \frac{\partial^2 t}{\partial \boldsymbol{x}_i \partial \boldsymbol{x'}_j} \quad \dots \boldsymbol{x} = [y, x]\,,\ \boldsymbol{x'} = \left[y', x'\right],\ i = \{1,2\},\ j = \{1,2\}\,. \end{aligned} \tag{3.76}$$

Depending on the point for which the differentiation is performed, the derivative is multiplied with the respective radius. Therefore, when applying the derivatives in spherical coordinates,

the result is independent of the radii and the following relations hold:

$$\begin{aligned}
t_{10} &= r\frac{\partial t}{\partial y} && = r\frac{1}{r\cos\varphi}\frac{\partial t}{\partial \lambda} && = \cos\varphi' \sin\Delta\lambda\,, \\
t_{20} &= r\frac{\partial t}{\partial x} && = r\frac{1}{r}\frac{\partial t}{\partial \varphi} && = \cos\varphi\sin\varphi' - \sin\varphi\cos\varphi'\cos\Delta\lambda\,, \\
t_{01} &= r'\frac{\partial t}{\partial y'} && = r'\frac{1}{r'\cos\varphi'}\frac{\partial t}{\partial \lambda'} && = -\cos\varphi\sin\Delta\lambda\,, \\
t_{02} &= r\frac{\partial t}{\partial x'} && = r'\frac{1}{r'}\frac{\partial t}{\partial \varphi'} && = \sin\varphi\cos\varphi' - \cos\varphi\sin\varphi'\cos\Delta\lambda\,, \\
t_{11} &= rr'\frac{\partial^2 t}{\partial y \partial y'} && = \ldots && = \cos\Delta\lambda\,, \\
t_{12} &= rr'\frac{\partial^2 t}{\partial y \partial x'} && = \ldots && = -\sin\varphi'\sin\Delta\lambda\,, \\
t_{21} &= rr'\frac{\partial^2 t}{\partial x \partial y'} && = \ldots && = \sin\varphi\sin\Delta\lambda\,, \\
t_{22} &= rr'\frac{\partial^2 t}{\partial x \partial x'} && = \ldots && = \cos\varphi\cos\varphi' + \sin\varphi\sin\varphi'\cos\Delta\lambda\,.
\end{aligned} \tag{3.77}$$

With these base functions all combinations of derivatives of the disturbing potential up to second order degree given in Appendix A.3 can be derived and stored in a four-dimensional matrix D_{ijmn} with $dim(D) = (4 \times 4 \times 4 \times 4)$ and $i, j, m, n = \{0, 1, 2, 3\}$. In this notation, index 0 means no derivative, 1 is a derivative w.r.t. y or y', 2 stands for a derivative w.r.t. x or x' and finally index 3 is indicating a radial derivative w.r.t. r or r'. As an example, the covariance between T_{xx} and $T_{x'x'}$ from Eq. (3.45) will be D_{2222}, and is composed of the base functions

$$\begin{aligned}
D_{2222} = \big[& C_{02}^1 - 2\,t\,C_{11} + \left(t_{20}^2 + t_{02}^2\right) C_{21} + t\,C_{10} + \left(t^2 + 2\,(t_{22}^2 - t_{20}^2 - t_{02}^2)\right) C_{20} \\
& + \left(4\,t_{22}\,t_{20}\,t_{02} - t\,(t_{20}^2 + t_{02}^2)\right) C_{30} + t_{20}^2\,t_{02}^2\,C_{40} \big] / (r\,r')^2\,,
\end{aligned} \tag{3.78}$$

For this case, the chain- and product rule of differentiation was applied as shown in Appendix A.2 in Eq. (A.11) for φ and φ' and the derivatives of $t = \cos\psi$ were reordered and combined by taking into account the rules for trigonometric identities. All other covariances can be expressed in the same way by the following formulas:

One derivative in P or Q

$$D_{i000} = t_{i0}\,C_{10}/r, \quad \ldots i = \{1, 2\}\,, \tag{3.79}$$

$$D_{3000} = C_{01}/r\,. \tag{3.80}$$

One derivative in P and Q

$$D_{i0j0} = \left[t_{i0}\, t_{0j}\, C_{20} + t_{ij}\, C_{10}\right]/(rr'), \quad \ldots i = \{1,2\},\, j = \{1,2\}\,, \tag{3.81}$$

$$D_{i030} = t_{i0}\, C_{11}/(rr'), \quad \ldots i = \{1,2\}\,, \tag{3.82}$$

$$D_{3030} = C_{02}^{1}/(rr')\,. \tag{3.83}$$

Two derivatives in P or Q

$$D_{ii00} = \left[C_{01} - t\, C_{10} + t_{i0}^{2}\, C_{20}\right]/(r^2), \quad \ldots i = \{1,2\}\,, \tag{3.84}$$

$$D_{1200} = t_{10}\, t_{20}\, C_{20}/(r^2)\,, \tag{3.85}$$

$$D_{i300} = t_{i0}\left(C_{11} - C_{10}\right)/(r^2), \quad \ldots i = \{1,2\}\,, \tag{3.86}$$

$$D_{3300} = C_{02}/(r^2)\,. \tag{3.87}$$

Two derivatives in P and one derivative in Q or vice versa

$$\begin{aligned} D_{iij0} = {} & \left[t_{0j}\left(C_{11} - C_{10} - C_{20}\, t + t_{i0}^{2}\, C_{30}\right) + 2\, t_{ij}\, t_{i0}\, C_{20}\right]/(r^2 r'), \\ & \ldots i = \{1,2\},\, j = \{1,2\}\,, \end{aligned} \tag{3.88}$$

$$D_{ii30} = \left[C_{02}^{1} + t_{i0}^{2}\, C_{21} - t\, C_{11}\right]/(r^2 r'), \quad \ldots i = \{1,2\}\,, \tag{3.89}$$

$$D_{12j0} = \left[\left(t_{10}\, t_{2j} + t_{20}\, t_{1j}\right) C_{20} + t_{20}\, t_{10}\, t_{0j}\, C_{30}\right]/(r^2 r'), \quad \ldots j = \{1,2\}\,, \tag{3.90}$$

$$D_{1230} = t_{10}\, t_{02}\, C_{21}/(r^2 r')\,, \tag{3.91}$$

$$D_{i3j0} = \left[t_{ij}\left(C_{11} - C_{10}\right) + t_{0j}\, t_{i0}\left(C_{21} - C_{20}\right)\right]/(r^2 r'), \quad \ldots i = \{1,2\},\, j = \{1,2\}\,, \tag{3.92}$$

$$D_{i330} = t_{i0}\, C_{12}/(r^2 r'), \quad \ldots i = \{1,2\}\,, \tag{3.93}$$

$$D_{33j0} = t_{0j}\, C_{12}/(r^2 r'), \quad \ldots j = \{1,2\}\,, \tag{3.94}$$

$$D_{3330} = C_{03}/(r^2 r')\,. \tag{3.95}$$

Two derivatives in P and two derivatives in Q

$$\begin{aligned} D_{iijj} = &\left[C_{02}^1 - 2\,t\,C_{11} + \left(t_{i0}^2 + t_{0j}^2\right) C_{21} + t\,C_{10} + \left(t^2 + 2\,(t_{ij}^2 - t_{i0}^2 - t_{0j}^2)\right) C_{20}\right. \\ &+ \left.\left(4\,t_{ij}\,t_{i0}\,t_{0j} - t\,(t_{i0}^2 + t_{0j}^2)\right) C_{30} + t_{i0}^2\,t_{0j}^2\,C_{40}\right]/(r\,r')^2, \\ &\ldots i = \{1,2\},\ j = \{1,2\}\,, \end{aligned} \tag{3.96}$$

$$\begin{aligned} D_{iij3} = &\left[t_{0j}\,(C_{10} - C_{11} + C_{12}) + (t\,t_{0j} - 2\,t_{i0}\,t_{ij})\,(C_{20} - C_{21}) + \right. \\ &\left. + t_{i0}^2\,t_{0j}\,(C_{31} - C_{30})\right]/(r\,r')^2, \quad \ldots i = \{1,2\},\ j = \{1,2\}\,, \end{aligned} \tag{3.97}$$

$$\begin{aligned} D_{12jj} = &\left[t_{10}\,t_{20}\left(C_{21} - 2\,C_{20} - t\,C_{30} + t_{0j}^2\,C_{40}\right) + 2\,t_{1j}\,t_{2j}\,C_{20}\right. \\ &\left. + 2\,t_{0j}\,(t_{20}\,t_{1j} + t_{10}\,t_{2j})\,C_{30}\right]/(r\,r')^2, \quad \ldots j = \{1,2\}\,, \end{aligned} \tag{3.98}$$

$$\begin{aligned} D_{1212} = &\left[(t_{11}\,t_{22} + t_{12}\,t_{21})\ C_{20} + (t_{10}\,t_{01}\,t_{22} + t_{20}\,t_{12}\,t_{01} + \right. \\ &\left. + t_{21}\,t_{10}\,t_{02} + t_{20}\,t_{02}\,t_{11})\,C_{30} + t_{10}\,t_{20}\,t_{01}\,t_{02}\,C_{40}\right]/(r\,r')^2\,, \end{aligned} \tag{3.99}$$

$$\begin{aligned} D_{12j3} = &\left[(t_{10}\,t_{2j} + t_{1j}\,t_{20})\,(C_{21} - C_{20}) + t_{10}\,t_{20}\,t_{0j}\,(C_{31} - C_{30})\right]/(r\,r')^2, \\ &\ldots j = \{1,2\}\,, \end{aligned} \tag{3.100}$$

$$\begin{aligned} D_{i3j3} = &\left[t_{i0}\,t_{0j}\,(C_{22} - C_{21} + C_{20}) + t_{ij}\,(C_{12} - C_{11} + C_{10})\right]/(r\,r')^2, \\ &\ldots i = \{1,2\},\ j = \{1,2\}\,, \end{aligned} \tag{3.101}$$

$$D_{33jj} = \left[t_{0j}^2\,C_{22} - t\,C_{12} + C_{03}\right]/(r\,r')^2, \quad \ldots j = \{1,2\}\,, \tag{3.102}$$

$$D_{3312} = t_{01}\,t_{02}\,C_{22}/(r\,r')^2\,, \tag{3.103}$$

$$D_{33j3} = t_{0j}\,(C_{13} - C_{12})\,/(r\,r')^2, \quad \ldots j = \{1,2\}\,, \tag{3.104}$$

$$D_{3333} = C_{04}/(r\,r')^2\,. \tag{3.105}$$

With the chosen notation it is straightforward to obtain the covariances if P and Q are interchanged. In this case, the corresponding expression is derived by simply interchanging the subscripts i, j and the radii r and r'.

Finally, for a demonstration of this approach, we can exemplarily calculate the covariance between a gravity anomaly Δg at point P and a gradient $T_{x'x'}$ at point Q, see Equation (3.43), simply by

$$cov(\Delta g, T_{x'x'}) = -D_{3022} - \frac{2}{r} D_{0022} \,. \tag{3.106}$$

3.7.1 Rotating covariances to an arbitrary reference frame

As already mentioned in the introduction to section 3.7, the chosen approach has the advantage that covariances derived in this way can be rotated to an arbitrary reference frame. Terrestrial gravity quantities are usually measured in a LNOF, which is in representation as spherical coordinates also the basic computational reference frame for LSC.

However, as we will see in the following sections, the gravity gradients of the GOCE mission are not observed in an LNOF, but in a rotated local reference frame. It would be possible to rotate these observations into a LNOF as well, but due to the specific measurement configuration, this is not an option in this case, see the remarks in section 6.1 or section 6.3. Instead, it is possible to rotate the covariances related to the gradients based on the covariance aggregation of the preceding section. A frame transformation can be achieved by tensor rotation of the permutations of the covariance matrix of a specific derivative at a station Q

$$D_{ij}^{Q} = R_Q \, D_{ij}(m,n) \, R_Q^T, \quad m,n = 1 \ldots 3 \,, \tag{3.107}$$

and a consecutive tensor rotation of the permutations at the other station P

$$D_{mn}^{P} = R_P \, D_{mn}(i,j) \, R_P^T, \quad i,j = 1 \ldots 3 \,. \tag{3.108}$$

In this sense, R_Q stands for the rotation matrix from a LNOF at evaluation point Q to an arbitrary other reference frame with its origin located at the same point, while R_P is the equivalent for the evaluation point P.

For a better understanding of this procedure, following explanations can be considered: For instance, if one wants to compute the covariance between two vertical gradients at two different orbit locations given in the reference frame where the measurements took place, at first all covariances up to second order derivatives of the disturbing potential have to be computed in the LNOF and arranged in the four-dimensional matrix D. Then, all covariances with respect to point Q are rotated to the measurement frame following Eq. (3.107), and consecutively the same is done for point P as given in Eq. (3.108). Afterwards, all covariances are given in the respective measurement frames. Another scenario might be the computation of the covariance between a gravity anomaly at location P given in LNOF and a gravity gradient at Q in its specific measurement frame. In this case, again all covariances are derived in the LNOF, however only those related to the gradient in Q are rotated to the measurement frame.

4 The Remove-Compute-Restore approach

According to the potential theory, the gravitational potential V given in Eq. (2.11) and consequently also the disturbing potential T of Eq. (2.54) are harmonic and thus satisfy the Laplace equation Eq. (2.13) only outside the attracting masses. The geoid, however, is per definition coinciding with the equipotential surface of the mean ocean at rest and will therefore usually be situated inside the attracting masses over land areas. Classical methods for geoid determination, for instance using Stokes' formula (Hofmann-Wellenhof and Moritz, 2005), therefore require that the masses above the geoid and thus the gravitational effects of these masses are reduced from the observation data in some way.

A second aspect is, that any interpolation or prediction method only leads to reasonable results, if the quantities used as input for the estimation of other unknown quantities are sufficiently smooth. In the case of LSC it is necessary to have smooth gravity field functionals in order to obtain a significant and representative statistical behaviour of the field in terms of a suitable covariance function. In mountainous regions for example, the local gravity field will be dominated by the gravitational effect of the topography, which causes undesirable high-frequency variations in particular in terrestrial gravity observations. Hence, the reduction of such influences will facilitate the interpolation and prediction process.

Furthermore, the reduction of systematic trends of the gravity field leads to a prerequisite of the LSC method, namely that the expectation value of gravity field quantities (derived from the disturbing potential T) should be zero, see Section 3.2. In this sense, known systematic effects of the gravity field should to be removed before the actual computations, which results in residual observables. From these quantities, the desired residual gravity quantities are estimated, and finally the systematic effects are reconsidered and thus restored again. This procedure is commonly denoted as the Remove-Compute-Restore (RCR) concept and is discussed in various literature, e.g. Hofmann-Wellenhof and Moritz (2005), Forsberg and Tscherning (1997) or Moritz (1980a).

Within the RCR approach, different systematic effects on gravity observations are considered, which can influence the gravity data in different ways. These systematics are discussed in the following sections. At the beginning, the long-wavelength effects based on a global Earth Gravity field Model (EGM) will be discussed in section 4.1. Then, the effect of atmospheric masses is investigated in section 4.2. Afterwards, the issue how to treat the impact of topography is shown in section 4.3, and finally the topic of isostasy is discussed in section 4.4.

4.1 Global gravity field models

In this thesis, the RCR will be of particular interest in chapter 7, where terrestrial gravity observations together with GOCE gravity gradients are used to estimate a regional geoid solution for Austria. Although the terrestrial gravity data is considered to be sensitive to the short-scale variations of the gravity signal, while gravity gradients measured at satellite altitude are observing in particular the medium wavelengths with high accuracy, both quantities are point observations which theoretically incorporate the entire gravity signal spectrum. However, due to their limited availability within a restricted area of interest for such a regional application, the long wavelengths of the gravity signal can not be resolved with sufficient accuracy.

Global EGMs are representing the Earth's static gravity field in terms of its exterior potential and are usually given as series of spherical harmonics coefficients truncated at a specific degree N_{max}. They are primarily derived from observations with a global data distribution and can thus be considered to resolve the gravity signal accurately especially in the long- to medium-wavelength spectral range. The EGMs can be classified into models that are based solely on satellite data and models that are deduced from a combination of satellite and terrestrial data. Since the year 2002, a series of dedicated gravity satellite missions and according gravity field solutions began with the launch of the CHAllenging Minisatellite Payload (CHAMP) mission (Reigber et al., 2002), which was followed by the GRACE project in 2002 (Tapley et al., 2003). The last gravity mission launched into space was the GOCE satellite, which is introduced in detail in chapter 5. Due to their individual measurement principles, these missions are complementary in terms of accuracy within certain spectral bandwidths. Hence, recent successful attempts to consistently combine all these missions were undertaken for instance by the Gravity Observation COmbination (GOCO) consortium, which also includes Satellite Laser Ranging (SLR) observations for the very long wavelength part of the gravity signal (Goiginger et al., 2011). The current maximum spectral resolution of satellite-only models is limited with Degree and Order (D/O) 280, which corresponds to a spatial resolution of approximately 70 km, and was in particular achieved due to the gravity gradient observations of the GOCE mission within the latest global GOCE_TIM_RL05 model (see section 5.4.3). In this context it should be mentioned, that a significant signal content can only be expected until D/O 254, where the signal-to-noise ratio reaches 1, while beyond the signal is dominated by regularization (Brockmann et al., 2014).

Apart from satellite-only models, also combination models including other data sources exist. The most prominent and still widely used is the EGM2008 model (Pavlis et al., 2012), which was published in 2008. Due to the inclusion of terrestrial data, airborne gravimetry and ocean altimetry data, this model was developed complete to D/O 2159 and contains additional coefficients up to D/O 2190 and thus resolves the gravity field with a spatial resolution of $5' \times 5'$. Although this model is still unrivaled with respect to the maximum resolution, the long-wavelength constituents are determined more accurately by more recent satellite-only models. The reason for that can be found due to the fact that EGM2008 includes long-wavelength information based on GRACE data according to the ITG-Grace03s model (Mayer-Gürr, 2007), while for instance the latest GOCO05s model incorporates updated data of the ITG-Grace2014s model (Mayer-Gürr et al., 2014) as well as SLR data (Maier et al., 2014).

In order to evaluate the characteristics of global EGMs, the signal degree variances can be computed from the spherical harmonics coefficients according to Eq. (3.32). In this way, the energy content of the gravity signal per spherical harmonic degree can be assessed. Similar to the signal content itself, the degree variances of the formal coefficient errors, which are usually also provided with an EGM, can be computed by

$$k_n^{\sigma} = \sum_{m=0}^{n} \left(\sigma^2_{\bar{c}_{nm}} + \sigma^2_{\bar{s}_{nm}} \right) \ . \tag{4.1}$$

In Figure 4.1, the signal degree variances of EGM2008 are illustrated as solid blue line and the corresponding error degree variances as dashed blue line in terms of geoid heights. The formal errors indicate that the low degrees are dominated by GRACE contributions up to D/O 90, where terrestrial data starts to have a beneficial impact. The degree variances of the coefficient differences between EGM2008 and the latest GOCE_TIM_RL05 model are given as green line, with the formal errors of the GOCE model depicted as dashed line in the same color. The actual signal differences are larger than the formal errors of GOCE until D/O 230, which means that the GOCE model can be considered to be more accurate in this spectral range compared to EGM2008. The fact that the differences are also larger than the formal EGM2008 errors lead to the conclusion that the accuracies of the terrestrial data sources in the EGM2008 model are considerably overestimated. Finally, the same kinds of curves are shown for the GOCO03s combination model in red. A look at the formal errors immediately shows that this model has an improved accuracy compared to the GOCE-only model in particular below D/O 110. Since the GOCE contribution in the GOCO03s model is according to an earlier release GOCE_TIM_RL03 with substantially less data, the GOCE_TIM_RL05 is superior to GOCO03s above D/O 110. The latest GOCO05s benefits from the additional data of the GOCE_TIM_RL05, which can be verified by the corresponding formal errors and signal differences given in orange. Since the GOCO05s model was officially released in April 2015, just before the completion of this thesis, its predecessor GOCO03s is used for the studies herein.

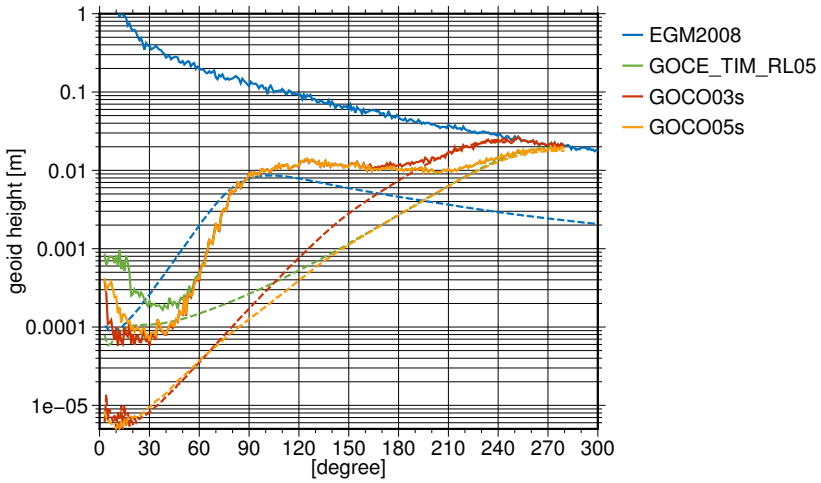

Figure 4.1: Signal degree variances of the EGM2008 (blue); degree variances of coefficient differences between EGM2008 and GOCE_TIM_RL05 (green), GOCO03s (red) and GOCO05s (orange); formal errors of the respective models are illustrated as dashed lines

The essence of this investigation is, that global EGMs can resolve the long-wavelength constituents of the gravity field signals considerably more accurately than terrestrial data. It is therefore recommended to reduce the long-wavelength gravity effect from terrestrial data by using an accurate EGM within the RCR procedure. In this way, a residual or anomalous gravity quantity Δg can be formed from the gravity observation g taken at the Earth's surface by

$$\Delta g = g - \gamma^{egm} \,, \tag{4.2}$$

where γ^{egm} can be considered as an improved version of the normal gravity γ, i.e. it is better approximating the actual gravity (see also the discussion in section 2.3.4). For a combination of different gravity field observations, this reduction will have to be performed in a consistent way for all measurement types, e.g. the long-wavelength effects have to be removed from GOCE gradient observations in the same manner.

The final question is, up to which spherical harmonic D/O N_{max} the long-wavelength signal should be removed from the gravity observables prior to the actual processing. This primarily depends on the type of input data, or more specifically on the spectral signal range of the data, where additional contributions can be expected and should therefore be exploited for an improved gravity field determination. In this thesis, this will be discussed in chapter 7, where the application of a regional geoid estimation for the Austrian area is presented.

4.2 Atmospheric reduction

At the beginning, a closer look on the gravitational effects of the atmospheric masses on gravity measurements is taken. In this work it is assumed that the atmosphere is static and temporal variations are either already accounted for in some preprocessing steps or that they can be neglected. When performing gravity reductions of terrestrial gravity measurements for further gravity field determination processes, it has to be considered that the measurements are taken on the Earth's surface while the atmospheric masses are above the observation point. Hence, the assumption of a mass-free exterior space and thus a harmonic potential outside the Earth's surface is violated for terrestrial observations. Conventionally, this is accounted for by reducing the interior gravity effect due to the atmospheric potential to the observed gravity on ground, see Moritz (1980a) or Sjöberg (1999). This corresponds to the International Association of Geodesy (IAG) approach, which assumes a spherical layering of the atmosphere without considering the variations due to the topography. Tabulated values for this gravity correction in dependence of the height of the observation station can be found in Moritz (1980b). For a consistent RCR, one further aspect has to be considered.

Any gravity field determination process is performed on the basis of a linearized gravity field, i.e. by building residual gravity quantities like gravity anomalies related to a disturbing potential that is formed by means of a normal gravity potential or an empirically determined EGM. Both, normal potential as well as an EGM, are including the atmospheric mass effect for the exterior space. Hence, when the residual gravity field quantities at the Earth's surface are formed, the atmosphere is implicitly reduced as well, although we want to treat the gravity observations in an atmosphere-free world. Therefore, the atmospheric effect should

also be considered when the contribution of the normal or EGM potential is subtracted from terrestrial gravity field observations. In this thesis, terrestrial and GOCE gradient observations at satellite altitude will be combined with the aim to determine a regional geoid (see chapter 7). In order to be consistent for all gravity observations, the atmosphere-free assumption has to be pursued for the satellite measurements as well. In this case, all relevant masses can be considered to be located below the observation points, so the exterior effect of the atmospheric potential is of interest.

For this study, the atmospheric potential is developed in terms of a spherical harmonics series, which also incorporates the effect of the variable topography. With this advantageous representation, it is possible to apply the atmospheric effect either directly in the spectral domain, or in the spatial domain for arbitrary gravity field quantities by an according spherical harmonics synthesis. The atmospheric potential V^a at an arbitrary point P can be expressed with the Newtonian volume integral formula Eq. (2.11) by

$$V^a(P) = G \iint_{\sigma} \int_{r_t}^{r_u} \rho^a(r_Q) \, \frac{r_Q^2}{l} \, \mathrm{d}r_Q \, \mathrm{d}\sigma \,, \tag{4.3}$$

where G is again the gravitational constant and l is the distance between computation point P and integration point Q. In contrast to Eq. (2.11), in this case the atmospheric density ρ^a is not assumed to be constant, but is depending on the radial distance r_Q of the integration point Q. The radial integration of the atmospheric masses has to be performed between the topography r_t and a specified upper limit of the atmosphere r_u, while the areal integration is done for the entire Earth's surface σ.

According to potential theory as explained in section 2.2, the gravitational potential can also be described in terms of spherical harmonics representation. Based on the location of the computational point P we have to distinguish between two solutions of the Laplace equation, one valid for the outer space $r_P > R$, and another one valid in the inner space $r_P < R$ for an arbitrary sphere with radius R, see Eq. (2.37) and Eq. (2.38). The solution for the outer space reads as follows

$$V_e^a(P) = \frac{GM}{R} \sum_{n=0}^{\infty} \left(\frac{R}{r_P} \right)^{n+1} \sum_{m=-n}^{n} \bar{a}_{nm}^{a,e} \, \bar{Y}_{nm}(P) \,, \tag{4.4}$$

with the fully normalized exterior atmospheric potential coefficients $\bar{a}_{nm}^{a,e}$

$$\bar{a}_{nm}^{a,e} = \frac{1}{M(2n+1)} \iint_{\sigma} \int_{r_Q} \left(\frac{r_Q}{R} \right)^n \rho^a(r_Q) \, r_Q^2 \, \bar{Y}_{nm}(Q) \, \mathrm{d}r_Q \, \mathrm{d}\sigma \,, \tag{4.5}$$

while for the inner space

$$V_i^a(P) = \frac{GM}{R} \sum_{n=0}^{\infty} \left(\frac{r_P}{R} \right)^n \sum_{m=-n}^{n} \bar{a}_{nm}^{a,i} \, \bar{Y}(P) \,, \tag{4.6}$$

with the interior potential coefficients $\bar{a}_{nm}^{a,i}$

$$\bar{a}_{nm}^{a,i} = \frac{1}{M(2n+1)} \iint_{\sigma} \int_{r_Q} \left(\frac{R}{r_Q}\right)^{n+1} \rho^a(r_Q)\, r_Q^2\, \bar{Y}(Q)\, \mathrm{d}r_Q\, \mathrm{d}\sigma\,, \tag{4.7}$$

is defined. As it was mentioned at the beginning of this section, both, the exterior and interior potentials are important when dealing with the atmosphere. In most space geodetic applications, where the observations are taken at satellite altitude, all relevant masses can be considered to be located below the observation point, so the exterior solution is of interest. However, in case of terrestrial observations also the interior solution is important. When performing gravity reductions of terrestrial gravity measurements for further gravity field determination processes, the measurement is taken on the Earth's surface while the atmospheric masses are above the observation point. Hence, the atmospheric effect of the interior solution has to be considered. Since we assume a radial symmetric layering of the atmosphere, for the interior potential mainly the deviations due to the topography will contribute to this potential.

4.2.1 Atmospheric Density Models

The coefficients of the spherical harmonics representation of a potential are depending on the radial integration of the density ρ. Considering the density of the atmosphere ρ^a, it is not a constant as it is assumed, e.g., for topographic masses, but it is a quantity that rapidly decreases with increasing height. Hence, for the derivation of the atmospheric potential, a corresponding Atmospheric Density Model (ADM) depending on the height has to be found.

U.S. Standard Atmosphere USSA76

The USSA76 can be considered as a widely used standard atmosphere and is a joint publication of the National Oceanic and Atmospheric Administration (NOAA), the National Aeronautics and Space Administration (NASA) and the U.S. Air Force (NOAA et al., 1976). This model is assumed to be valid for a period of moderate solar activity, while its predecessor USSA62 was defined for a environment of high solar activity. It defines models for pressure, temperature and density of the Earth's atmosphere and describes an idealized and static atmosphere from ground level to 1000 km. The ADM is based on the perfect gas law assuming dry air and defines the total density ρ^a as a function of geopotential height H by

$$\rho^a(H) = \frac{M\, P(H)}{R^*\, T(H)}\,, \tag{4.8}$$

in which $T(H)$ is the absolute temperature, $P(H)$ is the total pressure, R^* denotes the universal gas constant with value of $8.314\,32 \times 10^3\,\mathrm{Nm/kmol\,K}$ and M =28.9644 $\mathrm{kg\,kmol^{-1}}$ is the constant mean molecular weight of air.

The relationship between geopotential height H and geometric height h is given by

$$H = \frac{R\,h}{R+h}\,, \tag{4.9}$$

where R is the Earth's radius. The model is segmented into eight layers with linear temperature gradients L_b given in Table 4.1.

The temperature-height profile can then be determined for heights within a layer b according to the layer-by-layer evaluation of

$$T(H) = T_b + L_b\,(H - H_b); \qquad \forall b = \{0, 1, \ldots, 6\} \quad \wedge \quad H_b \leq H < H_{b+1}\,, \tag{4.10}$$

where T_b is the temperature at the base of the corresponding layer with the initial standard temperature at sea level $T_0 = 288.15\,\mathrm{K}$ (=15 °C). Subsequently, the absolute pressure can be derived by

$$P(H) = \begin{cases} P_b \left(\dfrac{T_b}{T(H)} \right)^{\dfrac{g_0\,M}{R^*\,L_b}} & \ldots\ L_b \neq 0 \\ P_b \left(\dfrac{-g_0\,M(H - H_b)}{R^*\,T(H)} \right) & \ldots\ L_b = 0 \end{cases}, \tag{4.11}$$

starting with the reference value for the absolute pressure at sea level, which is defined as $P_0 = 1013.25\,\mathrm{mbar}$. The quantity $g_0 = 9.806\,65\,\mathrm{m/s^2}$ represents the gravity at sea level assessed for this standard model. The corresponding height profiles for temperature, pressure and density are illustrated in Figure 4.2.

Table 4.1: Reference levels and linear temperature gradients of the temperature-height profiles from ground level to the beginning of the thermosphere at about 86 km geometric height according to USSA76

Layer	**Geopotential height H_b [km]**	**Temperature gradient L_b [K km^{-1}]**
0	0	−6.5
1	11	0.0
2	20	1.0
3	32	2.8
4	47	0.0
5	51	−2.8
6	71	−2.0
7	84.852	

The definitions of USSA76 would provide formulas for computations above 86 km height. However, it can be assumed that the majority of the atmospheric masses are concentrated within a certain layer close to the Earth's surface. For instance, Lambeck (1988) states that about 80% of the mass lies within the Troposphere with maximum heights between 12 to 15 km, while Ecker and Mittermayer (1969) expect 99% of the mass below 50 km. So for this application, an atmospheric density model up to 86 km will be more than sufficient.

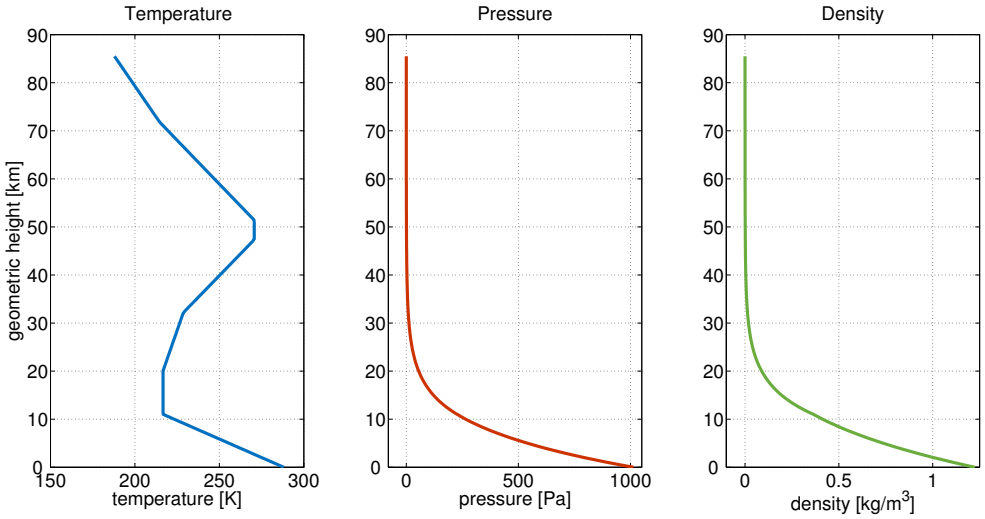

Figure 4.2: USSA76 height profiles for temperature, pressure and density

4.2.2 Review of existing atmospheric density models

Unfortunately, the USSA76 density model is not suitable for a vertical integration, which has to be performed when deriving the atmospheric potential. Therefore, a simplified and integrable ADM has to be found. To approximate the Earth's atmosphere, several approaches can be found in literature. Lambeck (1988) assumed a spherically layered exponential model

$$\rho^a(h) = \rho_0 \exp^{\alpha\, h} \ , \tag{4.12}$$

with h defined as height above sea level, ρ_0 is the reference density at sea level and α is fixed as constant value. Eshagh (2009) determined $\alpha = 1.3886 \times 10^{-4}$ considering ρ_0 =1.2227 kg/m^3 to get an appropriate fit to the USSA76 standard density.

Sjöberg (1998) proposed following spherically layered power model

$$\rho^a(h) = \rho_0 \left(\frac{R}{R+h} \right)^{\nu} \ , \tag{4.13}$$

where R is the Earth's mean radius and $\nu = 930$ is a constant factor which was re-fitted to USSA76 by Eshagh and Sjöberg (2009). Novak (2000) introduced a polynomial function of second order

$$\rho^a(h) = \rho_0 \left(1 + \alpha\, h + \beta\, h^2\right) \ , \tag{4.14}$$

with the density at sea level ρ_0 =1.2227 kg/m^{-3}, and the estimated coefficients $\alpha = -1.1436 \times 10^{-4}$ and $\beta = 3.4057 \times 10^{-9}$. He concludes that it fits the USSA76 with an accuray of 5×10^{-3} up to 9 km height. Eshagh and Sjöberg (2009) proposed to combine a polynomial model according to Eq. (4.14) for elevations $\leq$10 km with the simple power model of Eq. (4.13) for elevations from 10 km up to a certain maximum height Z, which leads to a density model of

the form

$$\rho^a(h) = \begin{cases} \rho_0 \left(1 + \alpha\, h + \beta\, h^2\right) & \dots 0 \leq h \leq h_0 \\ \rho^a(h_0) \left(\dfrac{R + h_0}{R + h}\right)^{\nu'} & \dots h_0 \leq h \leq Z \end{cases}, \tag{4.15}$$

with the coefficients $\alpha = -7.6495 \times 10^{-4}$, $\beta = 2.2781 \times 10^{-9}$ and $\nu' = 890$ and the intermediate reference level $h_0 = 10\,\text{km}$, at which $\rho^a(h_0) = 0.4127\,\text{kg/m}^3$.

To get an overview of the different atmospheric density models from literature, the ADMs were evaluated with a radius $R = 6\,378\,137\,\text{m}$ and the according parameters provided. The density profiles can be seen in Figure 4.3. The USSA76 standard density model is depicted in black. Looking at the first 20 km height, the exponential model (orange curve) as well as the power model (blue curve) are overestimating the decrease of density with height. The combined model (green curve) is supposed to overcome this deficiencies, however with the parameters provided, this model is underestimating the decay of density in the first 10 km. While the exponential model and the combined model show a reasonable close fit at higher altitudes, the power model implies lower densities in these heights compared to the reference USSA76 model, which becomes obvious when looking at the logarithmic scale plot on the right of Figure 4.3. However, this might not be too critical, as the densities are already very small and below $0.1\,\text{kg/m}^3$ for altitudes $\geq$20 km.

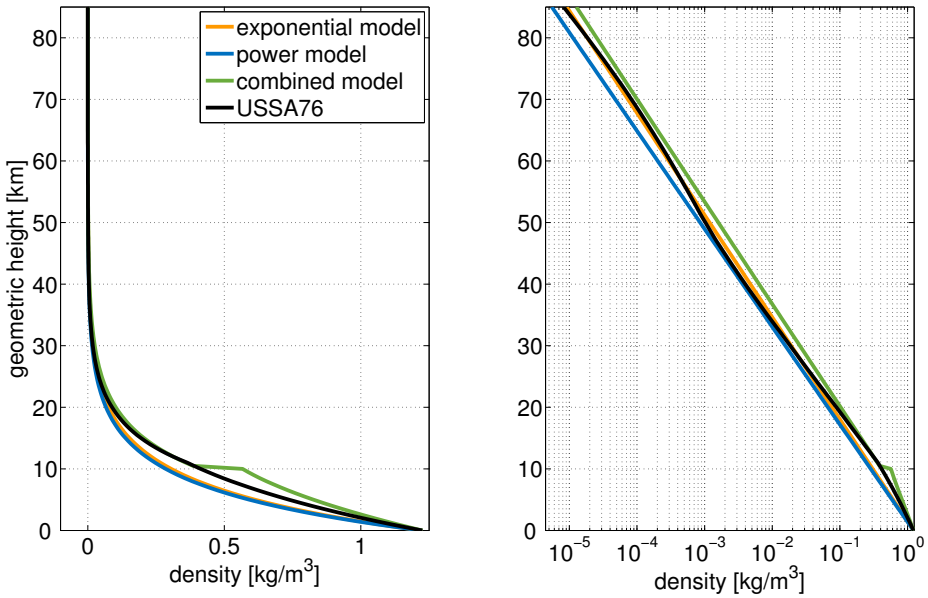

Figure 4.3: Comparison of different atmospheric density models from literature in conventional (left) and logarithmic scale (right)

4.2.3 The ITSG atmospheric density model

Since none of the investigated models is approximating the USSA76 standard atmosphere very well in particular in the most important lower altitudes, an own model, in the following called ITSG model, is defined.

As the analytical vertical integration of the atmospheric density for the derivation of the atmospheric potential is becoming quite complex for an exponential or polynomial model, a combined power model is chosen. According to the layer structure of the USSA76, the power model is split into one parametrization for altitudes $h \leq h_0$, and another one for heights $h_0 \leq h \leq Z$ with $h_0 = 11\,\mathrm{km}$ and Z as maximum height of evaluation:

$$\rho^a(h) = \begin{cases} \rho_0 \left(\dfrac{R}{R+h} \right)^{\nu} & \ldots 0 \leq h \leq h_0 \\ \rho^a(h_0) \left(\dfrac{R+h_0}{R+h} \right)^{\nu'} & \ldots h_0 \leq h \leq Z \end{cases} . \tag{4.16}$$

The coeffcients $\nu = 680$ and $\nu' = 932$ are determined by a least squares adjustment to fit the USSA76 model with $\rho_0 = 1.2250\,\mathrm{kg/m^3}$ and $\rho^a(h_0) = 0.3648\,\mathrm{kg/m^3}$ corresponding to the values given by USSA76 for these heights and a mean Earth's radius $R = 6\,378\,137\,\mathrm{m}$.

In Figure 4.4 the comparison of the ITSG model with the models introduced in the previous section is illustrated. In contrast to the other models, the new ITSG model (red curve) fits the USSA76 reference very well particularly in the low altitudes.

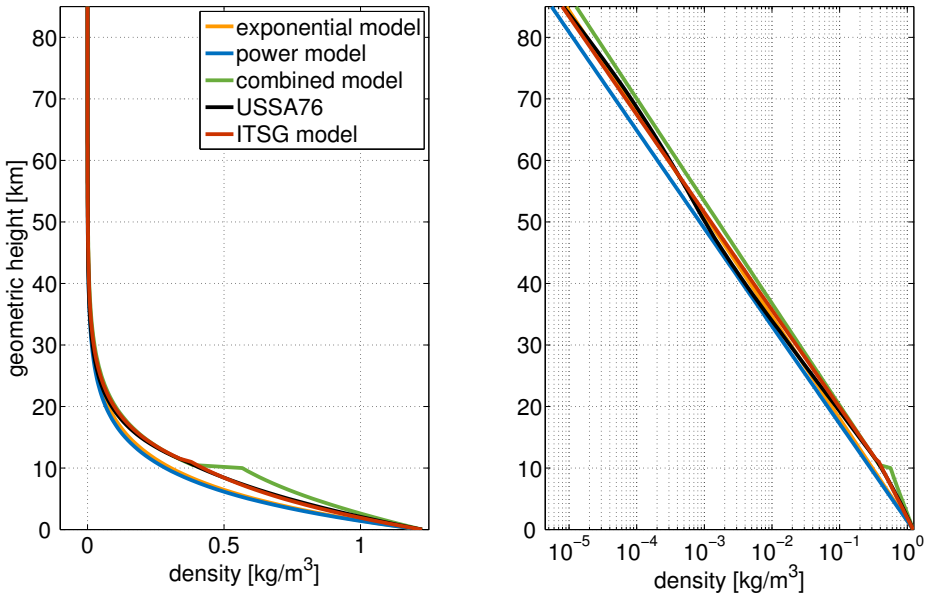

Figure 4.4: Comparison of the ITSG atmospheric density model with others in conventional (left) and logarithmic scale (right)

To assess the quality of the approximation, the differences of each model with respect to the USSA76 and the corresponding relative errors are shown in Figure 4.5 in the left and right plots, respectively. Obviously, the ITSG model performs best in terms of absolute deviation. Regarding the relative errors with respect to USSA76, it is also preferable especially in the most important low altitude range.

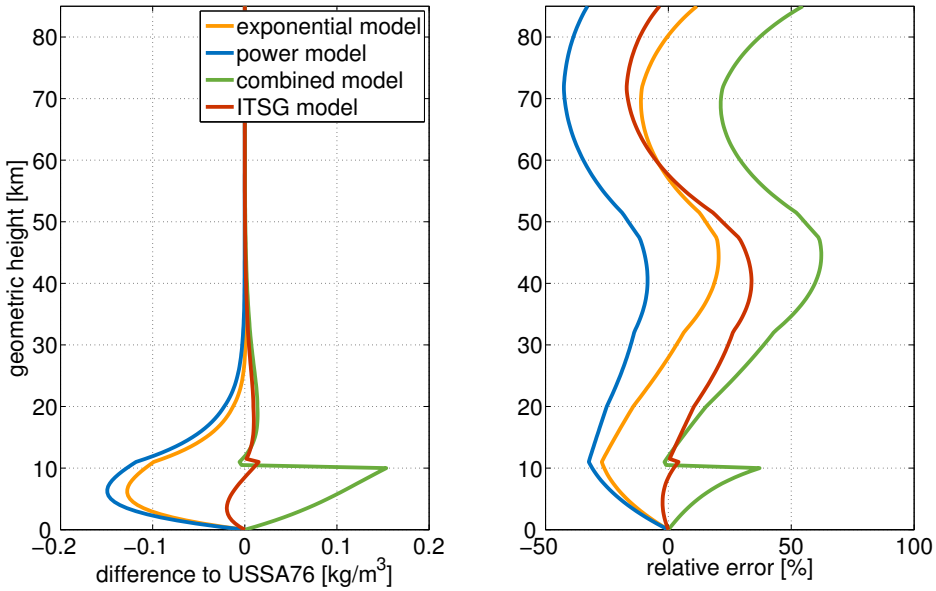

Figure 4.5: Differences of the ADMs with respect to USSA76 (left) and relative errors (right)

Based on these investigations, the ITSG model is chosen for further application and used for the derivation of the atmospheric potential in spherical harmonics representation.

4.2.4 Atmospheric potential based on the ITSG atmospheric density model

Recalling the representation of the atmospheric gravitational potential in spherical harmonics for the exterior space from Eq. (4.4) we have to derive the corresponding coefficients $\bar{a}_{nm}^{a,e}$ as given in Eq. (4.5)

$$\bar{a}_{nm}^{a,e} = \frac{1}{M(2n+1)} \iint_{\sigma} \int_{r_Q} \left(\frac{r_Q}{R}\right)^n \rho^a(r_Q)\, r_Q^2\, \bar{Y}_{nm}(Q)\, \mathrm{d}r_Q \mathrm{d}\sigma \,,$$

where $\rho^a(r_Q)$ is the atmospheric density in dependence of the radial distance r_Q and R is the mean Earth's radius. In a first step we want to perform the analytical vertical integration of

$$\int_{r_s}^{r_Z} \left(\frac{r_Q}{R}\right)^n \rho^a(r_Q)\, r_Q^2\, \mathrm{d}r_Q \,, \tag{4.17}$$

with the lower limit $r_s = R + h$ defined as the geocentric radius to the Earth's surface and some upper limit $r_Z = R + Z$, both h and Z to be considered as heights above the reference level. We therefore introduce the ITSG atmospheric density model of Eq. (4.16) which has the form

$$\rho^a(r_Q) = \rho_0 \left(\frac{R}{r_Q}\right)^{\nu} , \tag{4.18}$$

and insert this model into Eq. (4.17) to obtain the integral

$$\rho_0 \int_{r_s}^{r_Z} \left(\frac{r_Q}{R}\right)^{n} \left(\frac{R}{r_Q}\right)^{\nu} r_Q^2 \, \mathrm{d}r_Q \, . \tag{4.19}$$

Before going ahead, some considerations should be made. The spherical harmonics expansion is defined in spherical approximation for a sphere with mean Earth's radius R, but the points considered are still referring to the ellipsoid. The ITSG atmospheric density model as given in Eq. (4.16) is assuming a spherically layered atmosphere with a mean Earth's radius R. However, thinking of the Earth in a more realistic ellipsoidal shape, e.g. in case of the GRS80 ellipsoid, the differences between the semi-major axis at the equator and the semi-minor axis at the poles reach a magnitude of about 21 km.

As the massive part of the Earth's atmospheric masses are within the first 12 to 15 km, this simplification might be critical. Sjöberg (2006) investigated the effect of the ellipsoidal layering by developing the atmospheric potential in ellipsoidal harmonics and found differences in terms of geoid heights in the order of several centimeters. To avoid the more complicated ellipsoidal harmonics, we account for this fact in a simple approximation by correcting the spherical radius R to the more appropriate geocentric ellipsoidal radius $\bar{R} = R - \Delta r$, where Δr is the difference between spherical radius and ellipsoidal radius. Hence, we can rewrite Eq. (4.19) as

$$\rho_0 \frac{\bar{R}^{\nu}}{R^n} \int_{r_s}^{r_Z} r_Q^{(2+n-\nu)} \, \mathrm{d}r_Q \, , \tag{4.20}$$

and perform the integration

$$\rho_0 \frac{\bar{R}^{\nu}}{R^n} \left(\frac{r_Q^{3+n-\nu}}{3+n-\nu}\right) \Bigg|_{\bar{R}+h}^{\bar{R}+Z} = \frac{\rho_0 \, \bar{R}^{\nu}}{R^n \, (3+n-\nu)} \left[\left(\bar{R}+Z\right)^{3+n-\nu} - \left(\bar{R}+h\right)^{3+n-\nu}\right] . \tag{4.21}$$

By extracting $\bar{R}$ from the terms in squared brackets and inserting $\bar{R} = R + \Delta r$, this can be further rearranged to

$$\frac{\rho_0 \, R^3}{3+n-\nu} \left(\frac{\bar{R}}{R}\right)^{n+3} \left[\left(1+\frac{Z}{\bar{R}}\right)^{n+3-\nu} - \left(1+\frac{h}{\bar{R}}\right)^{n+3-\nu}\right] . \tag{4.22}$$

Examining the first denominator in Eq. (4.22) we find $1/(3+n-\nu)$, thus a discontinuity occurs in case that the spherical harmonic degree $n = \nu - 3$. To consider this fact, we can

insert $\nu = n + 3$ in Eq. (4.20) and get

$$\rho_0 \, \frac{\bar{R}^{n+3}}{R^n} \int_{r_s}^{r_Z} r_Q^{-1} \, \mathrm{d}r_Q \, , \tag{4.23}$$

which can be analytically integrated to

$$\rho_0 \, \frac{\bar{R}^{n+3}}{R^n} \, \ln(r_Q) \Big|_{\bar{R}+h}^{\bar{R}+Z} = \rho_0 \, R^3 \left(\frac{\bar{R}}{R}\right)^{n+3} \ln\left(\frac{\bar{R}+Z}{\bar{R}+h}\right) \, . \tag{4.24}$$

Finally, we can insert the integrals of Eq. (4.22) or Eq. (4.24) into Eq. (4.5), which leads us to the atmospheric potential coefficients for the exterior space

$$\bar{a}_{nm}^{a,e} = \begin{cases} \dfrac{\rho_0 \, R^3}{M(2n+1)(3+n-\nu)} \left(\dfrac{\bar{R}}{R}\right)^{n+3} \times \\ \left[\left(1+\dfrac{Z}{\bar{R}}\right)^{n+3-\nu} - \left(1+\dfrac{h}{\bar{R}}\right)^{n+3-\nu}\right] \displaystyle\iint_\sigma \bar{Y}_{nm}(Q) \, \mathrm{d}\sigma & \ldots \forall \, n \in \mathbb{N} \backslash \{\nu - 3\} \\ \dfrac{\rho_0 \, R^3}{M(2n+1)} \left(\dfrac{\bar{R}}{R}\right)^{n+3} \ln\left(\dfrac{\bar{R}+Z}{\bar{R}+h}\right) \displaystyle\iint_\sigma \bar{Y}_{nm}(Q) \, \mathrm{d}\sigma & \ldots n = \nu - 3 \end{cases} . \tag{4.25}$$

Equivalently to the external potential we obtain the interior atmospheric potential given in Eq. (4.6) by deriving the corresponding spherical harmonics coefficients $\bar{a}_{nm}^{a,i}$ of Eq. (4.7)

$$\bar{a}_{nm}^{a,i} = \frac{1}{M(2n+1)} \iint_\sigma \int_{r_Q} \left(\frac{R}{r_Q}\right)^{n+1} \rho^a(r_Q) \, r_Q^2 \, \bar{Y}_{nm}(Q) \, \mathrm{d}r_Q \mathrm{d}\sigma \, .$$

Again, first we do the vertical integration of the density model and radial quantities

$$\rho_0 \int_{r_s}^{r_Z} \left(\frac{R}{r_Q}\right)^{n+1} \left(\frac{\bar{R}}{r_Q}\right)^{\nu} r_Q^2 \, \mathrm{d}r_Q = \rho_0 \, \frac{R^{n+1} \, \bar{R}^\nu}{2-n-\nu} \, r_Q^{2-n-\nu} \Big|_{\bar{R}+h}^{\bar{R}+Z} \, , \tag{4.26}$$

which can be rearranged to

$$\frac{\rho_0 \, R^3}{2-n-\nu} \left(\frac{\bar{R}}{R}\right)^{2-n} \left[\left(1+\frac{Z}{\bar{R}}\right)^{2-n-\nu} - \left(1+\frac{h}{\bar{R}}\right)^{2-n-\nu}\right] \, , \tag{4.27}$$

and inserted into Eq. (4.7) to obtain the spherical harmonics coefficients for the interior atmospheric potential

$$\begin{aligned} \bar{a}_{nm}^{a,i} = & \frac{\rho_0 \, R^3}{M \, (2n+1) \, (2-n-\nu)} \left(\frac{\bar{R}}{R}\right)^{2-n} \times \\ & \left[\left(1+\frac{Z}{\bar{R}}\right)^{2-n-\nu} - \left(1+\frac{h}{\bar{R}}\right)^{2-n-\nu}\right] \iint_\sigma \bar{Y}_{nm}(Q) \, \mathrm{d}\sigma \, . \end{aligned} \tag{4.28}$$

In contrast to the coefficients for the exterior potential, we do not have to consider a special case for the spherical harmonic degree n as for the ITSG ADM the factor ν will always be > 2 and hence the denominator $2 - n - \nu$ will not become zero in any case.

4.2.5 Effects on terrestrial and GOCE data

Finally, the effect of atmospheric masses on gravity observations used in this thesis is quantified in this section. For this purpose, the exterior and interior atmospheric potential based on the ITSG ADM is derived using the global GTOPO30 Digital Elevation Model (DEM). Details on its data sources and compilation methods can be found in U.S. Geological Survey (2014). In order to diminish the computational efforts, the original spatial resolution of $30'' \times 30''$ was generalized to $2' \times 2'$. The maximum spectral resolution for the spherical harmonics expansion was defined with D/O 360.

First, the effects on the gravity as observed on the Earth's surface is investigated. As mentioned in the beginning of section 4.2, we can discriminate two atmospheric effects within a consistent RCR procedure. On the one hand, the reference gravity derived from an EGM γ^{egm} (or the normal gravity γ), which is introduced to obtain a residual quantity, i.e. a gravity anomaly Δg at the surface, incorporates the effect of the exterior atmospheric potential δg_e^a. Hence, for a consistent removal of the atmospheric masses from the gravity observation g, this effect has to be removed from the reference gravity γ^{egm} when building the surface gravity anomaly

$$\Delta g = g - (\gamma^{egm} - \delta g_e^a) = g - \gamma^{egm} + \delta g_e^a \,. \tag{4.29}$$

On the other hand, the gravity observation is affected by the atmospheric masses above the observation point, i.e. the interior effect of the atmospheric potential in terms of gravity δg_i^a has to be reduced in order to get an atmosphere-free observation quantity

$$\Delta g = g - \gamma^{egm} + \delta g_e^a - \delta g_i^a \,. \tag{4.30}$$

In Figure 4.6 the global atmospheric effects on gravity observations at topographic heights is illustrated. The exterior atmospheric effect in Figure 4.6a varies between 0.47 mGal in the high mountain areas like the Himalaya and 0.71 mGal at sea level. In contrast, the interior atmospheric effect, which is depicted in Figure 4.6b, only has an amplitude range from -0.03 mGal to 0.20 mGal, since the interior potential is mainly representing the deviations from a radial symmetric atmosphere layering due to topography. In a consistent remove step, both effects have to be considered and add up to a total effect that globally varies between 0.27 mGal and 0.74 mGal, as shown in Figure 4.6c. Although the influence is not very large, it can be favourable to consider the atmospheric effects in a consistent RCR procedure, since a smoothing of the residual gravity signal can be expected.

At last, the atmospheric effect on GOCE gradient observations is evaluated at an assumed mean satellite altitude of 250 km. Since all relevant atmospheric masses can be considered to be located well below the satellite, we only have to deal with the external atmospheric potential. The corresponding influence on the vertical V_{zz} is illustrated in Figure 4.6d.

The amplitude of the atmospheric effect is in the range from -0.4 mE to 2.5 mE on global scale, which might have a smoothing effect on the gradient data that should not be neglected

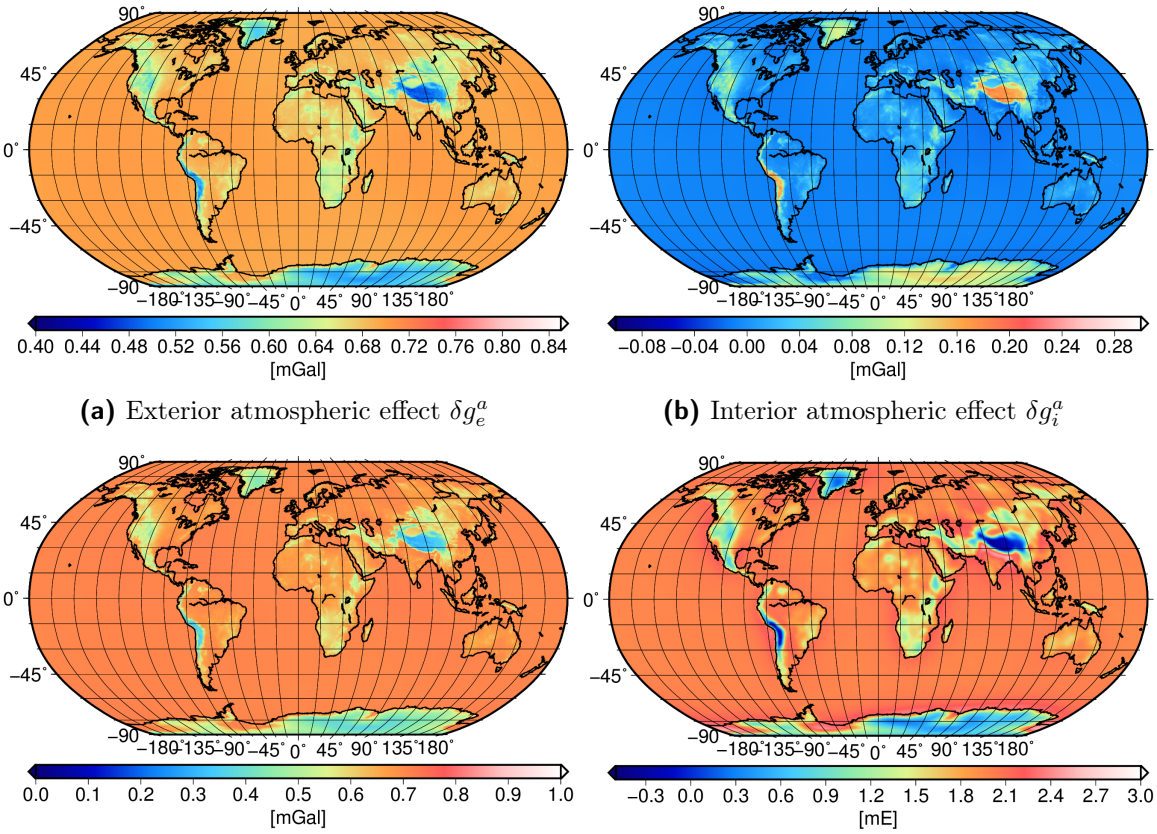

(a) Exterior atmospheric effect δg_e^a

(b) Interior atmospheric effect δg_i^a

(c) Combined atmospheric effect $\delta g_e^a - \delta g_i^a$

(d) Atmospheric effect on V_{zz} gradient

Figure 4.6: Atmospheric effects based on the ITSG ADM: effects of the exterior, interior and combined atmospheric potential on gravity observations at topographic heights from the GTOPO30 DEM (a-c), effect on vertical V_{zz} gradients at an assumed satellite altitude of 250 km (d)

within a consistent RCR approach. However, the major part will already be reduced when removing the normal field (or an EGM), and the remaining effects due to the lateral variations of the topography will be negligible (see chapter 7 or chapter 8).

4.3 Topographic reduction

The high-frequency variations of the gravity signal are primarily induced by the gravitational effects of the topographic masses. In case of LSC, such variations are undesirable, since they make it difficult to perform a reliable interpolation or prediction, as already discussed in the introduction to this present chapter 4. Hence, for any gravity field determination it is favourable to reduce the short-wavelength signal due to the topography prior to the actual estimation process. An overview of different methods for the reduction of terrain effects can for instance be found in Forsberg and Tscherning (1997) or in Wild-Pfeiffer (2007).

Since the influence of topographic masses on a certain point on Earth's surface decreases with the distance, different approximation methods can be used to evaluate the gravitational effect of the topography. In this thesis, the topographic mass effect is evaluated using the well known prism formula if the mass prism is located within a certain close distance to the evaluation point. For intermediate distances, such a mass prism can be approximated by a mass line, while for far distance topographic masses an approximation with point masses is sufficient (Wild-Pfeiffer, 2007). Using a sufficiently dense and accurate DEM and assuming a constant density for the topographic masses, conventionally chosen with $\rho = 2670\,\mathrm{kg\,m^{-3}}$, the topographic effect δg^{dem} can then be reduced from the gravity observations, see also Pock et al. (2014).

However, for a consistent RCR procedure it has to be considered that usually the long-wavelength effects of the gravity field are reduced by means of a global EGM, see section 4.1. Since an EGM incorporates all mass effects including those of the topography, a reduction of both, terrain effects and an EGM, would lead to a double consideration of the long wavelengths of the topographic gravity effect. To overcome this, the gravity effect of the topography

$$V^t(P) = G \iint_{\sigma} \int_{r_l}^{r_u} \rho \, \frac{r_Q^2}{l} \, \mathrm{d}r_Q \mathrm{d}\sigma \tag{4.31}$$

can be expanded into an according spherical harmonics series of the exterior topographic potential V^t of the form as given in Eq. (2.37). Similar to the atmospheric potential derived in section 4.2, corresponding fully normalized topographic potential coefficients $\bar{a}_{nm}^t$ can be derived by

$$\bar{a}_{nm}^t = \frac{1}{M(2n+1)} \iint_{\sigma} \int_{r_Q} \left(\frac{r_Q}{R}\right)^n \rho \, r_Q^2 \, \bar{Y}_{nm}(Q) \, \mathrm{d}r_Q \, \mathrm{d}\sigma \, . \tag{4.32}$$

The integration limits with respect to r_Q are given in this case by the radial distances to the lower bound r_l of the vertical mass column of a given DEM, i.e. the geoid level, and by the radial distance to the upper bound r_u, which is defined by the topographic height. Hence, the potential coefficients are finally obtained by

$$\bar{a}_{nm}^t = \frac{\rho}{M(2n+1)(n+3)} \, \frac{(r_u - r_l)^{n+3}}{R^n} \iint_{\sigma} \bar{Y}_{nm}(Q) \, \mathrm{d}\sigma \, . \tag{4.33}$$

In this way, the long-wavelength topographic effect $\delta g^{t,shc}$ which is incorporated in the reference gravity γ^{egm} of the EGM can be accounted for already in the spectral domain of the spherical harmonics expansion. The consistent consideration of the topographic mass effect from a gravity observation at the Earth's surface within a RCR approach can then be achieved by

$$\Delta g = g - (\gamma^{egm} - \delta g^{t,shc}) - \delta g^{dem} = g - \gamma^{egm} + \delta g^{t,shc} - \delta g^{dem} \,. \tag{4.34}$$

The expansion limit of $\delta g^{t,shc}$ has to be conform with the maximum degree N_{max} of the EGM. Investigations on the effect of the terrain reduction will be performed in more detail within the application for a regional geoid determination in chapter 7.

4.4 Isostasy

If we consider the crust as a homogeneous layer, one could assume that the reduction of topographic masses as suggested in the previous section would lead to decorrelated gravity observations. However, this is not the case in reality, which was already observed in the 18$^{\text{th}}$ century during the famous surveying campaign of the meridian arc in Peru lead by Pierre Bouguer (Lambeck, 1988). He noticed that his measurements of deflections of the vertical were significantly smaller than those expected from calculating the topographic attraction of the Andes Mountains. An equivalent phenomenon was also observed later in the 19$^{\text{th}}$ century by George Everest when surveying the Himalayan part of Northern India. These findings led to the conclusion that the effect of the topographic masses must be compensated to a certain extent in the Earth's interior, which was (and is) explained by introducing the concept of isostasy. According to this theory, there exists a certain level of compensation at which the equilibrium condition

$$\int_D^h \rho \, \mathrm{d}r = const \tag{4.35}$$

holds, meaning that the radial integration of the density ρ from the compensation depth D to the topographic height h is constant at the level of compensation.

For geodetic purposes different isostatic models have been developed, which are generally very simplified but nevertheless appropriate approaches considering the reduction of systematic effects within a remove-compute-restore scheme. The most prominent types of isostatic models, which are also described in standard literature like Hofmann-Wellenhof and Moritz (2005), Torge (1989) or Lambeck (1988), are introduced in the sequel.

4.4.1 Pratt-Hayford isostatic model

The Pratt-Hayford model is based on a constant compensation depth D, which is assumed to be in the order of around 100 km with respect to sea level, as indicated in Figure 4.7a. The masses above the compensation level are arranged in vertical columns. To each of these columns a certain density value is assigned, so they all have equal mass. Below the compensation depth, a uniform and homogeneous density distribution is assumed. For instance, in case

of the absence of topography ($h = 0$), the according density value of this column is commonly introduced as ρ_0 =2670 kg m^{-3}, the standard crustal density. The general isostatic condition for a certain column c_i with height h_i above sea level is then given by

$$\rho_{c_i} \, (D + h_i) = \rho_0 \, D \, , \tag{4.36}$$

while over ocean areas

$$\rho_{c_i} \, (D - d_i) + \rho_w \, d_i = \rho_0 \, D \, , \tag{4.37}$$

where d_i stands for the depth of the ocean of the corresponding column and ρ_w =1027 kg m^{-3} is the standard density of sea water.

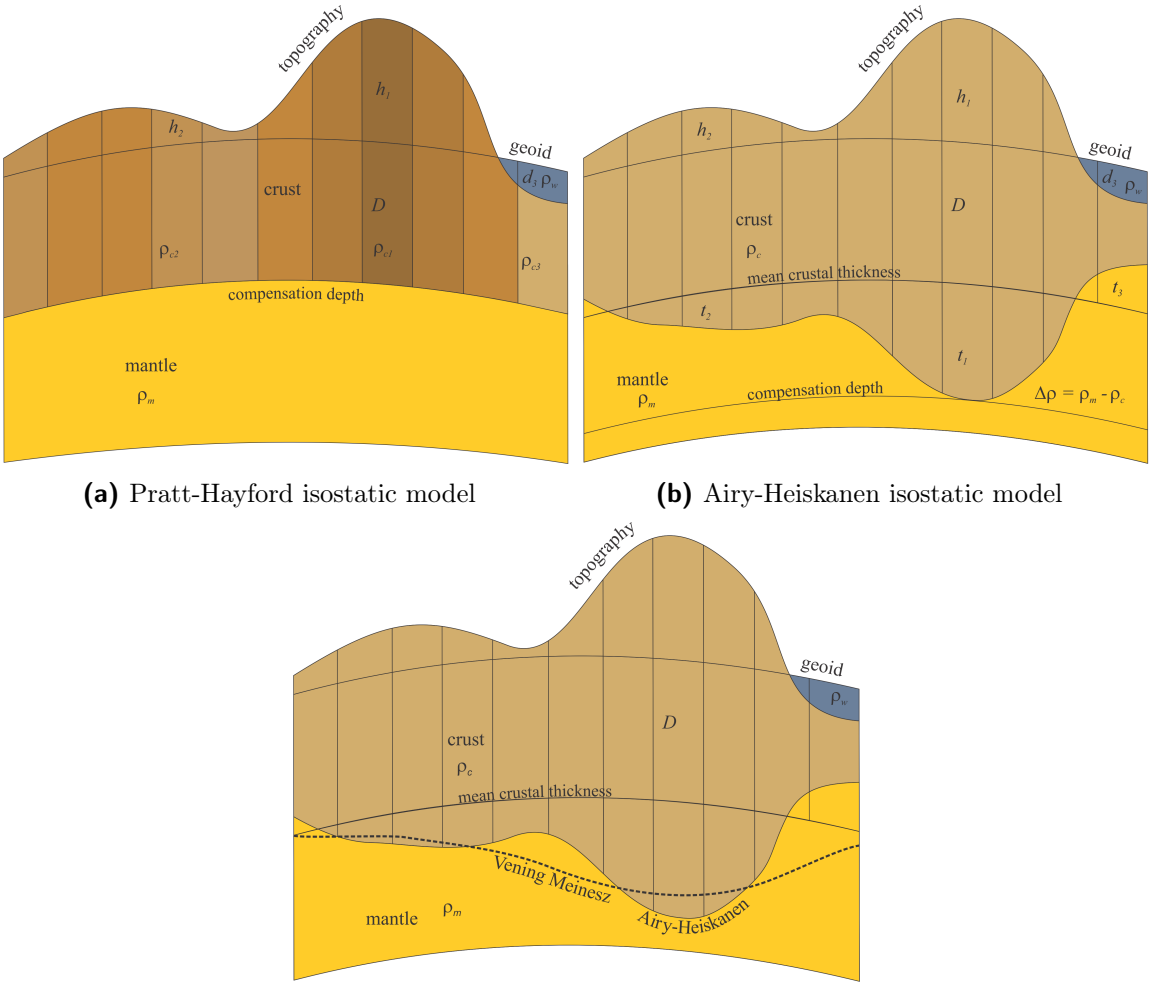

(a) Pratt-Hayford isostatic model

(b) Airy-Heiskanen isostatic model

(c) Vening Meinesz isostatic model

Figure 4.7: Isostatic models according to Pratt-Hayford, Airy-Heiskanen and Vening Meinesz

4.4.2 Airy-Heiskanen isostatic model

In the isostatic concept according to Airy-Heiskanen a different approach is pursued. Here, the topographic load consists of material of constant density ρ_c =2670 kg m^{-3}, which is settled above a considerably denser material, which commonly equals the mean mantle density ρ_m =3270 kg m^{-3}. To achieve the isostatic equilibrium condition, the model is assumed to behave similar to an iceberg, i.e. the crustal material comprising the topography is floating on the mantle. Hence, the higher the elevation of the topography is, the deeper the crust sinks into the mantle, which is illustrated in Figure 4.7b. Thus, isostatic equilibrium between penetration depth t_i with respect to an assumed mean crustal thickness D and the topographic height h_i for a certain column c_i over land is found by

$$\Delta\rho\, t_i = \rho_c\, h_i\ , \tag{4.38}$$

with the density contrast between mantle and crust $\Delta\rho = \rho_m - \rho_c$. For ocean areas the relation is given by

$$\Delta\rho\, t_i = (\rho_c - \rho_w)\, d_i\ , \tag{4.39}$$

where again d_i is the depth of the ocean and ρ_w =1027 kg m^{-3} is the standard density of sea water.

4.4.3 Vening Meinesz isostatic model

The Airy-Heiskanen as well as the Pratt-Hayford concept are strictly local approaches, which assume that the topographic masses only affect the vertical column underneath. However, in reality a surface load will more likely have a regional influence than the simplified localized characteristics. The Vening Meinesz model is a based on a modified Airy-Heiskanen approach that considers the crust to be elastic, which is regionally bending due to the topographic masses, see Figure 4.7c. In geophysical sense, this Vening Meinesz model is more realistic, however it is much more complex than, e.g., the Airy-Heiskanen concept. A general formulation of this model can be found in Moritz (1990a). The derivation of the bending curve of the crust is given for instance in Abd-Elmotaal (1993). He also shows that the Vening Meinesz model can be sufficiently approximated by smoothing an Airy-Heiskanen model. For geodetic purposes, the latter one is mostly considered as sufficient and therefore will also be used in this thesis.

4.4.4 Isostatic reduction

The isostatic effect on gravity observations based on the Airy-Heiskanen model

$$V^{iso}(P) = G \iint_{\sigma} \int_{r_l}^{r_u} \Delta\rho\, \frac{r_Q^2}{l}\, \mathrm{d}r_Q \mathrm{d}\sigma \tag{4.40}$$

can be expanded into an isostatic potential V^{iso} in terms of a spherical harmonics series very similar to the topographic potential in section 4.3, with the corresponding fully normalized

isostatic potential coefficients $\bar{a}_{nm}^{iso}$

$$\bar{a}_{nm}^{iso} = \frac{\Delta\rho}{M(2n+1)(n+3)} \frac{(r_u - r_l)^{n+3}}{R^n} \iint_{\sigma} \bar{Y}_{nm}(Q)\, \mathrm{d}\sigma \,. \tag{4.41}$$

In comparison to the topographic potential, there are some differences concerning the density assumptions and the integration limits. In this case, we want to obtain the gravitational effect of the variations of the crust-mantle boundary which are deviating from a homogeneous mass distribution with uniform density. Hence, instead of the standard rock density of $\rho_0 = 2670\,\mathrm{kg\,m^{-3}}$, the constant density contrast $\Delta\rho$ between crust and mantle is introduced. The upper limit r_u for the integration of a specific mass column i is represented by the radius of the mean crustal thickness D, while the radius of the lower limit r_l is defined by the penetration depth t_i w.r.t. to D, see Figure 4.7b. The penetration depth t_i over land can be found by rearranging Eq. (4.38) to

$$t_i = \frac{\rho_c}{\Delta\rho}\, h_i \,, \tag{4.42}$$

and for ocean areas Eq. (4.39) to

$$t_i = \frac{\rho_c - \rho_w}{\Delta\rho}\, d_i \,. \tag{4.43}$$

The reduction of the isostatic effect on any gravity observation can then be performed in the spatial domain by an spherical harmonics synthesis of Eq. (4.40) into the desired quantity. Again, within a consistent RCR process the removal of the long-wavelength gravity signals by means of a global EGM up to a maximum truncation limit of D/O N_{max}^{egm} already implies that the long-wavelength influences of the isostatic effect are removed as well. Thus, the isostatic effect only has to be considered from $N_{max}^{egm} + 1$ to the maximum resolution of the isostatic potential model. For a terrestrial gravity observation, the reduction of the isostatic effect δg^{iso} can in this sense be written as

$$\Delta g = g - \gamma^{egm} - \delta g^{iso} \,. \tag{4.44}$$

For further details on the influence of isostatic effect on gravity observations, the reader is referred to the application for a regional geoid determination in chapter 7.

5 The GOCE mission

The Living Planet Programme of the ESA is based on two branches of Earth observation concepts (ESA, 2014). The Earth Watch element comprises the operational data collection and delivery for instance from meteorological satellite missions like Meteosat or MetOp. The second element is the Earth Explorer category, which are dedicated scientific research missions to investigate specific aspects of the Earth's composition, environment and climate. The GOCE is the first core mission chosen to be launched by ESA (ESA, 1999) with the aim to recover the static gravity field of the Earth. As this thesis has its focus on the scientific exploitation of the data observed by the GOCE satellite, this chapter is summarizing the key aspects of this mission. A detailed overview can also be found, e.g., in Drinkwater et al. (2003), Drinkwater et al. (2007) or van der Meijde et al. (2015).

5.1 Mission objectives and design

The GOCE mission was launched on March 17$^{\text{th}}$ in 2009 from the Plesetsk Cosmodrome in Russia. The satellite was injected into a sun-synchronous orbit with an inclination of 96.7° at 279 km height. After a commissioning phase, GOCE started its nominal science operations end of October 2009 at an altitude of 255 km orbiting the Earth in approximately 90 minutes. The expected mission lifetime was initially defined with 20 months. However, due to the low solar activity during the measurement period, the satellite could be kept in space until late 2013, when GOCE stopped measuring in science mode on the 21$^{\text{st}}$ of October. During its last operational phase, GOCE had been lowered for further 30 km to an orbital height of about 224 km. The mission finally reentered the atmosphere on the 11$^{\text{th}}$ of November 2013 and remaining parts of it fell into the ocean between the Falkland Islands and the South American mainland.

The goal of the mission is the determination of the global static gravity field and its reference equipotential surface, the geoid, with outstanding high spatial resolution and accuracy. As the Earth's gravity field is the fundamental physical force for dynamic processes in the Earth's interior and on its surface, a variety of scientific applications benefit from a precise knowledge of the gravity field.

In geodesy, for instance, a precise geoid is the key to the global unification of height systems and enables the transformation from geometric heights gained from GPS measurements to orthometric heights (Rummel, 2012; Gerlach and Rummel, 2013). In oceanography, the combination of the static gravity field and the mean sea surface observed by satellite altimetry makes it possible to derive the mean dynamic ocean topography and consecutively the geostrophic ocean currents (Knudsen et al., 2011; Albertella et al., 2014). As a last field of applications to be mentioned here, the knowledge in solid earth physics is improving from a precise gravity field (Marotta, 2003). GOCE measurements are delivering valuable

information about density anomalies in the Earth's interior, and can be used as boundary values to determine Earth's lithosphere and upper-mantle structures, see for instance Basuyau et al. (2013) or Bouman et al. (2015). In particular, GOCE gravity gradients are also used for the derivation of the crust-mantle boundary, the so-called Mohorovičić discontinuity, which is also an application investigated in this thesis. Hence, a more detailed treatment on this issue can be found in chapter 8.

GOCE was designed in order to fulfil the demands of the scientific communities. The initial requirements on the mission were the determination of the gravity field with an accuracy of 1 mGal, or in terms of geoid heights of 1 to 2 cm, at a spatial resolution of 100 km half-wavelength (Drinkwater et al., 2003). To achieve this, GOCE flew at an extraordinary low average altitude of 255 km. At these heights the non-gravitational forces, in particular air drag and solar radiation pressure, acting on a satellite would force the satellite down back to Earth within a few days. Therefore, the GOCE satellite (Figure 5.1) was equipped with a so-called Drag-Free and Attitude Control System (DFACS).

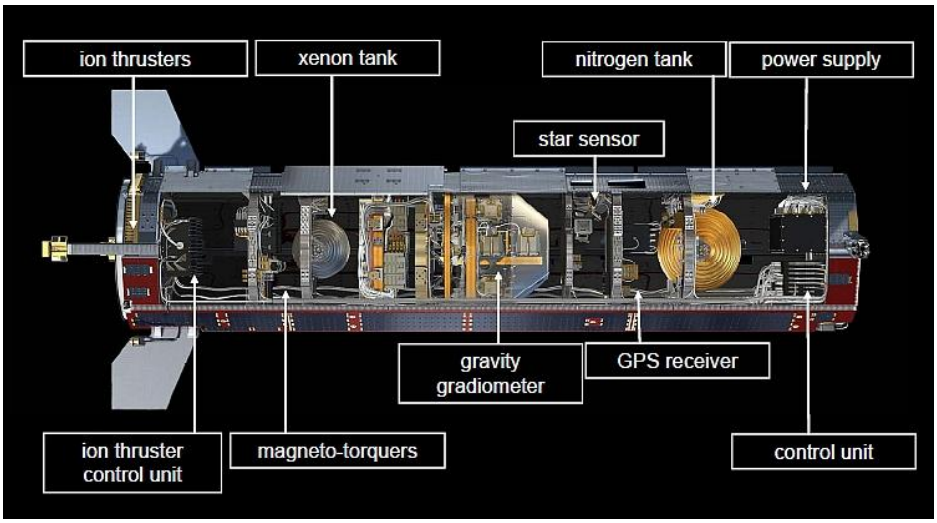

Figure 5.1: The GOCE satellite and its instrumentation (©ESA)

This device consisted of magnetic torquers to realign the spacecraft with respect to the Earth's magnetic field, three star trackers to provide information about the orientation and angular rate of the spacecraft, as well as of an ion thruster assembly which compensated the non-gravitational accelerations in along-track direction.

The core instrument of GOCE was the Electrostatic Gravity Gradiometer (EGG), which is shown in Figure 5.2a. The gradiometer instrument was designed to measure the medium to short wavelengths of the gravity field with high precision. To complement the EGG observations with information about the long wavelength gravity signals, GOCE had a GPS device onboard, which was used as Satellite-to-Satellite Tracking Instrument (SSTI) for the determination of the satellite's position and velocity. Together, all devices form the concept of Satellite Gravity Gradiometry (SGG) in combination with Satellite-to-Satellite Tracking in high-low mode (SST-hl).

5.2 GOCE Satellite Gravity Gradiometry

GOCE is the first satellite mission that realized the principle of gravity gradiometry in space. An extensive treatment on SGG can be found in the fundamental work of Rummel (1986), while more compact reviews are given for instance in Rummel et al. (2011), Hofmann-Wellenhof and Moritz (2005) or Stummer et al. (2012). The aim of SGG is to observe the gravity gradient tensor M (also called Marussi tensor)

$$M = \begin{pmatrix} \frac{\partial^2 V}{\partial x^2} & \frac{\partial^2 V}{\partial x \partial y} & \frac{\partial^2 V}{\partial x \partial z} \\ \frac{\partial^2 V}{\partial y \partial x} & \frac{\partial^2 V}{\partial y^2} & \frac{\partial^2 V}{\partial y \partial z} \\ \frac{\partial^2 V}{\partial z \partial x} & \frac{\partial^2 V}{\partial z \partial y} & \frac{\partial^2 V}{\partial z^2} \end{pmatrix} = \begin{pmatrix} V_{xx} & V_{xy} & V_{xz} \\ V_{xy} & V_{yy} & V_{yz} \\ V_{xz} & V_{yz} & V_{zz} \end{pmatrix}, \tag{5.1}$$

which represents the second order derivatives of the gravitational potential V in an arbitrary Cartesian coordinate system (x, y, z). The basic properties of the tensor are its symmetry and, according to Eq. (2.13), the fact that it is trace-free. The Marussi tensor can be retrieved from the measurements taken by the EGG. The gradiometer instrument consists of six accelerometers arranged pairwise on three orthogonal axes, which are mounted with a baseline of 0.5 m as illustrated in Figure 5.2b (Cesare, 2008). The axes define the instrumental reference frame, commonly denoted as the Gradiometer Reference Frame (GRF), which is centered almost perfectly at the satellite's COM. The X-axis of the GRF is pointing approximately in the satellite's flight direction, the Z-axis radially downwards and the Y-axis complementing an orthogonal system (Gruber et al., 2010a).

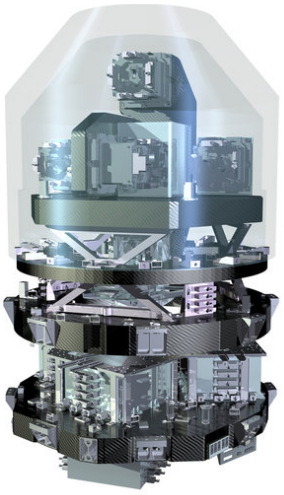

(a) Gradiometer instrument model (excluding harness), ©ESA

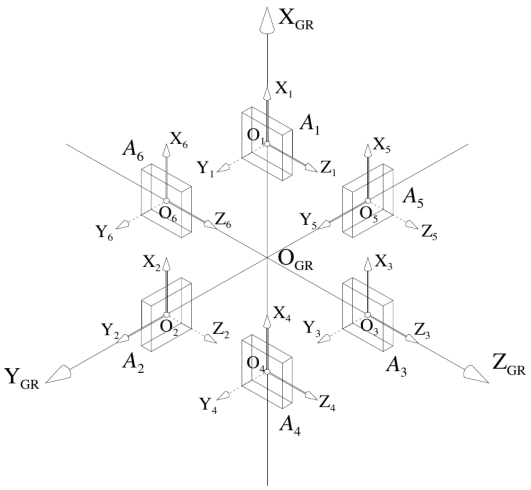

(b) Arrangement of the six accelerometers in the instrument frame GRF with the less sensitive axes as dashed arrows, ©Cesare (2008)

Figure 5.2: The GOCE gradiometer instrument

The actual acceleration observations of each accelerometer do not only contain the acceleration due to the Earth's gravitational field but include also centrifugal accelerations due to the satellite's rotation, Euler accelerations due to the satellite's angular accelerations and finally residual non-conservative accelerations which are not fully compensated by the DFACS. Hence, each accelerometer measurement $\boldsymbol{a}_i$ can be described as shown for instance

in Stummer et al. (2012) by

$$\boldsymbol{a}_i = -(M - \Omega^2 - \dot{\Omega})\boldsymbol{r}_i + \boldsymbol{d}\,, \tag{5.2}$$

where $\boldsymbol{r}_i$ is the distance between the accelerometer and the satellite's COM, $\Omega^2\boldsymbol{r}_i$ is the centrifugal and $\dot{\Omega}\boldsymbol{r}_i$ is the Euler term (note that in this notation lower case letters should be understood as vectors, while upper case letters are matrices). The uncompensated non-gravitational accelerations acting on the COM are represented by the vector $\boldsymbol{d}$. Since every accelerometer is exposed to the same non-conservative accelerations $\boldsymbol{d}$, it is possible to separate this term by building the so-called common mode accelerations $\boldsymbol{a}_c$ for each accelerometer pair $ij = 14, 25$ and 36 (see Figure 5.2b)

$$\boldsymbol{a}_{c,ij} = \frac{\boldsymbol{a}_i + \boldsymbol{a}_j}{2} \approx \boldsymbol{d}\,, \tag{5.3}$$

since $\boldsymbol{r}_i + \boldsymbol{r}_j \approx 0$. This information can then be used for the drag compensation of the satellite. On the other hand, a further linear combination of accelerations can be formed, which are known as differential mode accelerations $\boldsymbol{a}_d$

$$\boldsymbol{a}_{d,ij} = \frac{\boldsymbol{a}_i - \boldsymbol{a}_j}{2} = -\frac{1}{2}(M - \Omega^2 - \dot{\Omega})(\boldsymbol{r}_i - \boldsymbol{r}_j)\,, \tag{5.4}$$

which have the advantage that the disturbing non-conservative accelerations cancel out. As the geometry of the gradiometer system (and thus $\boldsymbol{r}_i$ and $\boldsymbol{r}_j$) is accurately known, the gravity gradients can be recovered from the differential mode accelerations. By introducing the quantity

$$\Gamma = M + \Omega^2 + \dot{\Omega}\,, \tag{5.5}$$

the Marussi tensor can be found with

$$M = \frac{1}{2}(\Gamma + \Gamma^T) - \Omega^2\,, \tag{5.6}$$

because the angular velocities and angular accelerations composing Ω and $\dot{\Omega}$ can be reconstructed from the combination of star sensor and gradiometer measurements. For a detailed step by step derivation of the individual tensor components see Stummer et al. (2012). The quite straightforward derivations of the GGT summarized until now are made under the assumption that we deal with a perfect gradiometer instrument. In the case of GOCE, this is not true in reality and two particular aspects have to be considered.

Due to their specific design (for details, see Cesare, 2008; Floberghagen et al., 2011), each accelerometer has two ultra-sensitive axes and one less sensitive direction, which are indicated in Figure 5.2b by solid and dashed arrows. As a consequence, it is not possible to resolve every gravity gradient of the Marussi tensor with the same precision, which is also illustrated in Figure 6.2. Due to the accelerometer arrangement, the tensor elements of the trace V_{xx}, V_{yy} and V_{zz} (which can be assumed to contain most of the gravity information), as well as V_{xz} can be obtained with highest precision. The off-diagonal elements V_{xy} and V_{yz} can only be determined with minor quality of about factor 100 to 1000 worse than the others (Müller, 2003; Rummel et al., 2011). Furthermore, the accelerometers are manufactured in order to maximize the measurement accuracy in a certain frequency range, the so-called Measurement Bandwidth (MBW), which is defined from 5 to 100 mHz. This was resulting from GOCE

feasibility studies on the optimum configuration of SGG and SST-hl in order to meet the goals of the mission (Cesare, 2008). The corresponding requirement for the noise level of the trace of the GGT was defined by $11\,\mathrm{mE}/\sqrt{\mathrm{Hz}}$ between 20 and 100 mHz, with allowance to reach $100\,\mathrm{mE}/\sqrt{\mathrm{Hz}}$ at the lower end of the MBW. Below the MBW the errors increase with $1/f$, with f being the frequency. In the time domain this behaviour corresponds to the drift of the gradiometer instrument. These two characteristics, the disparate measurement quality of the tensor elements and the superimposed errors, need special attention when using GOCE gravity gradients and will be discussed further in chapter 6.

5.3 GOCE reference frames

In addition to the conventional reference frames, which have already been introduced in section 2.1, three further mission-specific types of reference frames can be distinguished and are introduced below.

Local Orbital Reference Frame (LORF) The LORF has its origin in the actual COM of the satellite and is defined with the X-axis coinciding with the instantaneous direction of the orbital velocity vector $\boldsymbol{v}$. The Y-axis is defined to be normal to the plane given by $\boldsymbol{v}$ and the vector $\boldsymbol{r}$ from the Earth's center to the origin, i.e. it is pointing in the direction of the orbital angular momentum vector $\boldsymbol{n} = \boldsymbol{r} \times \boldsymbol{v}$. The Z-axis complements a right-handed system, so it is almost radially pointing outward. The LORF is illustrated as green triad in Figure 5.3.

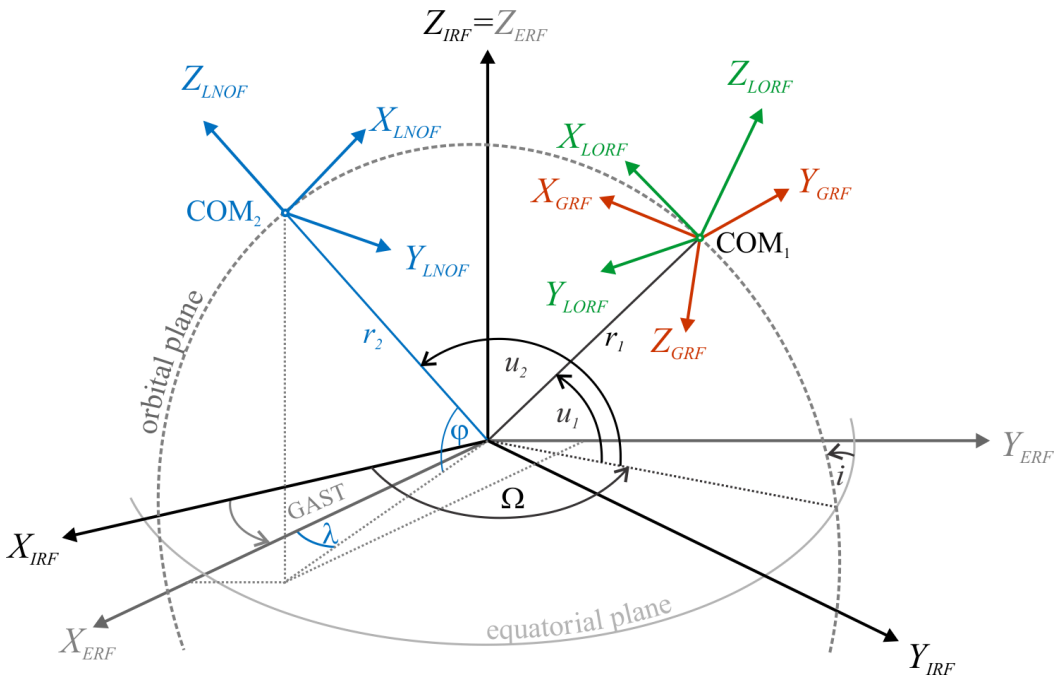

Figure 5.3: Different GOCE-related reference frames: GRF in red, LORF in green and LNOF in blue

Gradiometer Reference Frame (GRF) As mentioned in section 5.2, the axes of the accelerometer pairs define the instrumental reference frame GRF, which is centered at the satellite's COM. The accelerometer arrangement and the definition of the corresponding gradiometer axis is outlined in Figure 5.2b. The X-axis is formed by the accelerometer pair A4-A1, the Y-axis by A5-A2 and the Z-axis is pointing from A6 to A3. The triad is forming a right-handed Cartesian system, shown in Figure 5.3 in red. The X-axis of the GRF is kept parallel to the X-axis of the LORF as good as possible, which is controlled by the magnetic torquers. Thus, the Y- and Z-axis of the GRF are approximately pointing in the opposite direction of their equivalents in the LORF. The remaining misalignments between the two frames may reach several degrees (Pail, 2005).

Local North-Oriented reference Frame (LNOF) Similar to the LORF, the origin of this reference frame is at the COM of the satellite. The Z-axis is defined as the vector from the Earth's center to the origin radially pointing outwards. The Y-axis is parallel to the normal vector of the meridional plane through the GOCE COM pointing East, while the X-axis is complementing the triad to a left-handed Cartesian system pointing to the North direction given in blue in Figure 5.3. Note that the official GOCE standard definition for this frame is a right-handed North-West-Up frame (Gruber et al., 2010b). In order to be consistent to the conventional definition of local level system (see section 2.1.3), the LNOF in our case is introduced as a left-handed North-East-Up frame.

5.4 GOCE data processing and products

The data processing of the GOCE mission on ground is performed in three consecutive steps under the supervision of ESA. The Level 0 data contains the raw GOCE science payload instruments time series as well as their housekeeping and ancillary data. The scientific data processing to convert the raw data to so-called Level 1b data given in engineering units is performed by the Payload Data Segment (PDS), which is described in Frommknecht et al. (2011). A detailed overview on this products and its data formats can also be found in ESA (2006). The main tasks are to produce calibrated, corrected and geolocated EGG and SSTI observations as well as attitude information for the transformation from the GRF to the IRF.

Since the performance of the derivation of the gravity gradients did not meet the pre-launch expectations of the mission, the processing strategy for EGG and star tracker measurements has been revised and the gradiometer Level 1b processing scheme has been updated according to Stummer et al. (2012). These Level 1b data serve as input for the final category of data released by ESA, the Level 2 data which are the dedicated end user products.

The computations are performed within the High-level Processing Facility (HPF), a scientific data analysis and processing system distributed over ten participating institutions (Rummel et al., 2004). Level 2 data include for instance the final gradient observation time series, precise orbits, auxiliary data and ultimately the gravity field solutions in terms of spherical harmonics expansions and their accuracy information in terms of full variance-covariance matrices, see Table 5.1. The data can be accessed either via the ESA online client service EOLI-SA (`http://earth.esa.int/EOLi/EOLi.html`) or the GOCE virtual online

archive (`http://eo-virtual-archive1.esa.int/Index.html`). The processing strategies for Level 2 products as well as the corresponding data descriptions and user guidelines are summarized in Gruber et al. (2010b).

Table 5.1: Selected GOCE Level 2 products overview

Product	Description
Gravity gradients	
EGG_NOM_2	Level 2 gravity gradients in GRF
EGG_TRF_2	Level 2 gravity gradients in LNOF
Orbits	
EGG_PSO_2	Precise science orbits
Gravity fields	
EGM_GOC_2	Final GOCE gravity field model
EGM_GVC_2	Variance-covariance matrix of the final gravity field model
SST_AUX_2	Time variable gravity field due to non-tidal mass variations

In the subsequent sections, the Level 2 data that are essential for the investigations in this thesis are described.

5.4.1 Gravity gradients

Since GOCE gravity gradients serve as fundamental observation type in this thesis, the corresponding Level 2 data products are introduced in more detail. The gravity gradients processing in the frame of HPF is described in detail in Bouman et al. (2009, 2011). Basically, two different versions are available, the EGG_NOM_2 and the EGG_TRF_2 data sets.

The EGG_NOM_2 products are provided in daily files in the instrumental frame GRF with a sampling rate of approximately 1 s and are time-tagged according to GPS time. These gradients are corrected for both, tidal and non-tidal temporal gravity field variations, which are summarized in Table 5.2 (Gruber et al., 2010a).

Table 5.2: Temporal gravity field corrections and models applied to GOCE gravity gradients

Source	Type	Model/conventions
tidal	Direct tides	JPL DE405 ephemeris
	Solid Earth tides	IERS conventions 2003
	Ocean tides	FES2004
	Pole tides	IERS conventions 2003
non-tidal	Atmosphere and Ocean variability	ECMWF, OMCT
	Residual seasonal mass variations (hydrology)	GFZ RL04 GRACE fields

The magnitude of the temporal corrections for gravity gradients at orbit height can be considered to be below the actual noise level of the gradiometer (Abrikosov et al., 2006; Bouman et al., 2009). However, applying the corrections should improve the stochastic behaviour of

the gradient data and guarantees consistency with the GOCE SSTI data, which are corrected for the same effects (Bock et al., 2011), and are therefore applied to the gradients. The single tidal corrections and the combined non-tidal effects are also provided in the data files, hence the user is able to decide whether to work with gradients corrected for the temporal variations or not.

During the processing step, the gradient data is subject to an outlier detection (Bouman, 2004; Bouman et al., 2009). Furthermore, a calibration and validation of the GOCE gravity gradients with respect to external data is performed with the purpose to calculate calibration parameters (scale factors) and to check if these should be applied. Depending on these results, specific flags for each component of the gradient tensor are given in the data files (see Gruber et al., 2010b). A description of these flags is given in Table 5.3.

Table 5.3: Data flags in the EGG_NOM_2 data products and their description

Flag	Description	Temporal corrections applied	Outlier detected	Fill-in value provided	Calibration parameters applied
0	Level 1b data provided	-	-	-	-
1	Temporal corrections applied and validation with external data	x	-	-	-
2	As 1 and calibration applied	x	-	-	x
3	As 1, outlier suspected, fill-in value interpolated, (calibration applied)	x	x	x	(x)
4	As 1, outlier suspected, but no fill-in value, (calibration applied)	x	x	-	(x)
5	Level 1b data gap, fill-in value interpolated (as Flag 3)	x	(-)	x	(-)
6	Level 1b data gap, no fill-in value (gap > 5 s)	(-)	(-)	-	(-)

-...not applicable, (-)...no data, x...applied, (x)...applied if necessary

The nominal case is flag 1, which indicates that gradients from the Level 1b processing are corrected for time variable gravity effects and validated with external data. During the evolvement of the Level 2 processing with real data, the HPF decided not to provide fill-in values anymore after November 2010. Furthermore, due to the good performance of the in-flight calibration of the gradiometer, the external calibration results are not applied to the gradient data (see again Gruber et al., 2010b). Hence, the remaining flags that actually incur in the data files are restricted to flags 1, 4 (an outlier with no fill-in value provided) and 6 (a data gap with no fill-in value provided).

Besides the aforementioned information, the EGG_NOM_2 data files include error estimates from an HPF internal error model for all GGT components as well as the quaternions for the rotation from the GRF to the IRF.

The second available gradient data set is denoted as EGG_TRF_2, which are externally calibrated gravity gradients rotated to the LNOF as defined in Gruber et al. (2010b). Due to the large errors in the V_{xy} and V_{yz} tensor components and the $1/f$ error increase below

the MBW of all gradients (see section 5.2, last paragraph), a frame transformation would lead to leakage of these errors into the MBW and would deteriorate all gradients which nominally could be measured with high precision. For this reasons, V_{xy} and V_{yz} are completely replaced in the GRF with values computed from an EGM (the GOCE time-wise solution, see section 5.4.3), while the long wavelengths of the signal are also replaced by the model for every other gradient type.

This procedure is described in Fuchs and Bouman (2011) or Bouman et al. (2011). The ensuing rotation of the tensor to the LNOF implies that signal from the EGM is mapped into the gradients, so that the relative model content in the rotated gravity gradients for instance amounts up to 2% for V_{zz} and over 35% for V_{yy} (Fuchs and Bouman, 2011). Hence, a gravity field determination based on these rotated GOCE gravity gradients would be biased towards the EGM model used for the replacement, which is not desirable. As proposed by Gruber et al. (2007), Gruber et al. (2010b) or Fuchs and Bouman (2011) the EGG_TRF_2 products should therefore only be used for geophysical or oceanographic applications or interpretations and not for gravity field determination purposes.

5.4.2 Orbits

The orbit positions of the GOCE satellite are provided within the SST_PSO_2 precise science orbit files. They include an unconstrained kinematic orbit solution with 1 s sampling and a reduced-dynamic orbit solution with a sampling rate of 10 s, both given in the ERF. A detailed insight in the orbit determination in the frame of HPF is given in Bock et al. (2011) and references therein. Additionally, the rotation matrices for the transformation between ERF and IRF in terms of quaternions can be found in the data files.

5.4.3 Gravity field models

The ultimate products of the HPF processing chain are the global gravity field models in terms of coefficients of a spherical harmonics expansion representing the static part of the gravity field signal as well as their full variance-covariance information. There are three different methods implemented to generate these EGMs, which pursue complementary approaches for the gravity field computation, the so-called DIRect approach (DIR), the SPace-Wise approach (SPW) and the TIMe-wise approach (TIM). An overview of the processing strategies can be found in Pail et al. (2011).

While the SPW is based on a multi-step collocation procedure, DIR and TIM solve large normal equation systems in order to estimate spherical harmonics coefficients. The most important distinctive feature between DIR and TIM is the fact that the former uses external gravity field information from GRACE and SLR observations in combination with GOCE data, while the TIM solution can be considered as a 'GOCE-only' solution. This model is, apart from applying Kaula regularization, solely derived from GOCE data. Kaula regularization was introduced for zonal and near-zonal coefficients, which otherwise could only be determined insufficiently due to the polar gap, as well as for the highest degrees in order to improve the signal-to-noise ratio in this spectral range (Pail et al., 2011).

During the mission lifetime, several releases of models with increasing amount of incorporated GOCE data have been published. The last official release based on the SPW approach

was in November 2014 (release 4), while the DIR and TIM working groups published the final models (release 5) including all data of the whole GOCE mission in June 2014. The models can be accessed either via the official ESA online portals EO-LISA and GOCE virtual archive (see section 5.4), or the International Center for Global Earth Models (ICGEM) website `http://icgem.gfz-potsdam.de/ICGEM/`. The full variance-covariance matrices are only provided through the GOCE virtual archive.

6 Using real GOCE gravity gradients as point-wise observations

Within this thesis, GOCE gradients are aimed to be used as in-situ observations in a LSC procedure over a spatially restricted area. However, the optimum use of this data for local and regional applications poses additional scientific and methodological problems, which have two main causes that were already mentioned in section 5.2.

On the one hand, the gradiometer instrument was designed in such way, that the maximum accuracy of the measurements can be expected in the frequency range from 5 to 100 mHz, denoted as the Measurement Bandwidth (MBW). Nevertheless, the gradients are superimposed by measurement errors throughout the whole spectrum, which have particular characteristics depending on the frequency range under consideration. The properties of the gradient signals and their corresponding errors will be investigated in section 6.1. The spectral overlap of actual signal and noise make it necessary to preprocess and filter the gradient observations properly, prior to their use as direct observations within a computational process. This will be treated in section 6.2.

Furthermore, the measurement frame GRF describing the actual orientation of the instrumental axes of the gradiometer in orbit, does not coincide with an ideal frame such as the Local Orbital Reference Frame (LORF), which would be the favourable frame to perform the noise reduction (see section 6.2). The deviation between these two frames can amount to several degrees (Pail, 2005; Fuchs and Bouman, 2011). If the gradient tensor were rotated, the inaccurate gradient components would degrade all other measurements as well. Moreover, such a rotation would also cause leakage of the $1/f$ low-frequency error into the MBW, as documented by Bouman (2007). Therefore, different methodological concepts are developed and investigated in section 6.3.

6.1 Signal and noise characteristics

According to the pre-launch mission performance requirements (Cesare, 2008), the measurement errors of the gradient tensor trace, which represents the remaining noise after evaluating the Laplace condition in the exterior space $V_{xx} + V_{yy} + V_{zz} = 0$ (see also Eq. (2.13)), should have white noise behaviour between 20 to 100 mHz with a maximum magnitude of $11\,\mathrm{mE}/\sqrt{\mathrm{Hz}}$ ($1\,\mathrm{mE}{=}1 \times 10^{-12}\,\mathrm{m\,s^{-2}}$). Towards the lower end of the MBW, the allowed error budget is increasing to $18\,\mathrm{mE}/\sqrt{\mathrm{Hz}}$ at 10 mHz, reaching $100\,\mathrm{mE}/\sqrt{\mathrm{Hz}}$ at the edge frequency of 5 mHz. Below and above the MBW the noise is increasing systematically with $1/f$ respectively f^2, with f being the frequency. For a single GGT main diagonal component (and the off-diagonal V_{xz} gradient), the limiting white noise level therefore was expected to be between 5 and $8\,\mathrm{mE}/\sqrt{\mathrm{Hz}}$.

To illustrate this, the square roots of the Power Spectral Density (PSD) of a set of gravity gradients along a real GOCE orbit for November 2009, which were simulated from the GOCE TIM RL05 gravity field model to full D/O 280 in the GRF, are computed and plotted against the required error of the precisely measured GGT components in Figure 6.1. All PSD computations in this thesis are performed according to the method proposed by Welch (1967) using a Kaiser window function. For a description of the PSD, its computation and investigations concerning the choice of the window function, see Appendix B.2.

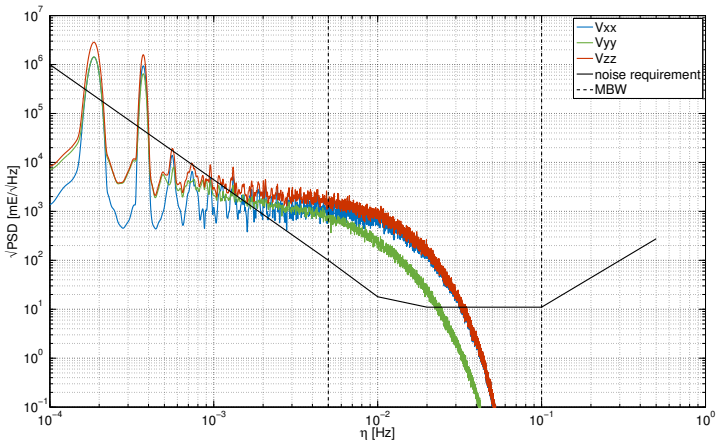

Figure 6.1: Square root of PSDs of the main diagonal GGT components for November 2009, simulated values from GOCE_TIM_RL05 to D/O 280 in the GRF; noise of GGT trace according to the performance requirements as black solid line; MBW from 5 to 100 mHz indicated with black dashed lines

Figure 6.1 shows that the signal content of V_{xx} and V_{zz} (blue and red curves) within the MBW is above the noise level from 5 to 35 mHz, while the V_{yy} component (green curve) has a generally lower signal content reaching the noise level already at around 25 mHz. As mentioned beforehand, below the MBW the gradiometer degrades with decreasing frequency $1/f$, which is comparable to a drift of the gradiometer (Rummel et al., 2011). Additionally, orbital and satellite attitude motions are modulated onto the gradiometer measurements. This causes further periodic effects that are visible in the noise spectrum at the frequency of one cycle per revolution (cpr) and multiples of it, which is clearly visible from Figure 6.2.

The second problem we have to face is the fact that the components of the gravity gradient tensor can not be measured with the same accuracy due to the specific orientation of the individual accelerometers composing the gradiometer assembly, see section 5.2. To obtain a realistic estimate for the noise of each GGT component, the differences between the actual time series and the reference signals simulated from the GOCE_TIM_RL05 model at the same orbit positions are computed in the GRF. The corresponding square root PSDs of the residuals are shown in Figure 6.2. In Figure 6.2a the main diagonal GGT components V_{xx} (blue curve), V_{yy} (green curve) and V_{zz} (red curve) are plotted together with the GGT trace error given by the gray dashed line and the pre-launch requirement shown as solid black line. The noise level of V_{xx} and V_{yy} within the frequency range from 20 to 100 mHz is around $10\,\mathrm{mE}/\sqrt{\mathrm{Hz}}$. The noise of the V_{zz} component does not reach this value but is with about $20\,\mathrm{mE}/\sqrt{\mathrm{Hz}}$ twice as high. This causes the error of the GGT trace to be at

a level of more than $20\,\mathrm{mE}/\sqrt{\mathrm{Hz}}$, which is considerably above the initial requirements of $11\,\mathrm{mE}/\sqrt{\mathrm{Hz}}$. The reason for this fact is not fully understood until now. Some first successful attempts to improve the situation were already performed, which resulted in a complete reprocessing in the Level-1b processing chain as reported, e.g., in Stummer et al. (2012) or Siemes et al. (2012). Although the expectations are not fully met in the frequency range where the highest precision was anticipated, the noise towards the lower end of the MBW is well below the requirements. Hence, the gradiometer performs better than originally specified in the low-frequency range.

While the error in the V_{xz} is comparable to V_{zz}, the noise level in the MBW for the V_{xy} and V_{yz} gradients is obviously up to 100 times higher than those of the well determined components as highlighted in Figure 6.2b. This is in accordance with the pre-launch expectations.

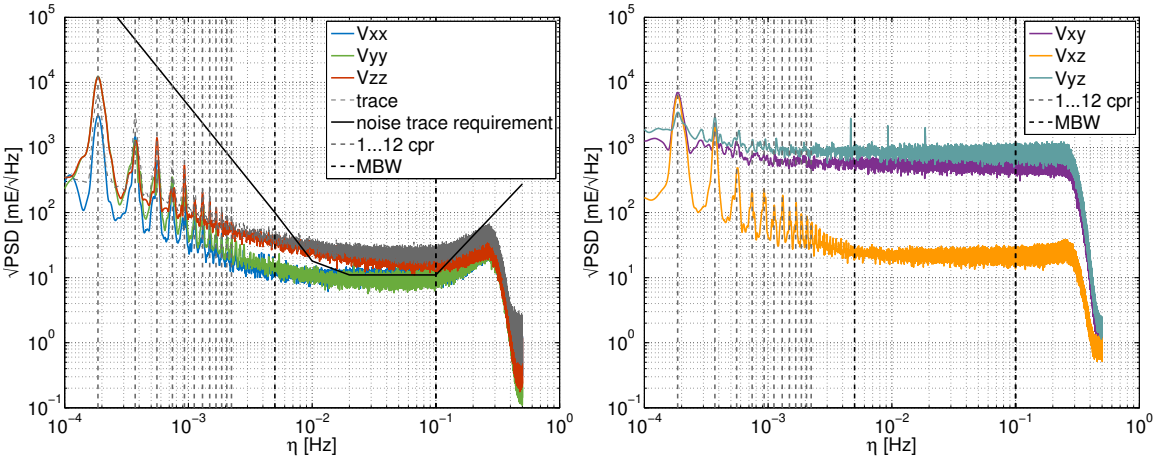

(a) Main diagonal components, trace, noise requirements for trace, frequencies at one to twelve cpr

(b) Off-diagonal components, frequencies at one to twelve cpr

Figure 6.2: Square root PSDs of the GGT noise estimated from the difference between EGG_NOM_2 observations and GOCE_TIM_RL05 model for November 2009

6.1.1 Outlier handling

As described in section 5.4.1, the EGG_NOM_2 data are already preprocessed to a certain extent, i.e. temporal corrections are applied and the gradients are validated. Depending on these results, flags are provided for each gradient component indicating the status of the data, see Table 5.3. Besides the nominal case Flag 1, also potential outliers are indicated with Flag 4 and data gaps are marked with Flag 6.

In the subsequent filter process, such outlier and data gaps can have negative impacts on the filter results. Transforming the data time series into the frequency domain, the erroneous data or gaps will imply a frequency behaviour which is actually not present in the data. In order to avoid this, outliers and data gaps are interpolated using spline interpolation. A minimum distance of ten epochs between two consecutive outliers is introduced as threshold.

If the amount of samples is lower, the outliers are concatenated and the whole time span is interpolated using the nine epochs before the first and after the last outlier that should be interpolated. The result of this procedure is exemplarily shown in Figure 6.3 for a set of outliers in the V_{xx} gravity gradient time series on the 13$^{\text{th}}$ of November 2009.

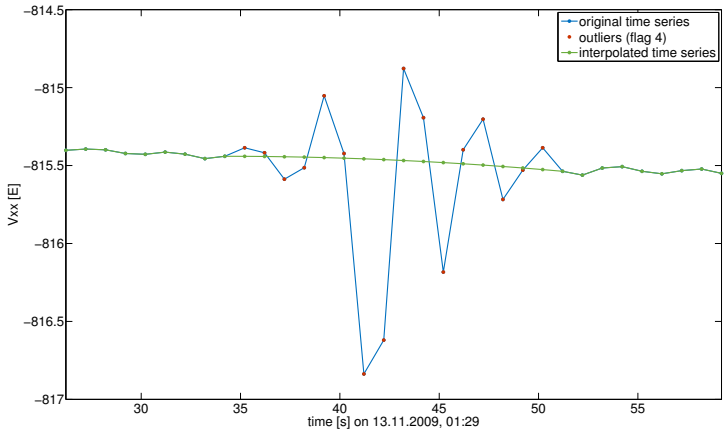

Figure 6.3: Original time series of V_{xx} gradients in blue, values flagged as outlier in red and interpolated signal in green

6.1.2 Bias and drifts

The gradient time series as provided in the EGG_NOM_2 product is compared to a reference signal simulated from the latest GOCE_TIM_RL05 gravity field model in Figure 6.4. The corresponding time series for each GGT component is shown for November 2009. Large offsets between actual measurements (blue curves) and reference signal (orange curves) can be seen, which are in the range of about $-28\,390$ E to 554 E.

Besides these biases, a further comparison of the centered time series, i.e. the time series subtracted by its mean value over the whole period under consideration, reveals some long term drifts, which is indicated in Figure 6.5. These drifts are clearly visible especially in the V_{yy}, V_{xy} and V_{yz} components, but are also present in all other gradient time series. This behaviour is for instance also reported by Visser (2011), and can be attributed to the drift behaviour of the accelerometers.

To reduce the biases and drifts from the original gradient time series a polynomial of order two is fitted to the data for each month, which is then removed from the observations. The corresponding time series are again illustrated for a period in November 2009 in Figure 6.6. The trend and bias free gradients now fit visually well to their centered simulated equivalents. This procedure is not adequate for the V_{xy} component, where still large deviations between reduced actual observations and the centered simulated gradients are obvious.

In fact, within each time series, there are still some long-wavelength oscillations and sudden jumps (not shown here), which would make it necessary to estimate biases and trends for selected periods within one month separately. However, in the present study this fact does not bother us since the long wavelengths of the gradient signals below the MBW will be filtered

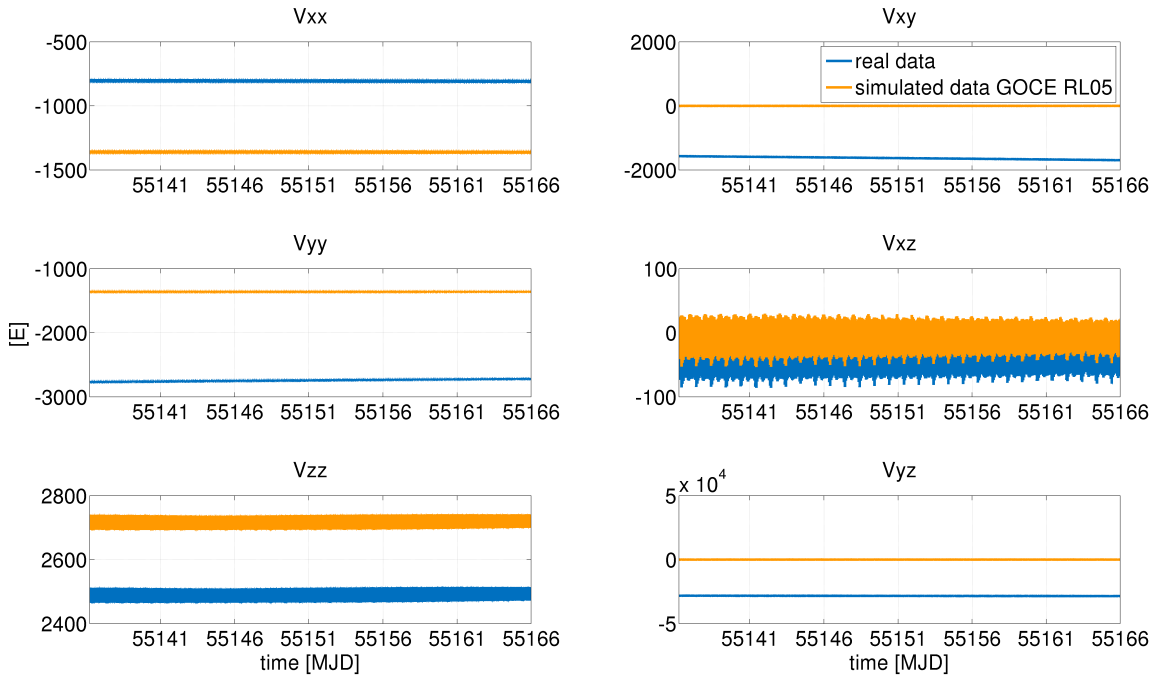

Figure 6.4: Original EGG_NOM_2 gravity gradient time series for November 2009 in blue, simulated values from GOCE_TIM_RL05 in orange

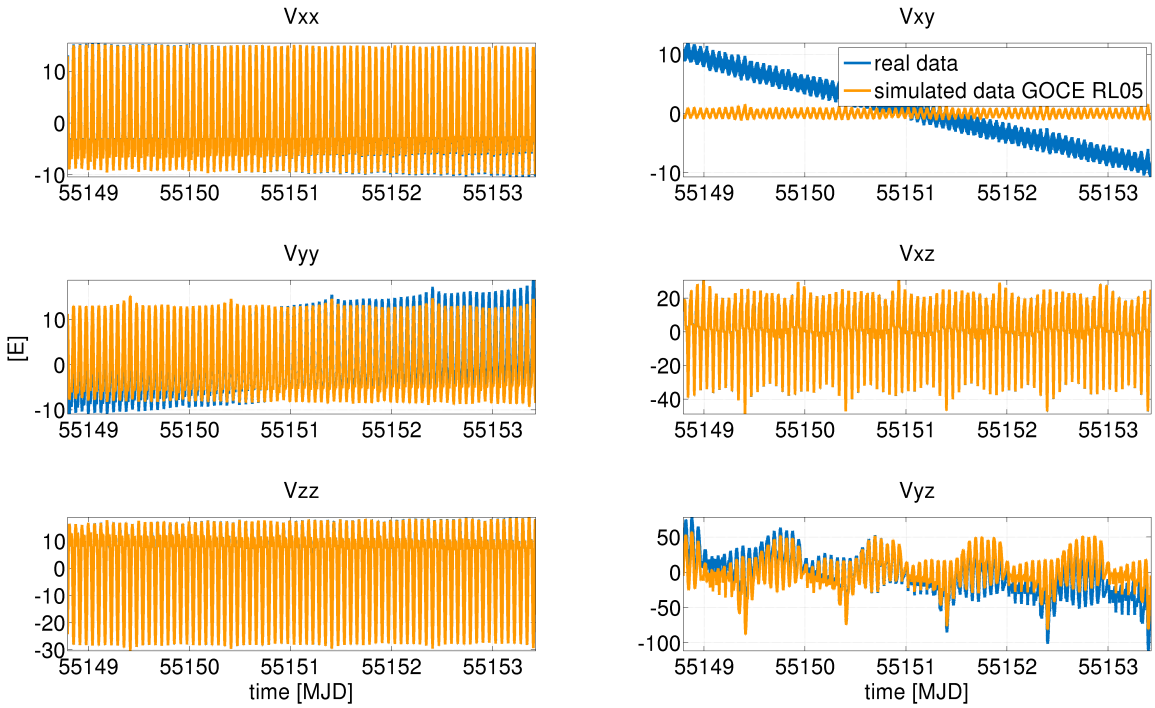

Figure 6.5: Centered EGG_NOM_2 gravity gradient time series for November 2009 in blue, centered simulated values from GOCE_TIM_RL05 in orange; time span from 13.11.2009 19:06:08 to 18.11.2009 10:12:48

out in the sequel. The simple trend and bias reduction is nevertheless performed, in order to obtain time series which are close to stationarity, which is a prerequisite for the following filter procedure. As the V_{xy} as well as the V_{yz} gradients can not be retrieved by GOCE with sufficient accuracy, they will not be used as observations in this thesis.

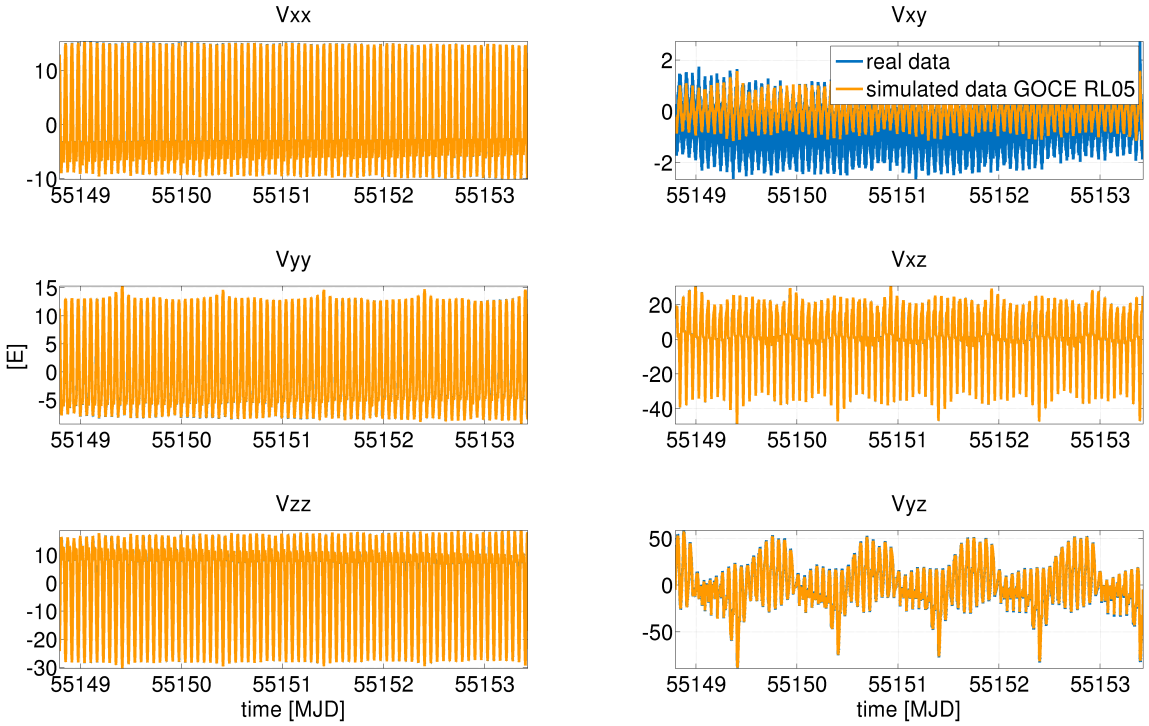

Figure 6.6: EGG_NOM_2 gravity gradient time series for November 2009 reduced by a polynomial of order two in blue, centered simulated values from GOCE_TIM_RL05 in orange; time span from 13.11.2009 19:06:08 to 18.11.2009 10:12:48

6.2 Noise reduction and filtering

Since this section is dedicated to the subject of filtering GOCE data, a brief introduction into the nomenclature and description of digital filters is given at the beginning. The basic theory of digital signal processing can also be found in standard literature like Oppenheim and Schafer (1975) or Koch and Schmidt (1994). In the case of GOCE we have to deal with gradient time series, the input signal $x(t)$, which we want modify in some way to reduce or remove undesired effects, so we get an output signal $y(t)$. The operation or algorithm which performs this transformation is denoted as system or filter S, which is applied to an input signal

$$x(t) \xrightarrow{S} y(t) \,. \tag{6.1}$$

In this study we assume the system S to be linear

$$x_1(t) \xrightarrow{S} y_1(t),\ x_2(t) \xrightarrow{S} y_2(t) \Longrightarrow a\,x_1(t) + b\,x_2(t) \xrightarrow{S} a\,y_1(t) + b\,y_2(t)\,, \tag{6.2}$$

and time-invariant w.r.t. any arbitrary time shift τ

$$x(t) \xrightarrow{S} y(t) \Longrightarrow x(t+\tau) \xrightarrow{S} y(t+\tau)\,. \tag{6.3}$$

Systems with these properties are commonly denoted as Linear Time-Invariant (LTI) systems in literature. Every LTI system can be described by the so-called impulse response $h(t)$, which is the response or output of a system invoked by a unit impulse that is represented by the Dirac function in the continuous case

$$\delta(t) = \begin{cases} \infty & \dots t = 0 \\ 0 & \dots t \neq 0 \end{cases}, \tag{6.4}$$

which is satisfying the condition

$$\int_{-\infty}^{\infty} \delta(t)\mathrm{d}t = 1\,. \tag{6.5}$$

In this way one can determine

$$\delta(t) \xrightarrow{S} h(t)\,, \tag{6.6}$$

where $h(t)$ is also denoted as filter function or system function. The application of a filter function $h(t)$ to an input signal $x(t)$ in the time domain corresponds to a convolution

$$y(t) = x(t) \star h(t) = \int_{-\infty}^{\infty} x(\tau)\,h(t-\tau)\,\mathrm{d}\tau\,, \tag{6.7}$$

or alternatively to a multiplication in the frequency domain

$$Y(\eta) = X(\eta)\,H(\eta)\,, \tag{6.8}$$

where $Y(\eta)$, $X(\eta)$ and $H(\eta)$ are the Fourier transforms $\mathcal{F}[y(t)]$, $\mathcal{F}[x(t)]$ and $\mathcal{F}[h(t)]$ according to Appendix B.1, and η denotes the frequency. $H(\eta)$ is furthermore denoted as the frequency response of an LTI system, which can be described by its amplitude response $|H(\eta)|$ and phase response $\angle H(\eta)$ (Oppenheim and Schafer, 1999)

$$H(\eta) = |H(\eta)|\,e^{i\angle H(\eta)}\,, \tag{6.9}$$

with i denoting the imaginary unit. The amplitude response $|H(\eta)|$ indicates the system's ability to amplify or attenuate the magnitude of a specific frequency of the input signal. Furthermore, the phase response $\angle H(\eta)$ describes how the system is modifying the phase of a particular frequency of the input signal. According to the characteristics of the phase response, systems can be classified into zero-phase, linear phase and non-linear phase response filters. In the first case there is no phase shift between input and output signal. If the system

is a linear phase filter the phase shift is a linear function of the frequency, which leads to an output signal that is shifted by a constant factor compared to the input signal. In contrast, there exist filters with a non-linear phase response, i.e. the frequencies of the input signal are subject to individual phase shifts, which lead to phase distortions in the output signal. In the case of filtering GOCE gravity gradients, any modification of the phase, i.e. a phase shift of the time series, must be avoided since otherwise the correct geolocation of the measured gradient signal would be lost. An according zero-phase filtering can be achieved by the forward-backward filtering procedure (Gustafsson, 1996), which is implemented in standard software packages like MATLAB.

In reality, the continuous signal $x(t)$ will be sampled by a sequence of discrete Dirac impulses with a particular sampling interval Δt to obtain a discrete signal $x(k)$

$$x(k) = x(t) \sum_{k=-\infty}^{\infty} \delta(t - k\Delta t) \,. \tag{6.10}$$

Hence, a discrete filter process can be described by the discrete convolution in the time domain

$$y(n) = \sum_{-\infty}^{\infty} x(k)\, h(n-k) \,. \tag{6.11}$$

An important class of LTI systems are those, for which the relation between input $x(n)$ and output $y(n)$ can be formulated in terms of a linear difference equation of the form

$$y(n) = \underbrace{\sum_{i=0}^{n_b} b_i\, x(k-i)}_{\text{moving average}} - \underbrace{\sum_{j=1}^{n_a} a_j\, y(n-j)}_{\text{auto regressive}} \,. \tag{6.12}$$

where a_i are b_i are constant filter coefficients and n_a and n_b define the filter order. In the case that $n_a = 0$, the remaining left term on the right side of Eq. (6.12) represents a moving average (MA) filter. Such a filter is also denoted as non-recursive, because it is independent of the past filter outputs $y(n-j)$. If $n_b = 0$, the remaining right term is called auto-regressive (AR) filter, which is due to its dependence on the past filter outputs also denoted a recursive filter. In combination, both filter types form a so-called auto-regressive moving average (ARMA) filter.

A further classification of LTI filters can be found by the characteristics of the according impulse response. Since the impulse response of MA filters has finite length, this type is also denoted as finite impulse response (FIR) filter. In the case of AR or general of ARMA the impulse response is of infinite duration, so these filters are also called infinite impulse response (IIR) filters.

6.2.1 Noise reduction using a Wiener filter approach

As we have seen in section 6.1, the gradiometer has a good performance only in the MBW, while below and above it is significantly worse. Especially the large long-wavelength errors lead to highly correlated observations along the orbit. In order to reduce this noise, a filtering step is introduced according to the Wiener filter theory (Papoulis, 1984). Such a filter is also applied within the SPW concept of GOCE HPF WP 7000 (Albertella et al., 2004; Migliaccio et al., 2004). This method assumes that a gravity gradient time series l consists of signal component t and a noise component n, which both are considered to be stationary signals (see Appendix B.2)

$$l = t + n \,. \tag{6.13}$$

Assuming that both, signal t and noise n are known, their Fourier transforms can be derived

$$F_t = \mathcal{F}[t] \quad \text{and} \quad F_n = \mathcal{F}[n] \,, \tag{6.14}$$

where $\mathcal{F}[\cdot]$ denotes the Fourier transform.

If t and n are centered, the covariance functions of signal and noise can be found by

$$C_{tt} = \mathrm{E}\{t\, t^T\} \quad \text{and} \quad C_{nn} = \mathrm{E}\{n\, n^T\} \,, \tag{6.15}$$

with $\mathrm{E}\{\cdot\}$ representing the expectation operator, which was already introduced in Eq. (3.2).

The Fourier transforms of the autocovariance functions are equivalent to the PSD of the signal under consideration

$$S_t = \mathcal{F}[C_{tt}] \quad \text{and} \quad S_n = \mathcal{F}[C_{nn}] \,. \tag{6.16}$$

For further details on autocorrelation, autocovariance and PSD refer to Appendix B.2 and B.3.

According to the Wiener filter theory, the filter W in the spectral domain can then be defined as

$$W = \mathcal{F}\,[w] = \frac{S_t}{S_t + S_n} \,, \tag{6.17}$$

where w is the filter representation in the time domain. This definition guarantees an optimum filter solution in the sense of a minimum remaining error according to the least squares principle. As already mentioned in the previous section, the filtering of the time series can either be performed in the time domain as a convolution

$$\hat{t} = w \star l \,, \tag{6.18}$$

or alternatively in the spectral domain by multiplication of the corresponding Fourier transforms

$$\hat{T} = \mathcal{F}[\hat{t}] = W \cdot \mathcal{F}[l] \,. \tag{6.19}$$

The filter error e of the estimate $\hat{t}$ with respect to the (in fact unknown) true signal t, is given by

$$S_e = S_t - W \cdot S_t \,. \tag{6.20}$$

Hence a corresponding error covariance function can be derived according to

$$C_{ee} = \mathcal{F}^{-1}\left[S_e\right] = \mathcal{F}^{-1}\left[\frac{S_t S_n}{S_t + S_n}\right] \,, \tag{6.21}$$

where $\mathcal{F}^{-1}[\cdot]$ is the inverse Fourier transform, see Appendix B.1. This is true since the Fourier transform of a signals' autocovariance function, e.g. C_{ee}, equals the PSD of the signal itself. With this step a consistent stochastic modeling of the error structure of the filtered signal is achieved, which is of great importance for a successful performance of the LSC processing.

For the application of such a Wiener filter to the real GOCE GGT observations, the key question is how to define the Wiener filter W. We have seen in Eq. (6.17) that the filter is based on the assumption that we know the noise-free signal t as well as the noise n itself. In reality, both pieces of information are a-priori unknown (otherwise filtering would not be necessary). Therefore, the noise-free signal t and the noise n have to be approximated. In the GOCE case, we can do so by simulating the GGT reference time series from the GOCE_TIM_RL05 model. This model is representing the best fit to the actual gravity field on global scale, which is estimated within a least squares procedure. Since the model is calculated solely from GOCE data, one can assume that gradients derived from this model represent the true noise-free gradient observations t globally in the best possible way. Consequently, also the measurement errors derived from the difference of real and simulated GGT observations can be considered as a realistic approximation of the actual noise n.

The Wiener filter process is exemplarily investigated for the gradient time series of November 2009 in the sequel. The real signal was preprocessed according to section 6.1.1 and section 6.1.2, i.e. outliers are interpolated and the time series is centered and de-trended. Next, the noise is approximated by the difference between real observations and a reference signal simulated from the GOCE_TIM_RL05 model with full resolution up to D/O 280. In Figure 6.7a the square root PSD of the resulting noise is shown as red line.

Due to the poor capability of the GOCE mission to resolve the low-frequency spectrum of the gravity signal, it was decided to a-priori reduce the long-wavelength signal constituents from the measured signal for the current study. Therefore, the signal constituents up to D/O 49 obtained from the reference model are subtracted. The effective spectral signal content in the measurements can therefore be assumed to start at D/O 50. The square root PSD of the corresponding reduced real signal is illustrated in Figure 6.7a as blue line, while the simulated reference signal based on the GOCE model from D/O 0 to 280 is shown in orange. The MBW from 5 to 100 mHz due to the gradiometer instrument design is again indicated by black dashed lines.

To facilitate interpretations, the spectral lines corresponding to D/O 50 and 280 are illustrated as grey dashed lines. According to Fuchs and Bouman (2011), a spherical harmonic D/O can be approximately represented in the frequency domain via the relation

$$\eta = \frac{\mathrm{D/O}}{T_r} \,, \tag{6.22}$$

where η is the frequency and $T_r = 5383\mathrm{s}$ is the approximated orbit revolution time of the GOCE satellite. As one can see from Figure 6.7a, the noise of the V_{zz} gradient is influencing the whole spectrum, with a considerable noise level within the MBW in the order of $20\,\mathrm{mE}/\sqrt{\mathrm{Hz}}$ and the tendency to increase towards both ends of the spectrum.

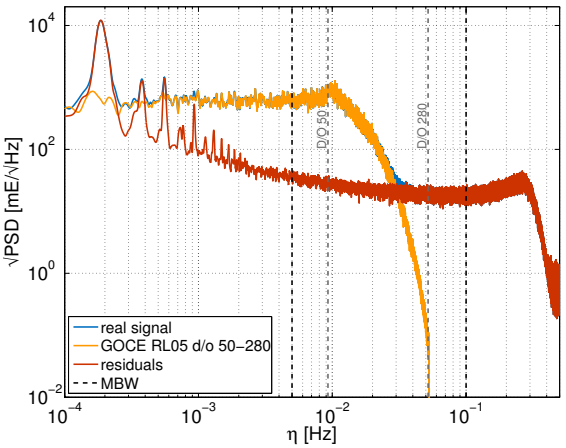

(a) Real signal, reference signal and noise

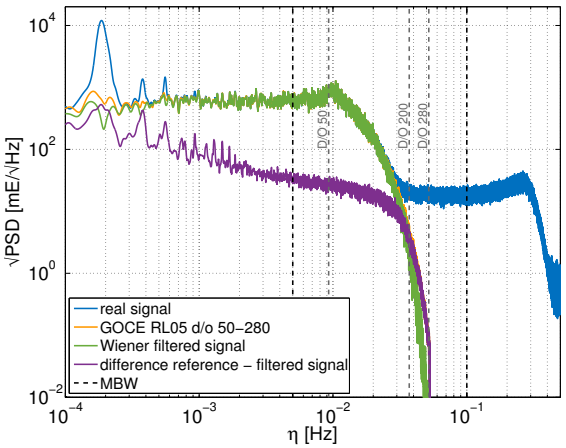

(b) Real signal, reference signal, Wiener-filtered real signal and difference

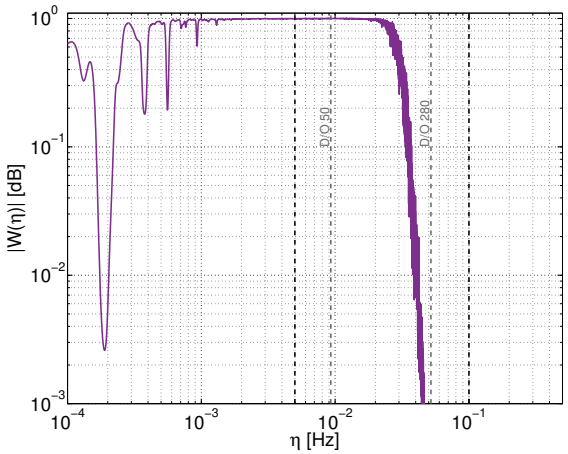

(c) Wiener filter amplitude response

Figure 6.7: Square root PSDs of the V_{zz} gradient time series for November 2009 before (a) and after Wiener filtering (b); trend (polynomial order 2) and long-wavelengths (GOCE_TIM_RL05 D/O 0-49) are a-priori reduced; Wiener filter amplitude response in the frequency domain (c)

In the next step, the Wiener filter is set up in the frequency domain according to Eq. (6.17) and applied to the real signal. Since the Wiener filter is based on the ratio between signal and noise, those frequencies where the noise power is high will be filtered out, while those where the signal power is high will pass the filter. This is essentially shown in the amplitude

response of the filter in Figure 6.7c. The PSD of the resulting filtered time series is illustrated in Figure 6.7b as green line. Compared to the real time series (blue line), the noise could obviously be reduced to a large extent in particular outside the MBW and the spectral signal content is very close to that of the reference signal from D/O 50 to 280, indicated in orange. The difference between the reference signal and the filtered signal depicted by the violet curve again demonstrates the characteristics of the Wiener filter, i.e. the frequencies with high noise power are largely filtered out.

In order to verify the filter result in the time domain, a subset of the filtered time series (green line) is opposed to the reference signal (orange line) for the time span 09:00:00 to 11:46:40 (10000 seconds) on 02.11.2009 in Figure 6.8. Their differences are illustrated as red line. As already indicated in the spectral domain (Figure 6.7b) the filtered V_{zz} gradients are in good correspondence with the GOCE_TIM_RL05 reference signal.

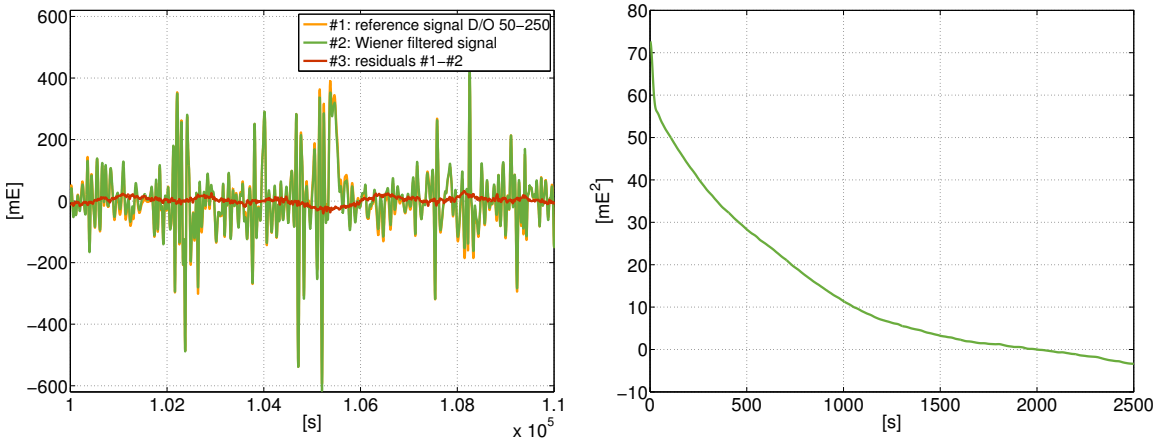

(a) Time series after Wiener filtering **(b)** Autocovariance function of filter error C_{ee}

Figure 6.8: Time series of GOCE_TIM_RL05 reference signal, Wiener filtered signal and residual differences (a); autocovariance function of filter error C_{ee} after Wiener filtering (b)

However, apart from the expected high-frequency variations, also some conspicuous long-wavelength deviations are clearly visible in the residuals. This is also confirmed by the autocovariance function of the filter error C_{ee}, which can be derived according to Eq. (6.21) and is shown for this filtering example in Figure 6.8b. The variance of the remaining noise after Wiener filtering amounts to $C_{ee}(0)$=72.6 mE^2 and the correlation length, at which $C_{ee} = C_{ee}(0)/2$, is 320 s.

To find an explanation for this behaviour, we once again return to Figure 6.7b. In the spectral domain, we can identify noticeable deviations between reference signal and filtered signal at the upper end of the spectrum between the frequencies according to spherical harmonic D/O 200 to 280. These differences can be explained by the increasing signal-to-noise ratio at the higher frequencies, which causes a stronger filtering. However, the differences are comparably small in amplitude and will only produce high-frequency deviations in the time domain.

Besides these deviations, we can also identify considerable differences below the MBW, in

particular at the frequencies that are multiples of one cpr of the GOCE orbit, see also section 6.1 and Figure 6.2. This is the origin of the long-wavelength differences between the reference signal and the filtered signal. A possible way to eliminate these long-wavelength errors would be a consecutive high-pass filtering of the already Wiener filtered gradient signal. This step can be justified for two reasons. As already mentioned, the gradients are of poor quality outside the MBW, so filtering is frequently applied to cut off the undesired frequencies, which is done for instance in Visser (2011) or Fuchs and Bouman (2011). Furthermore, for gravity field determination with LSC it is common practice to remove the long-wavelengths from the observations within a RCR procedure, see also chapter 4. Hence, in the next section a high-pass filter is applied in order to cope with the remaining long-wavelength structures that are still influencing the Wiener filtered signal.

6.2.2 High-pass filtering for low-frequency error reduction

The design of a digital filter is depending on various factors, which influence the filter result in different ways. Thus, at the beginning the characteristics of the filter have to be defined in order to get the desired result. In the present case, the digital filter to be used shall be a high-pass filter, i.e. only signal contents above a certain threshold frequency should pass, while signal contents below should be removed. Since this ideal case of a filter can not be realized due to the finite length of the filter, particular specifications and tolerance limits have to be defined in advance, see also Oppenheim and Schafer (1975). In this way, the spectral band is divided in different frequency sectors, which is outlined in Figure 6.9.

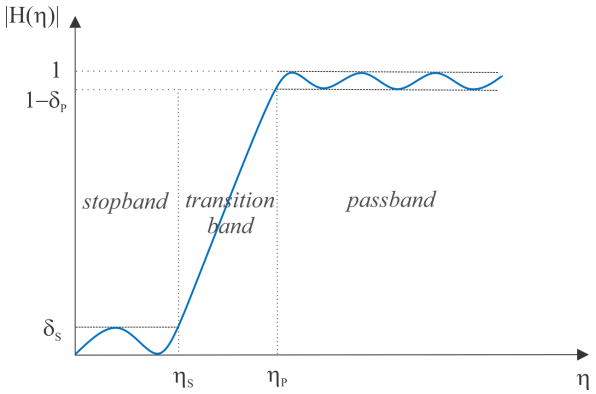

Figure 6.9: Filter specifications and tolerance limits for filter design

The range where signal contents should be suppressed is limited by the frequency η_s and is denoted as the stopband, while η_p indicates the start of the range where signal contents are preserved, the passband. As the digital filter can not perform like a step function, η_s and η_p can not be equal, which leads to a transition band where the filter function is allowed to ascend. Furthermore, the truncation of the filter to a finite length can lead to variations of the filter function in the pass- and stopband, which are limited by the passband ripple δ_p and the stopband attenuation δ_s.

Some investigative studies like Visser (2011) or Fuchs and Bouman (2011) use a Butterworth filter for high- or lowpass filtering of GOCE time series. However, as outlined in Polgár et al. (2012), there are several other filter types that could be used for filtering GOCE data. Hence,

at first different filters are investigated w.r.t. their applicability for the present purpose of high-pass filtering GOCE gradients.

Butterworth, Chebychev I, Chebychev II and Elliptic filters are chosen for this study, since they represent standard IIR filters that can be implemented and modified in order to meet the user requirements quite comfortably. These IIR filter types and functions are described in detail in Oppenheim and Schafer (1975). According to the example of the previous section we want to preserve the information content of the gradient signal that is higher than spherical harmonic D/O 50, which corresponds to a passband frequency of about η_p =9.3 mHz in the frequency domain. We exemplarily choose η_s =8.3 mHz for the stopband frequency, which corresponds to D/O 45. The tolerances for δ_p and δ_p are commonly expressed in the units Decibel [dB], which is a logarithmic function $\delta = 20\log_{10}(A_i/A_o)$ of the ratio between the input amplitude A_i and output amplitude A_o. Following this convention, for the passband ripple we use δ_p=1 dB and for the stopband attenuation δ_p=−10 dB. To verify the characteristics of the different IIR filters based on these specifications, their amplitude responses in the frequency domain are shown in Figure 6.10.

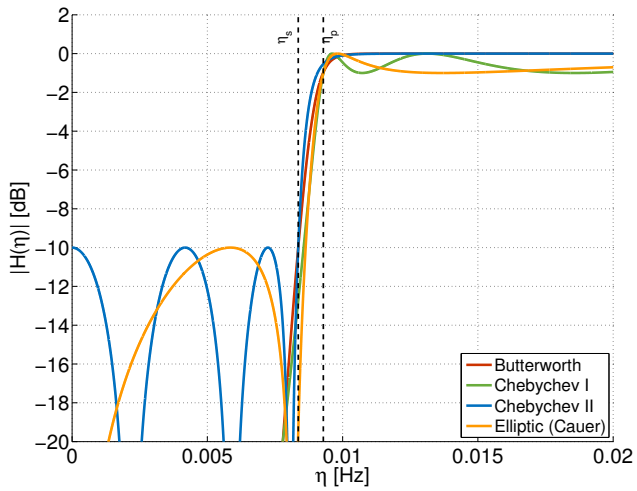

Figure 6.10: Amplitude response of different IIR filters according to the a-priori specifications η_p =9.3 mHz, η_s =8.3 mHz, δ_p=1 dB and δ_p=−10 dB

The filter response of the Butterworth filter is illustrated by the red line and shows its monotonic behaviour. The Chebychev I filter shown in green is defined in a way that it is monotonic in the stopband, but is allowed to oscillate in the passband. The opposite behaviour is true for a Chebychev II filter given as blue line, which has ripples in the stopband and is monotonic in the passband. The last filter used in these considerations is the Elliptic filter depicted in orange, which has ripples in the passband as well as in the stopband. Due to the restrictive definition of a monotonic curve, a Butterworth filter has the drawback that it needs a comparably high filter order of 17 (see Eq. (6.12)), i.e. a high number of filter coefficients is required to meet the specifications of this example. Since Chebychev I and II filters are allowed to have ripples in the pass- or stopband, they can be designed with a lower filter order of 6. The Elliptic filter can oscillate in both, passband and stopband, thus its approximation is possible with a filter order of 3.

Looking at the transition band between η_s and η_p, which are indicated in Figure 6.10 as black dashed lines, it can be seen that the Elliptic filter has the steepest slope, which means a rather abrupt jump from the stopband to the passband. In contrast, the Butterworth filter is not able to perform this transition that rapidly. An important aspect of the filter can also be investigated by looking at the ability to preserve the signal content at the beginning of the passband, i.e. at frequencies that are higher but close to the passband frequency η_p. Here, one can verify that the Butterworth filter still has a comparably long transition from η_p =9.3 mHz to about 10.1 mHz, where it finally reaches its desired passband magnitude of 1. In contrast, the Chebychev II filter is preserving this magnitude better towards η_p, with the limitation that the filter in the transition band takes longer to decay towards the stopband compared to the other filters. The filters which are allowed to have ripples in the passband, the Chebychev I and Elliptic filter, reach the passband magnitude 1 earlier, but have the disadvantage of a varying filter function in the passband.

The effect of applying the different filters to a V_{zz} reference signal, which is simulated from GOCE_TIM_RL05 from D/O 50 to 280, is shown in in terms of the square root PSDs in Figure 6.11. The PSD of the input signal is outlined in each plot as grey line in order to facilitate comparisons. Again, the transition band between η_s and η_p is indicated with black dashed lines in the plots and the colors are assigned to the filters according to Figure 6.10. Basically, the characteristics of the filter response functions of Figure 6.10 concerning their behaviour in the transition band can also be seen here. Furthermore, the main drawback of the Chebychev I and Elliptic filters shown in the right plots of Figure 6.11 can clearly be asserted. The variations due to the ripples in the passband of the filter functions are directly mapped into the filtered signal, which then also exhibit variations in the according spectral band, which are not present in the original reference signal. Thus, Chebychev I and Elliptic filters are not appropriate for the purpose of filtering GOCE gradients, since they corrupt the signal in the passband.

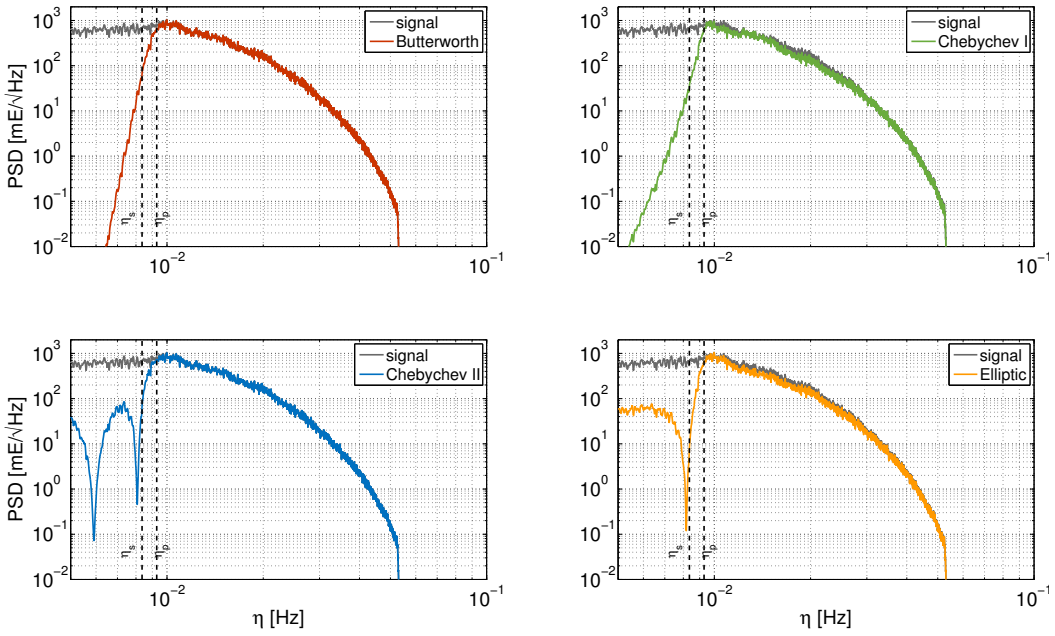

Figure 6.11: Square root PSDs of filter results from applying different IIR filters to a V_{zz} reference signal simulated from GOCE_TIM_RL05 from D/O 50 to 280

For the Butterworth and Chebychev II filter we can see that the signal content in the passband above η_p is preserved, except at the transition zones close to passband frequency. While the Butterworth filter is monotonically decreasing towards the lower frequencies in the stopband, the Chebychev II filter shows the expected ripples also in the PSD of the filtered signal. In the current example, these variations exhibit amplitudes of up to 90 mE and will imply according low frequency variations of the filtered signal also in the time domain, which is definitely not desired. Hence, for this example the Butterworth filter seems to be most appropriate for our needs. However, the specifications assumed for the example above will not be strict enough for a real application to GOCE gradients, since valuable signal content will be lost at frequencies close to η_p, where the Butterworth filter needs comparably long to reach the ideal filter function magnitude of 1, as already mentioned previously.

To circumvent this, the transition band can be defined more rigorously, e.g. with a stopband frequency of η_s =9.1 mHz, which corresponds to D/O 49. However, in this case the Butterworth filter requires a filter order of 606 and furthermore looses its stability, which can be seen in the corresponding filter response illustrated in Figure 6.12a as red line. Alternatively, a Chebychev II filter can be designed with a stricter specification of the stopband attenuation δ_p=−80 dB in order to diminish the influence of the stopband ripples on the filtered signal, which leads to a filter order of 65. The filter response is again represented in Figure 6.12a as blue line, which still shows a stable behaviour despite the more rigorous specifications. The PSDs of the input reference signal (grey line) as well as that of the filtered signal using the Chebychev II filter (blue line) are shown in Figure 6.12b. With this filter definition, the signal content of the input signal can be preserved to a large extent also close to the passband frequency η_p. Due to the restrictive choice of the stopband attenuation δ_s, the influence of the stopband ripples on the filtered signal can be reduced to an insignificant amplitude. Hence, the Chebychev II filter is chosen for the high-pass filtering of the GOCE gradient data.

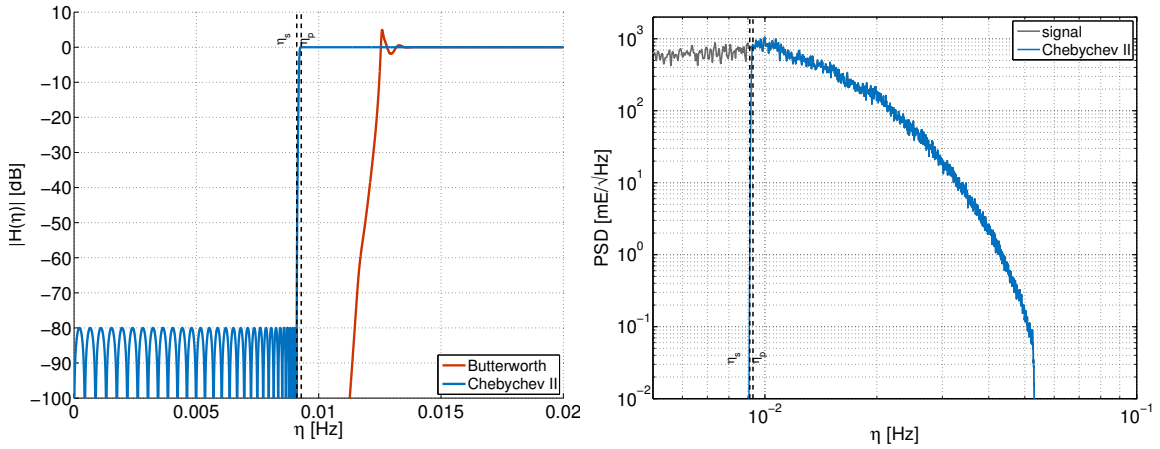

(a) Filter response of Butterworth and Chebychev II filters

(b) Square root PSDs of input signal and filtered signal

Figure 6.12: Amplitude response of Butterworth and Chebychev II filters according to the specifications η_p =9.3 mHz, η_s =9.1 mHz, δ_p=−80 dB (a); square root PSDs of signal filtered with Chebychev II filter (b)

Finally, we have to consider the fact that with the application of the high-pass filter, the

signal content is suppressed below D/O 50. Hence, one could expect that if the filter is applied to a noise free signal which is simulated from D/O 50 to 280, basically the same signal should be obtained. The corresponding signals in the time domain for a subset of 5000 s are exemplarily shown in Figure 6.13a, where the reference signal is depicted in grey and the filtered time series in blue. Obviously, both signals exhibit significant differences which are outlined in green. Although the input signal is simulated only from D/O 50, this does not imply that the signal content below this threshold is zero, which can also verified for instance in Figure 6.12b. This difference can be considered as cutoff error due to the high-pass filter, which is shown in the spectral domain in Figure 6.13b in green.

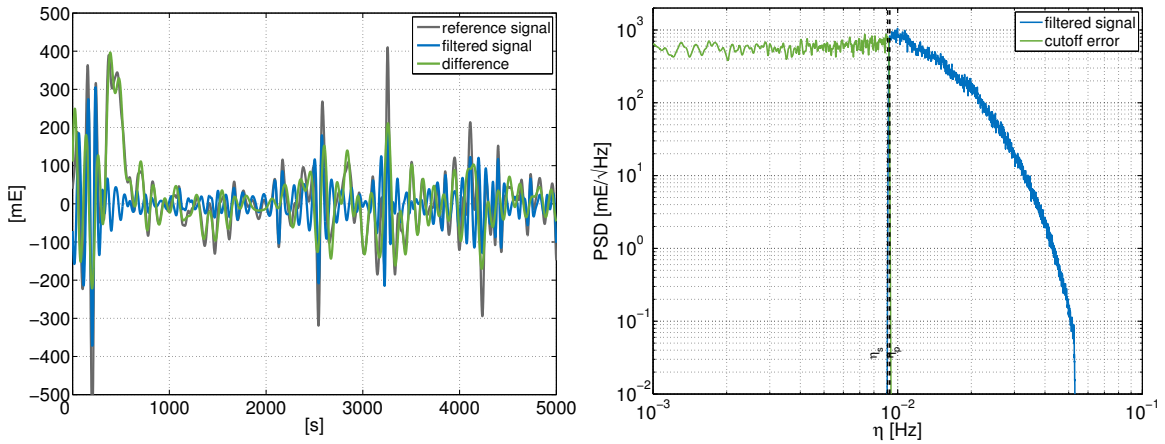

(a) Time series **(b)** Square root PSDs

Figure 6.13: Cutoff error due to high-pass filtering

Thus, referring to the initial purpose of applying a high-pass filter, which is to reduce the remaining long-wavelength errors in the Wiener filtered signal, we have to correct for this cutoff error. This can be achieved by high-pass filtering the a-priori Wiener filtered gradient time series and readding the cutoff error from the reference signal in order to restore the signal content in the low-frequency range.

6.2.3 Summary of the combined filter strategy

The filter procedure applied in this thesis is once again summarized and its workflow is also illustrated in Figure 6.14. In the initial situation we have a measured gradient time series which is corrupted by colored noise throughout the whole measurement spectrum. In a first step, existing trends and biases are reduced from the time series according to section 6.1.2. Furthermore, since the GOCE gradiometer has a low performance in particular in the low-frequency spectrum, the corresponding signal constituents are also a-priori reduced using a reference signal computed from a global EGM, for instance the GOCE_TIM_RL05 or GOCO03s. This is also justified, since the low-frequency components will be removed within a RCR procedure for gravity field determination. A realistic estimate for the colored noise in the measurements can be obtained by building the residuals between real signal and reference signal, see Figure 6.7a. With this information it is possible to set up a Wiener filter as described in section 6.2.1, which reduces much of the colored noise, as shown in Figure 6.7b.

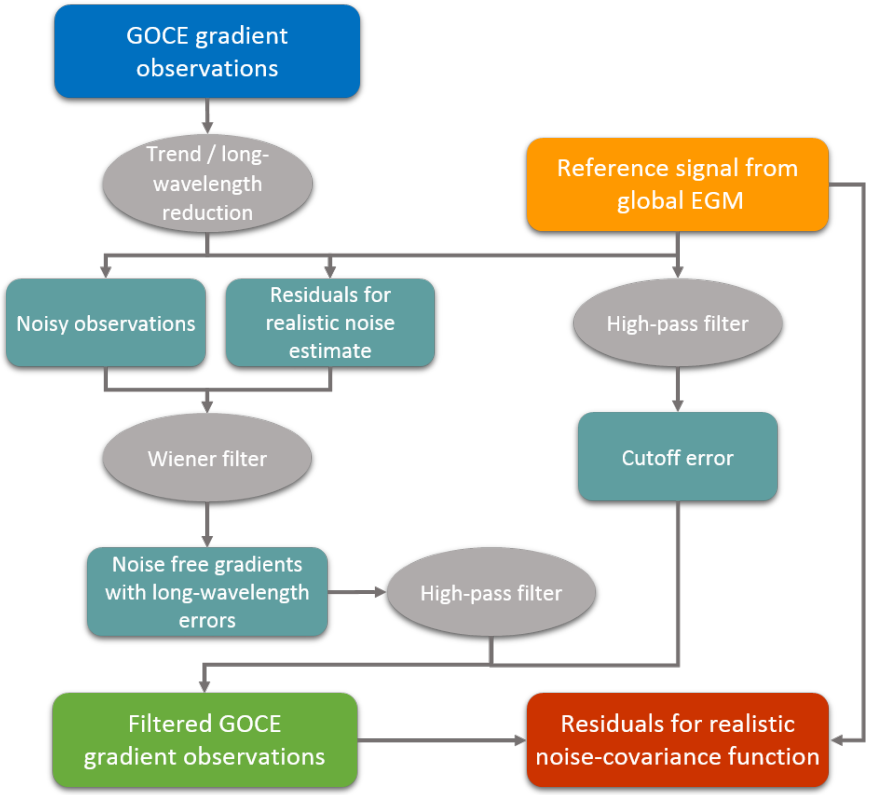

Figure 6.14: Workflow for the combined filter procedure

After the Wiener filtering, the time series is still deteriorated by long-wavelength errors, which is illustrated in Figure 6.8a and is discussed there. Thus, a high-pass filter is introduced according to section 6.2.2. This filter is applied to the a-priori Wiener filtered time series as well as to the reference signal from an EGM to retrieve a cutoff error, which is introduced due to the suppression of the signal content below the passband frequency, see Figure 6.13. The final preprocessed gradient time series is obtained by accounting for this cutoff error.

The square root PSD of the preprocessed signal is illustrated in Figure 6.15a as green line. Obviously, the filtered signal is now consistent with the reference signal (orange line) in the low-frequency spectrum. Compared to the original time series given in blue, the colored noise could be reduced to a large extent. In a last step, the difference between this time series and the reference signal can be calculated, see Figure 6.15b. These residuals can then be used to obtain a realistic estimate for the noise-covariance function of the remaining measurement errors after the filter procedure according to Appendix B.3. The resulting covariance function is illustrated in Figure 6.15c. In contrast to Figure 6.8b, the variance of the remaining noise after the filter procedure in this example can be decreased from 72.6 mE^2 to 7.9 mE^2 and the correlation length of the error covariance function from about 320 s to 10 s. Thus, with the introduced filter approach it is possible to reduce the correlations of the gradient observations as well as the measurement errors of the gradiometer instrument significantly.

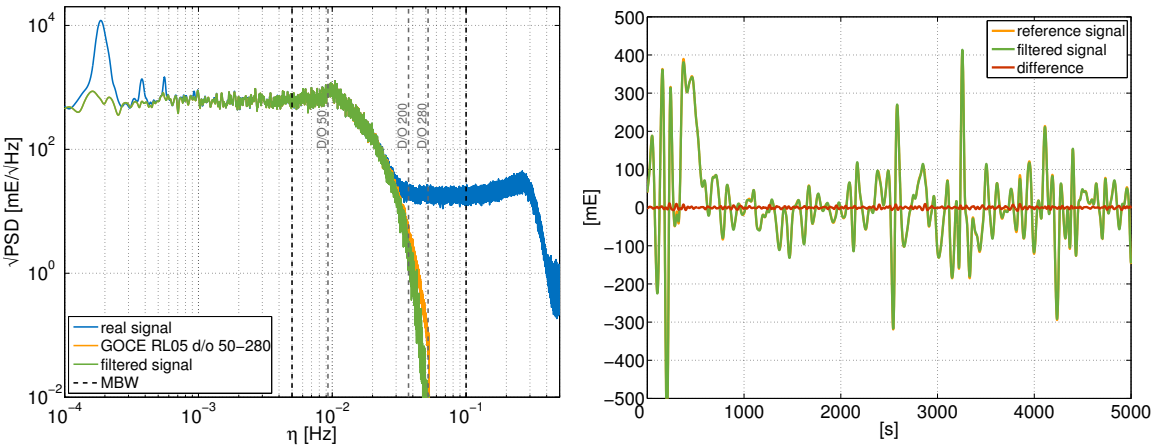

(a) Real signal, reference signal and final filter result

(b) Time series after Wiener filtering

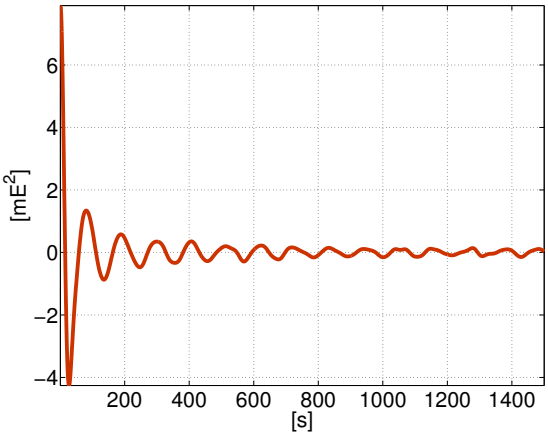

(c) Autocovariance function of filter error C_{ee}

Figure 6.15: Square root PSDs of the V_{zz} gradient time series for November 2009 after filter procedure (a); time series of reference signal, signal after filter procedure and residual differences (b); autocovariance function of the remaining filter error (c)

6.3 Strategies for using GOCE gravity gradients in Least Squares Collocation

As addressed in the introduction to chapter 6, the low-accuracy gradient tensor components V_{xy} and V_{yz} make it impossible to rotate the gradient observations measured in GRF to another reference frame without having a negative impact on the accuracy of the well-determined gradient types. This fact was already investigated and reported several times, for instance by Müller (2003), Bouman (2007) or Fuchs and Bouman (2011). For LSC this implies that the corresponding covariances, which are usually computed in a LNOF, have to be rotated to the GRF instead, which can be performed as outlined in section 3.7.1. Though, there is a theoretical restriction imprinted by the filtering processing steps introduced in section 6.2. The observed gravitational gradients in the GRF cannot be considered as a signal that is stationary in time due to the varying attitude of the satellite w.r.t. the LORF. However, in case of the Wiener filter theory, stationarity is a theoretical precondition, which is fulfilled in LORF, as explained in Albertella et al. (2004).

As a consequence, different solution strategies can be considered. The first one is to neglect this theoretical requirement of stationarity and to set the GRF as computational reference frame. This implies that the cross- and autocovariance matrix entries of C_{sl} and C_{ll} related to gravity gradient observations in the LSC concept of Eq. (3.20), which are derived from a suitable covariance function in the LNOF, have to be rotated to the GRF. Furthermore, the Wiener filtering step is directly applied to the gradient time series in GRF. With the assumption that the GGT components are uncorrelated amongst each other, the error covariance function of the filtered signal given by Eq. (6.21) can be used to set up the corresponding noise-covariance matrix C_{nn} for LSC in the GRF. A process chart for this first strategy is depicted in Figure 6.16a.

The second approach, which is outlined in Figure 6.16b, is to replace the critical gradients V_{xy} and V_{yz} with external information, i.e. the two components are derived from a gravity model in the GRF, and consecutively the whole GGT is rotated to the LORF. Fuchs and Bouman (2011) extensively investigated the impact of such a replacement of V_{xy} and V_{yz} in the GRF and the consecutive rotation to other reference frames. They stated that the relative model content of the gradients rotated to the LORF is approximately 3 to 4 % for V_{xx}, V_{xz} and V_{zz}. For V_{yy} the model content is with about 9 % the largest compared to the other components. However, this impact may be less dramatic since the signal strength of V_{yy} is lower in the MBW compared to V_{xx} or V_{zz}, see Figure 6.1. Nevertheless, with this approach we implicitly introduce a dependency on a-priori gravity field information in terms of an EGM. Such an EGM can be considered as best fitting model in global sense, but might mask some regional features due to the global smoothing. Since the current study aims to use the gravity gradients as direct point-wise observations in order to retain as much of the in-situ gravity signal as possible, this fact poses the main drawback of this strategy which we have to accept for the moment.

In order to reach the highest consistency with the actual values of V_{xy} and V_{yz}, an EGM based on GOCE observations can be considered to be favourable for deriving the model values. After the replacement, the GGT is rotated from the GRF to the LORF, where the Wiener filter can be applied in strict sense. Since now the LORF serves as computational frame, the covariances related to gradients have to be rotated to LORF as well in the already described manner in section 3.7.1. However, also this strategy bears some further complications, because due

to the rotation of gradients from the GRF to the LORF, the assumption of uncorrelated gradient observations is not fulfilled anymore and thus the simple block-diagonal structure of the noise-covariance matrix C_{nn} in the GRF is lost.

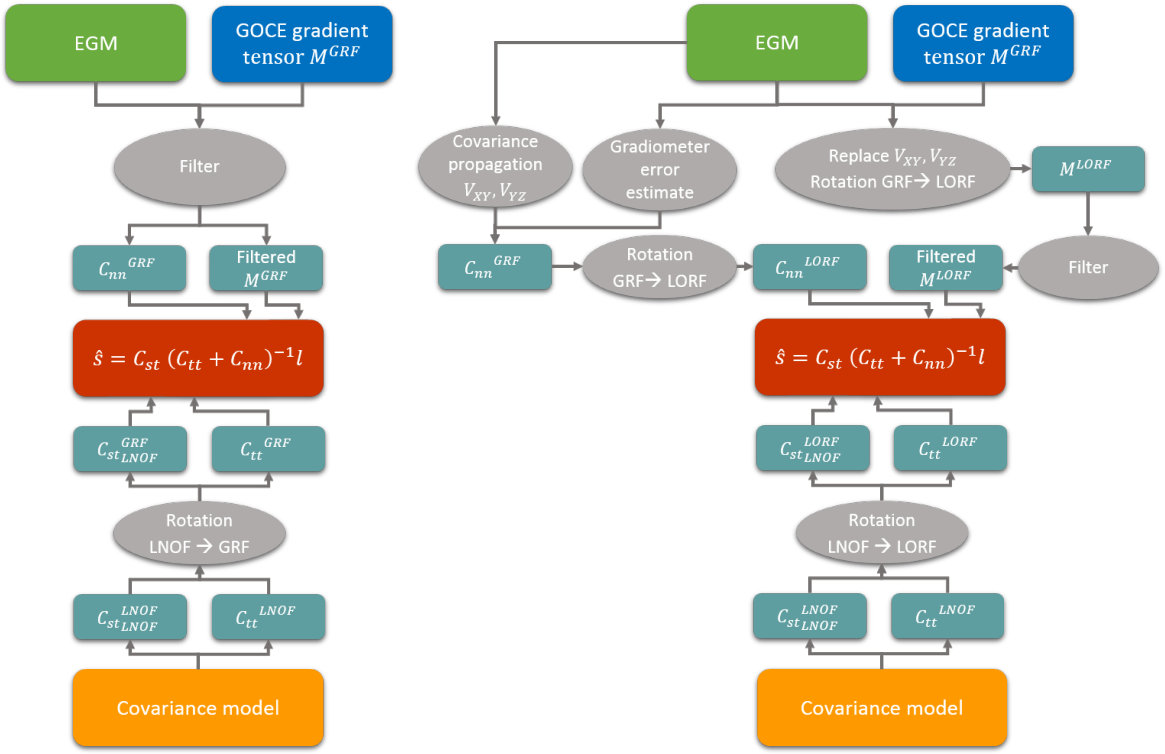

(a) Strategy 1 **(b)** Strategy 2

Figure 6.16: Solution strategies for handling GOCE observations given in the GRF within LSC

Therefore, a consistent covariance propagation of the noise-covariance matrix C_{nn} from the GRF to the LORF is necessary as well. This again requires the knowledge of the stochastics of the observed gradients in GRF as well as of the replaced gradient components which are derived from the gravity model. Considering the latter, a covariance propagation of the EGM errors for V_{xy} and V_{yz} has to be performed. In principle, the same algorithm that is used for the derivation of the covariances C_{ll} or C_{sl} of the LSC process as shown in Eq. (3.33) can be applied. Instead of using the degree variances k_n of the spherical harmonics coefficients themselves, which can be calculated following Eq. (3.32), the degree variances of the coefficients standard deviations are introduced according to Eq. (4.1)

$$k_n^{\sigma} = \sum_{m=0}^{n} \left(\sigma^2_{\bar{c}_{nm}} + \sigma^2_{\bar{s}_{nm}} \right) \ ,$$

which are usually also provided in the EGM file. However, this kind of covariance propagation is only justified, if it is assumed that the spherical harmonic coefficients of the EGM are uncorrelated. In case of the global gravity models like EGM96 or EGM2008, accuracy measures are only provided as standard deviations for the coefficients, hence the uncorrelatedness of the coefficients has to be assumed in either case. With the new gravity models

from the GOCE mission, a complete covariance information of the whole set of spherical harmonic coefficients is available. Thus the covariance propagation using this simplified method is deprecated and a complete covariance propagation would be possible. Despite that, for the following investigations about which of the proposed strategies is preferable, the simplified covariance propagation method with uncorrelated model coefficients is assumed to be sufficient.

For the remaining actual measured GGT components which are measured in the GRF, preliminary information on the error characteristics can be derived from the difference between simulated noise free reference values from an EGM and the real signals, which is already shown in section 6.2.1. With the resulting error covariance functions of the residuals, the error covariance matrix C_{nn} can then be set up in the GRF and finally rotated to the LORF. As a consequence, the noise covariances of the gradients are now correlated and a consistent stochastic modeling of the error structure is obtained. As last step in this second strategy, the cross- and autocovariance matrices C_{sl} and C_{ll} are set up in the LNOF using the covariance function and again, equivalent to strategy 1, the entries related to the gradient observations have to be rotated to the LORF.

For both strategies, we need the corresponding rotation matrices, from the LNOF either to the GRF (strategy 1) or to the LORF (strategy 2). The EGG_NOM_2 product includes the quaternions from the GRF to the IRF for each observation point, from which the respective rotation matrix R^{IRF}_{GRF} can be deduced (see Appendix C.1). To obtain the rotation between GRF and LNOF, we have to apply two further rotations, the first one from the IRF to the ERF and finally the rotation from the ERF to the LNOF

$$R^{LNOF}_{GRF} = R^{LNOF}_{ERF}\, R^{ERF}_{IRF}\, R^{IRF}_{GRF} \,. \tag{6.23}$$

While the derivation of the first rotation matrix R^{ERF}_{IRF} was shown in section 2.1.1, the inverse of the latter one is basically already introduced in Eq. (2.6). Similar to Eq. (6.23), the rotation from the LNOF to the LORF can be obtained by

$$R^{LNOF}_{LORF} = R^{LNOF}_{ERF}\, R^{ERF}_{IRF}\, R^{IRF}_{LORF} \,. \tag{6.24}$$

The rotation matrix R^{IRF}_{LORF} is found with

$$R^{IRF}_{LORF} = (\hat{\boldsymbol{v}}, \hat{\boldsymbol{n}}, \hat{\boldsymbol{v}} \times \hat{\boldsymbol{n}}) \;, \tag{6.25}$$

where $\hat{\boldsymbol{v}}$ is the normalized instantaneous orbital velocity vector and $\hat{\boldsymbol{n}}$ is the normalized angular momentum vector according to the definition of the LORF in section 5.3, both given in the IRF. For the noise covariance propagation in strategy 2 we furthermore need the rotation matrix R^{LORF}_{GRF}, which is simply given by multiplication of Eq. (6.23) with the inverse of Eq. (6.24)

$$R^{LORF}_{GRF} = R^{LORF}_{LNOF}\, R^{LNOF}_{GRF} \;. \tag{6.26}$$

A simple experiment in the test area of the Novaya Zemlya island is performed in the sequel, which should give an indication if there is a significant difference between the two strategies. For this reason, geoid heights are estimated solely from GOCE gradient data of the main diagonal tensor components V_{xx}, V_{yy} and V_{zz} of November 2009. The noise-free reference

signals are simulated from EGM2008 and are used to reduce the long-wavelength signal up to D/O 49.

Following strategy 1, the time series are then filtered in the GRF according to section 6.2. For the derivation of the covariance matrices C_{ll} or C_{sl} for the collocation process, degree variances of EGM2008 are used. The noise covariance matrix C_{nn} is set up in the GRF using the error covariance functions from the filter procedure. Following the second solution strategy, the real V_{xy} and V_{yz} measured in the GRF are replaced by simulated observations from the EGM2008 from D/O 50 to 250. Subsequently, the gradients are rotated to the LORF where the Wiener filtering is applied. In contrast to strategy 1 the noise covariance matrix C_{nn} has to be rotated from GRF to LORF as well, i.e. it has to be set up in GRF with a-priori stochastic information of the gradient errors. In case of real data this is obtained from difference between actual signal and reference signal, while for simulated observations, a covariance propagation of EGM2008 is performed.

The LSC results of the residual geoid heights corresponding to spherical harmonic D/O 50 to 250 are visualized for strategy 1 in Figure 6.17a and for strategy 2 in Figure 6.17b. In the top rows the estimated geoid height values are shown, while in the bottom rows the spatial distribution of the formal standard deviations is illustrated. The statistics of the results are summarized in Table 6.1.

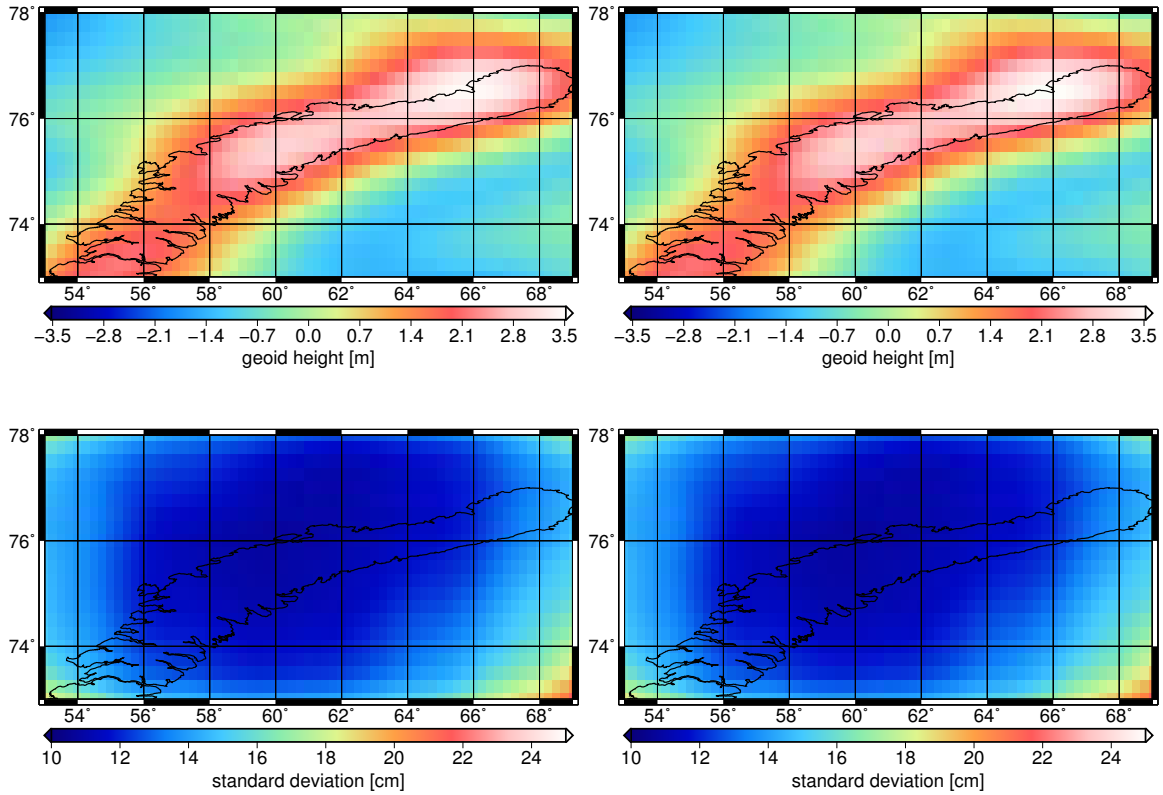

(a) Residual geoid heights in [m] (top) and standard deviations in [cm] (bottom) from strategy 1

(b) Residual geoid heights in [m] (top) and standard deviations in [cm] (bottom) from strategy 2

Figure 6.17: Comparison of strategy 1 (left) and strategy 2 (right) for geoid height computations using V_{xx}, V_{yy} and V_{zz} from November 2009

Furthermore, the difference between the geoid height solutions from both strategies is shown in Figure 6.18. The maximum differences are in the order of ±4 cm, while the RMS of the differences amounts 1.6 cm. Comparing the standard deviations, we can observe the same range of values, from a minimum of 10.8 cm in the central region to a maximum of about 21.5 cm at the borders of the area. Close to the test area margins, the accuracy is typically decreasing due to edge effects caused by the lack of observations outside the region. However, the highest formal accuracy that is achievable with solely GOCE gradients is around 11 cm. This is still almost three times higher than the maximum differences of the estimated geoid heights and therefore the deviations have to be considered as insignificant.

Table 6.1: Comparison of solution strategies, values given in [cm]

		Strategy 1	Strategy 2	Difference
Geoid height	min	−169.6	−167.9	−4.1
	max	348.0	350.6	3.8
	rms			1.6
Standard deviation	min	10.8	10.8	
	max	21.6	21.5	

Based on this investigation, both solution strategies lead to equivalent results. As we have seen, strategy 2 requires several additional computational steps like the simulation of model gradients for V_{xy} and V_{yz}, rotations and covariance propagation from the GRF to the LORF. This causes a tremendously higher effort, which does not improve the results significantly compared to strategy 1. In this sense, the unfulfilled requirement of stationarity in the GRF is not considered to be a critical factor during the filter procedure and subsequently in the gravity field determination. Therefore, the processing strategy 1 is regarded as sufficient for gravity field computations in this thesis.

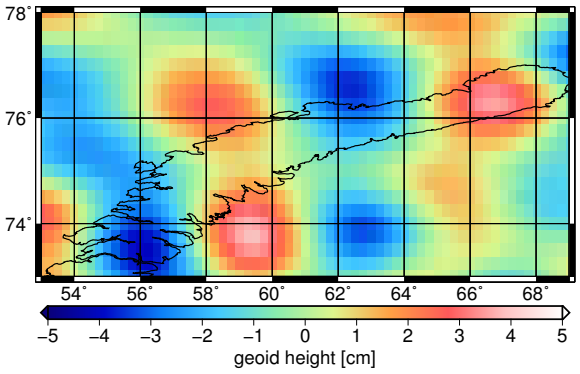

Figure 6.18: Geoid height differences between strategy 1 and 2 in [cm]

7 Application I: Computation of an Austrian geoid

In Austria, geoid modeling is a long established field of research. Sünkel et al. (1987) computed the first astrogeodetic geoid solely based on deflections of the vertical data using the LSC approach. A decade later, as a considerable amount of gravity measurements was available, Kühtreiber (1998) computed the first gravimetric geoid solution. Kühtreiber (2002) provided the first combined solution with deflections of the vertical and gravity anomalies. This solution was also based on the commonly used LSC technique, and combined the different spectral bands of the two gravity field quantities. Despite the good quality of this solution, it was still affected by local variations and long-wavelength error structures. Further attempts towards an improved Austrian geoid were carried out by Abd-Elmotaal and Kühtreiber (2003), who introduced an adaption of the Remove-Restore technique for the geoid computation.

In 2007, an Austrian geoid solution was derived by Pail et al. (2008), which is still representing the official geoid provided by the Bundesamt für Eich- und Vermessungswesen (BEV). By combining heterogeneous data in the LSC approach, the precision of the Austrian geoid could be improved to sub-decimeter level. Nevertheless, the unconstrained Austrian geoid solution shows trends in terms of long-wavelength errors when compared to GPS/levelling points, which are measured by the BEV in the Austrian height system. In order to be consistent to these GPS/levelling points, the present official solution was heavily weighted towards these points, which will be discussed in more detail in section 7.1.

A further attempt towards an improved geoid solution was performed by Kühtreiber et al. (2011), who used updated and extended data and verified alternative processing strategies. Although improvements could be achieved, the discrepancies between this geoid and the GPS/levelling points provided by the BEV still remained. Thus, the BEV did not adopt this solution but continues with the Austrian geoid derived in 2007.

With the project 'Geoid for Austria - Regional gravity FIELD improved' (GARFIELD) a current initiative for the generation of a new high-quality gravity field solution for the Austrian region has been initialized in 2012. The aim is to overcome the inconsistencies between previous geoid solutions and geoid heights from GPS/levelling campaigns. The computation of an Austrian geoid based on LSC as it is performed in this chapter is one of the key components of the project. In this context, GOCE gradients shall be used together with complementary gravity data sources, which have to be treated consistently within a RCR procedure. The according steps towards a new geoid are presented in the following.

In section 7.1 the official Austrian geoid solution is discussed in more detail and the current drawbacks are outlined. The data sets used for the geoid estimates in this thesis are described in section 7.2. The computational steps for the derivation of the geoid as well as the resulting solution is presented in section 7.3. The new geoid is validated and compared to the official

GPS/levelling observations in section 7.4. The chapter closes in section 7.5 with a summary and a discussion on possible further improvements.

7.1 The current Austrian geoid solution

The computation of the official Austrian geoid is based on the LSC method in combination with the RCR approach, see Pail et al. (2008). For this geoid solution a subset of 14001 gravity stations in and around Austria had been chosen. Although the original data set contains considerably more observations, numerical case studies concerning different input data distributions lead to the conclusion that a spatially homogeneous arrangement with an average distance of about 4 km between the stations is beneficial. Furthermore, an existing data set of deflections of the vertical was introduced in the LSC process. Since there were some inconsistencies between a purely astrogeodetic and a gravimetric geoid solution due to a poor data distribution, also some new measurements of deflections of the vertical have been performed in the South-East of Austria. With this complement a total number of 672 stations was included in the Austrian Geoid 2007 solution. An additional observation type was introduced by 170 GPS/levelling observations provided by the BEV. The spatial distribution of the described terrestrial data types can be seen in Figure 7.1a.

To model the long-wavelength components within the RCR concept, the global GRACE satellite-only gravity field model EIGEN-GL04S up to spherical harmonic degree and order 70 was chosen. In order to reduce the topographic-isostatic gravity effects, a uniform high-resolution DEM of about 44 m × 49 m was used. For the topographic-isostatic reduction the Airy-Heiskanen model with a standard density of 2670 kg m^{-3} was applied.

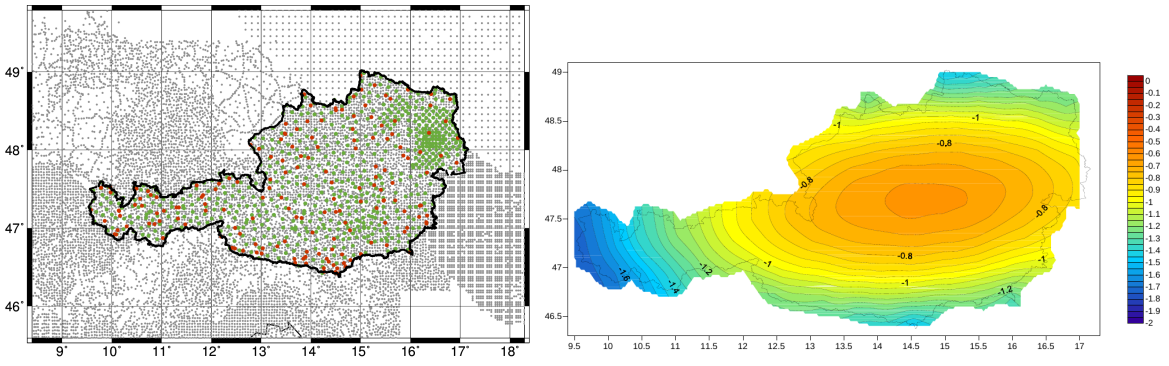

(a) Terrestrial data: gravity anomalies (grey), deflections of the vertical (green) and GPS/levelling observations (red)

(b) Differences between gravimetric geoid and GPS/levelling heights in [m] adopted from Pail et al. (2007)

Figure 7.1: Terrestrial gravity data used for the official Austrian geoid solution (a), and differences between gravimetric geoid and GPS/levelling heights (b)

The comparison of a gravimetric solution solely based on the 14001 gravity observations with the GPS/levelling geoid heights revealed considerable differences with a long-wavelength structure of up to 2 m, shown in Figure 7.1b. These systematic trends were accredited

to datum inconsistencies, distortions in the orthometric height system, systematic GPS errors or neglected correction terms for the transformation of height anomalies from the long-wavelength EGM to geoid heights, see Pail et al. (2007, 2008). In order to account for these trends, a correction surface in terms of a polynomial of order 3 was fitted to the difference between estimated gravimetric geoid heights and GPS/levelling geoid heights. This correction term was reduced from the GPS/levelling observations before the combined prediction, and restored to the predicted geoid heights afterwards.

During several case studies it turned out, that the choice of the weight that is given to the GPS/levelling observations was essential for the geoid solution. Giving the geoid height observations a relatively high weight of 1 mm, the deviations between predicted and observed geoid heights were small with a standard deviation of less than 6 mm. Degrading the observation accuracy to 10 mm lead to higher deviations with a standard deviation of about 30 mm. However, the opposite behaviour could be observed when predicting gravity anomalies with LSC and comparing them with the original data. This indicated some further inconsistencies between the GPS/levelling and gravimetric measurements. In a final step, individual weights for each GPS/levelling observation were introduced by using the geoid height residuals from the case study with 1 mm measurement accuracy. Thus, those GPS/levelling stations with expected lower accuracy were down-weighted, while the nearby gravity field measurements gained a higher relative weight. This weighted solution was chosen to form the official new Austrian Geoid 2007, which is illustrated in Figure 7.2. The accuracy of the solution is specified in the range of about 2 to 3 cm, however in some bordering regions, drastically worse accuracies have to be expected due to sparse data distribution in the neighbouring countries.

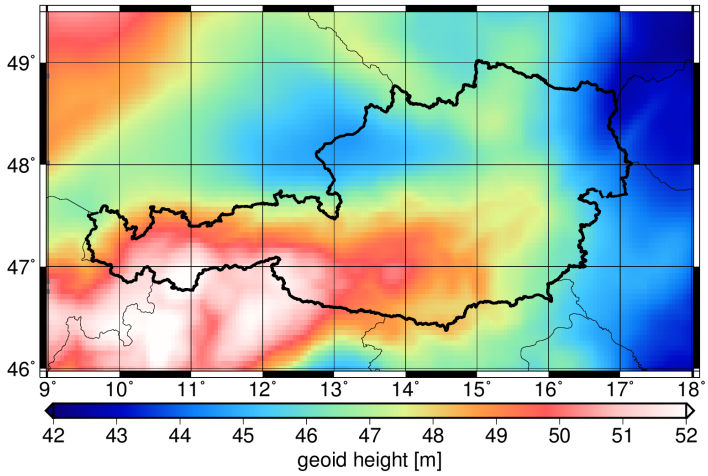

Figure 7.2: The official Austrian geoid solution

In this way, a geoid solution was generated which is heavily constrained towards the geoid heights from the GPS/levelling observations. This corresponds to the needs of the BEV who require a geoidal surface which can be used for the transformation of GPS heights into the orthometric heights in the Austrian height system. However, with this approach the physical meaning of the geoid, i.e. a surface of equal potential, is violated and the official geoid solution is rather representing a transformation surface than an actual geoid. In the present thesis, these discrepancies shall be avoided.

7.2 Data and models for geoid computation

For the appropriate consideration of high-frequency gravity effects induced by the topographic masses within a consistent RCR procedure, a dense DEM is necessary which will be introduced in section 7.2.1. The terrestrial input data for the geoid prediction is described in section 7.2.2, while the incorporated GOCE gradient data is explained in section 7.2.3. Furthermore, the GPS/levelling data from the BEV is introduced in section 7.2.4. This data set will only be used for validation purposes, see section 7.4.

7.2.1 Digital Elevation Model

The DEM used for this geoid determination is given in a uniform resolution of $1^\circ/2560$ in longitude and $1^\circ/1536$ in latitude, which corresponds to approximately 44 m × 49 m. It is available in the geographical extent between 5° to 22° East and 43° to 53° North. The compilation of this DEM originates from a photogrammetrically determined terrain model (Graf, 1996; Franzen and Mandelburger, 2003), which refers to the Austrian orthometric height system MGI. During the last Austrian geoid computation campaigns at the Institute of Geodesy, see Kühtreiber (2002), Pail et al. (2008) and Kühtreiber et al. (2011), the model was continuously updated and improved. In particular, additional data sets from neighbouring countries like Switzerland, Slovenia or Italy have been consistently included. In absence of other data, height information of the Shuttle Radar Topography Mission (SRTM) has been used to close the gaps (Pail et al., 2008). The average accuracy of the height model within Austria is in the range from 2 to 5 m. For the use in this thesis, the DEM heights and coordinates are transformed to the GRS80 ellipsoid.

7.2.2 Gravity data

In the Austrian territory a data set of 49345 gravity observations is available, which is provided for the use in this thesis by Norbert Kühtreiber and Christian Pock from the Institute of Geodesy via personal communication. The Austrian gravity reference frame is defined by 42 highly accurate reference gravity observations from absolute gravimetry serviced by the Austrian BEV. The majority of the observations was measured with a relative gravimeter w.r.t. the reference frame in various measurement campaigns of different institutions, e.g the BEV, the Institute of Geophysics of the Mining University Leoben or the Austrian Mineral Oil Administration OMV, see Pock et al. (2014). They can be roughly categorized according to different measurement instruments and measurement periods, dating back to the 1950's, which is indicated in Figure 7.3a. Outside of the Austrian borders, subsets of national gravity observations from neighbouring countries are available. In total, a terrestrial gravity data set of 74649 observations with inhomogeneous data distribution can be used for this thesis.

The accuracy of the Austrian data set is specified with 0.3 mGal in the worst case, which turned out to be rather unrealistic during the data processing for the former gravity field solutions. For most of the data from neighbouring states, accuracy information are not available. Based on numerical investigations, an empirically determined standard deviation of 1 mGal was chosen for all gravity observations for instance in the official Austrian geoid

solution. Due to the lack of further information, this value will also be adopted in this current study.

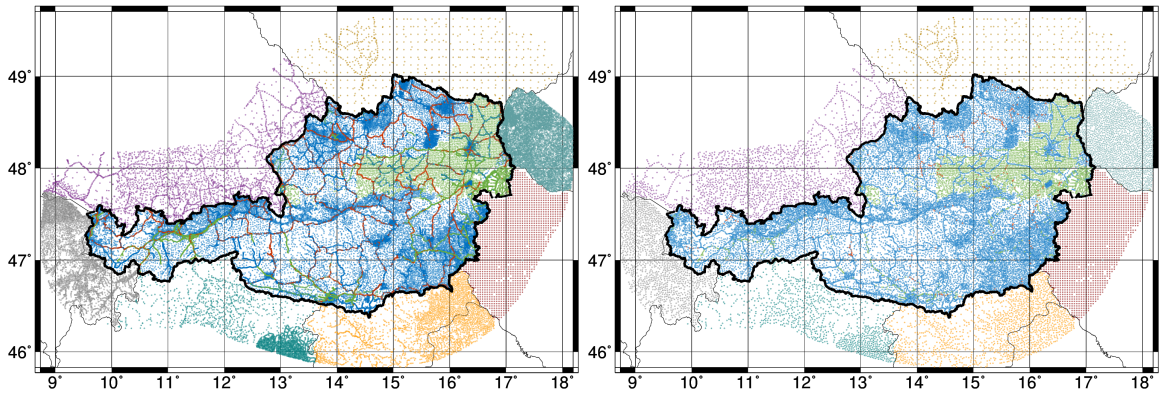

(a) Complete gravity data set **(b)** Reduced gravity data set

Figure 7.3: Terrestrial gravity data: Complete available data set of 74649 gravity points for Austria and neighbouring countries (a); reduced data set of 30015 gravity points thinned out with radius 1 km within Austria and 2 km for other countries (b)

To avoid clustered observations, which can lead to instabilities in LSC (Pail et al., 2008), and to reduce the computational effort for the LSC procedure, the data set is thinned out with a radius of 1 km within Austria and 2 km for other countries. This results in 30015 gravity observations that are used for the present computations. Their spatial distribution is illustrated in Figure 7.3b.

7.2.3 GOCE gradients data

Three months of EGG_NOM_2 gradient data given in the GRF from November to December 2009 and May 2010 were selected. This choice has been made due to the limited computing capacity of the implemented LSC approach, but should guarantee still a reasonable spatial distribution of gradient data within the investigated area.

According to the investigations in chapter 6, the data has to be preprocessed in order to reduce the measurement noise. The necessary realistic noise estimate for the filter process is derived by using the GOCE_TIM_RL05 global gravity field model as a reference. Since the long-wavelength gravity signals can not adequately be observed by the gradiometer instrument, the corresponding signal constituents are a-priori reduced from the measurements. For this step, the GOCO03s satellite-only model is used, which can be considered to be highly accurate in the low-frequency range according to Figure 4.1. For the current geoid computation, we want to preserve the superior gravity information of the GOCE gradients, which is the case from approximately D/O 110, see again Figure 4.1. On the other hand, essential parts of the long-wavelength gravity signal should be removed within a RCR procedure in order to reduce the systematic trends from the signal, as described in chapter 4. Thus, in this study a threshold of D/O 120 was chosen as a tradeoff for the reduction of the long wavelengths.

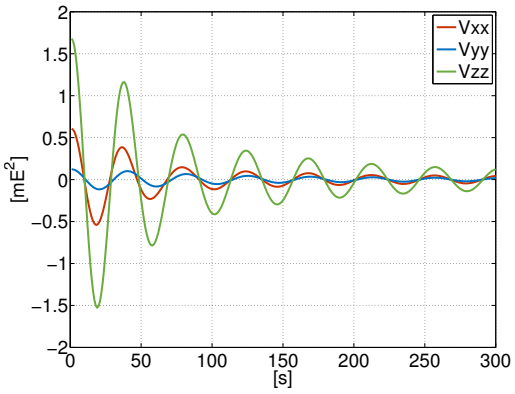

(a) Noise covariance functions of V_{xx} (red), V_{yy} (blue) and V_{zz} (green) for November 2009

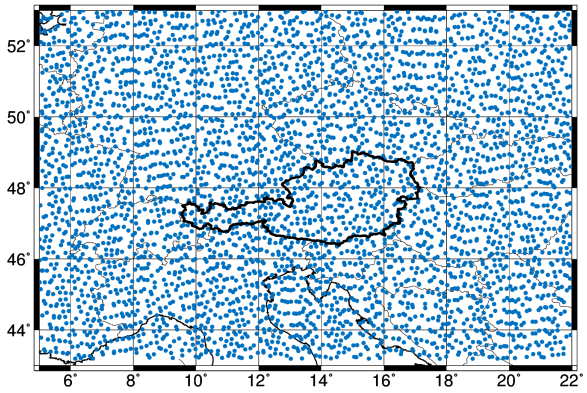

(b) 4182 gradient observation points over the extended Austrian region

Figure 7.4: Noise covariance function of the main diagonal gradient tensor components after preprocessing for November 2009 (left) and data distribution of EGG_NOM_2 gradient data with 5 s sampling for geoid prediction (right)

After the preprocessing steps, the autocovariance function of the remaining filter error in the gradient time series can be estimated as proposed in section 6.2.3. The corresponding noise covariance functions are illustrated in Figure 7.4a for the main diagonal components of the gradient tensor V_{xx}, V_{yy} and V_{zz}, which will be used for the setup of the noise covariance matrix within the geoid estimation. The variance of the error in the V_{zz} component is approximately 1.7 mE^2, and is lower for the V_{xx} gradient with 0.6 mE^2 and for the V_{yy} gradient with 0.1 mE^2. This can be attributed to the fact that the V_{zz} component has the highest signal amplitude, while it is considerably lower for V_{xx} or V_{yy} (see Figure 6.1).

Finally, the gradient data was reduced from the initial sampling rate of 1 s to 5 s and cut out for the region between 5° to 22° East and 43° to 53° North, which leads to the data distribution as shown in Figure 7.4b. Hence, for the presented geoid solution an input dataset of 4182 observation stations for each of the three gradient tensor components is used, which results in 12546 observations in total.

7.2.4 GPS/levelling data

For this study, 192 GPS/levelling observations are provided by the BEV. On the one hand, this data incorporates highly precise ellipsoidal height h measurements from GPS observations from GPS permanent stations and measurement campaigns that are forming the Austrian reference frame (AREF). This is linked to the European Terrestrial Reference System at epoch 1989 ETRS89 (BEV, 2013). The accuracy of these GPS heights is specified with 1 cm or less.

On the other hand, the BEV has determined orthometric heights H for these points with precise spirit levelling. Thus, at the given points absolute geoid heights N can be determined by evaluating $N = h - H$. The corresponding absolute geoid heights with respect to the GRS80 ellipsoid are illustrated in Figure 7.5. The accuracy of these GPS/levelling points is depending on the GPS measurements as well as on the levelling and the corresponding gravity measurements. According to the specifications of BEV, it is assumed to

be in the order of a few centimeters. However, revisions for specific points of the data base that were performed in the last years revealed considerable inconsistencies. Although these shortcomings were corrected, there might be still some further inconsistencies in the data set.

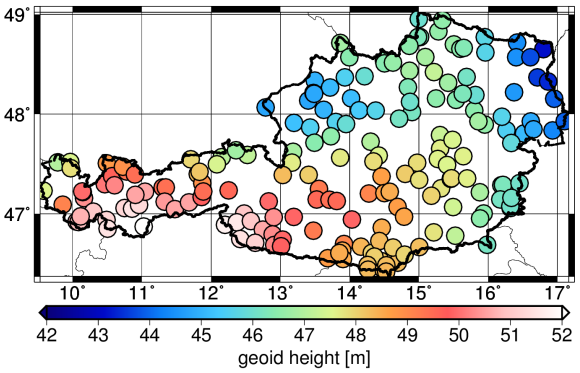

Figure 7.5: Absolute geoid heights with respect to the GRS80 ellipsoid from GPS/levelling provided by the BEV

In contrast to the official Austrian geoid solution, this data will not be used as an input observation type for the geoid prediction in this thesis. Instead, the GPS/levelling geoid heights will be used for the validation of the estimated geoid. In this way it is possible to obtain a measure for the consistency of the predicted geoid and the geoid heights determined by the BEV.

7.3 Geoid computation

7.3.1 Application of the Remove-Compute-Restore approach

Before the actual geoid computation with the LSC method can be performed, known systematic effects have to be reduced from all input data consistently according to the RCR approach, which was already discussed in detail in chapter 4. For the reduction of the long-wavelength component, the GOCO03s global gravity field model was chosen, since it represents one of the most accurate satellite-only models available. In this investigation the aim is to use GOCE gravity gradients as direct observations. Although the spherical harmonics series of GOCO03s could be used until D/O 250, only the long-wavelength signal up to D/O 120 will be reduced from both, terrestrial gravity and GOCE gradients consistently. In this way, the expected valuable medium-wavelength signal content of the gradients can be exploited.

Furthermore, the high-frequency gravity signals induced by the topographic masses are reduced with the prism formula, see the explanations in section 4.3. The height information is deduced from the DEM as described in section 7.2.1, and the calculations were done with the standard density value ρ =2670 kg m^{-3}. The gravity effect on terrestrial gravity data located on the topography is illustrated in Figure 7.6a. To account for the long-wavelength

effect of the topography which is already included in the GOCO03s, the topographic masses are transformed into a topographic potential represented by a spherical harmonics series expansion up to D/O 360. The corresponding topographic gravity signal up to D/O 120 which has to be corrected in the terrestrial data is shown in Figure 7.6b.

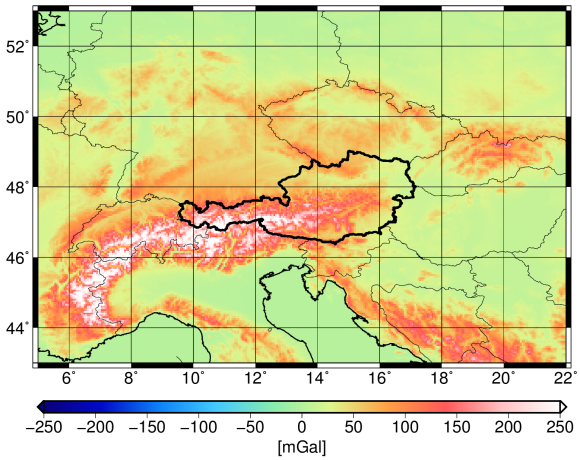

(a) Topographic effect on gravity observations calculated with the prism formula

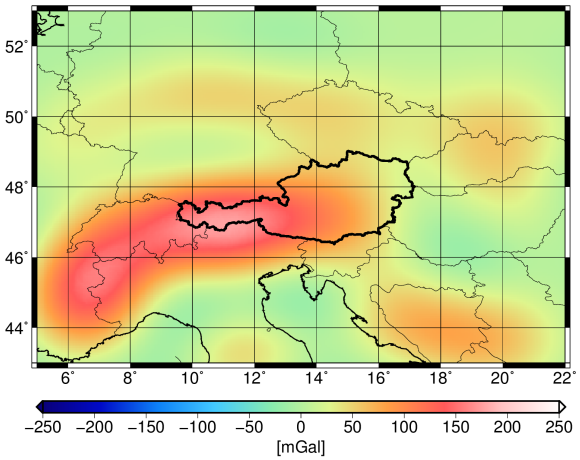

(b) Long-wavelength correction up to D/O 120 on gravity observations

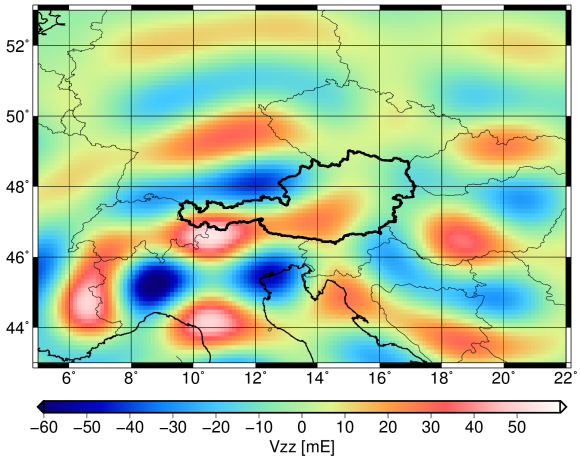

(c) Topographic effect on GOCE vertical gradients from D/O 121 to 360

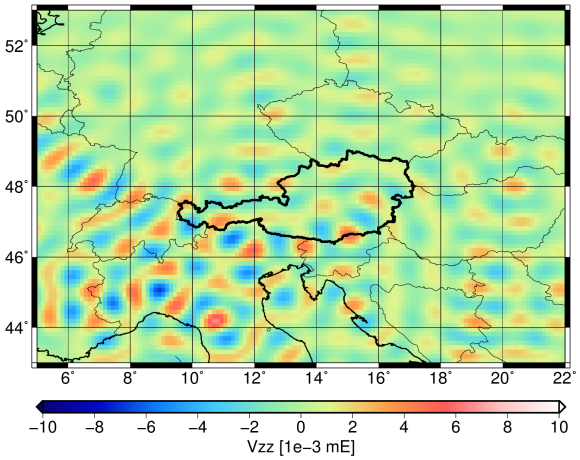

(d) Topographic effect on GOCE vertical gradients from D/O 361 to 720

Figure 7.6: Topographic mass effects on terrestrial gravity data located on the topography and on GOCE vertical gradients at altitude 250 km above the study area

For the reduction of the GOCE gravity gradients, the use of the series expansion is sufficient, since the high-frequency signal content due to the topography is significantly attenuated at the satellite altitude. This can be verified in Figure 7.6c and Figure 7.6d, where the signal content from D/O 121 to 360 and D/O 361 to 720 is illustrated for the vertical gradient at an assumed orbit altitude of 250 km. Obviously, the signal amplitude level for wavelengths shorter than D/O 360 is in the order of 10 micro-Eötvös or less, which is well below the measurement accuracy of the gradiometer instrument. Thus, a reduction of the topographic influences from the gradient observations up to D/O 360 is sufficient.

Besides the topographic effect, also the effect of the isostatic compensation is considered, see section 4.4.4. Again, the DEM is utilized in order to develop a spherical harmonics series of the isostatic potential according to the Airy-Heiskanen concept. The crustal density was chosen with ρ =2670 kg m^{-3}, while the density contrast between crust and mantle was set to $\Delta\rho$ =350 kg m^{-3}, which is based on realistic values for the central European region adopted from other studies (see also section 8.4). Although the DEM is given in much finer resolution, the expansion is truncated at D/O 720, which corresponds to a spatial resolution of approximately 30 km. On the one hand, this choice is considered to be justified because the isostatic effect on terrestrial gravity signals becomes relatively small ($<$ 1 mGal) for higher orders, which was investigated in a study not shown at this place. At GOCE satellite altitude, the influence becomes even smaller. On the other hand, a highly variable isostatic signal is also rather unrealistic in reality due to the flexural rigidity of the crust, which is discussed in section 4.4.3.

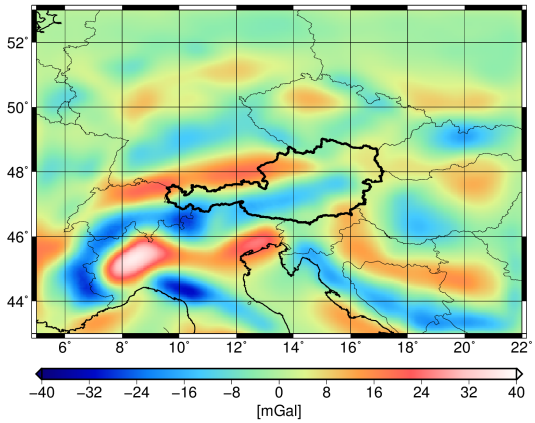

(a) Isostatic effect on gravity observations from D/O 121 to 720

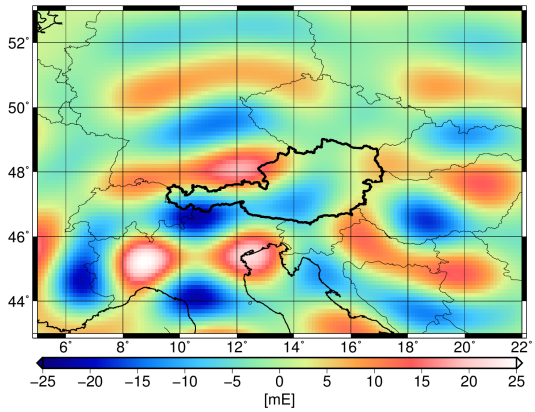

(b) Isostatic effect on GOCE vertical gradients from D/O 121 to 360

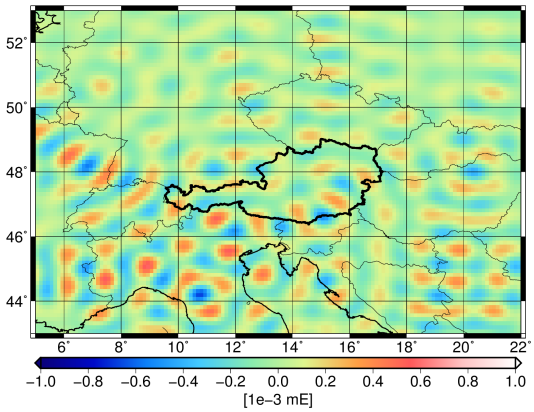

(c) Isostatic effect on GOCE vertical gradients from D/O 361 to 720

Figure 7.7: Isostatic effects on terrestrial gravity data located on the topography and on GOCE vertical gradients at altitude 250 km above the study area

Within the remove step, the isostatic effect is only reduced from the gravity observations for D/O 121 onwards, since the long-wavelength effects are already removed by GOCO03s.

In Figure 7.7a the influence of the isostatic effect on gravity observations located on the topography from D/O 121 to 720 is visualized. Furthermore, the effect on vertical gradients at an altitude of 250 km is illustrated in Figure 7.7b for the spectral range between D/O 121 to 360. Again, higher order influences are only in the range of some micro-Eötvös, see Figure 7.7c, so they have been neglected in the reduction.

Finally, the effect of the atmosphere is accounted for in the gravity reduction. In order to be consistent with the previous procedures, the atmospheric potential for exterior and interior space was calculated in the same manner as described in section 4.2. The maximum spectral resolution was defined with D/O 360. In the reduction step we have to discriminate between gradients and terrestrial gravity data. In case of the gradient data, the observations are taken outside the atmospheric masses, which would require the removal of the signal of the exterior potential. However, the GOCO03s model already incorporates the atmospheric masses, so the reduction is implicitly done when subtracting the EGM constituents from the gradient signal. Although GOCO03s is only considered up to D/O 120 in this study, higher frequency atmospheric signals are insignificant at an amplitude level of some micro-Eötvös, which is shown in Figure 7.8b, and can therefore be neglected.

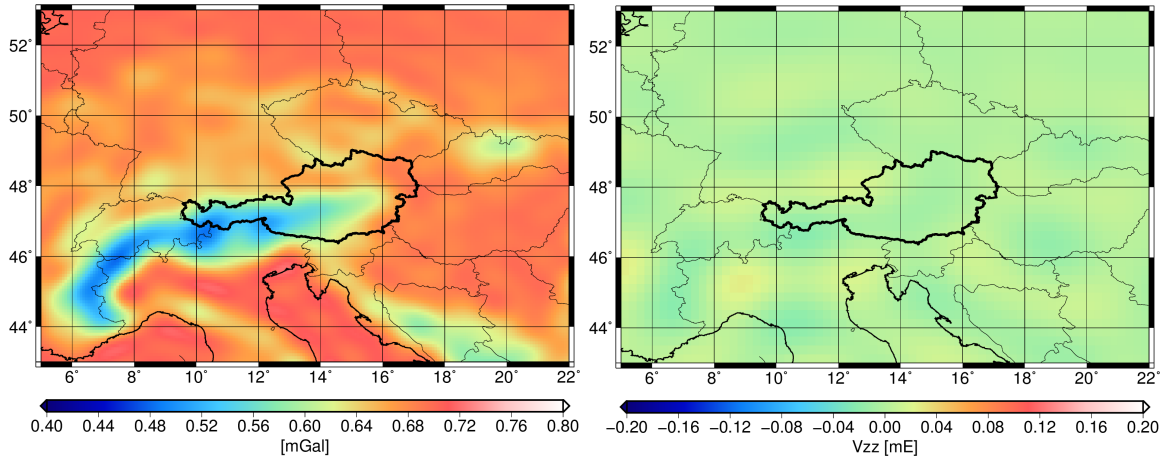

(a) Combined atmospheric effect on terrestrial gravity observations

(b) Atmospheric effect on GOCE vertical gradients from D/O 121 to 360

Figure 7.8: Combined atmospheric effects on terrestrial gravity data located on the topography (a) and residual signal from D/O 121 to 360 on GOCE vertical gradients at altitude 250 km above the study area (b)

In contrast, to get atmosphere-free observations on the Earth's surface, we have to correct for the exterior and interior potential as it is explained in section 4.2.5. The combined effect on gravity observations situated on the topography is illustrated in Figure 7.8a. The gravity variations due to the atmosphere are comparably small and range from 0.48 to 0.72 mGal but nevertheless are applied within the RCR procedure.

For the complete remove procedure for the reduction of gravity observations g, we can combine all effects and obtain

$$\Delta g = g - \left(\gamma^{egm} - \delta g^{t,shc} - \delta g_e^a\right) - \delta g^{dem} - \delta g^{iso} - \delta g_i^a \,, \tag{7.1}$$

where γ^{egm} is the gravity obtained from the GOCO03s spherical harmonics model evaluated to D/O 120, which is corrected for the long-wavelength signal of the topographic masses and exterior atmospheric masses up to D/O 120 by $\delta g^{t,shc}$ and δg_e^a. Furthermore, the topographic effect δg^{dem} is considered by evaluating the prism formula, δg^{iso} is the isostatic compensation effect from D/O 121 to 720, and finally δg_i^a represents the removal of the atmosphere corresponding to the interior atmospheric potential.

In Figure 7.9, the reduction steps of the RCR procedure are illustrated, which are applied to the 30015 gravity observations that are used for the geoid computation. The corresponding statistics of the residual values, i.e. the anomalies Δg, are summarized in Table 7.1. In the first step, the anomalies resulting from the reduction by the GOCO03s gravity are shown in Figure 7.9a. The values range from −201.5 to 143.3 mGal, with a considerable mean of −21.8 mGal and a variability of 47.2 mGal. As expected, the remaining variations show a high correlation with topography.

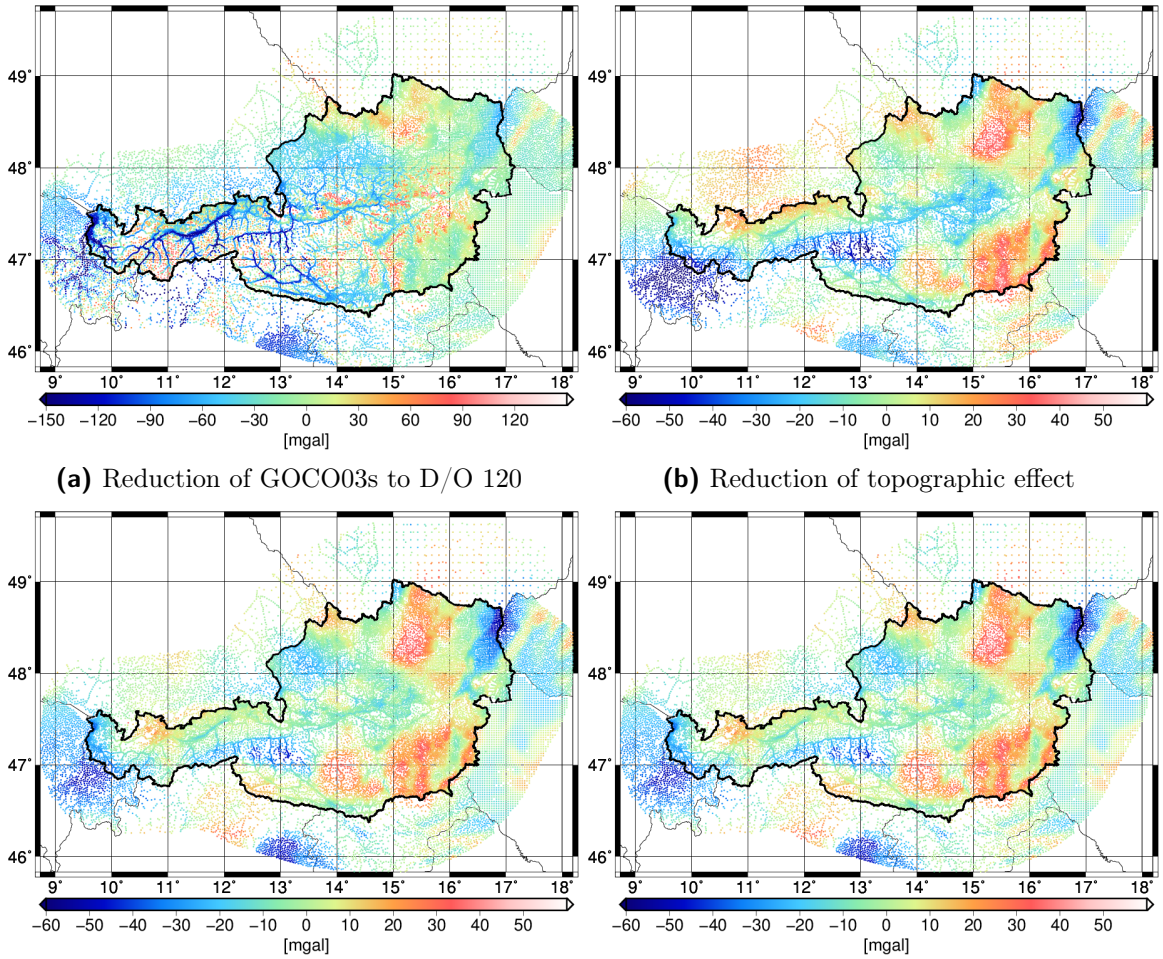

(a) Reduction of GOCO03s to D/O 120

(b) Reduction of topographic effect

(c) Reduction of isostatic effect

(d) Reduction of atmospheric effect

Figure 7.9: Terrestrial gravity data reduction in consecutive steps

By applying the topographic reduction as well as the long-wavelength correction for topography $-\delta g^{dem} + \delta g^{t,shc}$, the high-frequency correlations can be decreased considerably. The remaining anomalies are depicted in Figure 7.9b and range from to −69.7 to 53.8 mGal with a

RMS of only 17.3 mGal, while the mean can be reduced down to −1.4 mGal.

Table 7.1: Statistics of the gravity anomaly data set after applying the consecutive reduction steps

[mGal]	**GOCO03s**	**Topography**	**Isostasy**	**Atmosphere**
min	−201.5	−69.7	−59.3	−58.5
max	143.3	53.8	43.8	44.8
mean	−21.8	−1.4	−2.5	−1.5
rms	47.2	17.3	15.9	15.8

A further improvement in terms of decreasing variability of the residual anomalies can be achieved by considering the isostatic compensation $-\delta g^{iso}$, as shown in Figure 7.9c. After this reduction, the extreme values amount −59.3 mGal and 43.8 mGal and the RMS can be lowered to 15.9 mGal. The mean value changing from −1.4 mGal to −2.5 mGal and might be an indication that the applied isostatic model is slightly overcompensating the topographic influence. However, this is not considered to have a critical impact, since the effect will be compensated within the restore step.

Finally, the atmospheric corrections $-\delta g_i^a + \delta g_e^a$ are applied in Figure 7.9d. As we have seen already in Figure 7.8a this influence will be small. The amplitude of the anomalies is on average risen by 1 mGal, so the mean value of the remaining gravity residuals is −1.5 mGal. The minimum and maximum values are −58.5 mGal and 44.8 mGal and the variability of the data is slightly decreased to 15.8 mGal, which can be attributed to the proper consideration of the topography in the atmospheric potential.

The reduction steps for the GOCE gradient data are exemplarily illustrated for the V_{zz} vertical gradient in Figure 7.10. The gradients are already reduced by the GOCO03s long-wavelength components during the preprocessing. The resulting values are visualized in Figure 7.10a and range from −46.1 to 44.3 mE with a RMS of 11.2 mE and a mean value of 0.1 mE, see Table 7.2.

Table 7.2: Statistics of the vertical gradient data set after applying the consecutive reduction steps

[mE]	**GOCO03s**	**Topography**	**Isostasy**
min	−46.1	−32.3	−28.9
max	44.3	38.1	32.9
mean	0.1	−0.6	−0.2
rms	11.2	8.7	7.7

Reducing the effect of the topographic masses from the gradients at satellite altitude leads to a variability of 8.7 mE with a maximum and minimum value of 38.1 mE and −32.3 mE, respectively. Finally, the gradients can be further reduced by the isostatic effect, which decreases the amplitude range down to −28.9 to 32.9 mE with a RMS of 7.7 mE. Thus, the reduction steps lead to significantly smoothed input data. The remaining mean value is −0.2 mE, hence the input gradient field is almost perfectly centered.

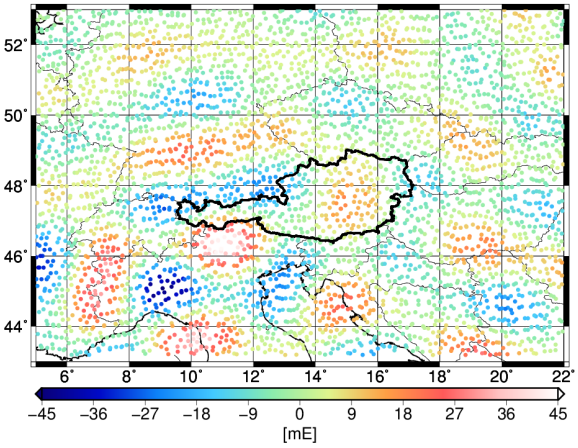

(a) Reduction of GOCO03s to D/O 120

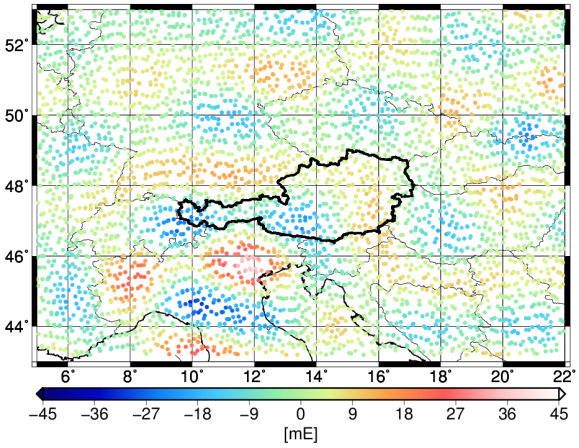

(b) Reduction of topographic effect

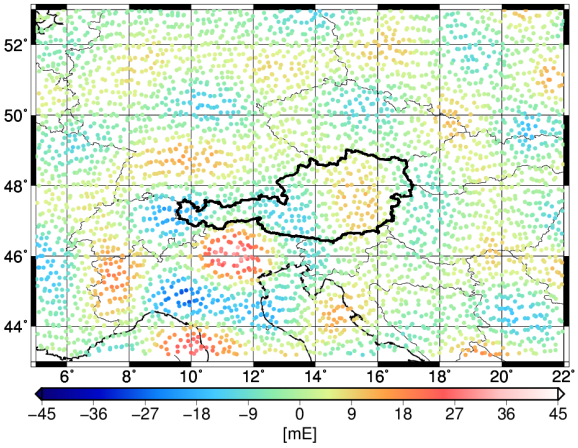

(c) Reduction of isostatic effect

Figure 7.10: Gradient data reduction in consecutive steps shown for the V_{zz} component

The consistently reduced gravity anomaly and gravity gradient input data can then be used for the derivation of an Empirical Covariance Function (ECF) and for the estimation of a Model Covariance Function (MCF), which will be treated in section 7.3.2. With this information, the residual geoid heights corresponding to the residual disturbing potential field represented by the input data can be estimated within the LSC procedure. After that, it is necessary to restore the preliminary reduced gravity signal constituents in terms of geoid heights in the same consistent manner as it was done in the remove step. This is achieved by reversing the reductions according to Eq. (7.1)

$$N = N^{LSC} + \left(N^{egm} - \delta N^{t,shc} - \delta N_e^a\right) + \delta N^{dem} + \delta N^{iso} + \delta N_i^a \,, \tag{7.2}$$

where all components are expressed as geoid heights. The corresponding contributions to the geoid height constituents that have to be restored are illustrated in Figure 7.11.

The majority of the restored geoid signal in the range from 43.5 to 50.5 m can be attributed to the signal N^{egm} of the GOCO03s model up to D/O 120. The long-wavelength signal structure can clearly by seen in Figure 7.11a. Furthermore, the topographic mass effect is depicted in Figure 7.11b. Since the long-wavelength signals of the topography are already

included in the GOCO03s, here only the effect $\delta N^{dem} - \delta N^{t,shc}$ has to be considered. The additional high-frequency contributions to the geoid heights are in the order of approximately ± 2.5 m.

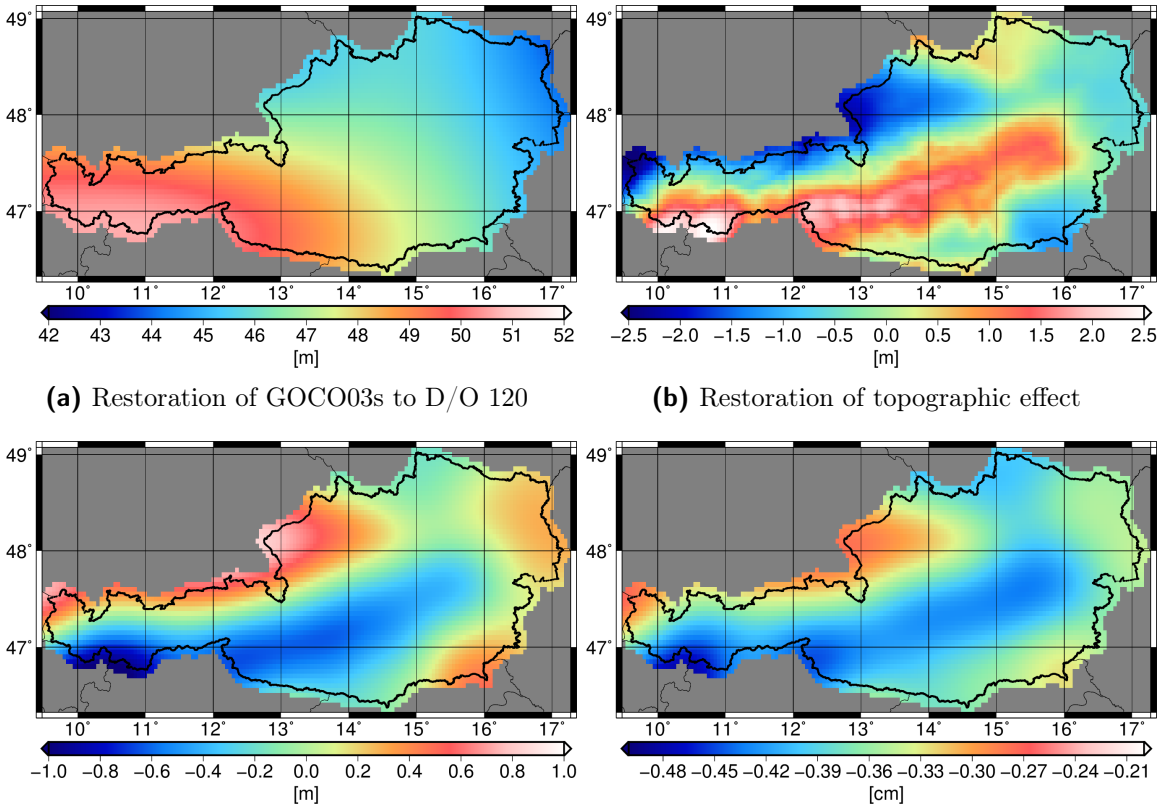

(a) Restoration of GOCO03s to D/O 120

(b) Restoration of topographic effect

(c) Restoration of isostatic effect

(d) Restoration of atmospheric effect

Figure 7.11: Contributions of the a-priori reduced gravity signals in terms of geoid heights for the restore process

The topographic signal is partly compensated due to isostasy. Similarly to the topographic mass effect, only the signal content which is not covered by the EGM has to be accounted for. Therefore, the residual isostatic gravity signal δN^{iso} from D/O 121 to 720 is shown in Figure 7.11c, which reaches amplitudes of roughly ± 1 m. Finally, the combined atmospheric effect $\delta N_i^a - \delta N_e^a$ is restored. While $-\delta N_e^a$ stands for the correction of the atmospheric masses included in the GOCO03s, the actual restoration of the atmosphere is indicated by the contribution of the interior atmospheric potential expressed in geoid heights δN_i^a. This effect is very small with amplitude variations from -0.5 cm to -0.3 cm. The corresponding signal is illustrated in Figure 7.11d and shows the expected correlation with the topography. Despite the small influence, the restoration of the atmosphere causes an average shift of approximately -0.4 cm and thus will be considered in the restore step.

7.3.2 Covariance function estimation

In order to obtain the necessary auto- and crosscovariance matrices between the observations and the gravity signals which should be estimated with the LSC method, one has to find a suitable statistical description in terms of a covariance function of the underlying residual disturbing potential field, see section 3.1 and section 3.2. In this work, a Tscherning-Rapp degree variance model as introduced in Eq. (3.55) is used to compute the degree variances k_n

$$k_n = \frac{A}{(n-1)(n-2)(n+B)} ,$$

for the basic Model Covariance Function (MCF) of the disturbing potential T given in Eq. (3.33)

$$K(r, r', \psi) = \sum_{n=2}^{\infty} \left(\frac{R^2}{rr'}\right)^{n+1} k_n \, P_n(\cos\psi) .$$

In order to account for the errors of the GOCO03s model, which has been reduced from the gravity signals up to D/O 120 in the previous section 7.3.1, we can write

$$K(r, r', \psi) = \sum_{n=2}^{120} \left(\frac{R^2}{rr'}\right)^{n+1} k_n^{\sigma} \, P_n(\cos\psi) \; + \sum_{n=121}^{N_{max}} \left(\frac{R^2}{rr'}\right)^{n+1} k_n \, P_n(\cos\psi) , \tag{7.3}$$

where k_n^{σ} are degree variances of the formal GOCO03s coefficient errors, which can be obtained by Eq. (4.1). Although a full covariance information for this EGM would be available, the correlations between the spherical harmonics coefficients are neglected in Eq. (7.3) for simplification. Furthermore, the implemented approach for the determination of covariances as introduced in section 3.7 does not use closed analytic covariance expressions. Thus, the series expansion can not be calculated to infinity but has to be truncated at a certain maximum degree N_{max}. To reduce the computational effort for the evaluation of the Legendre series, for the current study a limit of N_{max} =2160 will be used. The corresponding MCFs for gravity anomalies Δg and the vertical gradients V_{zz} can be derived from the covariance function of the disturbing potential in Eq. (3.33) by means of covariance propagation and have already been introduced in Eqs. (3.57) and (3.58).

Since two input data types, terrestrial gravity anomalies and GOCE gravity gradients reduced by systematic effects, are going to be used for the geoid estimation, the covariance function should reflect the statistics of both input data sets. Therefore, the three constants of the degree variance model A, B, and Bjerhammar radius R_B of the MCF are simultaneously estimated by fitting the MCFs to the actual empirical covariance functions (ECFs) of both data sets within a least squares adjustment. It should be noted that only the vertical gradient V_{zz} is used for this adjustment, because the derivation of the corresponding MCF is quite straightforward, whereas this would be much more extensive for other gradient types, see for instance section 3.4.

In order to get an estimate for the effect of the GOCO03s errors, the left term on the right side of Eq. (7.3) is evaluated for gravity anomalies. The resulting error covariance function is illustrated in Figure 7.12. Due to the high accuracy of the satellite model in the long wavelengths, the GOCO03s errors only contribute to the combined covariance function in

Eq. (7.3) in the order of 10^{-3} mGal. Therefore, this effect is neglected in the estimation of the MCF.

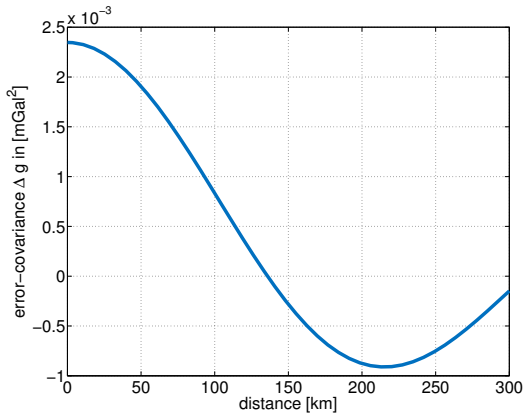

Figure 7.12: Covariance function of the GOCO03s coefficient errors up to D/O 120

The ECFs are determined according to Eq. (3.54) by subdividing the observation pairs in 100 distance classes, which results in a class width of approximately 7.2 km for the gravity anomaly data set and 16.3 km for the gravity gradients. The ECF of the gravity anomaly data set is illustrated in the left column of Figure 7.13 in blue. It has an empirical variance $C^e_{\Delta g}(0)$ =246.0 mGal and a correlation length $D^e_{C_{\Delta g}/2}$, at which $C^e_{\Delta g} = C^e_{\Delta g}(0)/2$, of 34.5 km (green cross). The ECF of the vertical gradient data is shown in the right column of Figure 7.13 again in blue. The variance $C^e_{V_{zz}}(0)$ =62.1 mE and the corresponding correlation length $D^e_{C_{V_{zz}}/2}$ =69.1 km.

In an initial adjustment step the three parameters A, B, and R_B are iteratively estimated and the resulting MCFs are visualized in Figure 7.13a for gravity anomalies on the left and for vertical gradients on the right, both indicated by red lines. The estimated parameters and the corresponding errors in terms of standard deviations are summarized in Table 7.3 in the first row.

Table 7.3: Estimated parameters of the Tscherning-Rapp degree variance model and variances of the resulting MCF

Step	**Parameter**			**Standard deviation**			**MCF Variance**	
	A $[(\mathrm{m/s})^4]$	R_B [m]	B	σ_A $[(\mathrm{m/s})^4]$	σ_{R_B} [m]	σ_B	$C^m_{\Delta g}(0)$ [mGal^2]	$C^m_{V_{zz}}(0)$ [mE^2]
A1	273186	6364893	-104.7	21995	384	2.4	244.2	61.8
A2	296408	6364400	-103	1464	-	-	243.4	61.3
A3	299493	6364400	-103	-	-	-	246.0	61.9

The Bjerhammar radius R_B is estimated with 6364893 ± 384 m, which is below the minimum radial distance of the terrestrial observations of approximately 6 366 027 m and thus guarantees the covariance function to converge. The dimensionless parameter B was determined with -104.7 ± 2.4, which is also below the critical $N_{min} = 121$. The parameter A is a constant scaling factor given in potential units $[(\mathrm{m/s})^4]$ and was adjusted to 273186 ± 21995 $(\mathrm{m/s})^4$.

The fitted MCF corresponding to these parameters is represented in Figure 7.13a for gravity anomalies on the left and for vertical gradients on the right by red curves. The variance of the MCF in terms of gravity anomalies is $C^m_{\Delta g}(0)$ =244.2 mGal and the correlation length amounts $D^m_{C_{\Delta g}/2}$ =32.4 km, which is already close to the values $C^e_{\Delta g}(0)$ =246.0 mGal and $D^e_{C_{\Delta g}/2}$ =34.5 km of the ECF. The match of MCF and ECF curves is very good, in particular within the first 90 km, where the significant correlations between the gravity signals can be expected. Similarly, the MCF of vertical gravity gradient is corresponding to the progression of the ECF to a high extent, and the model variance $C^m_{V_{zz}}(0)$ =61.8 mE is close to the empirical $C^e_{V_{zz}}(0)$ =62.1 mE.

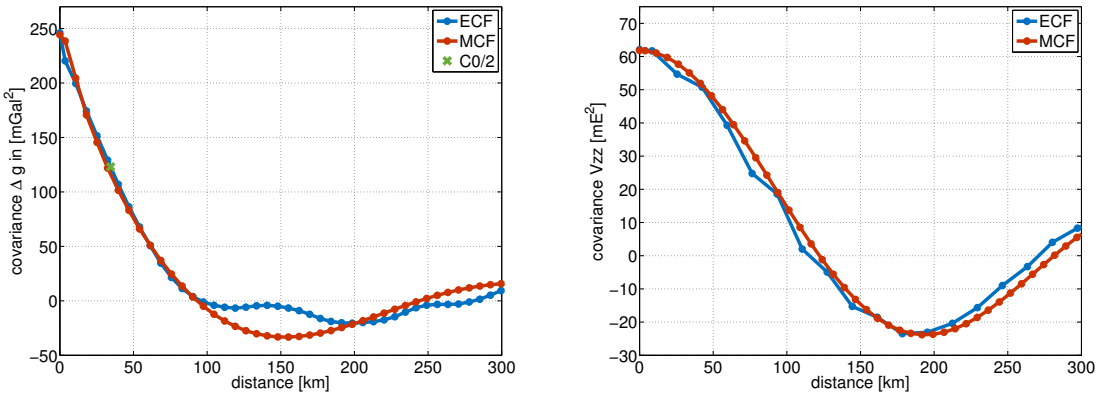

(a) Initial adjustment of the model parameters A, B and R_B

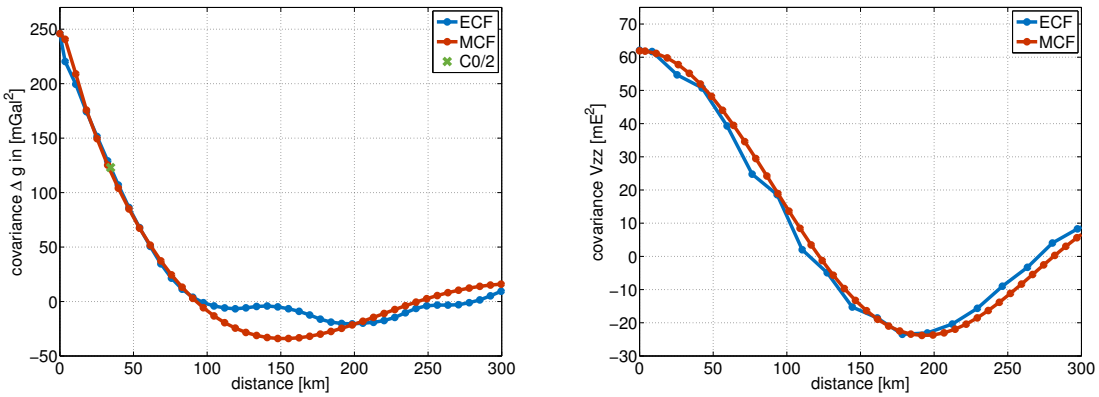

(b) Final fit with a scaled parameter A

Figure 7.13: Covariance function estimation: ECFs (blue lines) and fitted MCFs (red lines) for gravity anomalies on the left and vertical gradients on the right

In the next step, the parameter B is empirically fixed to the integer value -103 and the Bjerhammar radius is set to $RB = 6364400$ m. The remaining parameter A is again determined by least squares adjustment to a value of 296408 ± 1464 $(\mathrm{m/s})^4$, also shown in the second line of Table 7.3. In this way, the correlation length of the MCF for the gravity anomalies can be improved to $D^m_{C_{\Delta g}/2}$ =33.2 km. However the variances for Δg and V_{zz} are slightly decreasing to $C^m_{\Delta g}(0)$ =243.4 mGal and $C^m_{V_{zz}}(0)$ =61.3 mE.

To circumvent this misfit between ECF and MCF variances, the parameter A is finally

scaled by the quotient $C^e_{V_{zz}}(0)/C^m_{V_{zz}}(0) = 1.010408$, which leads to $A = 299493$ $(\mathrm{m/s})^4$. Hence, the MCF variances are $C^m_{\Delta g}(0)$ =246.0 mGal and $C^m_{V_{zz}}(0)$ =61.9 mE, and correspond to those of the ECF. The resulting MCF curves for gravity anomalies and vertical gradients are outlined in Figure 7.13b. The final values of the parameters for the Tscherning-Rapp MCF are summarized in the last line of Table 7.3. The corresponding MCF is used for the calculation of the auto- and crosscovariance matrices in the geoid estimation with LSC, which is done in the next section 7.3.3.

7.3.3 Results of the geoid computation

The gravity and gradient data sets, which have been reduced by systematic effects within the RCR procedure in the preceding section 7.3.1, are used to derive three different estimates of residual geoid heights. The MCF, which was adjusted to fit the statistics of the reduced gravity and vertical gradient data in the previous section 7.3.2, is the basis for the setup of auto- and crosscovariance matrices C_{tt} and C_{st} for the LSC process. The residual geoid heights are estimated on a grid with a spacing of $0.05° \times 0.05°$ which is covering the Austrian territory and slightly extended across the borders.

For the first solution, the 30015 reduced gravity measurements have been introduced as input data for the computations. All observations were weighted with the unified standard deviation of 1 mGal, which is chosen corresponding to former studies. The estimated residual geoid heights are illustrated in Figure 7.14a and the formal standard deviations of this estimate are given in Figure 7.14b. The residual geoid signal is in the range from −1.592 m to 1.035 m, while the accuracy derived from the LSC procedure is in the order of 2 mm to 4 mm in the central Austrian region and increasing to 3.5 cm towards the borders. This effect mainly has to be attributed to the geometrical distribution of the input data.

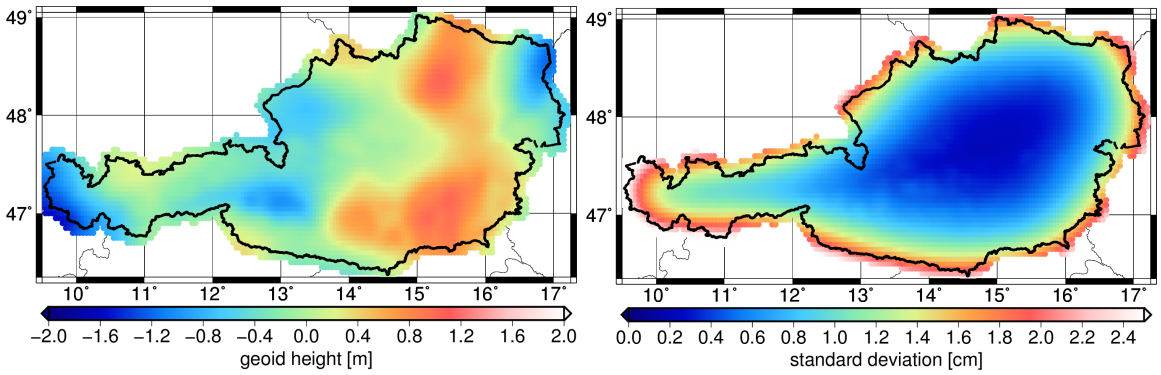

(a) Estimates of residual geoid heights

(b) Standard deviations

Figure 7.14: Residual geoid heights solution based on 30015 terrestrial gravity observations (a) and corresponding standard deviations (b)

Furthermore, a solution which is solely based on GOCE gravity gradients is processed. The residual geoid heights are derived from 4182 observation stations, which are distributed over an extended area as shown in Figure 7.4b. At each of these stations, the main diagonal components V_{xx}, V_{yy} and V_{zz} of the GGT are used for the geoid determination, hence 12546

observations are introduced in total. The resulting residual geoid heights and their accuracy information are shown in Figure 7.15a and Figure 7.15b, respectively. The formal errors of this estimate reveal that with GOCE gradients used as in-situ observations at orbit altitude, the geoid can be determined with a standard deviation in the order of 10 cm. This is mainly caused by the downward continuation from orbit altitude to geoid level, which amplifies not only the gravity signals but also the measurement noise. However, due to the extended area of available input data, the error structure is rather homogeneous within the Austrian territory.

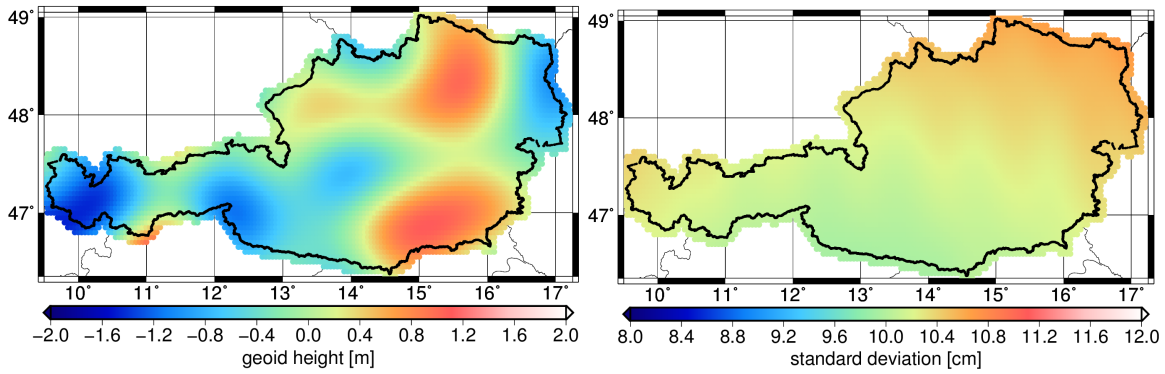

(a) Estimates of residual geoid heights **(b)** Standard deviations

Figure 7.15: Residual geoid heights solution based on 12546 GOCE gradient measurements at 4182 observation sites (a) and corresponding standard deviations (b)

The derived residual geoid heights vary between −1.478 m to 1.108 m, and the main spatial features are in correspondence with those of the gravity-only solution of Figure 7.14a. However, the gradient solution does not resolve the residual geoid signal with the same detailed spatial resolution. This had to be expected, since the gradiometer instrument at orbit altitude is not that sensitive to localized gravity signals compared to the terrestrial data. On the other hand, the terrestrial data is lacking medium- to long-wavelength information due to the limited extent of available data. Hence, the terrestrial gravity data and the GOCE gradient data can complement each other.

Therefore, a combined solution using both data sets is finally generated. The result is shown in Figure 7.16a with geoid height variations between −1.717 m and 1.015 m. The obtained standard deviations for the combined solution are now in the order of 3 mm throughout the whole area and show the benefit of the inclusion of GOCE gradient data, see Figure 7.16b.

To verify the contribution of the gradient data in comparison to the gravity-only solution, the difference between the combined and the gravity-only solution is illustrated in Figure 7.17a. The additional GOCE data is influencing the geoid estimate in particular in the western and south-western parts of Austria, where the data distribution of the terrestrial gravity data is not as dense as it is in the East, see Figure 7.3b. This is mainly induced by the topographic situation within Austria. Furthermore, the contributions of GOCE data are especially affecting the not so well determined border regions. In general, the spatial structures reveal that the influence of the gradient observations is appearing in particular at medium

spatial scales, where the GOCE data was expected to contain additional valuable gravity signals.

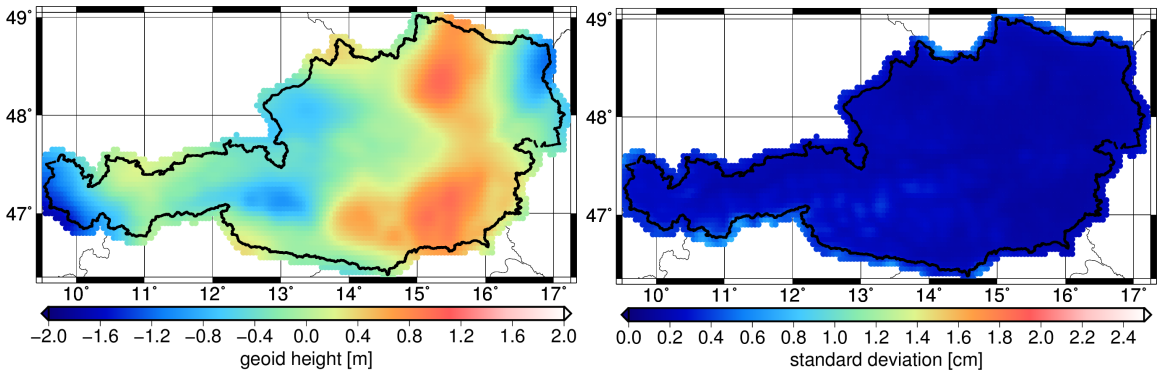

(a) Estimates of residual geoid heights **(b)** Standard deviations

Figure 7.16: Residual geoid heights solution based on the combination of terrestrial gravity observations and GOCE gradient measurements (a) and corresponding standard deviations (b)

In order to obtain the final absolute geoid heights, the signal constituents that were reduced from the gravity observations beforehand have to be restored, see section 7.3.1. Hence, the effects according to Figure 7.11 are readded to the residual geoid heights which were derived from the combined estimate. The final absolute geoid height values are presented in Figure 7.17b and have an amplitude range from 42.443 m to 51.990 m. The formal errors of the geoid estimate from LSC mainly reflect the distribution of the input data and their relative weighting according to the introduced accuracy information. For a verification of the actual quality of the geoid solution, a validation of the results with independent data is necessary, which is treated in the following section.

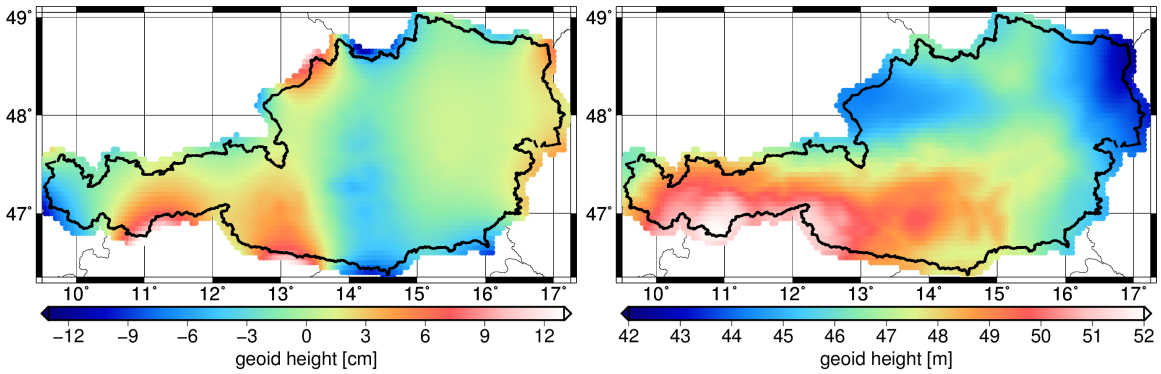

(a) **(b)**

Figure 7.17: Differences between the combined and the gravity-only solution indicating the influence of the additional GOCE data (a); absolute geoid heights from the combined solution after the restore step (b)

7.4 Validation of the Austrian geoid solution

In this section, the calculated geoid heights are validated in order to obtain a measure for the achieved quality. On the one hand, the solutions can be compared to the official Austrian geoid which was derived in 2007, see section 7.1. On the other hand, the results can be validated with the GPS/levelling data set provided by the BEV, which represents independent geoid heights.

The official Austrian geoid solution was derived from gravity and deflections of the vertical data as well as from geoid height observations of 170 GPS/levelling measurements. In order to generate a geoid which is in accordance with the orthometric height system in Austria, this geoid was heavily weighted towards the GPS/levelling observations, which was discussed in detail in section 7.1. As a consequence, this solution lost its physical meaning and thus shows inconsistencies in comparison with gravimetric geoids. Since the time of the generation of the official solution, the GPS/levelling data set was extended to 192 stations and several points that were used for the geoid computation have been revised and corrected for gross measurement errors. Thus, the official solution will not be conform to these GPS/levelling geoid heights anymore. In order to verify the differences, geoid heights for the updated GPS/levelling data set were interpolated from the official Austrian geoid solution grid, which was shown in Figure 7.2. The grid is given in a resolution $1.5' \times 2.5'$, which is approximately corresponding to a grid spacing of 3 km×3 km. The differences between the interpolated geoid heights and those of the updated GPS/levelling data set are illustrated in Figure 7.18.

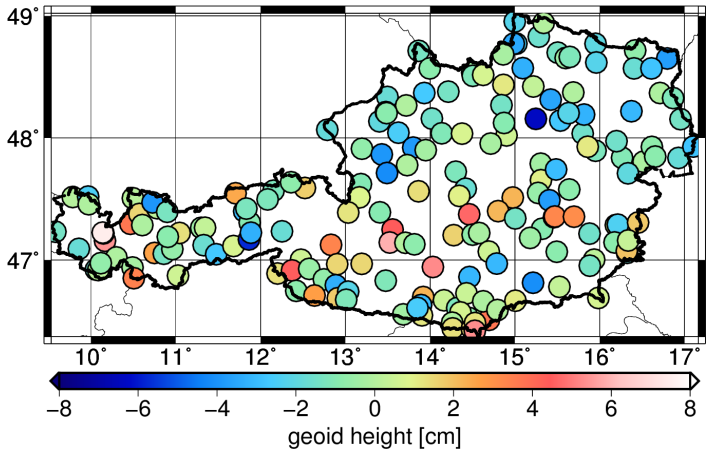

Figure 7.18: Differences between the updated GPS/levelling data set and the official Austrian geoid solution

The maximum variations of the geoid height differences range from −6.4 cm to 7.5 cm with an RMS of 2.2 cm. This investigation leads to two conclusions. On the one hand, it highlights the shortcomings of the official geoid solution, i.e. due to its strong dependency on the GPS/levelling measurements, a change in this data set would require a complete adjustment of the geoid surface. Therefore, a comparison between the official solution and the solution derived in this thesis will not lead to a conclusion about the quality of the presented geoid estimate. On the other hand, this verification indicates that the specified accuracy for

the official solution of approximately 3 cm is comparable with the RMS of the differences in Figure 7.18, but the actual deviations might be considerably higher. Furthermore, although some gross errors are corrected, there may be still some further inconsistencies in the GPS/levelling data set, which has to be kept in mind for the following validation with the geoid that is derived in this thesis.

At first, the geoid heights of the gravity-only solution are compared with the GPS/levelling data and illustrated in Figure 7.19a. The statistics of the differences are summarized in Table 7.4. The amplitudes of the differences range from −16.1 cm to 11.4 cm and have a RMS value of 5.5 cm. Looking at the spatial distribution of the deviations, a pronounced negative trend (i.e. the estimated geoid heights are smaller than those from GPS/levelling) can be found in particular in the alpine high-mountain areas of western and south-western Austria, as well as in the North-East. On the other hand, clear positive trends are obvious in North-South direction at the longitude of about 15.5° East, and in the far West.

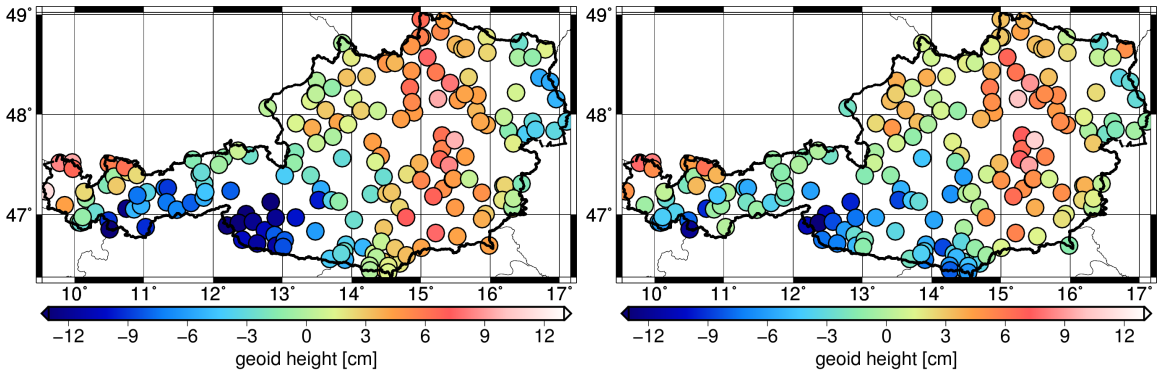

(a) Differences to the gravity-only solution, bias 35.1 cm removed

(b) Differences to combined solution based on gravity and GOCE gradient data, bias 37.8 cm removed

Figure 7.19: Differences between geoid heights from 192 GPS/levelling observations within Austria and geoid heights from the gravity-only solution (a) and the combined solution (b)

Table 7.4: Statistics of the differences between geoid heights from the gravity-only as well as the combined solution and geoid heights from 192 GPS/levelling observations within Austria given in [cm]

Solution	min	max	bias	rms
gravity-only	−16.1	11.4	−35.1	5.5
combined	−13.2	10.8	−37.8	4.6

The differences between the estimated geoid heights and GPS/levelling observations reveal an offset of −35 cm, which has already been removed in this plot. As stated in Pavlis et al. (2012), the bias between the GPS/levelling observations and a gravimetric geoid represents the combined effect of mainly two possible sources. On the one hand, there can be an offset in the realization of the vertical levelling datum and the gravimetric geoid. On the other hand, the

ellipsoid that fits the gravimetric geoid in the best possible way, i.e. the geoid variations w.r.t. to this ellipsoid have a global average of zero, might differ from the ellipsoid which is used for the calculation of the ellipsoidal GPS heights. For the EGM2008 gravity model Pavlis et al. (2012) found a difference between the semi-major axis of the best-fitting ellipsoid and that of the WGS84 ellipsoid of -41 cm, which is a global value.

The difference to the bias which is present in the comparison between the geoid solutions and the GPS/levelling points from the BEV may have several reasons. The presented geoid solution is a regional fit to the gravity observations given in a restricted area, therefore the best-fitting ellipsoid can be different from that of the EGM2008. Furthermore, the GPS/levelling observations of the BEV are connected to the European Vertical Reference System 2000 (EVRS2000), which is defined as a zero-tide system as far as the treatment of the permanent tide is concerned (Ihde et al., 2008). However, its realization EVRF2000 is based on the United Levelling Network (UELN) 95/98, and has to be considered as a mixed-tide system, since the treatment of the permanent tide in the incorporated national levelling data sets is widely unknown. It is assumed that the majority of the observations were provided in the mean-tide system. On the other hand, the presented geoid solution is calculated w.r.t. GOCO03s, which is given in the tide-free system. Hence, these inconsistencies in the datum definitions also contribute to the differences between geoid heights and GPS/levelling observations.

In Figure 7.19b the differences between the combined solution and the GPS/levelling points are presented. The deviations are now between a minimum of -13.2 cm and a maximum of 10.8 cm, see Table 7.4. Compared to the gravity-only solution, this is a considerably lower bandwidth indicating the beneficial impact of the additional GOCE gradients data. This is also confirmed by the decreased RMS of 4.6 cm. The advantageous influence of the gravity gradients is especially visible in the western and south-western parts of Austria, where the pronounced negative trend could be diminished. Furthermore, also the positive differences in the far West could be decreased. In the East and North of Austria, the GOCE observations obviously do not influence the situation very much, which could be expected from the comparison between gravity-only and combined solution in Figure 7.17a. Nevertheless, the overall positive impact of including the GOCE gravity gradients could be proven in this example.

In general, the remaining irregularities seem to be correlated with the topographic situation in Austria. From this, one might infer that these inconsistencies are induced by an insufficient topographic reduction. A probable source for these errors can be found in the geological structures of the topography. For this reason, the geological map for Austria is shown in Figure 7.20, which should highlight the variety of the geological features without giving a detailed explanation about their composition.

However, it is obvious that different geological structures result in different densities of the corresponding rock materials, which is in conflict with the assumption of the constant rock density of $\rho = 2670\,\mathrm{kg\,m^{-3}}$ that was used for the reduction of the topographic masses. In reality, the density can be expected to vary from about $2000\,\mathrm{kg\,m^{-3}}$ for the sedimentary basins at the eastern border of Austria (light yellow areas in Figure 7.20) to $2900\,\mathrm{kg\,m^{-3}}$ for some mountainous regions in southern and western Austria (orange areas in Figure 7.20).

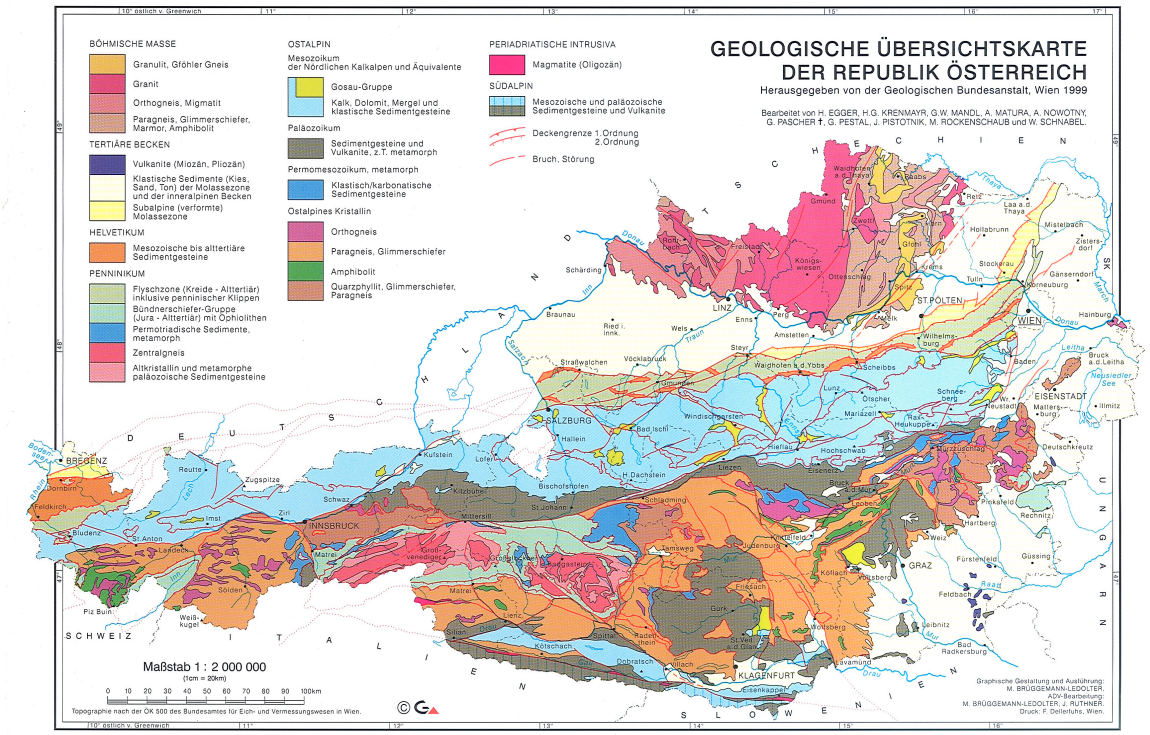

Figure 7.20: Geological map of Austria (©Geological Survey Austria)

Thus, the proper consideration of the density variations will improve in particular the consistency of the terrestrial data after the topographic reduction. Due to the signal attenuation at the orbital height of the GOCE satellite and its limited ability to resolve gravity signals at small spatial scales, the impact on the gradient observations is expected to be less pronounced but nevertheless may lead to improvements. For a consistent topographic reduction that accounts for the geological setting, a detailed map of density variations for the whole area where data are available has to be at hand. This is not the case at the current stage of this thesis, so this issue poses a possibility for future investigations.

A further element of uncertainty is the applied isostatic compensation effect, which is also based on the assumption of a uniform density of the topographic masses. Here, the consideration of the density variations below the Earth's surface will also lead to a different picture. Futhermore, a correct treatment of the isostatic effect would require the knowledge of the crustal thickness, which is represented by the Moho surface (see Section 8.1). In combination with a three-dimensional density model, this information can be used to derive a more realistic influence of the compensating masses.

7.5 Summary and conclusions of the geoid estimation

In this chapter the influence of the inclusion of GOCE gravity gradients on a regional geoid estimation for the Austrian territory using the LSC approach is investigated. The current official geoid solution, which is provided by the Austrian BEV, shows considerable distortions between a purely gravimetric geoid and the geoid heights from the official precise GPS/levelling observations derived by the BEV. To overcome these inconsistencies, at that time the remaining differences were adjusted by the introduction of a regression polynomial surface and a subsequent geoid estimate that was heavily constrained towards the GPS/levelling points. Consequently, the official geoid solution does not represent a geophysically meaningful surface of equal potential. The new geoid solution presented in this chapter is aimed to avoid these irregularities.

The solution derived in this thesis is based on the combination of 30015 terrestrial gravity measurements, which are available within Austria and for adjacent areas of neighbouring countries, and three months of GOCE gravity gradient data. The colored noise that is deteriorating the GOCE observations is removed by the preprocessing and filter strategy as proposed earlier in this thesis. To reduce the computational effort and to obtain a more homogeneous data distribution, the gradients data was reduced to a sampling rate of 5 s and cut out for the region between 5° to 22° East and 43° to 53° North, which leads to 4182 observation sites at which the main diagonal components of the GGT are used for the geoid estimation.

In order to obtain a smooth input data set, which is a prerequisite for a successful geoid estimation with the LSC method, the systematic effects of a global EGM, the topography, the isostatic compensation and the atmosphere are considered for both data types within a consistent RCR procedure. The long-wavelength effects are removed using the GOCO03s satellite-only EGM up to D/O 120. This choice is made, since the GOCE observations are expected to contribute in particular in the medium spectral range of the gravity signal starting approximately at this threshold. Furthermore, the high-frequency gravity effects on the terrestrial gravity observations induced by the topographic masses are accounted for by using a dense DEM with the standard crustal density $\rho = 2670\,\mathrm{kg\,m^{-3}}$. To avoid a double consideration of the long-wavelength topographic signal that is included in the GOCO03s, a correction in terms of a spherical harmonics expansion of the topographic potential up to D/O 120 is applied. For GOCE gradients it is sufficient to consider the topographic signal up to D/O 360 due to the signal attenuation at the orbit height of the satellite.

Additionally, the gravitational potential of the isostatic compensation effect is developed in a spherical harmonics series up to D/O 720 on the basis of the DEM and a constant density contrast, which is assumed to be $\Delta\rho = 350\,\mathrm{kg\,m^{-3}}$. While the isostatic effect is removed from the terrestrial observations from D/O 121 to 720, it is shown that the influence of degrees higher than 360 is negligible at GOCE satellite altitude. Finally, the influence of atmosphere is reduced using the atmospheric density model that was derived within this thesis. The atmosphere is already implicitly removed from the gradient measurements by reducing the GOCO03s contribution. In case of terrestrial data, a consistent reduction is achieved by accounting for the fact that the observations are located within the atmospheric masses.

Due to the consistent reduction steps, the value range of the terrestrial gravity data could be significantly reduced. While the variability of the anomalies in terms of a RMS is 47.2 mGal after the removal of the long-wavelengths of the GOCO03s model, the finally obtained RMS amounts to 15.8 mGal after the complete reduction. Similarly, the RMS value of the GOCE gradients observations is decreased from 11.2 mE to 7.7 mE.

For the statistical description of the correlation between observations and estimated gravity signals, which is the basis of the LSC approach, a MCF using a Tscherning-Rapp degree variance model is fitted to the ECFs of both, reduced terrestrial anomalies and GOCE gradients, simultaneously in a least squares adjustment procedure.

Residual geoid heights are estimated from solely terrestrial data, gradients data and finally a combination of both data sets in order to verify the influence of the GOCE data. As expected, the terrestrial data can resolve the high frequencies of the geoid signal. The accuracy of the solution is increasing from 3 mm in the central areas towards 3.5 cm at the Austrian borders due to the limited availability of data. In contrast, the gradients-only solution is dominated by long- to medium-wavelength geoid signals, which is corresponding to the sensitivity of the gradiometer instrument at orbit height. The estimated formal errors are in the order of 10 cm, which can be attributed to the downward continuation problem, but have a homogeneous structure due to the extended area of available input data. Finally, the joint solution combines the signal content of terrestrial and satellite data, where the latter especially contributes to the medium-wavelength constituents. With this combination, the formal errors from the LSC estimate are decreased to 3 mm also at the Austrian border regions. In order to obtain absolute geoid height values, the preliminary removed systematic influences are then restored consistently.

To assess the quality of the gravity-only and the combined geoid solutions, a comparison with the official GPS/levelling values is performed. The RMS of the differences between gravity-only and GPS/levelling geoid heights is 5.5 cm. Including GOCE data, this can be decreased to 4.6 cm for the combined solution. It could be shown, that the GOCE gradients have a positive impact in particular in the mountainous regions as well as at the border areas, where the distribution of terrestrial input data is less dense and the topographic situation is more challenging than in other well-surveyed areas. The improvements due to GOCE gradients are occuring in the expected medium-wavelength geoid signal range. In contrast to the official Austrian geoid solution, the geoid derived herein is representing an unconstrained equipotential surface with a high consistency to the independent GPS/levelling observations.

Still, there are several issues that can improve the geoid determination in further investigations. First, the assumed constant and uniform density of the topography is a hypothesis which is not in agreement with the actual situation. Therefore, the use of a density model could improve the topographic reduction within the RCR procedure. Likewise, the consideration of the isostatic effect would be more realistic, if a 3D density model and the actual Moho surface was used for the derivation of the isostatic potential that is applied for the reduction.

Furthermore, the currently used LSC approach has some limitations. At the moment, the implementation is designed for a single processor architecture. Since the size of the autocovariance matrix of the observations is increasing quadratic with the number of input

observations, the amount of the data that can be used in LSC is limited by the size of available computer memory. Hence, for the presented investigations only subsets of the actually available data, terrestrial as well as GOCE gradients, have been used. This situation could be improved by a redesign using parallel processing strategies. Besides that, for the calculation of the covariances the summation of a Legendre series has to be performed, which is theoretically defined to infinity. Other LSC software packages use closed analytical formulas for covariance computations that are derived for particular degree variance models, see Tscherning and Rapp (1974). This is not the case for the approach implemented in this thesis, which leads to the drawback that the summation has to be truncated at a certain degree. However, due to the avoidance of the analytic expressions, the current approach is rather independent of the choice of the covariance or degree variance model, which facilitates the adjustment of a MCF to the ECF of the input data.

Finally, a more realistic weighting of the input observations is an open problem. In the case of GOCE gradients, the error information from the preprocessing procedure is considered to deliver a realistic assessment of the actual accuracy. However, the terrestrial gravity data is introduced with a uniform measurement accuracy. This is not very likely the case in reality. Nevertheless, this was accepted in these investigations due to the lack of other information.

Concluding, the investigations have shown that the regional geoid determination benefits from the use of GOCE gravity gradients as in-situ observations. Compared to a solution purely derived from terrestrial gravity data, the combined geoid estimate is improving in the medium-wavelengths of the gravity signal, which cannot be resolved properly solely from terrestrial data given in a restricted area. The presented geoid is consistent to the GPS/levelling observations to a large extent, which can be further improved by dissolving the discussed limitations.

8 Application II: Moho estimation in central Europe

The determination of the geoid as shown in the preceding chapter can be considered as the classical application of LSC in physical geodesy. This thesis also aims at identifying a different field of application, for which LSC can be utilized with a special focus on the exploitation of GOCE gradient data. The determination of the Mohorovičić discontinuity, commonly abbreviated as Moho, is such a special application which can be expected to benefit from the medium-wavelength gravity information exclusively provided by the GOCE mission. This chapter describes the determination of the Moho applying LSC with GOCE gradients.

First, a general introduction about the structure of the Earth's interior, the Moho and its relation to the concept of isostasy is provided in section 8.1. Afterwards, the formalism for estimating the Moho with LSC is derived in section 8.2. Furthermore, the used data and the computation of the Moho are described in the consecutive sections 8.3 and 8.4. Finally, in section 8.5 the results of this approach are validated with independent Moho models and the chapter closes with a summary and a discussion of the approach and its results in section 8.6.

8.1 The Earth's structure, the Mohorovičić discontinuity and the link to Isostasy

As introduction for this current chapter, a general overview on the structure of the Earth's interior is provided, which is necessary for the definition of the Mohorovičić discontinuity. A standard model for the average Earth structure called Preliminary Reference Earth Model (PREM) was developed by Dziewonski and Anderson (1981) which includes elastic properties, densities, pressure, gravity and other geophysical quantities. Further information on the Earth's interior can be found for instance in Fowler (2004), Lambeck (1988) or also Torge (1989).

Basically, the composition of the Earth can, in a very simplified way, be considered as a system of spherical layers, which can be classified either by their chemical or their mechanical properties. Following the definition according to the mechanical, in particular their rheologic, properties the Earth is composed (from the surface to the geocenter) by the rigid lithosphere with an average depth of about 100 km, the ductile asthenosphere down to about 400 km, and the mesospheric mantle. This layer is passing on to the fluid outer core at about 2900 km depth, which is denoted as the Gutenberg discontinuity, and finally a solid inner core from approximately 5100 km to the Earth's center is forming the nucleus of the Earth. On the other hand, the classification according the chemical composition of the layers leads to the division

into the crust with an average thickness of 35 km, the upper mantle going down to 670 km, the lower mantle with 2900 km depth, an outer core and the inner core.

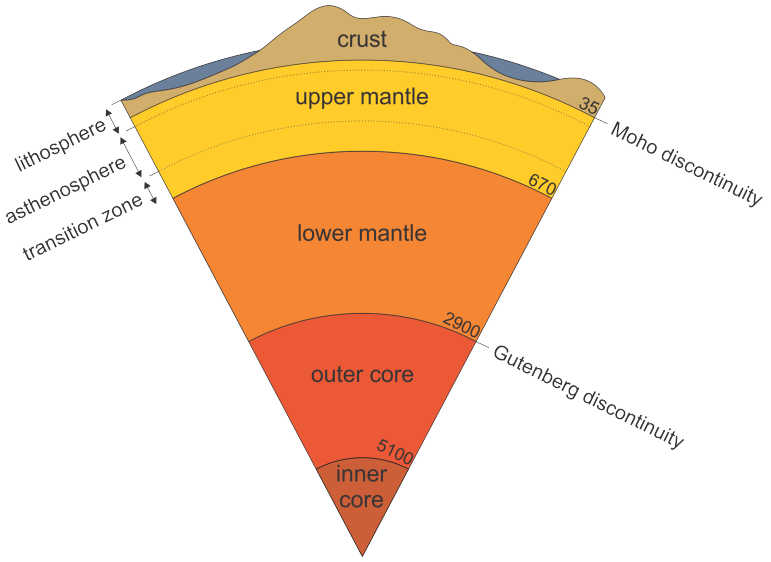

Figure 8.1: Schematic illustration of the radial structure of the Earth's interior (not to scale) according to Fowler (2004). Approximated depth declarations are given in [km]

As indicated in the schematic Figure 8.1, the two different classifications are partly overlapping and may need some further explanations. The lithosphere is the outermost rigid layer, which comprises the Earth's crust (oceanic or continental) and the uppermost part of the mantle. This shell is not continuous but is splitted into the so-called lithospheric or tectonic plates, which are moving on top of the asthenosphere according to plate tectonics theory. Looking at the main geological constituents of the different layers, the continental crust is mainly formed by granitic rock, the oceanic crust by basaltic rock, and the solid upper mantle is composed by peridotite. This material is predominant in the whole mantle, thus it is also forming the asthenosphere, but in contrast to the solid upper mantle in a ductile condition.

As mentioned at the beginning, all these classifications of different spherical layers are only a very rough approximation. In reality, the boundaries between the layers are varying considerably, for instance due to geodynamical processes like mantle convection or subduction of tectonic plates and the inherent mass transports and redistributions. The assumption of abrupt changes from one layer to another is also not always realistic, instead various intermediate transition zones exist. Furthermore, the classification can not only be performed by means of rheologic or chemical properties, but also, for instance, based on seismic velocities, elastic moduli or temperature. An extensive treatment of all of these geophysical topics is beyond of the scope of this thesis, thus the reader is referred to Fowler (2004) or Lambeck (1988) for more detailed information. In this work we will primarily restrict our interest to the lithospheric part of the Earth.

The most effective and widely used geophysical technique to probe the Earth's interior is the method of seismology, which is the study of the propagation of elastic waves through the Earth. These observations are based on the fact that the propagation characteristics of

seismic waves are depending on the density, bulk modulus and shear modulus of the material which they are travelling through.

In general one can distinguish between two kinds of elastic waves provoked by an earthquake or an explosion, the body waves and the surface waves. According to their names, body waves propagate through the Earth's body and can again be classified in P-waves or S-waves. Since body waves behave similar to electromagnetic light waves, they are reflected or refracted at a border of changing media according to Snell's law. P-waves, also denoted as primary or pressure waves, are longitudinal waves that have the highest travel speed. They behave similar to a sound wave and thus the motion of the material they are travelling through is in the same direction as the one of the wave propagation itself. The S-waves, alternatively also secondary or shear waves, are transversal waves and invoke a vibration of the passed medium perpendicular to the direction of wave propagation. In contrast to P-waves, these S-waves can only travel through elastic media, so for instance they do not propagate through the fluid outer core.

The second major group of waves are the surface waves, which only appear at the surface or in near-surface layers of the Earth. In general they are slower than body waves, but their signals can reach higher amplitudes. Surface waves can be further discriminated into Rayleigh and Love waves, which are described in more detail in Fowler (2004). Besides body and surface waves, the free oscillations of the entire Earth are completing the seismic spectrum at very long periods, which was for instance of great importance to prove the solidness of the inner core (Woodhouse and Deuss, 2007).

A distinct feature in the structure of the Earth's interior, which can be determined by seismic refraction and reflection experiments, is the surface that is indicating the transition from the crustal to the upper mantle layer. This surface is denoted as the Mohorovičić discontinuity, which is named after the Croatian geophysicist Andrija Mohorovičić (1857-1936). He discovered the discontinuity in 1910, when studying the seismograms of an earthquake that occurred near Zagreb in 1909. He recognized that some seismic waves did not arrive at the expected time and therefore expected them to be diffracted at some specific border. The main reason for this can be found in a sudden increase of density. The rock of continental crust has an average density of roughly $2700\,\mathrm{kg\,m^{-3}}$, the oceanic crust's density is approximately $2900\,\mathrm{kg\,m^{-3}}$, while the mean density of the upper mantle is considerably higher with $3300\,\mathrm{kg\,m^{-3}}$. Considering the velocity of a P-wave, this leads to an average propagation speed of $6.5\,\mathrm{km\,s^{-1}}$ in the crust, while at the top of upper mantle such a wave is travelling with $8.1\,\mathrm{km\,s^{-1}}$ on average. Hence, by investigating the wave propagation paths and travel times of seismic waves, the depth of the Moho can be inferred.

Although the seismic exploration approach can reliably deliver Moho depth information, it has strong limitations regarding the spatial resolution. The measurement campaigns to obtain seismic profiles are elaborate and cost-intensive and thus the availability of seismic observations is often restricted. Hence, the generation of regional or even global Moho maps is often based on a very limited number of seismic data, and the lack of information is compensated by interpolation between the available profiles. Thus, on a more local scale these Moho depths may be quite unrealistic, in particular in areas without adequate seismic data.

Apart from the seismic approach, evidence of the Moho can also be found by gravimetric-isostatic methods using gravity data. In section 4.4 we have already discussed the concept of

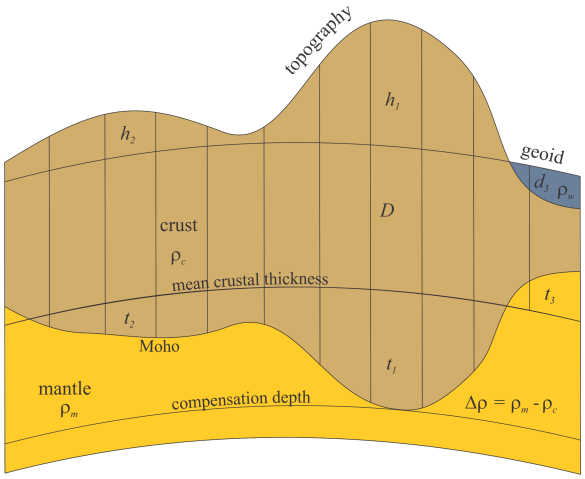

Figure 8.2: The Airy-Heiskanen isostatic concept and the Moho

isostasy, which was introduced to explain systematic inconsistencies of geodetic observations when compared to the expectations if one assumes a homogeneously layered Earth's interior. In particular in the Airy-Heiskanen model (but also in the Vening Meinesz concept) a varying border between a lighter crust and a denser mantle has been introduced, which actually can be interpreted as the Moho discontinuity, as shown in Figure 8.2. This concept will be the basis for the derivation of the LSC approach for the determination of the Moho from GOCE gradient data in the following sections.

8.2 A Least Squares Collocation approach for Moho estimation

The derivation of subsurface density structures from gravity measurements is a typical ill-posed inverse problem in geophysics or physical geodesy (Hofmann-Wellenhof and Moritz, 2005), and it leads to a non-unique solution. Two different ways to solve this problem are common: forward and inverse modeling methods. In case of forward modeling approaches, the interior density distributions and layers are preliminary assumed in an a-priori model, from which the resulting gravity effect is computed. After comparison with actual observation data, the density model is iteratively modified until synthetic and measured values match (Ebbing et al., 2001).

The second class of approaches is the direct inversion of gravimetric data, which in its simplest version is based on a two-layer model with a constant density contrast and a mean Moho depth, which serve as boundary conditions to circumvent the non-uniqueness of the inverse gravimetric problem. The solution in the Fourier domain using planar approximation is known as Parker-Oldenburg algorithm and is used in various studies, like Prasanna et al. (2013), Steffen et al. (2011), or Shin et al. (2007). Based on the Vening Meinesz isostatic concept, Moritz (1990b) formulated the derivation of Moho depths from isostatic gravity anomaly data in global spherical approximation. This approach was further developed by Sjöberg (2009), solving the inverse problem by means of integral equations. This approach was applied and refined in several studies, for instance in Bagherbandi and

Sjöberg (2011) or Bagherbandi and Tenzer (2013). Bagherbandi (2011) investigated its application to Moho estimation with GOCE-type SGG data on regional basis for Scandinavia and Iran. An alternative approach for the derivation of the global Moho based on the inversion of GOCE data and a preliminary seismic model CRUST2.0 (Bassin et al., 2000) using spectral Wiener methods was introduced by Reguzzoni et al. (2013), with a regional application given in Sampietro et al. (2014). Recently, Barzaghi and Biagi (2014) published some first results of a closed loop simulation of a collocation approach in planar approximation. This method was investigated for a regional area and combined simulated terrestrial gravity anomalies and seismic depths.

In this thesis, a different approach using the GOCE SGG data in the spatial domain utilizing the LSC method is developed. Similar to most of the studies mentioned above, this concept is based on the simplified two-layer isostatic model of the Airy-Heiskanen type (Figure 8.2), with the hydrostatic equilibrium relation over continental areas, which was already introduced in Eq. (4.38)

$$\Delta\rho\, t_i = \rho_c\, h_i \,,$$

which is relating the topographic load of a mass column with height h_i to the depth t_i, the measure of how deep the crust is sinking into the mantle material as a consequence of the load. Implicitly, there are already two basic assumptions included in Eq. (4.38), which are the requirement to obtain a unique solution of the following inversion procedure. First, we consider the densities of the crustal material ρ_c above the separating Moho surface as well as the mantle material ρ_m below the Moho to be constant. Consequently, the density contrast $\Delta\rho = \rho_m - \rho_c$ is also a fixed value. Second, we interpret the depths t_i as variations with respect to some mean crustal thickness D, which is again an a-priori assumption.

Using this isostatic concept, we can furthermore set up the following hypothesis: Since we assume that there is, apart from the lateral variations due to the Moho, a homogeneous density distribution in the Earth's interior, the external gravity field is only varying due to the changing topographic masses and the corresponding isostatic compensation. As the GOCE observations take place in the exterior space at about 250 km height, we could also consider the underlying atmospheric masses, although this contribution will be only of minor importance. If we then reduce the gravitational effects of topographic and atmospheric masses from the gravity observations, we obtain a residual gravity field which should only reflect the remaining isostatic compensation effect and thus provide the information about the Moho variations.

Next, let us imagine that this residual gravity field can also be interpreted as the result of the residual potential of a single surface layer according to Heiskanen and Moritz (1967)

$$T = G \iint_S \frac{\rho_s}{l}\, \mathrm{d}S \tag{8.1}$$

in which ρ_s is the surface layer density, G the gravitational constant, l is the distance, and S a distinct closed surface of thickness zero. The surface layer density is therefore a quantity with the unit $[\mathrm{kg\,m^{-2}}]$, i.e. mass per area. If we choose the surface S to coincide with the

mean Moho at depth D, then the relation

$$\Delta\rho\, t_i = \rho_s \,, \tag{8.2}$$

can be formulated, from which finally the Moho depth variations can be derived by a simple division of surface layer density by constant density contrast

$$t_i = \frac{\rho_s}{\Delta\rho} \,. \tag{8.3}$$

The integral Eq. (8.1) of the residual (or disturbing) potential T can be solved in spherical approximation as shown in Heiskanen and Moritz (1967), leading to

$$T = \frac{2\,R}{3}\left(2\pi G\rho_s - \Delta g\right) \,. \tag{8.4}$$

The substitution of the gravity anomaly Δg with its equivalent in spherical approximation of a sphere with radius R given by the fundamental equation of physical geodesy (Eq. (2.79)) leads to

$$T = \frac{2\,R}{3}\left(2\pi G\rho_s + \left.\frac{\partial T}{\partial r}\right|_{r=R} + \frac{2}{R}T\right) \,, \tag{8.5}$$

from which we can solve for the surface layer density ρ_s and get

$$\rho_s = -\frac{1}{4\pi G}\left(2\,\left.\frac{\partial T}{\partial r}\right|_{r=R} + \frac{T}{R}\right) \,. \tag{8.6}$$

This is the linear operator relating the surface layer density to the disturbing potential.

8.2.1 Covariance propagation of surface layer density and other gravity quantities

With the relationship given in Eq. (8.6) it is now possible to perform the covariance propagations according to Eq. (3.13), which lead to the necessary expressions for the covariances between surface layer density quantities and other gravity quantities. In the sequel, some of the covariance expressions are derived in the same fashion as in section 3.3. Additionally, the formulas according to the method introduced in section 3.7 are provided.

The covariance between the surface layer density ρ_s at a point P and a geoid height N in point Q can be described by

$$cov(\rho_s, N') = -\frac{1}{4\pi G}\left(2\,\frac{\partial}{\partial r} + \frac{1}{r}\right)\,\frac{K}{\gamma_0'} \equiv -\frac{1}{4\pi G\,\gamma_0'}\left(2\,D_{3000} + \frac{D_{0000}}{r}\right) \,, \tag{8.7}$$

with K representing the covariance function, γ_0 is the normal gravity at Q and D is the matrix containing all covariances up to the second order derivatives of the disturbing potential according to section 3.7.

If we are interested in the covariance between the surface layer density in P and a gravity anomaly Δg in Q, the following derivation is necessary:

$$\begin{aligned} cov(\rho_s, \Delta g') &= -\frac{1}{4\pi G}\left(2\,\frac{\partial}{\partial r}+\frac{1}{r}\right)\left(-\frac{\partial K}{\partial r'}+\frac{2\,K}{r'}\right) \\ &= \frac{1}{4\pi G}\left(2\,\frac{\partial^2 K}{\partial r \partial r'}+\frac{4}{r'}\frac{\partial K}{\partial r}+\frac{1}{r}\frac{\partial K}{\partial r'}+\frac{2}{rr'}K\right) \\ &\equiv \frac{1}{4\pi G}\left(2\,D_{3030}+\frac{4}{r'}D_{3000}+\frac{1}{r}D_{0030}+\frac{2}{rr'}D_{0000}\right)\,. \end{aligned} \tag{8.8}$$

The covariance between two surface layer densities, one in point P and the other in Q, is given by

$$\begin{aligned} cov(\rho_s, \rho_s') &= \frac{1}{16\pi^2 G^2}\left(2\,\frac{\partial}{\partial r}+\frac{1}{r}\right)\left(2\,\frac{\partial K}{\partial r'}+\frac{K}{r'}\right) \\ &= \frac{1}{16\pi^2 G^2}\left(4\,\frac{\partial^2 K}{\partial r \partial r'}+\frac{2}{r'}\frac{\partial K}{\partial r}+\frac{2}{r}\frac{\partial K}{\partial r'}+\frac{1}{rr'}K\right) \\ &\equiv \frac{1}{16\pi^2 G^2}\left(4\,D_{3030}+\frac{2}{r'}D_{3000}+\frac{2}{r}D_{0030}+\frac{1}{rr'}D_{0000}\right)\,. \end{aligned} \tag{8.9}$$

In order to compute the covariance between surface layer density at point P and a vertical gradient $T_{z'z'}$ in point Q one has to implement the relation

$$\begin{aligned} cov(\rho_s, T_{z'z'}) &= -\frac{1}{4\pi G}\left(2\,\frac{\partial}{\partial r}+\frac{1}{r}\right)\frac{\partial^2 K}{\partial r'^2} = -\frac{1}{4\pi G}\left(2\,\frac{\partial^3 K}{\partial r \partial r'^2}+\frac{1}{r}\frac{\partial^2 K}{\partial r'^2}\right) \\ &\equiv -\frac{1}{4\pi G}\left(2\,D_{3033}+\frac{D_{0033}}{r}\right)\,. \end{aligned} \tag{8.10}$$

Similarly, the covariance between surface layer density in P and the gradient in East direction in point Q is given by

$$cov(\rho_s, T_{y'y'}) \equiv -\frac{1}{4\pi G}\left(2\,D_{3011}+\frac{D_{0011}}{r}\right)\,, \tag{8.11}$$

and the covariance related to gradient in North direction by

$$cov(\rho_s, T_{x'x'}) \equiv -\frac{1}{4\pi G}\left(2\,D_{3022}+\frac{D_{0022}}{r}\right)\,. \tag{8.12}$$

Hence, the generalized formulation for covariances between surface layer densities and gravity gradients can be written as

$$cov(\rho_s, T_{ij}) \equiv -\frac{1}{4\pi G}\left(2\,D_{30ij}+\frac{D_{00ij}}{r}\right), \quad \ldots i = \{1,2,3\},\; j = \{1,2,3\}\,, \tag{8.13}$$

where the indices $i, j = 1, 2, 3$ indicate a derivative with respect to y', x', z'. In the case that P and Q are interchanged, the corresponding expression can be derived by interchanging the subscripts nm with ij in D_{nmij} as well as the radii r and r'.

8.3 Data and models for Moho computation

In order to obtain Moho depth estimates from GOCE gravity gradients based on the previously proposed LSC approach, it is necessary to reduce the gravitational effects of the topography and atmosphere from the observations. As explained in section 8.2, in this way the Moho can be related to the variations of the residual gravity field expressed as surface layer densities. The topographic and atmospheric models are introduced in section 8.3.1, with an investigation on the necessary degree of reduction. The GOCE data used for this study is briefly described in section 8.3.2. As test area, the central European region between 5° to 22° East and 42° to 52° North is selected for these investigations. Thus it includes the Austrian country as well as its surrounding regions. With this choice, some interesting geophysical and tectonic features in Europe are expected to be revealed, which are discussed in detail in section 8.5.

8.3.1 Topographic and atmospheric effects

First, the effect of the atmospheric masses on the GOCE gradients observations is investigated. For this reason, the ITSG atmospheric potential model derived in section 4.2, which is based on the global GTOPO height data set, is used to estimate the impact on V_{zz} vertical gradients at a mean altitude of 250 km. As one can see from Figure 8.3a, the total impact from spherical harmonic D/O 0 to 360 leads to variations of 1 to 2 mE. However, during the preprocessing of the gradient observations, the long-wavelength constituents will already be reduced up to a specified å9, see section 8.3.2. The remaining atmospheric effect from D/O 50 to 360 is illustrated in Figure 8.3b. Obviously, the amplitude is varying in a very small range of about ±0.2mE, which is well below the remaining measurement noise after the filtering of the gradient observations. For this reason, the effect of the atmospheric masses does not necessarily have to be considered in this study and is therefore neglected in the sequel.

For the reduction of the topographic mass effect the Rock-Water-Ice (RWI) model is used in this study. This potential model was developed by Grombein et al. (2014) and is published in terms of a spherical harmonics series representation up to D/O 1800. Based on the DTM2006.0 digital terrain model, the Earth's topography is classified in rock, water and ice mass layers with individual density values. From these data the global topographic potential model RWI_TOPO_2012 is derived by means of forward modeling using tesseroid bodies (Grombein et al., 2013) and then transformed into spherical harmonics coefficients. Apart from the topographic potential model, also an isostatic as well as a combined topographic-isostatic model is provided. The underlying isostatic concept is based on a modified Airy-Heiskanen approach incorporating preliminary Moho depth and crust-mantle density contrast information from the CRUST2.0 model (Bassin et al., 2000). For the current application, only the topographic potential model is of interest, since we want to preserve the information on isostatic effects in the GOCE gradient data. All models can be accessed via the ICGEM website `http://icgem.gfz-potsdam.de/ICGEM/`. To verify the impact of the topography on the gravity gradients at orbital height, the vertical gradients V_{zz} in the LNOF are evaluated from the RWI model at a mean altitude of 250 km for different spherical degree ranges starting at the chosen D/O 50.

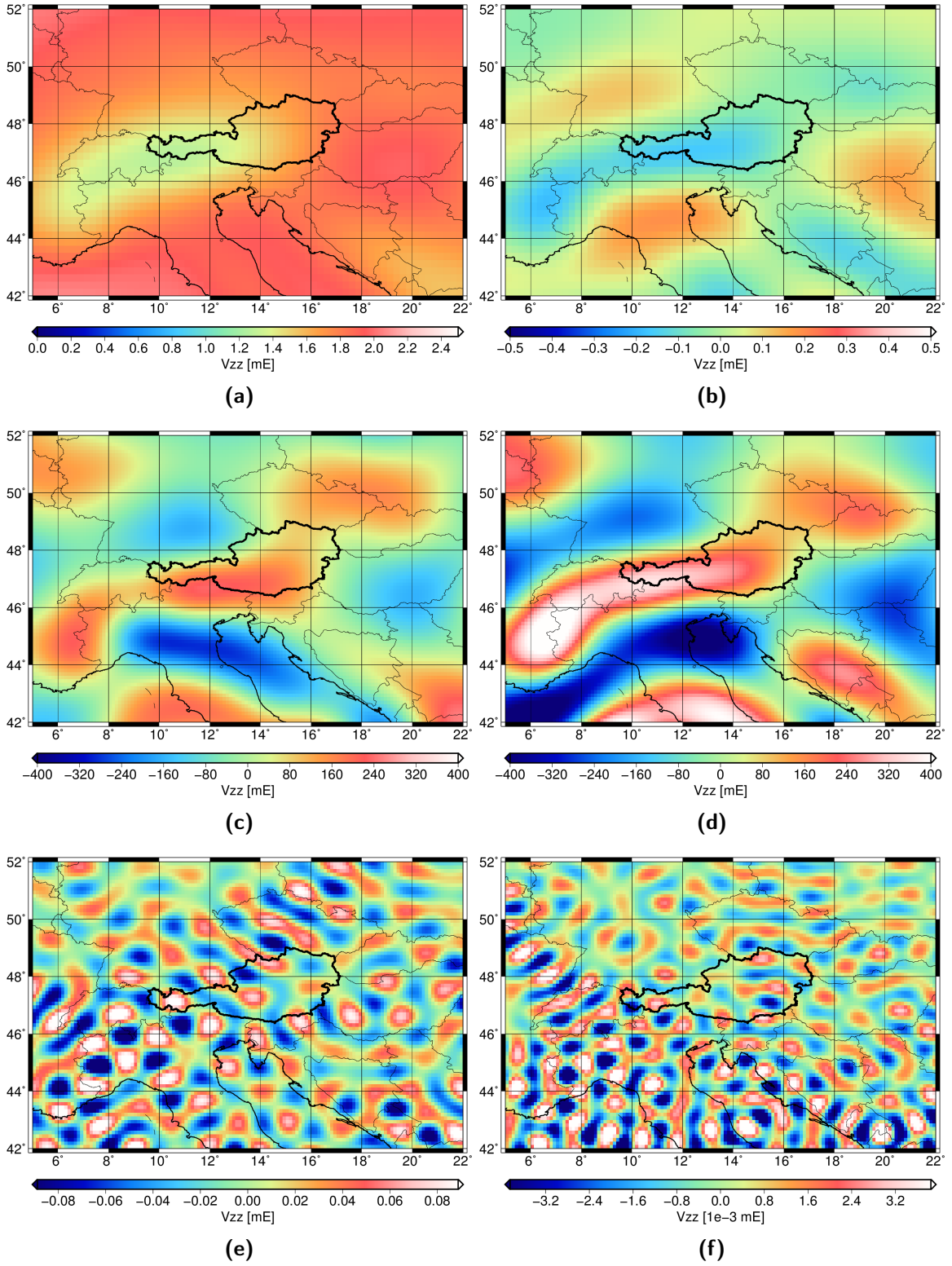

Figure 8.3: Simulated vertical gradients V_{zz} at mean altitude 250 km in the LNOF based on: the ITSG atmospheric potential model from D/O 0 to 360 (a) and D/O 50 to 360 (b); the GOCE_TIM_RL05 model from D/O 50 to 280 (c); the RWI topographic potential model from D/O 50 to 280 (d), D/O 281 to 360 (e) and D/O 361 to 1800 (f)

The results are illustrated in Figure 8.3d to Figure 8.3f. For a comparison with the gravity signal that can be expected at such heights, the vertical gradients are also computed from the GOCE_TIM_RL05 model between D/O 50 and the maximum available D/O 280 and shown in Figure 8.3c. The comparison of Figure 8.3c and Figure 8.3d highlights that the expected gravity signal is actually smaller than the topographic signal, since the topography is isostatically compensated to a considerable extent. Evaluating the topographic effect at GOCE altitude in the spectral range D/O 281 to 360, the signal content drops to around ±0.15mE, shown in Figure 8.3e. The signal amplitude is further decreasing to some micro-Eötvös in the range between D/O 361 to 1800, see Figure 8.3f, which confirms that the GOCE measurement system is not sensitive for higher frequency topographic signals at satellite altitude. Since the remaining measurement noise after the filtering of the real gradient observations can be expected to be in the order of a few milli-Eötvös, a reduction of the topographic mass effect from D/O 50 up to 360 can be considered as sufficient for our purposes.

8.3.2 GOCE gradient data

The GOCE EGG_NOM_2 products are used for the derivation of Moho depths in this thesis, which are given in the GRF, see section 5.4.1. To reduce the noise, filtering methods as described in section 6.2 are applied. Due to the measurement configuration, the GOCE gradiometer instrument is only able to deliver precise observations from frequencies between 5 to 100 mHz (see section 5.2 or chapter 6). According to Eq. (6.22) this can be approximately converted into a spherical harmonic degree range from D/O 27 to 540. One of the key questions therefore is, to which D/O the long-wavelength information of gradient data should be reduced. Torge (1989) states that variations in the mantle structure effects the gravity field up to D/O 30, while lithospheric influences dominate from D/O 30 to 180, and shorter wavelength effects origin merely from crustal inhomogeneities. Lambeck (1988) mentioned that gravity anomalies predicted from convections in the asthenosphere could have wavelengths in the order of 500 km and longer, which corresponds to D/O 40. Kuhn and Featherstone (2006) expect that differences between their synthetic Earth gravity model and observed gravity are stemming from unmodeled mantle effects between D/O 10 and 100.

Based on this background information, for this study the choice to use gravity gradients from D/O 50 onwards is made. In this way, it should be guaranteed that the Moho depths calculated herein are the result of the isostatic compensation process of crust and mantle, and that possible influences of anomalies deeper in the Earth's interior are reduced as much as possible. Hence, the gradient data can be expected to contain gravity information between the spectral range according to D/O 50 and 280, which is the highest resolvable frequency according to the latest GOCE_TIM_RL05 global gravity field model based on solely GOCE data (Pail et al., 2011). In the spatial domain, this corresponds to resolvable wavelengths between 70 to 400 km. However, the reduction of the long-wavelength signal also implies, that the Moho depths derived from this inversion do not result in absolute values. Instead, they are also restricted to the corresponding spectral signal content from D/O 50 to 280, which requires the restoration of the missing signal from other sources, see the discussions in section 8.4 or section 8.6.

Six months of gradient data, from November to December 2009 and April to June 2010, were selected to be the basis for the Moho inversion. This choice was made in order to keep the computational efforts manageable, but still assuring a good data coverage in the

study area. Due to some hardware problems of the GOCE satellite in February and March 2010, these two months were intentionally not considered. After a preprocessing phase, the topographic effect based on the RWI topographic potential model (see previous section) has been reduced from the gradients in the GRF from D/O 50 to 360. Furthermore, the main diagonal components of the gradient tensor V_{xx}, V_{yy} and V_{zz} at a sampling rate of 5 s have been selected as observations in the investigation area. This results in an input dataset of 8294 observation stations for each of the three gradient tensor components, as illustrated in Figure 8.4, which leads to 24882 observations in total.

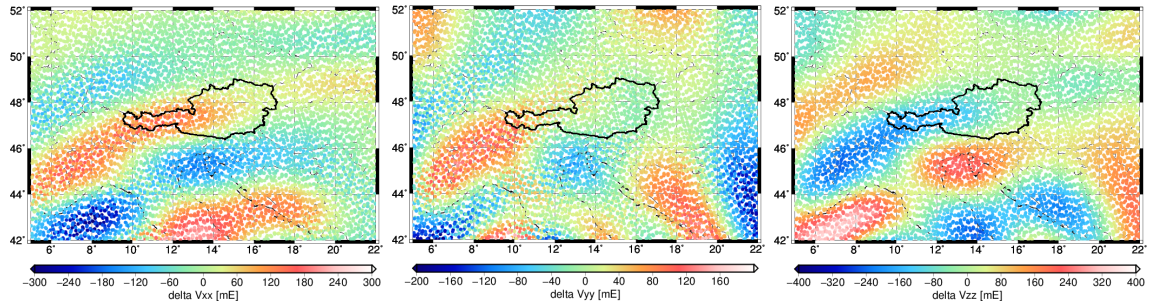

Figure 8.4: Six months of GOCE gravity gradient input data for Moho inversion reduced by gravity effects from the RWI topographic potential model. V_{xx} (left), V_{yy} (middle) and V_{zz} (right) gradient tensor components in the GRF (signal content below D/O 50 removed)

8.4 Moho computation and results

For the inversion of the GOCE gradient data into Moho depths, two basic assumptions have to be made in order to obtain a unique solution as discussed in section 8.2. On the one hand, the problem is defined in a way that we can calculate Moho variations w.r.t. to an a-priori chosen mean Moho depth D. On the other hand, we assume a constant density contrast $\Delta\rho$ between crust and mantle for the final conversion of the estimated surface density values ρ_s into Moho depth variations. Frequently used global average values, which can be found, e.g., in Hofmann-Wellenhof and Moritz (2005), are 30 km for the reference Moho depth D and 600 kg m^{-3} for the density contrast $\Delta\rho$.

In this study, we concentrate on the central European region between 5° to 22° East and 42° to 52° North, so realistic values for D and $\Delta\rho$ might be different from the global averages. Ebbing et al. (2001) proposed to use 350 kg m^{-3} and 30 km for gravity inversion processes in the Eastern Alps region in order to be consistent to seismic profile observations made within the research project TRANSALP. In Simeoni and Brückl (2009) similar values of 300 kg m^{-3} and 33 km were used for studying the gravity effect of the upper crust on the Moho discontinuity in the Eastern Alps and surrounding regions. In an earlier study investigating the crustal thickness in the Swiss Alps, Kahle et al. (1976) found an average density contrast of 330 kg m^{-3} which was derived from a seismic Moho varying between 30 to 58 km. Based on this information, the values to be used in the current study are defined as D=30 km for the mean Moho depth and $\Delta\rho$=350 kg m^{-3} for the average constant density contrast.

The surface layer densities ρ_s are estimated on a $1/8° \times 1/8°$ grid at the assumed mean Moho depth D=30 km. The calculation of these estimates with the LSC method is performed according to the solution strategy 1 as proposed in section 6.3. For the modeling of the covariances between the gradient observations and the surface layer density signals to be estimated, a covariance function equivalent to Eq. (3.33) for D/O 50 to 280 was used with a Bjerhammar radius set to R=6333 km. The corresponding degree variances k_n were derived as shown in Eq. (3.32), using the spherical harmonic coefficients differences between the GOCE_TIM_RL05 global gravity field model and the RWI topographic potential model. The stochastic behaviour of the remaining measurement noise is accounted for by introducing the error-covariance function that was obtained during the gradient data preprocessing and filtering, see chapter 6. The resulting surface layer densities are finally converted to Moho depth variations using the previously defined constant density contrast $\Delta\rho$=350 kg m^{-3}. In Figure 8.5, the Moho depth variations w.r.t. to the mean depth of D=30 km are shown on the left.

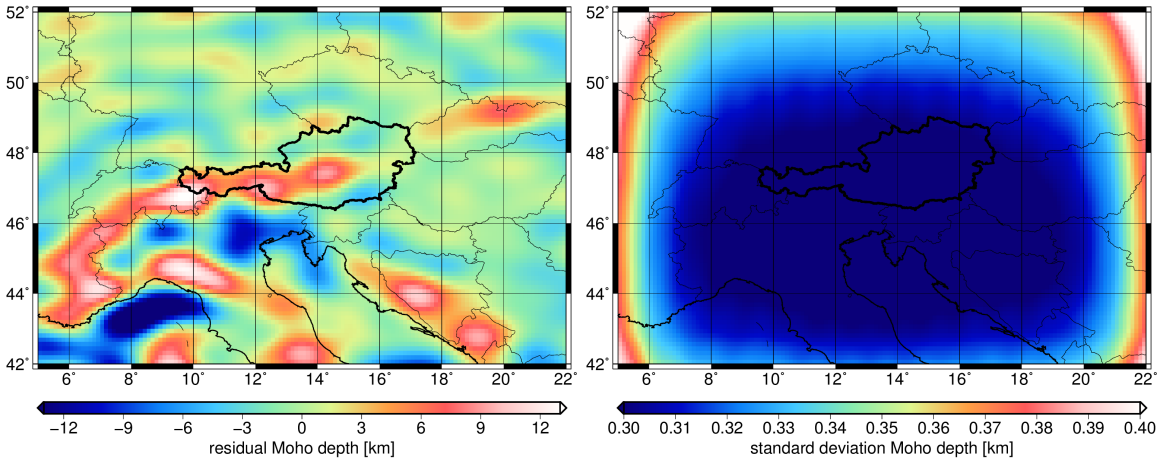

Figure 8.5: Moho depths (left) and standard deviations (right) estimated in the spectral range from D/O 50 to 280 based on the LSC approach

The resulting signal shows a high degree of correlation with the main topographic structures in the investigated area. Since this study is based on the Airy-Heiskanen isostatic concept, which directly relates the topography to the penetration depth of the crust into the mantle, this is the expected outcome. Nevertheless, the revealed Moho signal is not only due to the topographic load, but can also be associated to other geophysical phenomena. Since this will be investigated in detail in section 8.5, further interpretations will not be given at this place.

The amplitude of the estimated Moho variations in Figure 8.5 ranges from −19.9 km to 13.5 km, which would imply a Moho depth of 10.1 km to 43.5 km. However, these calculations do not contain the long-wavelength signal content below D/O 50 due to the reasons mentioned already in section 8.3.2, so an essential amount of signal is not included in these values. A restoration of this signal content could theoretically be performed using an accurate global gravity field model. This option is intentionally not considered in this study, since it bears a potential risk to introduce disturbing gravity signals, for instance due to mantle anomalies, which would have to be accounted for prior to the Moho inversion.

Finally, the error estimates obtained from the LSC process is illustrated in Figure 8.5 on the right. The estimated standard deviations lie between 0.3 km in the central parts of the study area and 0.4 km at the borders, where the usual edge effects of the LSC prediction methods occur. Again, these values must not be seen as absolute values due to the missing long-wavelength information, but are only valid for the estimate in the spectral range between D/O 50 to 280.

A critical factor in the Moho inversion process is the choice of the a-priori assumptions for the mean Moho depth D and the constant density contrast $\Delta\rho$. As mentioned in the beginning of this section, these parameters initially have been set to D=30 km and $\Delta\rho$=350 kg m^{-3} based on empirical values from previous geophysical studies. In order to investigate the impact of these assumptions, an additional numerical study is performed with different values used for these constant parameters. In this way, the variations of the estimated Moho depths in dependence of the a-priori assumptions can be assessed. The first scenario is based on the constant mean Moho depth D=30 km but uses different density contrasts of $\Delta\rho$=330 kg m^{-3} and $\Delta\rho$=370 kg m^{-3}, respectively. In the second scenario, the density contrast is set to $\Delta\rho$=350 kg m^{-3}, however the mean Moho depth is chosen to be D=29 km and D=31 km. The resulting differences w.r.t. the Moho estimate with the initial values as illustrated in Figure 8.5 are shown in Figure 8.6. The statistics of the corresponding Moho estimates from D/O 50 to 280 are summarized in the second column of Table 8.1. Additionally, the differences of the amplitude ranges between the Moho results of the empirical assumptions and the four case studies are quoted in the third column.

Table 8.1: Statistics of Moho depth estimates in the spectral range from D/O 50 to 280 with different assumptions for D and $\Delta\rho$, and differences w.r.t. the result based on the a-priori empirical values

Parameters		**Statistics**			**Differences**	
D	$\Delta\rho$	min	max	rms	min	max
[km]	[kg m^{-3}]	[km]			[km]	
30	350	-19.9	13.5	3.9		
30	330	-21.1	14.3	4.2	−1.2	0.8
	370	-18.8	12.7	3.7	1.1	−0.7
29	350	-19.4	13.1	3.8	0.5	−0.4
31		-20.4	13.8	4.0	−0.5	0.4

The comparison shows, that a decrease in the assumed density contrast by 20 kg m^{-3} leads to an amplification of the resulting residual Moho depth in dependence of the amplitude of the estimated surface density, see Figure 8.6a. The amplification amounts to −1.2 km w.r.t. the initial minimum value of −19.9 km and further 0.8 km for the maximum residual Moho depth of 13.5 km. In contrast, an increased density contrast of 370 kg m^{-3} implies a damping of the Moho amplitudes by 1.1 km and −0.7 km in the extreme values, which is illustrated in Figure 8.6b.

If the density contrast for the Moho inversion remains the same compared to the initial assumptions, but the mean Moho depth for the evaluation of the surface density is changed from D=30 km to D=29 km, the Moho signal is again attenuated, see Figure 8.6c. The

initial minimum value is increased from −19.9 km to −19.4 km, while the maximum amplitude is reduced from 13.5 km to 13.1 km. The inverse behaviour can be observed, if the evaluation depth is lowered to D=31 km. This leads to a gain in the Moho signal amplitudes as depicted in Figure 8.6d, with an amplification of the extreme values in the order of 0.5 km.

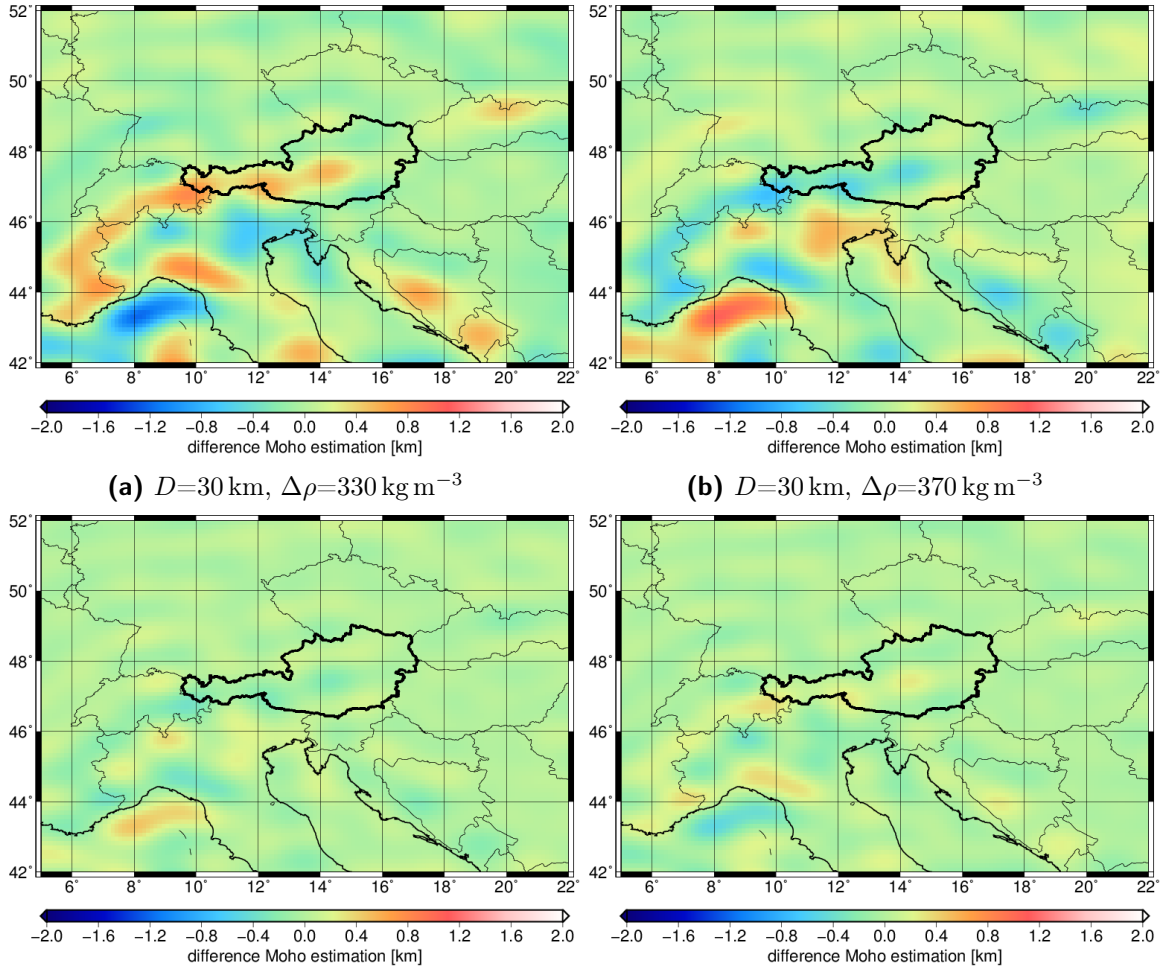

(a) D=30 km, $\Delta\rho$=330 kg m^{-3} **(b)** D=30 km, $\Delta\rho$=370 kg m^{-3}

(c) D=29 km, $\Delta\rho$=350 kg m^{-3} **(d)** D=31 km, $\Delta\rho$=350 kg m^{-3}

Figure 8.6: Differences between the Moho estimate with D=30 km and $\Delta\rho$=350 kg m^{-3} and Moho estimates based on different assumptions for D and $\Delta\rho$ in the spectral range from D/O 50 to 280

Summarizing, the investigation shows that the assumptions for the density contrast $\Delta\rho$ and the mean Moho depth D have to be chosen carefully, as they directly influence the result of the surface density estimation and the consecutive Moho inversion. In the region under investigation, an uncertainty of ±20 kg m^{-3} in the choice of $\Delta\rho$ results in variations of the Moho in the order of ±1.2 km. A different assumption of the mean Moho depth by ±1 km would affect the Moho result approximately by ±0.5 km. As already stated, for the selected European region $\Delta\rho$ and D are chosen according to realistic empirical values from seismic studies. The justification of the a-priori values will be verified by a thorough validation of the obtained Moho results with external models in the next section.

8.5 Validation and interpretation of the Moho estimates with other sources

The results obtained in the previous section show reasonable features and amplitudes of the Moho estimates within the spectral range from D/O 50 to 280. However, an evidence about correctness and soundness of the results can only be achieved by validation with other data sources. In this section, the estimated Moho is verified by a comparison with three different independent external Moho models, which are publicly available and cover the investigated region. Two models are primarily based on seismic data sets, while the other model is also estimated from GOCE data with some seismic information used as background input. The models are summarized in the following section 8.5.1. In the beginning of section 8.5.2, the different models are first compared with regard to their signal characteristics and statistics. Their distinct features will then be analyzed considering the geological and tectonic setting in the investigated region. Finally, the Moho of selected areas will also be compared with the results of recent other studies.

8.5.1 External Moho models

The GEMMA1.0 model

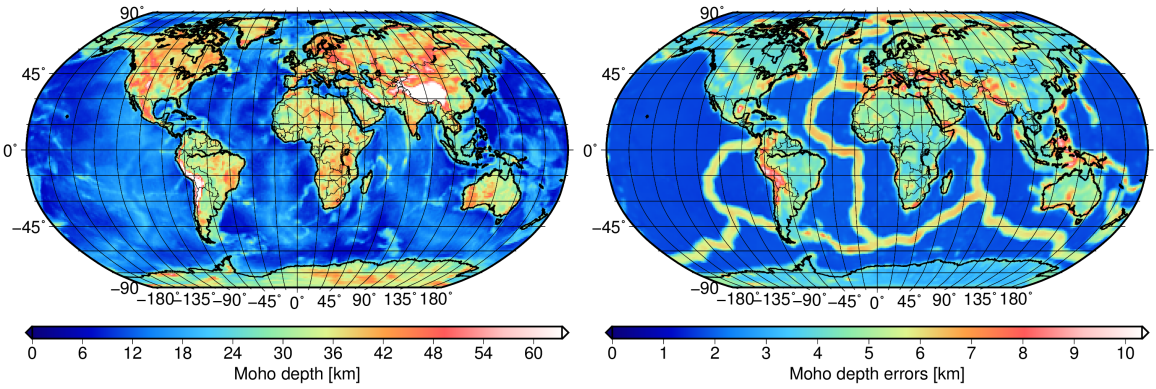

Figure 8.7: GEMMA1.0 Moho depths (left) and estimated standard deviations (right)

The GEMMA1.0 global crustal model is developed within the ESA-funded project GOCE Exploitation for Moho Modeling and Applications (GEMMA). A first release was described in Reguzzoni et al. (2013), while the latest and currently available updated model is discussed in Reguzzoni and Sampietro (2014). A local study in the Himalayan region was performed by Sampietro et al. (2014). This GEMMA1.0 model is based on a gravimetric inversion algorithm of GOCE data and incorporates also a-priori information of the crustal structures and seismic features.

The inversion uses the concept of Wiener deconvolution in the spectral domain and resolves the Moho up to spherical harmonic D/O 210 (Reguzzoni et al., 2013). The gravitational potential as well as radial GOCE gradients grids, which are derived within the

GOCE space-wise approach of the HPF processing chain (see section 5.4.3), serve as input observations in order to deduce the residual Moho variations with respect to a mean reference depth. The final Moho depths are obtained by an iterative procedure of Moho inversion and re-estimation of constraining parameters like mean Moho depth or radially varying crustal density (Reguzzoni and Sampietro, 2014). The global Moho map is publicly available through the web page `http://gocedata.como.polimi.it` as $0.5° \times 0.5°$ ASCII grid and is illustrated in the left plot of Figure 8.7. The GEMMA1.0 Moho model is also accompanied by corresponding error estimates in terms of standard deviations, which are estimated from the combined effect of the a-priori Moho model and the GOCE data errors (Reguzzoni et al., 2013). The global standard deviation for this model is found with 1.7 km, with maximum amplitudes reaching up to 10 km, see Figure 8.7 on the right. These large values can be found in particular at tectonic plate boundaries or for example in the Andes or Himalayan region, and are ascribed to an insufficient modeling of actual density anomalies in these areas.

The ESC model

In 2009, Grad et al. (2009) compiled the first Moho depth map covering the whole European plate, which was a joint project of a dedicated European Seismological Comission (ESC) working group and will therefore be called ESC model. Prior to this date, only rough global models of $5° \times 5°$ or $2° \times 2°$ resolution were available for the continental-wide perspective of the Moho structure. The ESC model is a compilation of numerous seismic data sets and different local and regional Moho maps based on seismic and/or gravimetric observations. The ESC Moho depth map was generated by building 10×10 km block averages out of the various data, and finally was low-pass filtered with 100 km half wavelength. The final map is available online via `http://www.seismo.helsinki.fi/mohomap/` and is also provided in ASCII format in the range between $-41°$ to $71°$ East and $27°$ to $87°$ North with a resolution of $0.1° \times 0.1°$, which is shown in Figure 8.8a. Additionally, the ESC Moho map comes along with uncertainty estimates illustrated in Figure 8.8b, which are depending on the type of the data source and are specified between 3 to 6 km. In particular regions, the standard deviations exceed this range and can even reach 10 km.

The EPcrust model

One further regional Moho model publicly available is the EPcrust model. It was published by Molinari and Morelli (2011) and covers the region between $-40°$ to $70°$ East and $20°$ to $90°$ North with a grid size of $0.5° \times 0.5°$. The EPcrust model is a crustal model for the European plate, which distinguishes between a sediment layer as well as an upper and a lower crustal layer. For each layer, the density values are provided together with seismic P- and S-wave velocities and depth information at each grid point. Besides these quantities, topography, ice layer thickness and Moho depth can be extracted from the model, which is available online via `http://bo.ingv.it/eurorem/EPcrust`. Similar to the ESC model, EPcrust is a compilation of several sources, which are homogenized in terms of a consistent spatial resolution of $0.1° \times 0.1°$. As such it also incorporates the ESC model and can therefore be regarded as its successor. The final values are derived by forming a weighted mean of the available data for each grid point and a consecutive Gaussian filtering with 60 km half-wavelength resolution.

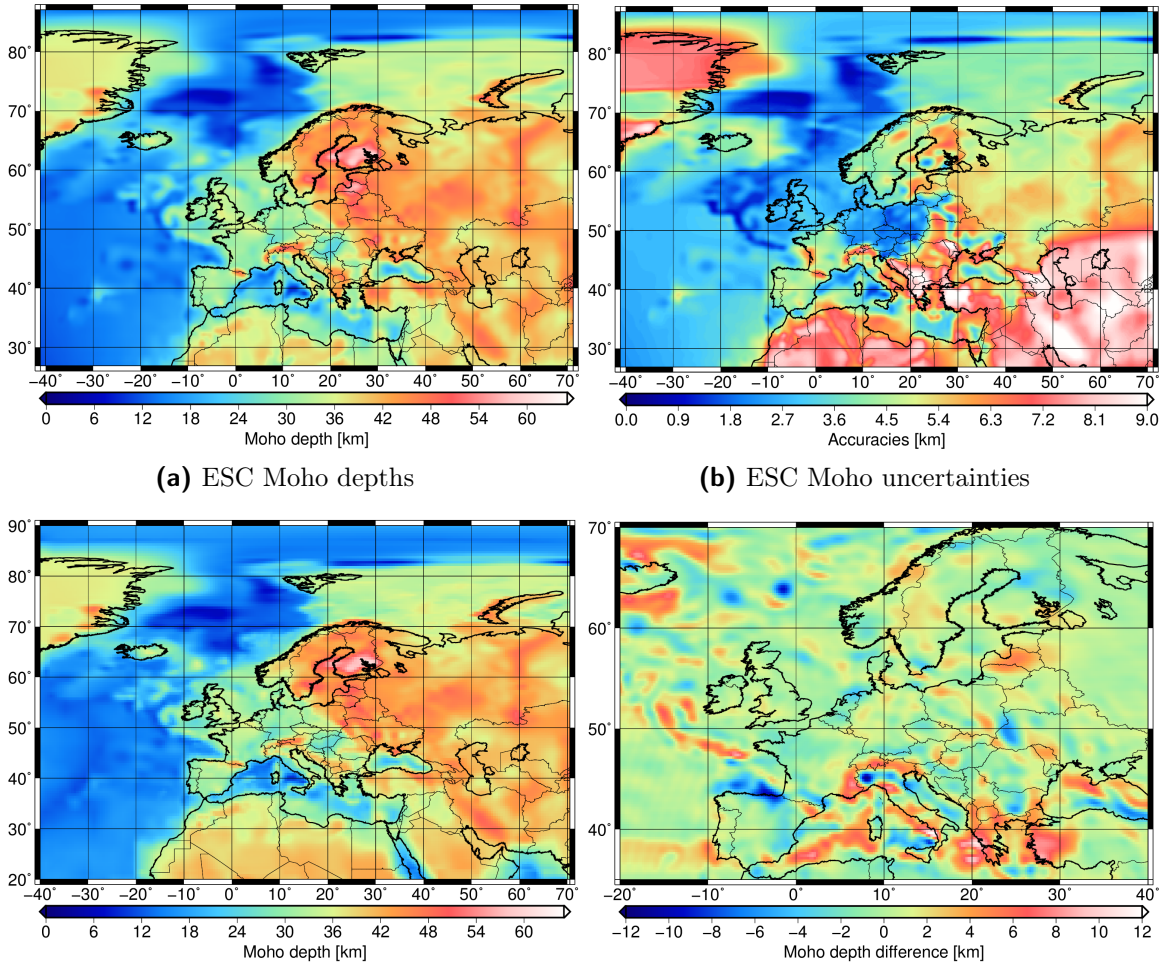

(a) ESC Moho depths

(b) ESC Moho uncertainties

(c) EPcrust Moho depths

(d) Difference between ESC and EPcrust Moho depths

Figure 8.8: The ESC Moho depths (a), ESC Moho uncertainties (b), EPcrust Moho depths (c) and differences between both models (d)

The distributed $0.5° \times 0.5°$ Moho depth map is illustrated in Figure 8.8c. In contrast to the ESC model, no accuracy information is provided. Instead, the variability of the Moho from different data sources is discussed in Molinari and Morelli (2011), which can be in the order of 10 km. In order to assess the consistency of the Moho models, the difference between ESC and EPcrust is illustrated in Figure 8.8d for the region between $-20°$ to $40°$ East and $35°$ to $70°$ North. The deviations between the two models can amount up to 12 km and highlight that the currently available models have large discrepancies.

8.5.2 Validation and interpretation

A direct comparison between the Moho calculated herein and the external models can not be performed straightforward for mainly two reasons. First, as we have seen in the previous section 8.5.1, the external models have varying spatial and also spectral resolutions. Second, the GOCE gradient data used for the present computations were reduced by the long-wavelength constituents of the gravity signal up to D/O 49, see section 8.3.2. Therefore, the three external Moho maps were converted in corresponding sets of spherical harmonic coefficients up to D/O 360 by spherical harmonic analysis. This corresponds to the spatial resolution of $0.5° \times 0.5°$, with which the GEMMA1.0 and EPcrust models are provided. Although the ESC model is nominally available with a considerable higher resolution of $0.1° \times 0.1°$, the expected spectral signal content due to the 100 km low-pass filtering is only in the order of D/O 200. Hence, a spherical harmonics decomposition to D/O 360 will be sufficient to preserve the model signal content.

For a better visual comparison, the estimated Moho depth variations w.r.t. to the mean Moho depth D =30 km are once more shown in Figure 8.9a and will be denoted as ITSG model in the sequel. The Moho depths of the external models GEMMA1.0, ESC and EPcrust are also recomputed as residuals against the average depth D =30 km in Figure 8.9b to Figure 8.9d. During the spherical harmonics synthesis, the long-wavelength signal content below D/O 50 is omitted in order to achieve consistency with the ITSG Moho variations. In this context is has to be emphasized that this validation is not aiming at the analysis of absolute Moho depths, but it is only valid for the Moho signal constituents between D/O 50 and the according maximum resolution of the models. This fact does not necessarily have to be regarded as a drawback. Instead, more regional features of the Moho variations can be observed and even be linked to geophysical and tectonic features more easily, as we will see in the following interpretations.

The first visual comparison between the ITSG Moho model and the other models in Figure 8.9 reveals that ITSG model obviously resolves the Moho signal at slightly finer spatial scales. This can be explained by the different techniques and input data for the generation of the Moho maps. The presented estimation is based on GOCE gradient data, which we assume to contain potential gravity signals up to D/O 280. A significant signal content until D/O 254, where the signal to noise ratio reaches 1, is proven within the computation of the latest global GOCE_TIM_RL05 model (Brockmann et al., 2014). Hence, the effective spatial resolution at which significant signals can be expected will approximately be between 70 km 80 km.

According to the processing strategy as described in Reguzzoni et al. (2013), the GEMMA1.0 model resolves the Moho up to D/O 210, which is equivalent to 95 km half wavelength. As mentioned in the previous paragraph, the ESC model is not able to reflect variations of the Moho at smaller spectral scales than D/O 200 (∼100 km) due to spatial averaging. Compared to ESC, the EPcrust model does include some more data sources with nominally higher spatial resolution. However, their laborious retracement was not performed in detail in this thesis. Since the additional data in EPcrust is also based on mainly seismic profiles and point observations, which are then combined by forming a weighted mean of all sources, it is assumed that the resulting signal content is not significantly different from the one in ESC. Looking at the signal in Figure 8.9c and Figure 8.9d confirms that the spatial variability is similar in the investigated region. Furthermore, the difference plot in Figure 8.8d does not

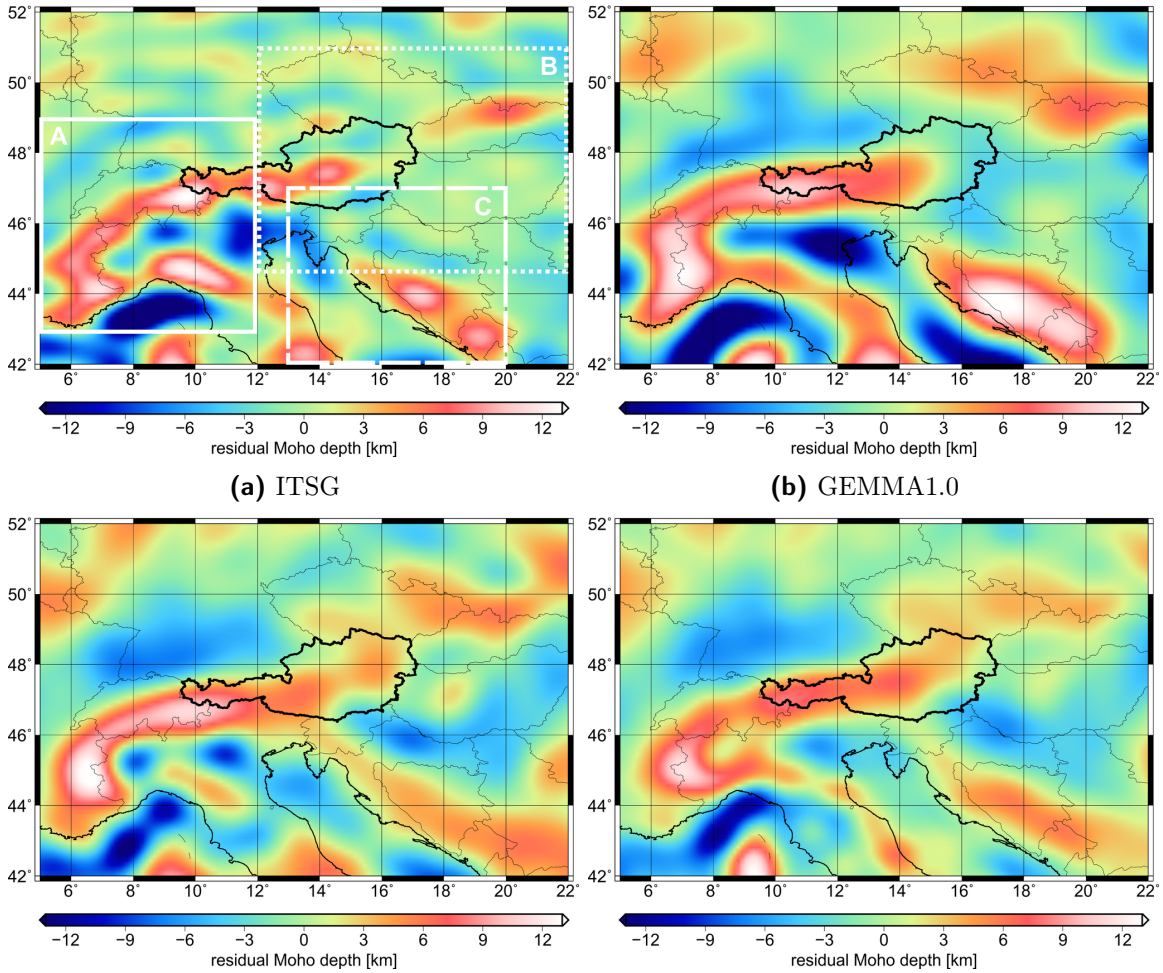

(a) ITSG **(b)** GEMMA1.0

(c) ESC **(d)** EPcrust

Figure 8.9: Comparison of Moho depth models given as variations w.r.t. the mean Moho depth D =30 km from D/O 50 onwards: ITSG model (a) with subset areas indicated by white boxes A, B and C for localized comparisons with results from Wagner et al. (2012), Molinari et al. (2012) and Stipčević et al. (2011); GEMMA1.0 model (b); ESC model (c); EPcrust model (d)

show considerable high frequency deviations between the models. Thus, also the EPcrust Moho model provides a smoothed and a little bit less detailed picture of the Moho variations compared to the ITSG model.

The statistics of the Moho variations of each model are summarized in Table 8.2. The maximum Moho depth of the ITSG model with regard to the reference depth of 30 km is in the order of 13.5 km and located in the central Alps at the Swiss border. Although this value is consistent with the maximum depths of the other models, these can be found at different locations. The GEMMA1.0 model has its maximum in the Dinarides, while the maximum of the ESC model is found in the southern Alps and the EPcrust model has its deepest residual Moho beneath Corsica. Hence, the models deviate considerably in this context. The minimum of the ITSG model is located in the Ligurian Sea and amounts to −19.9 km, which is similar to that of the GEMMA1.0 model. In contrast, the two seismic models show minima

of only −12.6 km and −13.6 km, respectively. However, the location of these extreme values is similar in all models and can be found in the Ligurian Sea. The spatial variability in terms of RMS values is comparable for all models and lies within 3.5 km and 5.1 km. Nevertheless, a comparison only based on these statistics does not lead to a meaningful conclusion about the reliability of the results.

Table 8.2: Statistics of Moho models from D/O 50 onwards (values in km)

Model	**min**	**max**	**rms**
ITSG	-19.9	13.5	3.9
GEMMA1.0	-19.1	13.7	5.1
ESC	-13.6	13.9	4.0
EPcrust	-12.6	13.1	3.5

Thus, we want to focus on the spatial characteristics of the different models. In order to validate if the results are meaningful and to verify which of the models might be more reliable in certain regions, the Moho has to be investigated by considering the geophysical and tectonic setting of the region under investigation. In Figure 8.10 the topographic and bathymetric relief based on the ETOPO1 data set (Amante and Eakins, 2010) is shown for central and South-Eastern Europe as well as for parts of the Mediterranean Sea including the Italian peninsula. In this area, three important tectonic units are located: the European plate, the Ligurian plate and the Adriatic plate. The European plate border in the South is approximately coinciding with the French coastline, then it is following the Alpine arc along the so-called Periadriatic Line until it reaches the Italian/Slovenian border, from where it continues to the South-East close to the Adriatic coastline. The Ligurian plate is located South of the European plate, with its Eastern border coinciding roughly with the Apennine mountains on the Italian peninsula. Finally, the Adriatic microplate is jammed between the Ligurian and the European plate, covering the areas of the Adriatic Sea, the Po plain as well as the Eastern half of the Italian peninsula.

The plate boundaries are schematically outlined in Figure 8.10 as red dashed lines and are drawn according to the illustrations in Wagner et al. (2012), Di Stefano et al. (2011) and Ustaszewski et al. (2010). Driven by tectonic movements of the African plate in northward direction, the European, Ligurian and Adriatic plates are undergoing tectonic processes like lithospheric subduction and crustal faulting. This caused the formation of the main mountain chains like the Alps, Apennines or Dinarides at the collision zones of the plates, which are likely to result in a thickening of the crust in these areas according to the isostatic theory.

Furthermore, the illustrated region is ruled by particular subduction characteristics, which are for instance shown in Wagner et al. (2012). On the one hand, the European plate is subducting under the Adriatic plate and the Ligurian plate at its Southern borders. On the other hand, the Adriatic plate is dipping beneath the Ligurian plate at the common boundary. Hence, at these plate boundaries the rather instantaneous changes in the crust can also be expected to lead to pronounced changes in the Moho depths. The actual classification of geological structures and subdivisions of different faulting zones in Figure 8.10 is much more complex in reality, and would need more specific explanations on more localized scales. Therefore, the reader is referred to literature like Schmid et al. (1989), Meletti et al. (2000),

Dal Piaz et al. (2003), Lombardi et al. (2008), Ustaszewski et al. (2010), or Carminati and Doglioni (2012). For the purposes of this current study, we want to limit the classifications of tectonic and geological units to the simplified extent given in Figure 8.10.

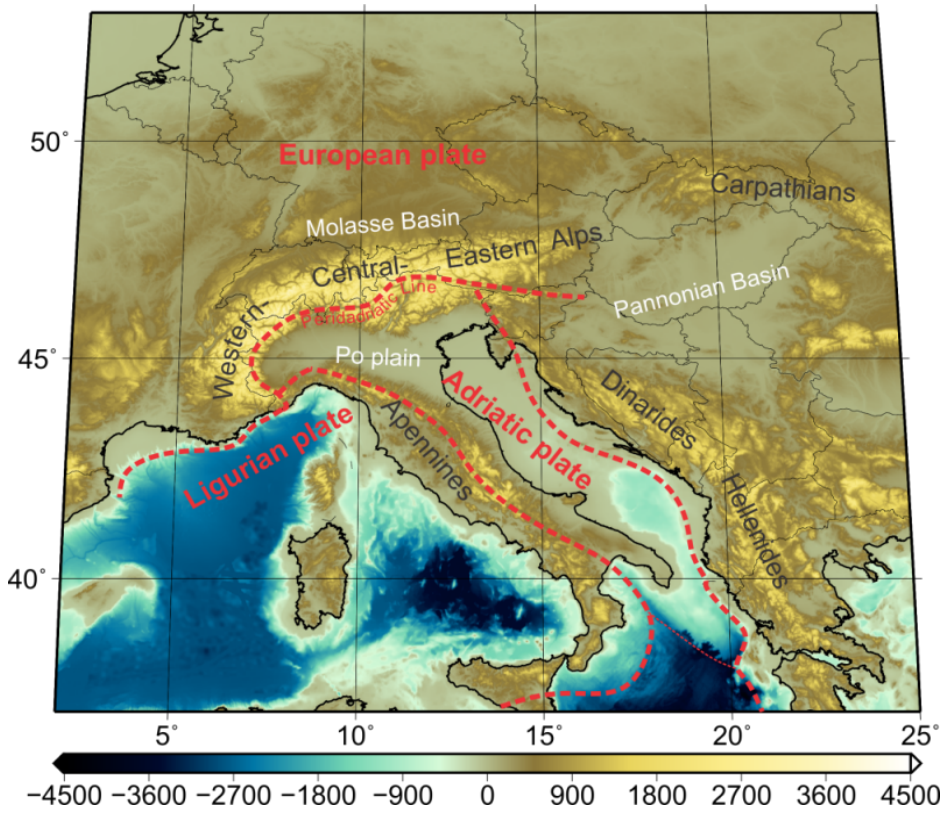

Figure 8.10: A topographic map of central Europe and the Mediterranean Sea based on the ETOPO1 data set (Amante and Eakins, 2010) with some of the main tectonic features based on Wagner et al. (2012), Di Stefano et al. (2011) and Ustaszewski et al. (2010)

At a first glance, the majority of the most pronounced spatial features of the Moho depth variations can be found in each of the models illustrated in Figure 8.9. For instance, clear positive signals are indicating a thicker crust beneath the European Alps, the Apennine Mountains on the Italian peninsula, the Dinarides East of the Adriatic Sea, the Carpathian Mountains at the border between Slovakia and Poland, or for instance beneath the island of Corsica. Likewise, a thinner crust can be found in each model in parts of the Mediterranean and Adriatic Seas or the Po plain between the Alps and the Apennines. However, when looking at more regional features, several differences between the models can be identified even if the according standard deviations in the order of several kilometres of the model estimates are taken into consideration. Hence, more detailed discussions are performed for selected subsets of the Moho maps.

The first geophysically interesting area that is analyzed is indicated in Figure 8.9a by the solid rectangular box denoted with letter *A*. This local region is also chosen in recent studies from Wagner et al. (2012) and Lombardi et al. (2008), who derived a 3D crustal model and Moho maps from seismic data. The corresponding Moho estimate of Wagner et al. (2012) is

illustrated for comparison in Figure 8.11a.

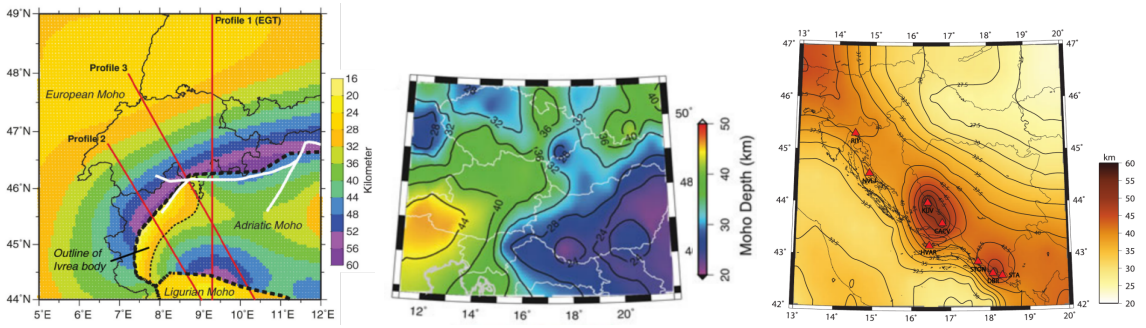

(a) Wagner et al. (2012) **(b)** Molinari and Morelli (2011) **(c)** Stipčević et al. (2011)

Figure 8.11: Local scale Moho estimates from three different recent studies based on seismic observations

It shows a distinct outline of the deep Moho in the subduction zones of the European/Adriatic plates, the Periadriatic Line, and Adriatic/Ligurian plates with a less pronounced Moho depth in the area where all three plates collide. The Adriatic Moho between the subduction zones is considerably lower with distinct minima at about 12°E/45.5°N and in the area that is indicated in Figure 8.11a as the Ivrea body. These regional features can also be identified very well in the ITSG Moho map, thus this can be considered as an indication of the reliability of the achieved results. In this context, the remarkable match of the abrupt Moho change at the Southern Alps boundary with the Peridadriatic Line is pointed out. Concerning the other models, the ESC model is showing similar features, while GEMMA1.0 and EPcrust Mohos do not resolve these characteristics in detail. North of the Alpine arc, the crust in Figure 8.11a is thinning towards the Molasse Basin (see Figure 8.10), which is a sedimentary basin formed during the evolution of the Alps. The GEMMA1.0, ESC and EPcrust models also show a pronounced shallow Moho in this area, while the ITSG Moho does not reveal this basin clearly. The reason may be found by the fact that the sedimentary layers, which have a considerably lower density of on average $2400\,\mathrm{kg\,m^{-3}}$ compared to the assumed standard crustal density of $2700\,\mathrm{kg\,m^{-3}}$, are not considered adequately within this study. Hence, the preliminary assumed constant density contrast for the Moho inversion from gravity observations does not reflect the actual situation properly. In reality, the average crustal density is lower than assumed in the current Moho inversion approach, which consequently leads to a systematic overestimation of the Moho depth in such basin areas.

A similar behaviour can also be observed when looking at the selected area B in Figure 8.9a (outlined as dotted box), which comprises the Pannonian basin, see Figure 8.10. Here, the three external Moho models show the distinct feature of the basin. This is also confirmed by a more recent local seismic study performed by Molinari et al. (2012) for Eastern Europe, which is illustrated in Figure 8.11b. The ITSG model does not explicitly reveal a thinner crust for the Pannonian basin, which is an indication that unmodeled sedimentary layers are a major limitation of the simplified approach proposed in this thesis.

Finally, as a last example the localized area including the Dinarides mountain chain is selected as validation area, which is marked in Figure 8.9a by a dashed box denoted with the

letter C. This region was also aim of a study published by Stipčević et al. (2011) who focused on the determination of the crustal structure beneath the Dinarides. The resulting Moho estimate is depicted in Figure 8.11c and in general shows a deep crustal structure ranging from South-East to North-West, while the Moho in the North-East (Pannonian basin) and South-West (Adriatic Sea) is considerable shallower. In the Dinarides area, Stipčević et al. (2011) revealed two eye-catching maxima of the Moho depth, centered at about 18°E/42.5°N and 16.5°E/44°N. A comparison of these findings with the GEMMA1.0, ESC and EPcrust models of Figure 8.9 shows that the general structures can be noticed therein as well, however the two maxima are not that evident due to the lower resolution of these models. In contrast, the ITSG model draws a clear picture of these local features, which are comparable to those in Stipčević et al. (2011), while the Pannonian basin structure is underrepresented, as already mentioned in the preceding paragraph.

8.6 Summary and conclusions of the Moho estimation

In this chapter an approach for the estimation of the Mohorovičić (Moho) surface based on the LSC method has been proposed. First, the Moho discontinuity has been defined as the surface that separates the crustal layer from the upper mantle layer, which together are forming the Earth's lithosphere. This was then related to the concept of isostasy according to Airy-Heiskanen, a simple two-layer model which assumes that a lighter crust is floating on a dense mantle material. By pinning the density contrast between crust and mantle to a fixed value, the penetration depth of the crust into the mantle w.r.t. a mean Moho depth can classically be derived from the topographic heights. The presented approach assumes that the removal of the effect of the topography from the gravitational potential leads to a residual gravity field that mainly reflects the state of isostatic compensation. This in turn can be expressed as the disturbing potential of a theoretical surface layer coinciding with the mean Moho depth surface. By introducing the quantity of surface layer density, the Moho variations can then be inverted from the disturbing potential. Based on this theory, the covariance expressions for surface layer densities and other gravity field quantities are derived for the LSC approach.

Since GOCE gradient data are of minor quality especially in the spectral range below 5 mHz, it was decided to use data only above spherical harmonic D/O 50. With this choice it should also be guaranteed that the effects of possible long-wavelength density anomalies in the interior of the Earth are reduced as much as possible. Six months of EGG_NOM_2 gradient data were preprocessed according to the strategy proposed earlier in this work, i.e., at first the gradients have been Wiener filtered and consecutively high-pass filtered in the GRF in order to reduce colored noise and long-wavelength signals. The central European region between 5° to 22° East and 42° to 52° North, covering Austria and the surrounding areas, has been selected for the current investigations.

The RWI_TOPO_2012 topographic model has been used to remove the topographic gravitational effect from the measurements. It has been shown, that a reduction of the topographic signal up to D/O 360 is sufficient to cover most of the significant signal at GOCE orbit heights. Since the effect of atmospheric masses above D/O 50 is below the remaining

measurement noise of the gradient observations after the preprocessing steps, the atmospheric effect is not considered in this study. The computation of surface layer density values from GOCE gradient observations with the LSC method was done using a covariance function that is based on the signal degree variances derived from the GOCE_TIM_RL05 and RWI_TOPO_2012 models. For the final Moho inversion, a mean Moho depth of D=30 km and a constant density contrast of $\Delta\rho$=350 kg m^{-3} have been chosen as constraints for the investigated area according to literature studies. The resulting Moho estimates (called ITSG Moho model) in the investigated region show Moho depth variations between −19.9 km and 13.5 km (rms=3.9 km) for the spectral range from D/O 50 to an effective spectral resolution approximately between D/O 250 and 280.

The results are compared with three external and publicly available regional and global Moho models. While the ESC and EPcrust models are mainly based on seismic observations, the GEMMA1.0 is a global model also based on GOCE data. In order to achieve a fair comparison w.r.t. the ITSG Moho, the signal content lower than D/O 50 has been removed from the external models. The amplitudes of the ITSG Moho are comparable to those from GEMMA1.0, while the seismic models show less pronounced minima in the order of about −13 km. Concerning the spatial characteristics of the Moho signal, the general structures like those inferred from the main mountain chains, e.g., the Alps, Apennines or Dinarides, are visible in all models. However, the ITSG estimates show a more detailed view in terms of spatial resolution.

The soundness of these features is verified with recent seismic studies on a more localized scale. For this reason, three specific validation areas have been selected, which are comprising some prominent geophysical and tectonic characteristics. In this way, a very good agreement of the ITSG Moho estimates with the local seismic studies in the subduction zones in the Western and Central Alps or at the Adriatic coast could be identified. The three external Moho models do not draw such a clear picture due to a lack of spatial resolution. The limitations of the presented study are evident in particular in sedimentary basin areas like the Molasse or Pannonian basins, where the effect of unmodeled sedimentary layers leads to systematic overestimation of the Moho depth.

It could be shown that the novel approach of using GOCE gravity gradient observations as direct observations for the estimation of the Moho surface within the LSC method leads to promising results. In terms of spatial resolution, the ITSG Moho is resolving more detailed structures compared to other regional Moho models. In this case, on the one hand the ITSG model clearly benefits from the dense observation distribution which is possible due to the global data coverage of the GOCE mission. On the other hand, the GOCE gravity gradients are able to recover the gravity signal with high accuracy in particular in the spectral range where also Moho variations can be expected to occur. Thus, it is possible to overcome the main limiting factor of seismic approaches on regional scale like the ESC or EPcrust models, which usually do not have access to spatially comprehensive databases. For this reason, in such models areas with a sparse data distribution are commonly filled by means of interpolation methods, which can lead to misinterpretations of the actual devolution of the Moho. Although the GEMMA1.0 model is also based on GOCE data, its purpose is to represent a global Moho map. As such, it currently does not take advantage of the entire available signal spectrum, which can be expected to exceed the spectral resolution of D/O 210, the current limit of GEMMA1.0. The comparison with localized studies showed, that ITSG Moho structures are in a very good agreement with such detailed investigations and that the resulting

Moho features can be directly linked to geophysical and tectonic units. Thus, the proposed approach is a possible candidate for supra-regional analysis of the crust-mantle boundary based on a consistent database and a uniform processing strategy.

Nevertheless, there are still a couple of aspects of the approach that need to be improved in future works. For instance, the presented method is currently not capable to resolve the absolute Moho depths, since the long-wavelength constituents of the gravity signals used for the inversion are neglected due to the specific signal characteristics of the GOCE gradients. This is not necessarily a drawback during the processing, because in this way also possible undesirable influences like mantle anomalies or other disturbances in the Earth's interior can be avoided. Basically, it would be possible to recover the low-frequency signal of the Moho also from accurate global gravity field models like the GOCE or GOCO models, however the mentioned disturbances would be fully introduced as errors in the resulting absolute Moho depth estimates. To overcome this, a respective model of the mantle structures would be essential, with which it could be possible to correct for the corresponding disturbing gravitational effects.

Furthermore, it is also only a rather hypothetical assumption that the density contrast applied in the Moho inversion is constant throughout a whole region under investigation. In reality, also the lower crust and the mantle are heterogeneous compositions of various materials with densities different from the assumed constant values like the global averages of $2670\,\mathrm{kg\,m^{-3}}$ or $3270\,\mathrm{kg\,m^{-3}}$. Within the current investigations, this was roughly accounted for by using a more realistic but still constant density contrast based on the information from other sources. However, from more detailed knowledge of deep density structures of crust and also mantle it would be possible to derive a laterally varying density contrast, which could improve the Moho estimation.

Concerning the reduction of the gravitational effect of the topographic masses prior to the Moho inversion, a global model that is based on constant density values for rock, water and ice masses is used herein. In general, this can be considered as a good assumption, which leads to reasonable results like in the current study. However, a reduction considering a more realistic density model for the topography above sea level may produce even better results. Furthermore, the proper consideration of crustal density variations below sea level, in particular due to sedimentary layers, can avoid a defective Moho inversion, as it is the case in this study for basins with a considerable content of sedimental deposit. Besides the already mentioned deficiencies, the concept of the proposed approach will fail in regions where the assumption of a layered structure of crust and mantle is not valid. One can for instance think of divergent plate boundaries like the mid-oceanic ridge in the Atlantic Ocean, where upwelling mantle material is constantly forming new lithosphere. Similarly, this method will be of limited applicability also in volcanic areas.

Although there are still several issues that have been disregarded so far, the developed method for Moho determination is competitive with other Moho models already at this stage. The advantages as well as the disadvantages have been discussed extensively, and it could be shown that the approach is capable of revealing meaningful structures of the crust-mantle boundary. In this way, the ITSG Moho inversion method can be considered as a valuable tool for future geophysical applications.

9 Summary and outlook

According to the initial purpose of the GOCE mission, the gravity gradient observations of the onboard gradiometer instrument, which represent the second order derivatives of the Earth's gravitational potential, are primarily used to derive the Earth's gravity potential on global scale with least squares adjustment procedures. Within this thesis, the gradients are exploited as in-situ observations for regional scale applications using the LSC method, which is commonly applied for regional gravity field determination.

Due to several mission-specific characteristics, the introduction of the GOCE gradients into the LSC approach bears some problems. More specifically, the gradiometer instrument is designed in a way that not every component of the gravity gradient tensor could be determined with the same precision. Since the measurements are taken in the gradiometer reference frame, it is not possible to perform any rotation of the gradient tensor without spoiling the observations. To circumvent this, a collocation approach was implemented that is independent of the reference frame. In this way it is possible to rotate the covariances, which are describing the statistical correlations of the observations that form the basis of LSC, while the observations can be used unchanged in their instrument-specific measurement frame.

Furthermore, the measurements are deteriorated by colored noise, which is influencing in particular the low- and high-frequency measurement spectrum and leads to highly correlated observations. To reduce the influence of the noise, a preprocessing strategy has been developed, which is composed of a Wiener filter approach and a consecutive application of a high-pass filter. The Wiener filter decreases the colored noise in the sense of a minimum filter error according to the least squares principle. The remaining long-wavelength distortions are corrected with a Chebychev II high-pass filter. Apart from the filtered observations, also the information of the remaining measurement errors after the preprocessing is an essential result, which can be used for an adequate stochastic modeling of the error characteristics in LSC.

The RCR concept was revised in the context of LSC for regional scale applications. Concerning an intended combination of GOCE gradients with other data sources, e.g. terrestrial gravity data, a consistent RCR approach is inevitable. Based on the investigations of currently available global EGMs, it can be argued that GOCE gradients contain superior gravity field signals above spherical harmonic D/O 110. For a combination with terrestrial data it is therefore favourable to reduce the longer wavelengths by means of an accurate EGM. The treatment of systematic effects induced by the topographic masses and the isostatic compensation effect as well as the influence of the atmospheric masses was investigated. For a consistent consideration of the atmospheric potential, a corresponding atmospheric density model has been derived.

In a first application, the preprocessed main diagonal components of the GOCE gradient tensor were used to estimate a regional geoid for Austria in combination with terrestrial gravity

observations. To reduce the long-wavelength constituents from the observations within the RCR procedure, the GOCO03s model up to D/O 120 was used. Furthermore, the topographic and isostatic effects were consistently reduced from both data sets on the basis of a DEM that is available for an extended area. The effect of the atmosphere is implicitly removed from gradients at orbit altitude due to the reduction of the signal from the EGM, which incorporates the atmospheric masses. In case of the terrestrial data, a consistent reduction was achieved by accounting for the fact that the observations are taken within the attracting masses. Although this contribution is small, it should be applied for reasons of consistency. In order to describe the statistical behaviour of the resulting smoothed gravity anomalies and gradients, a MCF was fitted simultaneously to the ECFs of anomalies and vertical gradients using an adapted Tscherning-Rapp degree variance model.

Residual geoid heights were estimated from each data set separately, as well as from their combined use. It could be shown, that the GOCE gradients significantly contribute to the combined solution in particular in the expected medium-wavelength range of the gravity signal and thus can complement a terrestrial gravity-only solution. The gravity-only and combined solutions were validated with independent GPS/levelling observations. With the inclusion of gradient data, the average deviation could be decreased from 5.5 cm to 4.6 cm. In contrast to the current official Austrian geoid solution, which is heavily constrained towards GPS/levelling observations, the presented geoid is a consistent equipotential surface.

As a second application, the determination of the Moho surface in central Europe using GOCE gravity gradients was introduced, which poses a new field of application of the LSC approach. The method was developed on the basis of the Airy-Heiskanen isostatic concept and assumes that the removal of the topographic effect from the gravitational potential leads to a residual potential, whose variations are reflecting the state of isostatic compensation. In this sense, a global topographic potential model was used to reduce the topographic signal from the preprocessed GOCE gradient observations. Since GOCE gradients can not resolve the long-wavelength signals of the gravity signal, they have been used for the Moho inversion in the spectral range between D/O 50 to 280. Although the disregarded long-wavelength signal could theoretically be restored for instance from a global accurate EGM, this step was intentionally not performed in order to avoid possible disturbances from deep Earth structures like mantle anomalies. The resulting residual Moho was compared with external regional and global models based on seismic and gravity observations in the same spectral range. It was shown, that the presented solution can resolve localized geophysically meaningful features in more detail. This could be confirmed by a validation with local seismic Moho studies.

The successful utilization of GOCE gravity gradients for regional applications was demonstrated in this thesis. However, for both examples, regional geoid determination and Moho estimation, further improvements are possible in particular in terms of more realistic background models. Concerning the geoid determination, the modeling of topographic and isostatic effects within the consistent RCR procedure could be enhanced by the introduction of a density model and a model of absolute Moho depths. Likewise, also the Moho estimation would benefit from the detailed knowledge of the density structures within the topography. With further information about anomalies in the mantle structure, it would also be possible to safely restore the neglected long-wavelength signal constituents in order to obtain absolute

Moho depths. Besides modeling issues, the main limitation of the LSC approach is the computational effort, since the size of the covariance matrix of the observations that has to be inverted is increasing quadratic with the number of input observations. Hence, for the presented investigations only subsets of the actually available data have been used. This situation could be improved by a redesign using parallel processing strategies.

List of Figures

List of Tables

Bibliography

Abd-Elmotaal H. (1993). Vening Meinesz moho depths: traditional, exact and approximated. *Manuscripta Geodetica* 18, 171–181.

Abd-Elmotaal H. A. and Kühtreiber N. (2003). Geoid determination using adapted reference field, seismic Moho depths and variable density contrast. *Journal of Geodesy* 77(1-2), 77–85. doi:10.1007/s00190-002-0300-7.

Abrikosov O., Jarecki F., Müller J., Petrovic S. and Schwintzer P. (2006). The Impact of Temporal Gravity Variations on GOCE Gravity Field Recovery. In Flury, J. and Rummel, R. and Reigber, C. and Rothacher, M. and Boedecker, G. and Schreiber, U. (Ed.), *Observation of the Earth System from Space* (pp. 255–269). Springer Berlin Heidelberg. doi:10.1007/3-540-29522-4-18.

Albertella A., Migliaccio F., Reguzzoni M. and Sansò F. (2004). Wiener filters and collocation in satellite gradiometry. In F. Sansò (Ed.), *V Hotine-Marussi Symposium on Mathematical Geodesy* (pp. 32–38). International Association of Geodesy Symposia, Vol. 127. Springer Berlin Heidelberg. doi:10.1007/978-3-662-10735-5_5.

Albertella A., Savcenko R., Janjić T., Rummel R., Bosch W. and Schröter J. (2014). Mean Dynamic Ocean Topography in the Southern Ocean from GRACE and GOCE and Multi-mission Altimeter Data. In C. Rizos, and P. Willis (Eds.), *Earth on the Edge: Science for a Sustainable Planet* (pp. 81–87). International Association of Geodesy Symposia, Vol. 139. Springer Berlin Heidelberg. doi:10.1007/978-3-642-37222-3_10.

Amante C. and Eakins B. W. (2010). *ETOPO1 1 Arc-Minute Global Relief Model: Procedures, Data Sources and Analysis*. NOAA Technical Memorandum NESDIS NGDC-24. National Geophysical Data Center, NOAA. doi:10.7289/V5C8276M accessed on 2015-01-13.

Bagherbandi M. (2011). *An Isostatic Earth Crustal Model and Its Applications*. Ph.D. thesis, Royal Institute of Technology (KTH), Division of Geodesy and Geoinformatics, Stockholm, Sweden.

Bagherbandi M. and Sjöberg L. (2011). Comparison of crustal thickness from two isostatic models versus CRUST2.0. *Studia Geophysica Geodetica* 55, 641–666.

Bagherbandi M. and Tenzer R. (2013). Comparative analysis of Vening-Meinesz Moritz isostatic models using the constant and variable crust-mantle density contrast - a case study of Zealandia. *Journal of Earth System Sciences* 122(2), 339–348.

Barzaghi R. and Biagi L. (2014). The collocation approach to Moho estimate. *Annals of Geophysics* 57(1).

Bassin C., Laske G. and Masters G. (2000). The current limits of resolution for surface wave tomography in North America. *EOS Transactions AGU* 81.

Basuyau C., Diament M., Tiberi C., Hetényi G., Vergne J. and Peyrefitte A. (2013). Joint inversion of teleseismic and GOCE gravity data: application to the Himalayas. *Geophysical Journal International* 193(1), 149–160. doi:10.1093/gji/ggs110.

BEV (2013). *3-D Referenzsysteme in Österreich*. URL: http://www.bev.gv.at/portal/page?_pageid=713,1571675&_dad=portal&_schema=PORTAL accessed on 2015-01-10.

Bock H., Jäggi A., Meyer U., Visser P., IJssel J., Helleputte T., Heinze M. and Hugentobler U. (2011). GPS-derived orbits for the GOCE satellite. *Journal of Geodesy* 85(11), 807–818. doi:10.1007/s00190-011-0484-9.

Bouman J. (2004). Quick-look outlier detection for GOCE gravity gradients. *Newton's Bulletin* (2), 78–87.

Bouman J. (2007). *Alternative method for rotation to TRF*. GO-TN-HPF-GS-0193, Issue 1.0.

Bouman J., Ebbing J., Meekes S., Fattah R. A., Fuchs M., Gradmann S., Haagmans R., Lieb V., Schmidt M., Dettmering D. and Bosch W. (2015). GOCE gravity gradient data for lithospheric modeling. *International Journal of Applied Earth Observation and Geoinformation* 35, Part A, 16–30. doi:10.1016/j.jag.2013.11.001.

Bouman J., Fiorot S., Fuchs M., Gruber T., Schrama E., Tscherning C., Veicherts M. and Visser P. (2011). GOCE gravitational gradients along the orbit. *Journal of Geodesy* 85(11), 791–805. doi:10.1007/s00190-011-0464-0.

Bouman J., Rispens S., Gruber T., Koop R., Schrama E., Visser P., Tscherning C. and Veicherts M. (2009). Preprocessing of gravity gradients at the GOCE high-level processing facility. *Journal of Geodesy* 83(7), 659–678. doi:10.1007/s00190-008-0279-9.

Brockmann J. M., Höck E., Loth I., Mayer-Gürr T., Pail R., Schuh W.-D. and Zehentner N. (2014). *A Gravity Field Model From the Entire GOCE Mission: EGM_TIM_RL05*. Presentation, 5th GOCE User Workshop 2014, 25.11.2014, Paris.

Carminati E. and Doglioni C. (2012). Alps vs. Apennines: The paradigm of a tectonically asymmetric Earth . *Earth-Science Reviews* 112(1–2), 67–96. doi:10.1016/j.earscirev.2012.02.004.

Cesare S. (2008). *Performance requirements and budgets for the gradiometric mission*. Technical Report, Issue 04, GO-TN-AI-0027, Thales Alenia Space.

Clenshaw C. (1955). A note on the summation of Chebychev series. *Mathematical Tables and other Aids to Computation* 9(51), 118.

Dal Piaz G. V., Bistacchi A. and Massironi M. (2003). Geological outline of the Alps. *Episodes* 26(3), 175–180.

Darbeheshti N. and Featherstone W. (2009). Non-stationary covariance function modelling in 2D least-squares collocation. *Journal of Geodesy* 83(6), 495–508. doi:10.1007/s00190-008-0267-0.

Darbeheshti N. and Featherstone W. (2010). A review on non-stationary spatial methods for least-squares collocation. *Journal of Spatial Science* 55(2), 185–204. doi:10.1080/14498596.2010.521971.

Di Stefano R., Bianchi I., Ciaccio M. G., Carrara G. and Kissling E. (2011). Three-dimensional Moho topography in Italy: New constraints from receiver functions and controlled source seismology. *Geochemistry, Geophysics, Geosystems* 12(9). doi:10.1029/2011GC003649.

Drinkwater M., Floberghagen R., Haagmans R., Muzi D. and Popescu A. (2003). GOCE: ESA's First Earth Explorer Core Mission. In G. Beutler, M. Drinkwater, R. Rummel, and R. Steiger (Eds.), *Earth Gravity Field from Space — From Sensors to Earth Sciences* (pp. 419–432). Space Sciences Series of ISSI, Vol. 17. Springer Netherlands. doi:10.1007/978-94-017-1333-7_36.

Drinkwater M., Haagmans R., Muzi D., Popescu A., Floberghagen R., Kern M. and Fehringer M. (2007). The GOCE gravity mission: ESA's First Core Earth Explorer. In *Proceedings of the 3rd International GOCE User Workshop* (pp. 1–8). Frascati, Italy: ESA SP-627.

Dziewonski A. M. and Anderson D. L. (1981). Preliminary reference Earth model . *Physics of the Earth and Planetary Interiors* 25(4), 297–356. doi:10.1016/0031-9201(81)90046-7.

Ebbing J., Braitenberg C. and Götze H.-J. (2001). Forward and inverse modelling of gravity revealing insight into crustal structures of the Eastern Alps. *Tectonophysics* 337, 191–208.

Ecker E. and Mittermayer E. (1969). Gravity corrections for the influence of the atmosphere. *Bollettino di Geofisica Teorica ad Applicata* 11, 70–80.

ESA (1999). *Gravity Field and Steady-State Ocean Circulation Mission*. Reports for Mission Selection: The four candidate Earth Explorer core missions. ESA SP-1233 (1), ESA Publications Division ESA/ESTEC, Noordwijk, Netherlands.

ESA (2006). *GOCE L1B Products User Handbook*. GOCE-GSEG-EOPG-TN-06-0137.

ESA (2014). *ESA Living Planet Programme*. URL: http://www.esa.int/livingplanet accessed

on 2014-05-16.

Eshagh M. (2009). *On Satellite Gravity Gradiometry*. Ph.D. thesis, Royal Institute of Technology (KTH), Division of Geodesy Stockholm, Sweden.

Eshagh M. and Sjöberg L. E. (2009). Atmospheric effects on satellite gravity gradiometry data. *Journal of Geodynamics* 47(1), 9–19.

Ferreira V. G., Zhang Y. and de Freitas S. R. C. (2013). Validation of GOCE gravity field models using GPS-leveling data and EGM08: a case study in Brazil. *Journal of Geodetic Science* 3(3), 143–249. doi:10.2478/jogs-2013-0027.

Floberghagen R., Fehringer M., Lamarre D., Muzi D., Frommknecht B., Steiger C., Piñeiro J. and Costa A. (2011). Mission design, operation and exploitation of the gravity field and steady-state ocean circulation explorer mission. *Journal of Geodesy* 85(11), 749–758. doi:10.1007/s00190-011-0498-3.

Forsberg R. and Tscherning C. C. (1997). Topographic Effects in Gravity Field Modelling for BVP. In F. Sansò, and R. Rummel (Eds.), *Geodetic Boundary Value Problems in View of the One Centimeter Geoid*. Lecture Notes in Earth Sciences, Vol. 65. Springer-Verlag, Berlin Heidelberg.

Fowler C. M. R. (2004). *The Solid Earth*. (2nd ed.). Cambridge University Press. doi:10.1017/CBO9780511819643.

Franzen M. and Mandelburger G. (2003). Die neue Generation des digitalen Geländemodells von Österreich. *Österreichische Zeitschrift für Vermessung und Geoinformation VGI* 91(3), 154–162.

Frommknecht B., Lamarre D., Meloni M., Bigazzi A. and Floberghagen R. (2011). GOCE level 1b data processing. *Journal of Geodesy* 85(11), 759–775. doi:10.1007/s00190-011-0497-4.

Fuchs M. J. and Bouman J. (2011). Rotation of GOCE gravity gradients to local frames. *Geophysical Journal International* 187(2), 743–753. doi:10.1111/j.1365-246X.2011.05162.x.

Gatti A., Migliaccio F., Reguzzoni M. and Sansò F. (2013). *Space-wise global grids of GOCE gravity gradients at satellite altitude*. Presentation, EGU General Assembly 2013, 7-12 April, Vienna.

Gerlach C. and Rummel R. (2013). Global height system unification with GOCE: a simulation study on the indirect bias term in the GBVP approach. *Journal of Geodesy* 87(1), 57–67. doi:10.1007/s00190-012-0579-y.

Goiginger H., Rieser D., Mayer-Gürr T., Pail R., Schuh W.-D., Jäggi A. and Maier A. (2011). *The combined satellite-only global gravity field model GOCO02S*. EGU General Assembly, Vienna, Presentation on the 04.04.2011.

Grad M., Tiira T. and ESC Working Group (2009). The Moho depth map of the European Plate. *Geophysical Journal International* 176, 279–292. doi:10.1111/j.1365-246X.2008.03919.x.

Graf J. (1996). Das digitale Geländemodell für Geoidberechnungen und Schwereereduktionen in Österreich. In *Proceedings of the 7th International Meeting on Alpine Gravimetry.* Österreichische Beträge zu Meteorologie und Geophysik (pp. 121–136). Vienna.

Grombein T., Luo X., Seitz K. and Heck B. (2014). A wavelet-basedassessment of topographic-isostatic reductions for GOCE gravity gradients. *Surveys in Geophysics* 35(4). doi:10.1007/s10712-014-9283-1.

Grombein T., Seitz K. and Heck B. (2013). Optimized formulas for the gravitational field of a tesseroid. *Journal of Geodesy* 87(7). doi:10.1007/s00190-013-0636-1.

Gruber T. (2009). Evaluation of the EGM2008 gravity field by means of GPS-levelling and sea surface topography solutions. *Newton's Bulletin* (4), 3–17.

Gruber T., Abrikosov O. and Hugentobler U. (2010a). *GOCE standards*. GO-TN-HPF-GS-0111, Issue 3.2.

Gruber T., Rummel R., Abrikosov O. and van Hees R. (2010b). *GOCE Level2 Product Data Handbook*. GO-MA-HPF-GS-0110, Issue 4.3.

Gruber T., Rummel R. and Koop R. (2007). How to use GOCE Level 2 products. In *Proceedings of*

the 3rd International GOCE User Workshop (pp. 205–212). ESA SP-627.

Gruber T., Visser P. N. A. M., Ackermann C. and Hosse M. (2011). Validation of GOCE gravity field models by means of orbit residuals and geoid comparisons. *Journal of Geodesy* 85, 845–860. doi:10.1007/s00190-011-0486-7.

Gustafsson F. (1996). Determining the initial states in forward-backward filtering. *Signal Processing, IEEE Transactions on* 44(4), 988–992. doi:10.1109/78.492552.

Heiskanen W. and Moritz H. (1967). *Physical Geodesy*. W.H. Freeman and Company, San Francisco.

Hobson E. W. (1931). *The theory of spherical and ellipsoidal harmonics*. University Press, Cambridge.

Hofmann-Wellenhof B. and Moritz H. (2005). *Physical Geodesy*. SpringerWienNewYork.

Ihde J., Sacher M. and Mäkinen J. (2008). *Conventions for the Definition and Realization of a European Vertical Reference System (EVRS) - EVRS Conventions 2007*. URL: http://www.bkg.bund.de/geodIS/EVRS/SharedDocs/Downloads/Publications/EVRFConventions2007,templateId=raw,property=publicationFile.pdf/EVRFConventions2007.pdf accessed on 2015-02-10.

Kahle H., Klingele E., Mueller S. and Egloff R. (1976). The variation of crustal thickness across the Swiss Alps based on gravity and explosion seismic data. *pure and applied geophysics* 114(3), 479–494. doi:10.1007/BF00876947.

Knudsen (1987). Estimation and modelling of the local empirical covariance function using gravity and satellite altimeter data. *Bulletin géodésique* 61(2), 145–160. doi:10.1007/BF02521264.

Knudsen P., Bingham R., Andersen O. and Rio M.-H. (2011). A global mean dynamic topography and ocean circulation estimation using a preliminary GOCE gravity model. *Journal of Geodesy* 85(11), 861–879. doi:10.1007/s00190-011-0485-8.

Koch K. R. and Schmidt M. (1994). *Deterministische und stochastische Signale*. Ferd. Dümmlers Verlag, Bonn.

Krarup T. (1969). A contribution to the mathematical foundation of physical geodesy. Danish Geodetic Institute, Copenhagen.

Kuhn M. and Featherstone W. E. (2006). Construction of an Synthetic Earth Gravity Model by Forward Gravity Modelling. In F. Sansò (Ed.), *A Window on the Future of Geodesy* (pp. 350–355). International Association of Geodesy Symposia, Vol. 128. doi:10.1007/3-540-27432-4_60.

Kühtreiber N. (1998). Improved Gravimetric Geoid AGG97 of Austria. In R. Forsberg, M. Feissel, and R. Dietrich (Eds.), *Geodesy on the Move* (pp. 306–311). International Association of Geodesy Symposia, Vol. 119. Springer Berlin Heidelberg. doi:10.1007/978-3-642-72245-5_45.

Kühtreiber N. (2002). *High Precision Geoid Determination for Austria*. Habilitation, Graz University of Technology, Austria.

Kühtreiber N., Wirnsberger H., Pock C., Wasle B., Pail R., Of G., Steinbach O. and Unger G. (2011). *Improved Austrian geoid solution combining terrestrial and satellite gravity data (GEOID+)*. Technical Report, Austrian Space Application Programme Phase VI, Final Report. Graz University of Technology, Austria.

Lambeck K. (1988). *Geophysical Geodesy*. Oxford University Press, New York.

Lombardi D., Braunmiller J., Kissling E. and Giardini D. (2008). Moho depth and Poisson's ratio in the Western–Central Alps from receiver functions. *Geophysical Journal International* 173(1), 249–264. doi:10.1111/j.1365-246X.2007.03706.x.

Maier A., Krauss S. and Baur O. (2014). The role of Satellite Laser Ranging in terrestrial gravity field recovery. *Österreichische Zeitschrift für Vermessung und Geoinformation VGI* 102(1).

Marotta A. (2003). Benefits from GOCE Within Solid Earth Geophysics. *Space Science Reviews* 108(1-2), 95–104. doi:10.1023/A:1026273832697.

Mayer-Gürr T. (2007). *The latest GRACE gravity field solution computed in Bonn*. International GSTM and SPP Symposium, Potsdam, Germany, Presentation on the 17.10.2007.

Mayer-Gürr T., Zehentner N., Klinger B. and Kvas A. (2014). *ITSG-Grace2014: a new GRACE gravity field release cimputed in Graz*. RACE Science Team Meeting, Potsdam, Germany, Presentation on the 29.09.2014.

McCarthy D. D. and Petit G. (Eds.) (2004). *IERS Conventions (2003)*. IERS Technical Note No. 32. Verlag des Bundesamts für Kartographie und Geodäsie, Frankfurt am Main.

van der Meijde M., Pail R., Bingham R. and Floberghagen R. (2015). GOCE data, models, and applications: A review. *International Journal of Applied Earth Observation and Geoinformation* 35, Part A, 4–15. doi:10.1016/j.jag.2013.10.001.

Meletti C., Patacca E. and Scandone P. (2000). Construction of a Seismotectonic Model: The Case of Italy. In G. Panza, M. Radulian, and C.-I. Trifu (Eds.), *Seismic Hazard of the Circum-Pannonian Region* Pageoph Topical Volumes (pp. 11–35). Birkhäuser Basel. doi:10.1007/978-3-0348-8415-0_2.

Migliaccio F., Reguzzoni M., Gatti A., Sansò F. and Herceg M. (2011). A GOCE-only global gravity field model by the space-wise approach. In *Proceedings of 4th International GOCE User Workshop*. European Space Agency, ESA.

Migliaccio F., Reguzzoni M. and Sansò F. (2004). Space-wise approach to satellite gravity field determination in the presence of coloured noise. *Journal of Geodesy* 78, 304–313. doi:10.1007/s00190-004-0396-z.

Mohr P. J., Taylor B. N. and Newell D. B. (2012). CODATA Recommended Values of the Fundamental Physical Constants: 2010. *Journal of Physical and Chemical Reference Data* 41(4). doi:10.1063/1.4724320.

Molinari I. and Morelli A. (2011). EPcrust: a reference crustal model for the European Plate. *Geophysical Journal International* 185, 352–364. doi:10.1111/j.1365-246X.2011.04940.x.

Molinari I., Raileanu V. and Morelli A. (2012). A Crustal Model for the Eastern Alps Region and a New Moho Map in Southeastern Europe. *Pure and Applied Geophysics* 169(9), 1575–1588. doi:10.1007/s00024-011-0431-y.

Moritz H. (1962). *Interpolation and prediction of gravity and their accuracy*. Technical Report, No. 24, Institute of Geodesy, Photogrammetry and Cartography, Ohio State University.

Moritz H. (1972). *Advanced Least-Squares Methods*. Technical Report, No. 175, Department of Geodetic Science, Ohio State University.

Moritz H. (1980a). *Advanced Physical Geodesy*. Wichmann Verlag, Karlsruhe.

Moritz H. (1980b). Geodetic Reference System 1980. *Bulletin Geodesique* 54, 395–405.

Moritz H. (1990a). *The Figure of the Earth: Theoretical Geodesy and the Earth's Interior*. Wichmann Verlag, Karlsruhe.

Moritz H. (1990b). The inverse Vening Meinesz problem in isostasy. *Geophysical Journal International* (102), 733–738.

Müller J. (2003). GOCE gradients in various reference frames and their accuracies. *Advances in Geosciences* 1, 33–38.

NOAA, NASA and US Air Force (1976). *U.S. Standard Atmosphere 1976*. Technical Report, U.S. Government Printing Office Washington DC.

Novak P. (2000). *Evaluation of gravity data for the Stokes-Helmert solution to the geodetic boundary-value problem*. Technical Report, 207, Department of Geodesy and Geomatics Engineering, University of New Brunswick Fredericton, Canada.

Oppenheim A. V. and Schafer R. W. (1975). *Digital Signal Processing*. PRENTICE-HALL, INC., Englewood Cliffs, New Jersey.

Oppenheim A. V. and Schafer R. W. (1999). *Discrete-time signal processing*. (2nd ed.). Prentice-Hall, Inc., New Jersey.

Pail R. (2005). A parametric study on the impact of satellite attitude errors on GOCE gravity field

recovery. *Journal of Geodesy* 79, 231–241. doi:10.1007/s00190-005-0464-z.

Pail R., Bruinsma S., Migliaccio F., Förste C., Goiginger H., Schuh W.-D., Höck E., Reguzzoni M., Brockmann J., Abrikosov O., Veicherts M., Fecher T., Mayrhofer R., Krasbutter I., Sansò F. and Tscherning C. (2011). First GOCE gravity field models derived by three different approaches. *Journal of Geodesy* 85(11), 819–843. doi:10.1007/s00190-011-0467-x.

Pail R., Kühtreiber N., Lackner B., Preimesberger T., Wiesenhofer B., Of G. and Steinbach O. (2007). *The Austrian Geoid 2007 (GEOnAUT)*. Technical Report, Austrian Space Application Programme Phase III, Final Report. Graz University of Technology, Austria.

Pail R., Kühtreiber N., Wiesenhofer B., Hofmann-Wellenhof B., Of G., Steinbach O., Höggerl N., Imrek E., Ruess D. and Ullrich C. (2008). The Austrian Geoid 2007. *Österreichische Zeitschrift für Vermessung und Geoinformation VGI* 96(1), 3–14.

Papoulis A. (1984). *Signal analysis*. McGraw Hill, New York.

Pavlis N. K., Holmes S. A., Kenyon S. C. and Factor J. K. (2012). The development and evaluation of the Earth Gravitational Model 2008 (EGM2008). *Journal of Geophysical Research: Solid Earth* 117(B4). doi:10.1029/2011JB008916.

Petit G. and Luzum B. (Eds.) (2010). *IERS Conventions (2010)*. IERS Technical Note No. 36. Verlag des Bundesamts für Kartographie und Geodäsie, Frankfurt am Main.

Pock C., Mayer-Guerr T. and Kuehtreiber N. (2014). Consistent Combination of Satellite and Terrestrial Gravity Field Observations in Regional Geoid Modeling: A Case Study for Austria. In U. Marti (Ed.), *Gravity, Geoid and Height Systems* (pp. 151–156). International Association of Geodesy Symposia, Vol. 141. Springer International Publishing. doi:10.1007/978-3-319-10837-7_19.

Polgár Z., Sujbert L., Földváry L., Asbóth P. and Ádám J. (2012). Filter design for GOCE gravity gradients. *Geocarto International* 28(1), 28–36. doi:10.1080/10106049.2012.687401.

Prasanna H. M. I., Chen W. and Iz H. B. (2013). High resolution local Moho determination using gravity inversion: A case study in Sri Lanka. *Journal of Aisan Earth Sciences* 74, 62–70.

Reguzzoni M. and Sampietro D. (2014). GEMMA: An Earth crustal model based on GOCE satellite data. *International Journal of Applied Earth Observation and Geoinformation* 35(0), 31–43. doi:10.1016/j.jag.2014.04.002.

Reguzzoni M., Sampietro D. and Sansò F. (2013). Global Moho from the combination of the CRUST2.0 model and GOCE data. *Geophysical Journal International* 195(1), 222–237.

Reigber C., Balmino G., Schwintzer P., Biancale R., Bode A., Lemoine J.-M., König R., Loyer S., Neumayer H., Marty J.-C., Barthelmes F., Perosanz F. and Zhu S. Y. (2002). A high-quality global gravity field model from CHAMP GPS tracking data and accelerometry (EIGEN-1S). *Geophysical Research Letters* 29(14), 37–1–37–4. doi:10.1029/2002GL015064.

Rummel R. (1986). Satellite Gradiometry. In H. Sünkel (Ed.), *Mathematical and Numerical Techniques in Physical Geodesy*. Lecture Notes in Earth Sciences, Vol. 7. Springer-Verlag, Berlin.

Rummel R. (2012). Height unification using GOCE. *Journal of Geodetic Science* 2(4), 355–362. doi:10.2478/v10156-011-0047-2.

Rummel R., Gruber T. and Koop R. (2004). High Level Processing Facility for GOCE: Products and Processing Strategy. In H. Lacoste (Ed.), *Proceedings of the 2nd International GOCE User Workshop* GOCE, the Geoid and Oceanography. Frascati, Italy: ESA SP-569.

Rummel R., Yi W. and Stummer C. (2011). GOCE gravitational gradiometry. *Journal of Geodesy* 85, 777–790. doi:10.1007/s00190-011-0500-0.

Sampietro D., Reguzzoni M. and Braitenberg C. (2014). GOCE Estimated Moho Beneath the Tibetan Plateau and Himalaya. In C. Rizos, and P. Willis (Eds.), *Earth on the Edge: Science for a Sustainable Planet* (pp. 391–397). International Association of Geodesy Symposia, Vol. 139. Springer Berlin Heidelberg. doi:10.1007/978-3-642-37222-3_53.

Schmid S. M., Aebli H. R., Heller F. and Zingg A. (1989). The role of the Periadriatic Line in the tectonic evolution of the Alps. *Geological Society, London, Special Publications* 45(1), 153–171.

doi:10.1144/GSL.SP.1989.045.01.08.

Seeber G. (1993). *Satellite Geodesy*. De Gruyter, Berlin.

Shin Y. H., Xu H., Braitenberg C., Fang J. and Wang Y. (2007). Moho undulations beneath Tibet from GRACE-integrated gravity data. *Geophysical Journal International* 170, 971–985. doi:10.1111/j.1365-246X.2007.03457.x.

Siemes C., Haagmans R., Kern M., Plank G. and Floberghagen R. (2012). Monitoring GOCE gradiometer calibration parameters using accelerometer and star sensor data: methodology and first results. *Journal of Geodesy* 86(8), 629–645. doi:10.1007/s00190-012-0545-8.

Simeoni O. and Brückl E. (2009). The Effect of Gravity Stripping on the Resolution of Deep Crustal Structures in the Eastern Alps and Surrounding Regions. *Austrian Journal of Earth Sciences* 102(2), 157–169.

Sjöberg L. (1998). The atmospheric geoid and gravity corrections. *Bollettino di Geodesia e Scienze Affini* 57(4), 421–435.

Sjöberg L. (2006). The effects of Stokes's formula for an ellipsoidal layering of the Earth's atmosphere. *Journal of Geodesy* 79(12), 675–681. doi:10.1007/s00190-005-0018-4.

Sjöberg L. (2009). Solving Vening Meinesz-Moritz inverse problem in isostasy. *Geophysical Journal International* 179(3), 1527–1536.

Sjöberg L. E. (1999). The IAG approach to the atmospheric geoid correction in Stokes' formula and a new strategy. *Journal of Geodesy* 73(7), 362–366. doi:10.1007/s001900050254.

Steffen R., Steffen H. and Jentzsch G. (2011). A three-dimensional Moho depth model for the Tien Shan from EGM2008 gravity data. *Tectonics* 30.

Stipčević J., Tkalčić H., Herak M., Markušić S. and Herak D. (2011). Crustal and uppermost mantle structure beneath the External Dinarides, Croatia, determined from teleseismic receiver functions. *Geophysical Journal International* 185(3), 1103–1119. doi:10.1111/j.1365-246X.2011.05004.x.

Stummer C. (2013). *Gradiometer Data Processing and Analysis for the GOCE Mission*. Ph.D. thesis, DGK, Reihe C, 617, Verlag der Bayerischen Akademie der Wissenschaften, München. ISBN: 978-3-7696-5107-2.

Stummer C., Siemes C., Pail R., Frommknecht B. and Floberghagen R. (2012). Upgrade of the GOCE Level 1b gradiometer processor. *Advances in Space Research* 49(4), 739–752. doi:10.1016/j.asr.2011.11.027.

Sünkel H., Bartelme N., Fuchs H., Hanafy M., Schuh W.-D. and Wieser M. (1987). The Gravity Field in Austria. In A. G. Commission (Ed.), *The Gravity Field in Austria* VI (pp. 47–75). Austrian Geodetic Commission.

Tapley B. D., Chambers D. P., Bettadpur S. and Ries J. C. (2003). Large scale ocean circulation from the GRACE GGM01 Geoid. *Geophysical Research Letters* 30(22). doi:10.1029/2003GL018622.

Torge W. (1989). *Gravimetry*. De Gruyter, Berlin.

Tscherning C. C. (1976). Computation of the Second-Order Derivatives of the Normal Potential Based on the Representation by a Legendre Series. *Manuscripta Geodetica* 1, 71–92.

Tscherning C. C. (1993). Computation of covariances of derivatives of the anomalous gravity potential in a rotated reference frame. *Manuscripta Geodetica* 83, 115–125.

Tscherning C. C. and Rapp R. (1974). *Closed covariance expressions for gravity anomalies, geoid undulations, and deflections of the vertical implied by anomaly degree variance models*. Technical Report, No. 208, Department of Geodetic Science and Surveying, Ohio State University.

U.S. Geological Survey (2014). *GTOPO30 Documentation*. URL: http://webgis.wr.usgs.gov/globalgis/gtopo30/gtopo30.htm accessed on 2014-03-10.

Ustaszewski K., Kounov A., Schmid S. M., Schaltegger U., Krenn E., Frank W. and Fügenschuh B. (2010). Evolution of the Adria-Europe plate boundary in the northern Dinarides: From continent-continent collision to back-arc extension. *Tectonics* 29(6). doi:10.1029/2010TC002668.

Visser P. N. A. M. (2011). A glimpse at the GOCE satellite gravity gradient observations. *Advances in Space Research* 47(3), 393–401. doi:10.1016/j.asr.2010.09.015.

Wagner M., Kissling E. and Husen S. (2012). Combining controlled-source seismology and local earthquake tomography to derive a 3-D crustal model of the western Alpine region. *Geophysical Journal International* 191, 789–802. doi:10.1111/j.1365-246X.2012.05655.x.

Welch P. D. (1967). The Use of Fast Fourier Transform for the Estimation of Power Spectra: A Method Based on Time Averaging Over Short, Modified Periodograms. *IEEE Transactions on Audio and Electroacoustics* AU-15(2).

Wild-Pfeiffer F. (2007). *Auswirkungen topographisch-isostatischer Massen auf die Satellitengradiometrie*. Ph.D. thesis, DGK, Reihe C, 604, Verlag der Bayerischen Akademie der Wissenschaften, München. ISBN: 3-7696-5043-3.

Woodhouse J. H. and Deuss A. (2007). Theory and Observations - Earth's Free Oscillations. In G. Schubert (Ed.), *Treatise on Geophysics* (pp. 31–65). Elsevier , Vol. 1.

Appendix A

A.1 Associated Legendre functions and polynomials

The Legendre function is defined as a solution of Legendre's differential equation and reads

$$P_{nm}(t) = \frac{1}{2^n\, n!} \left(1 - t^2\right)^{m/2} \frac{d^{n+m}}{dt^{n+m}} (t^2 - 1)^n \,, \tag{A.1}$$

with the integers n defining the degree and m the order of the Legendre function. For $m \neq 0$ this function is also called associated Legendre function. In case of $m = 0$, the Legendre function reduces to

$$P_{n0}(t) = P_n(t) = \frac{1}{2^n\, n!} \frac{d^n (t^2 - 1)^n}{dt^n} \,, \tag{A.2}$$

which are the Legendre polynomials of degree n given in terms of the Rodrigues formula. Alternatively, the Legendre polynomials can be evaluated recursively by Bonnet's recursion formula

$$P_{n+1}(t) = \frac{2n+1}{n+1}\, t\, P_n(t) - \frac{n}{n+1}\, P_{n-1}(t) \,. \tag{A.3}$$

By inserting Eq. (A.2) into Eq. (A.1), the Legendre function can also be represented by Legendre polynomials as

$$P_{nm}(t) = \left(1 - t^2\right)^{m/2} \frac{d^m P_n(t)}{dt^m} \,. \tag{A.4}$$

The fully normalized Legendre functions can be derived by

$$\bar{P}_{nm}(t) = \sqrt{(2 - \delta_{0m})(2n+1)\frac{(n-m)!}{(n+m)!}} P_{nm}(t) \,. \tag{A.5}$$

A.2 Applying the chain- and product rule of differentiation

The covariance function K is a function of the radii r, r' and of $t = \cos\psi$, where the latter is in turn depending on the coordinates φ, λ and φ', λ'. The derivatives with respect to $\varphi, \lambda, \varphi'$ or λ' up to order four by applying the chain- and product rule of differentiation

$$\frac{\partial K}{\partial \lambda} = \frac{\partial K}{\partial t}\,\frac{\partial t}{\partial \lambda}\,, \tag{A.6}$$

$$\frac{\partial^2 K}{\partial \lambda^2} = \frac{\partial^2 K}{\partial t^2}\left(\frac{\partial t}{\partial \lambda}\right)^2 + \frac{\partial K}{\partial t}\,\frac{\partial^2 t}{\partial \lambda^2}\,, \tag{A.7}$$

$$\frac{\partial^2 K}{\partial \lambda \partial \lambda'} = \frac{\partial^2 K}{\partial t^2}\frac{\partial t}{\partial \lambda}\frac{\partial t}{\partial \lambda'} + \frac{\partial K}{\partial t}\,\frac{\partial^2 t}{\partial \lambda \partial \lambda'}\,, \tag{A.8}$$

$$\frac{\partial^3 K}{\partial \lambda^2 \partial \lambda'} = \frac{\partial^3 K}{\partial t^3}\left(\frac{\partial t}{\partial \lambda}\right)^2 \frac{\partial t}{\partial \lambda'} + 2\frac{\partial^2 K}{\partial t^2}\frac{\partial^2 t}{\partial \lambda \partial \lambda'}\frac{\partial t}{\partial \lambda} + \frac{\partial^2 K}{\partial t^2}\frac{\partial^2 t}{\partial \lambda^2}\frac{\partial t}{\partial \lambda'} + \frac{\partial K}{\partial t}\,\frac{\partial^3 t}{\partial \lambda^2 \partial \lambda'}\,, \tag{A.9}$$

$$\begin{aligned}\frac{\partial^3 K}{\partial \varphi \partial \lambda \partial \lambda'} =& \frac{\partial^3 K}{\partial t^3}\frac{\partial t}{\partial \varphi}\frac{\partial t}{\partial \lambda}\frac{\partial t}{\partial \lambda'} + \frac{\partial^2 K}{\partial t^2}\frac{\partial^2 t}{\partial \lambda \partial \lambda'}\frac{\partial t}{\partial \varphi} + \frac{\partial^2 K}{\partial t^2}\frac{\partial^2 t}{\partial \phi \partial \lambda}\frac{\partial t}{\partial \lambda'} + \frac{\partial^2 K}{\partial t^2}\frac{\partial^2 t}{\partial \phi \partial \lambda'}\frac{\partial t}{\partial \lambda} + \\ &+ \frac{\partial K}{\partial t}\,\frac{\partial^3 t}{\partial \phi \partial \lambda \partial \lambda'}\,,\end{aligned} \tag{A.10}$$

$$\begin{aligned}\frac{\partial^4 K}{\partial \lambda^2 \partial \lambda'^2} =& \frac{\partial^4 K}{\partial t^4}\left(\frac{\partial t}{\partial \lambda}\right)^2\left(\frac{\partial t}{\partial \lambda'}\right)^2 + 4\frac{\partial^3 K}{\partial t^3}\frac{\partial^2 t}{\partial \lambda \partial \lambda'}\frac{\partial t}{\partial \lambda}\frac{\partial t}{\partial \lambda'} + \frac{\partial^3 K}{\partial t^3}\left(\frac{\partial t}{\partial \lambda}\right)^2\frac{\partial^2 t}{\partial \lambda'^2} \\ &+ \frac{\partial^3 K}{\partial t^3}\frac{\partial^2 t}{\partial \lambda^2}\left(\frac{\partial t}{\partial \lambda'}\right)^2 + 2\frac{\partial^2 K}{\partial t^2}\left(\frac{\partial^2 t}{\partial \lambda \partial \lambda'}\right)^2 + 2\frac{\partial^2 K}{\partial t^2}\frac{\partial t}{\partial \lambda}\frac{\partial^3 t}{\partial \lambda \partial \lambda'^2} + \\ &+ 2\frac{\partial^2 K}{\partial t^2}\frac{\partial t}{\partial \lambda'}\frac{\partial^3 t}{\partial \lambda^2 \partial \lambda'} + \frac{\partial^2 K}{\partial t^2}\frac{\partial^2 t}{\partial \lambda^2}\frac{\partial^2 t}{\partial \lambda'^2} + \frac{\partial K}{\partial t}\,\frac{\partial^4 t}{\partial \lambda^2 \partial \lambda'^2}\,,\end{aligned} \tag{A.11}$$

$$\begin{aligned}\frac{\partial^4 K}{\partial \varphi \partial \lambda \partial \varphi' \partial \lambda'} =& \frac{\partial^4 K}{\partial t^4}\frac{\partial t}{\partial \varphi}\frac{\partial t}{\partial \lambda}\frac{\partial t}{\partial \varphi'}\frac{\partial t}{\partial \lambda'} + \frac{\partial^3 K}{\partial t^3}\frac{\partial^2 t}{\partial \varphi \partial \varphi'}\frac{\partial t}{\partial \lambda}\frac{\partial t}{\partial \lambda'} + \frac{\partial^3 K}{\partial t^3}\frac{\partial t}{\partial \varphi}\frac{\partial^2 t}{\partial \lambda \partial \varphi'}\frac{\partial t}{\partial \lambda'} + \\ &+ \frac{\partial^3 K}{\partial t^3}\frac{\partial t}{\partial \varphi}\frac{\partial t}{\partial \lambda}\frac{\partial^2 t}{\partial \varphi' \partial \lambda'} + \frac{\partial^3 K}{\partial t^3}\frac{\partial^2 t}{\partial \varphi \partial \lambda'}\frac{\partial t}{\partial \lambda}\frac{\partial t}{\partial \varphi'} + \frac{\partial^2 K}{\partial t^2}\frac{\partial^3 t}{\partial \varphi \partial \lambda' \partial \varphi'}\frac{\partial t}{\partial \lambda} + \\ &+ \frac{\partial^2 K}{\partial t^2}\frac{\partial^2 t}{\partial \varphi \partial \lambda'}\frac{\partial^2 t}{\partial \lambda \partial \varphi'} + \frac{\partial^3 K}{\partial t^3}\frac{\partial t}{\partial \varphi}\frac{\partial t}{\partial \varphi'}\frac{\partial^2 t}{\partial \lambda \partial \lambda'} + \frac{\partial^2 K}{\partial t^2}\frac{\partial^2 t}{\partial \varphi \partial \varphi'}\frac{\partial^2 t}{\partial \lambda \partial \lambda'} + \\ &+ \frac{\partial^2 K}{\partial t^2}\frac{\partial t}{\partial \varphi}\frac{\partial^3 t}{\partial \lambda \partial \lambda' \partial \varphi'} + \frac{\partial^3 K}{\partial t^3}\frac{\partial t}{\partial \lambda'}\frac{\partial t}{\partial \varphi'}\frac{\partial^2 t}{\partial \varphi \partial \lambda} + \frac{\partial^2 K}{\partial t^2}\frac{\partial^2 t}{\partial \varphi \partial \lambda}\frac{\partial^2 t}{\partial \varphi' \partial \lambda'} + \\ &+ \frac{\partial^2 K}{\partial t^2}\frac{\partial t}{\partial \lambda'}\frac{\partial^3 t}{\partial \varphi \partial \lambda \partial \varphi'} + \frac{\partial^2 K}{\partial t^2}\frac{\partial t}{\partial \varphi'}\frac{\partial^3 t}{\partial \varphi \partial \lambda \partial \lambda'} + \frac{\partial K}{\partial t}\,\frac{\partial^4 t}{\partial \varphi \partial \lambda \partial \varphi' \partial \lambda'}\,.\end{aligned} \tag{A.12}$$

Note that the differentiations are valid for λ or φ in the same manner, if the variables are consistently interchanged in the corresponding equations.

A.3 Covariance expressions for quantities up to second order derivatives of the anomalous potential

First order derivatives in P

$$cov(T_y, T) = \frac{1}{r\cos\varphi}\,\frac{\partial K}{\partial \lambda}$$

$$cov(T_x, T) = \frac{1}{r}\frac{\partial K}{\partial \varphi}$$

$$cov(T_z, T) = \frac{\partial K}{\partial r}$$

For first order derivatives in Q interchange coordinates with r', φ' and λ'.

First order derivatives in P and Q

$$cov(T_y, T_{y'}) = \frac{1}{r\cos\varphi}\,\frac{\partial}{\partial \lambda}\left(\frac{1}{r'\cos\varphi'}\,\frac{\partial K}{\partial \lambda'}\right) = \frac{1}{rr'\cos\varphi\cos\varphi'}\,\frac{\partial^2 K}{\partial\lambda\partial\lambda'}$$

$$cov(T_y, T_{x'}) = \frac{1}{r\cos\varphi}\,\frac{\partial}{\partial \lambda}\left(\frac{1}{r'}\,\frac{\partial K}{\partial \varphi'}\right) = \frac{1}{rr'\cos\varphi}\,\frac{\partial^2 K}{\partial\lambda\partial\varphi'}$$

$$cov(T_y, T_{z'}) = \frac{1}{r\cos\varphi}\,\frac{\partial}{\partial \lambda}\left(\frac{\partial K}{\partial r'}\right) = \frac{1}{r'\cos\varphi}\,\frac{\partial^2 K}{\partial\lambda\partial r'}$$

$$cov(T_x, T_{x'}) = \frac{1}{r}\,\frac{\partial}{\partial \varphi}\left(\frac{1}{r'}\,\frac{\partial K}{\partial \varphi'}\right) = \frac{1}{rr'}\,\frac{\partial^2 K}{\partial\varphi\partial\varphi'}$$

$$cov(T_x, T_{z'}) = \frac{1}{r}\,\frac{\partial}{\partial \varphi}\left(\frac{\partial K}{\partial r'}\right) = \frac{1}{r}\,\frac{\partial^2 K}{\partial\varphi\partial r'}$$

$$cov(T_z, T_{z'}) = \frac{\partial^2 K}{\partial r\partial r'}$$

Second order derivatives in P

$$cov(T_{yy}, T) = \frac{1}{r}\,\frac{\partial K}{\partial r} - \frac{\tan\varphi}{r^2}\,\frac{\partial K}{\partial \varphi} + \frac{1}{r^2\,\cos^2\varphi}\,\frac{\partial^2 K}{\partial \lambda^2}$$

$$cov(T_{yx}, T) = \frac{1}{r^2\,\cos\varphi}\,\frac{\partial^2 K}{\partial\varphi\partial\lambda} + \frac{\tan\varphi}{r^2\,\cos\varphi}\,\frac{\partial K}{\partial \lambda}$$

$$cov(T_{yz}, T) = \frac{1}{r\,\cos\varphi}\,\frac{\partial^2 K}{\partial r\partial\lambda} - \frac{1}{r^2\,\cos\varphi}\,\frac{\partial K}{\partial \lambda}$$

$$cov(T_{xx}, T) = \frac{1}{r}\,\frac{\partial K}{\partial r} + \frac{1}{r^2}\,\frac{\partial^2 K}{\partial \varphi^2}$$

$$cov(T_{xz}, T) = \frac{1}{r}\,\frac{\partial^2 K}{\partial r\partial\varphi} - \frac{1}{r^2}\,\frac{\partial K}{\partial \varphi}$$

$$cov(T_{zz}, T) = \frac{\partial^2 K}{\partial r^2}$$

For second order derivatives in Q interchange coordinates with r', φ' and λ'.

Second order derivatives in P and first order derivatives in Q

$$\begin{aligned} cov(T_{yy}, T_{y'}) &= \left(\frac{1}{r}\frac{\partial}{\partial r} - \frac{\tan\varphi}{r^2}\frac{\partial}{\partial\varphi} + \frac{1}{r^2\,\cos^2\varphi}\frac{\partial^2}{\partial\lambda^2}\right)\left(\frac{1}{r'\cos\varphi'}\frac{\partial K}{\partial\lambda'}\right) = \\ &= \frac{1}{rr'\cos\varphi'}\frac{\partial^2 K}{\partial r\partial\lambda'} - \frac{\tan\varphi}{r^2r'\cos\varphi'}\frac{\partial^2 K}{\partial\varphi\partial\lambda'} + \frac{1}{r^2r'\,\cos^2\varphi\,\cos\varphi'}\frac{\partial^3 K}{\partial\lambda^2\partial\lambda'} \\ cov(T_{yy}, T_{x'}) &= \left(\frac{1}{r}\frac{\partial}{\partial r} - \frac{\tan\varphi}{r^2}\frac{\partial}{\partial\varphi} + \frac{1}{r^2\,\cos^2\varphi}\frac{\partial^2}{\partial\lambda^2}\right)\left(\frac{1}{r'}\frac{\partial K}{\partial\varphi'}\right) = \\ &= \frac{1}{rr'}\frac{\partial^2 K}{\partial r\partial\varphi'} - \frac{\tan\varphi}{r^2r'}\frac{\partial^2 K}{\partial\varphi\partial\varphi'} + \frac{1}{r^2r'\,\cos^2\varphi}\frac{\partial^3 K}{\partial\lambda^2\partial\varphi'} \\ cov(T_{yy}, T_{z'}) &= \left(\frac{1}{r}\frac{\partial}{\partial r} - \frac{\tan\varphi}{r^2}\frac{\partial}{\partial\varphi} + \frac{1}{r^2\,\cos^2\varphi}\frac{\partial^2}{\partial\lambda^2}\right)\left(\frac{\partial K}{\partial r'}\right) = \\ &= \frac{1}{r}\frac{\partial^2 K}{\partial r\partial r'} - \frac{\tan\varphi}{r^2}\frac{\partial^2 K}{\partial\varphi\partial r'} + \frac{1}{r^2\,\cos^2\varphi}\frac{\partial^3 K}{\partial\lambda^2\partial r'} \end{aligned}$$

$$\begin{aligned} cov(T_{yx}, T_{y'}) &= \left(\frac{1}{r^2\cos\varphi}\frac{\partial^2}{\partial\varphi\partial\lambda} + \frac{\tan\varphi}{r^2\cos\varphi}\frac{\partial}{\partial\lambda}\right)\left(\frac{1}{r'\cos\varphi'}\frac{\partial K}{\partial\lambda'}\right) = \\ &= \frac{1}{r^2r'\cos\varphi\cos\varphi'}\frac{\partial^3 K}{\partial\varphi\partial\lambda\partial\lambda'} + \frac{\tan\varphi}{r^2r'\cos\varphi\cos\varphi'}\frac{\partial^2 K}{\partial\lambda\partial\lambda'} \\ cov(T_{yx}, T_{x'}) &= \left(\frac{1}{r^2\cos\varphi}\frac{\partial^2}{\partial\varphi\partial\lambda} + \frac{\tan\varphi}{r^2\cos\varphi}\frac{\partial}{\partial\lambda}\right)\left(\frac{1}{r'}\frac{\partial K}{\partial\varphi'}\right) = \\ &= \frac{1}{r^2r'\cos\varphi}\frac{\partial^3 K}{\partial\varphi\partial\lambda\partial\varphi'} + \frac{\tan\varphi}{r^2r'\cos\varphi}\frac{\partial^2 K}{\partial\lambda\partial\varphi'} \\ cov(T_{yx}, T_{z'}) &= \left(\frac{1}{r^2\cos\varphi}\frac{\partial^2}{\partial\varphi\partial\lambda} + \frac{\tan\varphi}{r^2\cos\varphi}\frac{\partial}{\partial\lambda}\right)\left(\frac{\partial K}{\partial r'}\right) = \\ &= \frac{1}{r^2\cos\varphi}\frac{\partial^3 K}{\partial\varphi\partial\lambda\partial r'} + \frac{\tan\varphi}{r^2\cos\varphi}\frac{\partial^2 K}{\partial\lambda\partial r'} \end{aligned}$$

$$\begin{aligned} cov(T_{yz}, T_{y'}) &= \left(\frac{1}{r\,\cos\varphi}\frac{\partial^2}{\partial r\partial\lambda} - \frac{1}{r^2\,\cos\varphi}\frac{\partial}{\partial\lambda}\right)\left(\frac{1}{r'\cos\varphi'}\frac{\partial K}{\partial\lambda'}\right) = \\ &= \frac{1}{rr'\,\cos\varphi\cos\varphi'}\frac{\partial^3 K}{\partial r\partial\lambda\partial\lambda'} - \frac{1}{r^2r'\,\cos\varphi\cos\varphi'}\frac{\partial^2 K}{\partial\lambda\partial\lambda'} \\ cov(T_{yz}, T_{x'}) &= \left(\frac{1}{r\,\cos\varphi}\frac{\partial^2}{\partial r\partial\lambda} - \frac{1}{r^2\,\cos\varphi}\frac{\partial}{\partial\lambda}\right)\left(\frac{1}{r'}\frac{\partial K}{\partial\varphi'}\right) = \\ &= \frac{1}{rr'\,\cos\varphi}\frac{\partial^3 K}{\partial r\partial\lambda\partial\varphi'} - \frac{1}{r^2r'\,\cos\varphi}\frac{\partial^2 K}{\partial\lambda\partial\varphi'} \end{aligned}$$

$$cov(T_{yz}, T_{z'}) = \left(\frac{1}{r\ \cos\varphi}\ \frac{\partial^2}{\partial r \partial \lambda} - \frac{1}{r^2\ \cos\varphi}\ \frac{\partial}{\partial \lambda}\right)\left(\frac{\partial K}{\partial r'}\right) = \\ = \frac{1}{r\ \cos\varphi}\ \frac{\partial^3 K}{\partial r \partial \lambda \partial r'} - \frac{1}{r^2\ \cos\varphi}\ \frac{\partial^2 K}{\partial \lambda \partial r'}$$

$$cov(T_{xx}, T_{y'}) = \left(\frac{1}{r}\ \frac{\partial}{\partial r} + \frac{1}{r^2}\ \frac{\partial^2}{\partial \varphi^2}\right)\left(\frac{1}{r' \cos\varphi'}\ \frac{\partial K}{\partial \lambda'}\right) = \\ = \frac{1}{rr' \cos\varphi'}\ \frac{\partial^2 K}{\partial r \partial \lambda'} + \frac{1}{r^2 r' \cos\varphi'}\ \frac{\partial^3 K}{\partial \varphi^2 \partial \lambda'}$$

$$cov(T_{xx}, T_{x'}) = \left(\frac{1}{r}\ \frac{\partial}{\partial r} + \frac{1}{r^2}\ \frac{\partial^2}{\partial \varphi^2}\right)\left(\frac{1}{r'}\ \frac{\partial K}{\partial \varphi'}\right) = \frac{1}{rr'}\ \frac{\partial^2 K}{\partial r \partial \varphi'} + \frac{1}{r^2 r'}\ \frac{\partial^3 K}{\partial \varphi^2 \partial \varphi'}$$

$$cov(T_{xx}, T_{z'}) = \left(\frac{1}{r}\ \frac{\partial}{\partial r} + \frac{1}{r^2}\ \frac{\partial^2}{\partial \varphi^2}\right)\left(\frac{\partial K}{\partial r'}\right) = \frac{1}{r}\ \frac{\partial^2 K}{\partial r \partial r'} + \frac{1}{r^2}\ \frac{\partial^3 K}{\partial \varphi^2 \partial r'}$$

$$cov(T_{xz}, T_{y'}) = \left(\frac{1}{r}\ \frac{\partial^2 K}{\partial r \partial \varphi} - \frac{1}{r^2}\ \frac{\partial K}{\partial \varphi}\right)\left(\frac{1}{r' \cos\varphi'}\ \frac{\partial K}{\partial \lambda'}\right) = \\ = \frac{1}{rr' \cos\varphi'}\ \frac{\partial^3 K}{\partial r \partial \varphi \partial \lambda'} - \frac{1}{r^2 r' \cos\varphi'}\ \frac{\partial^2 K}{\partial \varphi \partial \lambda'}$$

$$cov(T_{xz}, T_{x'}) = \left(\frac{1}{r}\ \frac{\partial^2 K}{\partial r \partial \varphi} - \frac{1}{r^2}\ \frac{\partial K}{\partial \varphi}\right)\left(\frac{1}{r'}\ \frac{\partial K}{\partial \varphi'}\right) = \frac{1}{rr'}\ \frac{\partial^3 K}{\partial r \partial \varphi \partial \varphi'} - \frac{1}{r^2 r'}\ \frac{\partial^2 K}{\partial \varphi \partial \varphi'}$$

$$cov(T_{xz}, T_{z'}) = \left(\frac{1}{r}\ \frac{\partial^2 K}{\partial r \partial \varphi} - \frac{1}{r^2}\ \frac{\partial K}{\partial \varphi}\right)\left(\frac{\partial K}{\partial r'}\right) = \frac{1}{r}\ \frac{\partial^3 K}{\partial r \partial \varphi \partial r'} - \frac{1}{r^2}\ \frac{\partial^2 K}{\partial \varphi \partial r'}$$

$$cov(T_{zz}, T_{y'}) = \frac{\partial^2}{\partial r^2}\left(\frac{1}{r' \cos\varphi'}\ \frac{\partial K}{\partial \lambda'}\right) = \frac{1}{r' \cos\varphi'}\ \frac{\partial^3 K}{\partial r^2 \partial \lambda'}$$

$$cov(T_{zz}, T_{x'}) = \frac{\partial^2}{\partial r^2}\left(\frac{1}{r'}\ \frac{\partial K}{\partial \varphi'}\right) = \frac{1}{r'}\ \frac{\partial^3 K}{\partial r^2 \partial \varphi'}$$

$$cov(T_{zz}, T_{z'}) = \frac{\partial^2}{\partial r^2}\left(\frac{\partial K}{\partial r'}\right) = \frac{\partial^3 K}{\partial r^2 \partial r'}$$

Second order derivatives in P and Q

$$cov(T_{yy}, T_{y'y'}) = \left(\frac{1}{r}\frac{\partial}{\partial r} - \frac{\tan\varphi}{r^2}\frac{\partial}{\partial\varphi} + \frac{1}{r^2\,\cos^2\varphi}\frac{\partial^2}{\partial\lambda^2}\right)\left(\frac{1}{r'}\frac{\partial K}{\partial r'} - \frac{\tan\varphi'}{r'^2}\frac{\partial K}{\partial\varphi'} + \right.$$
$$\left. + \frac{1}{r'^2\,\cos^2\varphi'}\frac{\partial^2 K}{\partial\lambda'^2}\right) = \frac{1}{rr'}\frac{\partial^2 K}{\partial r\partial r'} - \frac{\tan\varphi'}{rr'^2}\frac{\partial^2 K}{\partial r\partial\varphi'} + \frac{1}{rr'^2\,\cos^2\varphi'}\frac{\partial^3 K}{\partial r\partial\lambda'^2} +$$
$$- \frac{\tan\varphi}{r^2r'}\frac{\partial^2 K}{\partial\varphi\partial r'} + \frac{\tan\varphi\tan\varphi'}{r^2r'^2}\frac{\partial^2 K}{\partial\varphi\partial\varphi'} - \frac{\tan\varphi}{r^2r'^2\,\cos^2\varphi'}\frac{\partial^3 K}{\partial\varphi\partial\lambda'^2} +$$
$$+ \frac{1}{r^2r'\,\cos^2\varphi}\frac{\partial^3 K}{\partial\lambda^2\partial r'} - \frac{\tan\varphi'}{r^2r'^2\cos^2\varphi}\frac{\partial^3 K}{\partial\lambda^2\partial\varphi'} + \frac{1}{r^2r'^2\,\cos^2\varphi\cos^2\varphi'}\frac{\partial^4 K}{\partial\lambda^2\partial\lambda'^2}$$

$$cov(T_{yy}, T_{y'x'}) = \left(\frac{1}{r}\frac{\partial}{\partial r} - \frac{\tan\varphi}{r^2}\frac{\partial}{\partial\varphi} + \frac{1}{r^2\,\cos^2\varphi}\frac{\partial^2}{\partial\lambda^2}\right)\left(\frac{1}{r'^2\cos\varphi'}\frac{\partial^2 K}{\partial\varphi'\partial\lambda'} + \right.$$
$$\left. + \frac{\tan\varphi'}{r'^2\cos\varphi'}\frac{\partial K}{\partial\lambda'}\right) = \frac{\tan\varphi'}{rr'^2\cos\varphi'}\frac{\partial^2 K}{\partial r\partial\lambda'} - \frac{\tan\varphi\tan\varphi'}{r^2r'^2\cos\varphi'}\frac{\partial^2 K}{\partial\varphi\partial\lambda'} +$$
$$+ \frac{tan\varphi'}{r^2r'^2\cos\varphi\cos^2\varphi'}\frac{\partial^3 K}{\partial\lambda^2\partial\lambda'} + \frac{1}{rr'^2\cos\varphi'}\frac{\partial^3 K}{\partial r\partial\varphi'\partial\lambda'} +$$
$$- \frac{\tan\varphi}{r^2r'^2\cos\varphi'}\frac{\partial^3 K}{\partial\varphi\partial\varphi'\partial\lambda'} + \frac{1}{r^2r'^2\cos^2\varphi\cos\varphi'}\frac{\partial^4 K}{\partial\lambda^2\partial\varphi'\partial\lambda'}$$

$$cov(T_{yy}, T_{y'z'}) = \left(\frac{1}{r}\frac{\partial}{\partial r} - \frac{\tan\varphi}{r^2}\frac{\partial}{\partial\varphi} + \frac{1}{r^2\,\cos^2\varphi}\frac{\partial^2}{\partial\lambda^2}\right)\left(\frac{1}{r'\,\cos\varphi'}\frac{\partial^2 K}{\partial r'\partial\lambda'} + \right.$$
$$\left. - \frac{1}{r'^2\,\cos\varphi'}\frac{\partial K}{\partial\lambda'}\right) = \frac{1}{rr'\cos\varphi'}\frac{\partial^3 K}{\partial r\partial r'\partial\lambda'} - \frac{\tan\varphi}{r^2r'\cos\varphi'}\frac{\partial^3 K}{\partial\varphi\partial r'\partial\lambda'} +$$
$$+ \frac{1}{r^2r'\,\cos^2\varphi\cos\varphi'}\frac{\partial^4 K}{\partial\lambda^2\partial r'\partial\lambda'} - \frac{1}{rr'^2\,\cos\varphi'}\frac{\partial^2 K}{\partial r\partial\lambda'} +$$
$$+ \frac{\tan\varphi}{r^2r'^2\,\cos\varphi'}\frac{\partial^2 K}{\partial\varphi\partial\lambda'} - \frac{1}{r^2r'^2\,\cos^2\varphi\cos\varphi'}\frac{\partial^3 K}{\partial\lambda^2\partial\lambda'}$$

$$cov(T_{yy}, T_{x'x'}) = \left(\frac{1}{r}\frac{\partial}{\partial r} - \frac{\tan\varphi}{r^2}\frac{\partial}{\partial\varphi} + \frac{1}{r^2\,\cos^2\varphi}\frac{\partial^2}{\partial\lambda^2}\right)\left(\frac{1}{r'}\frac{\partial K}{\partial r'} + \frac{1}{r'^2}\frac{\partial^2 K}{\partial\varphi'^2}\right) =$$
$$= \frac{1}{rr'}\frac{\partial^2 K}{\partial r\partial r'} - \frac{\tan\varphi}{r^2r'}\frac{\partial^2 K}{\partial\varphi\partial r'} + \frac{1}{r^2r'\,\cos^2\varphi}\frac{\partial^3 K}{\partial\lambda^2\partial r'} +$$
$$+ \frac{1}{rr'^2}\frac{\partial^3 K}{\partial r\partial\varphi'^2} - \frac{\tan\varphi}{r^2r'^2}\frac{\partial^3 K}{\partial\varphi\partial\varphi'^2} + \frac{1}{r^2r'^2\,\cos^2\varphi}\frac{\partial^4 K}{\partial\lambda^2\partial\varphi'^2}$$

$$cov(T_{yy}, T_{x'z'}) = \left(\frac{1}{r}\frac{\partial}{\partial r} - \frac{\tan\varphi}{r^2}\frac{\partial}{\partial\varphi} + \frac{1}{r^2\,\cos^2\varphi}\frac{\partial^2}{\partial\lambda^2}\right)\left(\frac{1}{r'}\frac{\partial^2 K}{\partial r'\partial\varphi'} - \frac{1}{r'^2}\frac{\partial K}{\partial\varphi'}\right) =$$
$$= \frac{1}{rr'}\frac{\partial^3 K}{\partial r\partial r'\partial\varphi'} - \frac{\tan\varphi}{r^2r'}\frac{\partial^3 K}{\partial\varphi\partial r'\partial\varphi'} + \frac{1}{r^2r'\,\cos^2\varphi}\frac{\partial^4 K}{\partial\lambda^2\partial r'\partial\varphi'} +$$
$$- \frac{1}{rr'^2}\frac{\partial^2 K}{\partial r\partial\varphi'} + \frac{\tan\varphi}{r^2r'^2}\frac{\partial^2 K}{\partial\varphi\partial\varphi'} - \frac{1}{r^2r'^2\,\cos^2\varphi}\frac{\partial^3 K}{\partial\lambda^2\partial\varphi'}$$

$$cov(T_{yy}, T_{z'z'}) = \left(\frac{1}{r}\frac{\partial}{\partial r} - \frac{\tan\varphi}{r^2}\frac{\partial}{\partial\varphi} + \frac{1}{r^2\,\cos^2\varphi}\frac{\partial^2}{\partial\lambda^2}\right)\left(\frac{\partial^2 K}{\partial r'^2}\right) =$$
$$= \frac{1}{r}\frac{\partial^3 K}{\partial r\partial r'^2} - \frac{\tan\varphi}{r^2}\frac{\partial^3 K}{\partial\varphi\partial r'^2} + \frac{1}{r^2\,\cos^2\varphi}\frac{\partial^4 K}{\partial\lambda^2\partial r'^2}$$

$$
\begin{aligned}
cov(T_{yx}, T_{y'x'}) &= \left(\frac{1}{r^2\cos\varphi}\,\frac{\partial^2}{\partial\varphi\partial\lambda} + \frac{\tan\varphi}{r^2\cos\varphi}\,\frac{\partial}{\partial\lambda}\right)\left(\frac{1}{r'^2\cos\varphi'}\,\frac{\partial^2 K}{\partial\varphi'\partial\lambda'} + \frac{\tan\varphi'}{r'^2\cos\varphi'}\,\frac{\partial K}{\partial\lambda'}\right) = \\
&= \frac{1}{r^2r'^2\,\cos\varphi\cos\varphi'}\,\frac{\partial^4 K}{\partial\varphi\partial\lambda\partial\varphi'\partial\lambda'} + \frac{\tan\varphi}{r^2r'^2\,\cos\varphi\cos\varphi'}\,\frac{\partial^3 K}{\partial\lambda\partial\varphi'\partial\lambda'} + \\
&\quad + \frac{\tan\varphi'}{r^2r'^2\,\cos\varphi\cos\varphi'}\,\frac{\partial^3 K}{\partial\varphi\partial\lambda\partial\lambda'} + \frac{\tan\varphi\tan\varphi'}{r^2r'^2\,\cos\varphi\cos\varphi'}\,\frac{\partial^2 K}{\partial\lambda\partial\lambda'} \\
cov(T_{yx}, T_{y'z'}) &= \left(\frac{1}{r^2\cos\varphi}\,\frac{\partial^2}{\partial\varphi\partial\lambda} + \frac{\tan\varphi}{r^2\cos\varphi}\,\frac{\partial}{\partial\lambda}\right)\left(\frac{1}{r'\,\cos\varphi'}\,\frac{\partial^2 K}{\partial r'\partial\lambda'} - \frac{1}{r'^2\,\cos\varphi'}\,\frac{\partial K}{\partial\lambda'}\right) = \\
&= \frac{1}{r^2r'\,\cos\varphi\cos\varphi'}\,\frac{\partial^4 K}{\partial\varphi\partial\lambda\partial r'\partial\lambda'} + \frac{\tan\varphi}{r^2r'\,\cos\varphi\cos\varphi'}\,\frac{\partial^3 K}{\partial\lambda\partial r'\partial\lambda'} + \\
&\quad + \frac{1}{r^2r'^2\,\cos\varphi\cos\varphi'}\,\frac{\partial^3 K}{\partial\varphi\partial\lambda\partial\lambda'} + \frac{\tan\varphi}{r^2r'^2\,\cos\varphi\cos\varphi'}\,\frac{\partial^2 K}{\partial\lambda\partial\lambda'} \\
cov(T_{yx}, T_{x'x'}) &= \left(\frac{1}{r^2\cos\varphi}\,\frac{\partial^2}{\partial\varphi\partial\lambda} + \frac{\tan\varphi}{r^2\cos\varphi}\,\frac{\partial}{\partial\lambda}\right)\left(\frac{1}{r'}\,\frac{\partial K}{\partial r'} + \frac{1}{r'^2}\,\frac{\partial^2 K}{\partial\varphi'^2}\right) = \\
&= \frac{1}{r^2r'\cos\varphi}\,\frac{\partial^3 K}{\partial\varphi\partial\lambda\partial r'} + \frac{\tan\varphi}{r^2r'\cos\varphi}\,\frac{\partial^2 K}{\partial\lambda\partial r'} + \frac{1}{r^2r'^2\cos\varphi}\,\frac{\partial^4 K}{\partial\varphi\partial\lambda\partial\varphi'^2} + \\
&\quad + \frac{\tan\varphi}{r^2r'^2\cos\varphi}\,\frac{\partial^3 K}{\partial\lambda\partial\varphi'^2} \\
cov(T_{yx}, T_{x'z'}) &= \left(\frac{1}{r^2\cos\varphi}\,\frac{\partial^2}{\partial\varphi\partial\lambda} + \frac{\tan\varphi}{r^2\cos\varphi}\,\frac{\partial}{\partial\lambda}\right)\left(\frac{1}{r'}\,\frac{\partial^2 K}{\partial r'\partial\varphi'} - \frac{1}{r'^2}\,\frac{\partial K}{\partial\varphi'}\right) = \\
&= \frac{1}{r^2r'\cos\varphi}\,\frac{\partial^4 K}{\partial\varphi\partial\lambda\partial r'\partial\varphi'} + \frac{\tan\varphi}{r^2r'\cos\varphi}\,\frac{\partial^3 K}{\partial\lambda\partial r'\partial\varphi'} - \frac{1}{r^2r'^2\cos\varphi}\,\frac{\partial^3 K}{\partial\varphi\partial\lambda\partial\varphi'} + \\
&\quad - \frac{\tan\varphi}{r^2r'^2\cos\varphi}\,\frac{\partial^2 K}{\partial\lambda\partial\varphi'} \\
cov(T_{yx}, T_{z'z'}) &= \left(\frac{1}{r^2\cos\varphi}\,\frac{\partial^2}{\partial\varphi\partial\lambda} + \frac{\tan\varphi}{r^2\cos\varphi}\,\frac{\partial}{\partial\lambda}\right)\left(\frac{\partial^2 K}{\partial r'^2}\right) = \\
&= \frac{1}{r^2\cos\varphi}\,\frac{\partial^4 K}{\partial\varphi\partial\lambda\partial r'^2} + \frac{\tan\varphi}{r^2\cos\varphi}\,\frac{\partial^3 K}{\partial\lambda\partial r'^2}
\end{aligned}
$$

$$
\begin{aligned}
cov(T_{yz}, T_{y'x'}) &= \left(\frac{1}{r\,\cos\varphi}\,\frac{\partial^2}{\partial r\partial\lambda} - \frac{1}{r^2\,\cos\varphi}\,\frac{\partial}{\partial\lambda}\right)\left(\frac{1}{r'^2\cos\varphi'}\,\frac{\partial^2 K}{\partial\varphi'\partial\lambda'} + \frac{\tan\varphi'}{r'^2\cos\varphi'}\,\frac{\partial K}{\partial\lambda'}\right) = \\
&= \frac{1}{rr'^2\,\cos\varphi\cos\varphi'}\,\frac{\partial^4 K}{\partial r\partial\lambda\partial\varphi'\partial\lambda'} - \frac{1}{r^2r'^2\,\cos\varphi\cos\varphi'}\,\frac{\partial^3 K}{\partial\lambda\partial\varphi'\partial\lambda'} + \\
&\quad + \frac{\tan\varphi'}{rr'^2\,\cos\varphi\cos\varphi'}\,\frac{\partial^3 K}{\partial r\partial\lambda\partial\lambda'} - \frac{\tan\varphi'}{r^2r'^2\,\cos\varphi\cos\varphi'}\,\frac{\partial^2 K}{\partial\lambda\partial\lambda'}
\end{aligned}
$$

$$cov(T_{yz}, T_{y'z'}) = \left(\frac{1}{r\ \cos\varphi}\ \frac{\partial^2}{\partial r \partial\lambda} - \frac{1}{r^2\ \cos\varphi}\ \frac{\partial}{\partial\lambda}\right)\left(\frac{1}{r'\ \cos\varphi'}\ \frac{\partial^2 K}{\partial r' \partial\lambda'} - \frac{1}{r'^2\ \cos\varphi'}\ \frac{\partial K}{\partial\lambda'}\right) =$$
$$= \frac{1}{rr'\ \cos\varphi\cos\varphi'}\ \frac{\partial^4 K}{\partial r\partial\lambda\partial r'\partial\lambda'} - \frac{1}{r^2 r'\ \cos\varphi\cos\varphi'}\ \frac{\partial^3 K}{\partial\lambda\partial r'\partial\lambda'} +$$
$$- \frac{1}{rr'^2\ \cos\varphi\cos\varphi'}\ \frac{\partial^3 K}{\partial r\partial\lambda\partial\lambda'} + \frac{1}{r^2 r'^2\ \cos\varphi\cos\varphi'}\ \frac{\partial^2 K}{\partial\lambda\partial\lambda'}$$

$$cov(T_{yz}, T_{x'z'}) = \left(\frac{1}{r\ \cos\varphi}\ \frac{\partial^2}{\partial r \partial\lambda} - \frac{1}{r^2\ \cos\varphi}\ \frac{\partial}{\partial\lambda}\right)\left(\frac{1}{r'}\ \frac{\partial^2 K}{\partial r' \partial\varphi'} - \frac{1}{r'^2}\ \frac{\partial K}{\partial\varphi'}\right) =$$
$$= \frac{1}{r^2 r'^2\ \cos\varphi}\ \frac{\partial^2 K}{\partial\lambda\partial\varphi'} - \frac{1}{r^2 r'\ \cos\varphi}\ \frac{\partial^3 K}{\partial\lambda\partial r'\partial\varphi'} - \frac{1}{rr'^2\ \cos\varphi}\ \frac{\partial^3 K}{\partial r\partial\lambda\partial\varphi'} +$$
$$+ \frac{1}{rr'\ \cos\varphi}\ \frac{\partial^4 K}{\partial r\partial\lambda\partial r'\partial\varphi'}$$

$$cov(T_{yz}, T_{z'z'}) = \left(\frac{1}{r\ \cos\varphi}\ \frac{\partial^2}{\partial r \partial\lambda} - \frac{1}{r^2\ \cos\varphi}\ \frac{\partial}{\partial\lambda}\right)\left(\frac{\partial^2 K}{\partial r'^2}\right)$$
$$= \frac{1}{r\ \cos\varphi}\ \frac{\partial^4 K}{\partial r\partial\lambda\partial r'^2} - \frac{1}{r^2\ \cos\varphi}\ \frac{\partial^3 K}{\partial\lambda\partial r'^2}$$

$$cov(T_{xx}, T_{x'x'}) = \left(\frac{1}{r}\ \frac{\partial}{\partial r} + \frac{1}{r^2}\ \frac{\partial^2}{\partial\varphi^2}\right)\left(\frac{1}{r'}\ \frac{\partial K}{\partial r'} + \frac{1}{r'^2}\ \frac{\partial^2 K}{\partial\varphi'^2}\right) =$$
$$= \frac{1}{rr'}\ \frac{\partial^2 K}{\partial r\partial r'} + \frac{1}{r^2 r'}\ \frac{\partial^3 K}{\partial\varphi^2\partial r'} + \frac{1}{rr'^2}\ \frac{\partial^3 K}{\partial r\partial\varphi'^2} + \frac{1}{r^2 r'^2}\ \frac{\partial^4 K}{\partial\varphi^2\partial\varphi'^2}$$

$$cov(T_{xx}, T_{x'z'}) = \left(\frac{1}{r}\ \frac{\partial}{\partial r} + \frac{1}{r^2}\ \frac{\partial^2}{\partial\varphi^2}\right)\left(\frac{1}{r'}\ \frac{\partial^2 K}{\partial r'\partial\varphi'} - \frac{1}{r'^2}\ \frac{\partial K}{\partial\varphi'}\right) =$$
$$= \frac{1}{rr'}\ \frac{\partial^3 K}{\partial r\partial r'\partial\varphi'} + \frac{1}{r^2 r'}\ \frac{\partial^4 K}{\partial\varphi^2\partial r'\partial\varphi'} - \frac{1}{rr'^2}\ \frac{\partial^2 K}{\partial r\partial\varphi'} - \frac{1}{r^2 r'^2}\ \frac{\partial^3 K}{\partial\varphi^2\partial\varphi'}$$

$$cov(T_{xx}, T_{z'z'}) = \left(\frac{1}{r}\ \frac{\partial}{\partial r} + \frac{1}{r^2}\ \frac{\partial^2}{\partial\varphi^2}\right)\left(\frac{\partial^2 K}{\partial r'^2}\right) = \frac{1}{r}\ \frac{\partial^3 K}{\partial r\partial r'^2} + \frac{1}{r^2}\ \frac{\partial^4 K}{\partial\varphi^2\partial r'^2}$$

$$cov(T_{xz}, T_{x'z'}) = \left(\frac{1}{r}\ \frac{\partial^2}{\partial r\partial\varphi} - \frac{1}{r^2}\ \frac{\partial}{\partial\varphi}\right)\left(\frac{1}{r'}\ \frac{\partial^2 K}{\partial r'\partial\varphi'} - \frac{1}{r'^2}\ \frac{\partial K}{\partial\varphi'}\right) =$$
$$= \frac{1}{rr'}\ \frac{\partial^4 K}{\partial r\partial\varphi\partial r'\partial\varphi'} - \frac{1}{r^2 r'}\ \frac{\partial^3 K}{\partial\varphi\partial r'\partial\varphi'} - \frac{1}{rr'^2}\ \frac{\partial^3 K}{\partial r\partial\varphi\partial\varphi'} + \frac{1}{r^2 r'^2}\ \frac{\partial^2 K}{\partial\varphi\partial\varphi'}$$

$$cov(T_{xz}, T_{z'z'}) = \left(\frac{1}{r}\ \frac{\partial^2}{\partial r\partial\varphi} - \frac{1}{r^2}\ \frac{\partial}{\partial\varphi}\right)\left(\frac{\partial^2 K}{\partial r'^2}\right) = \frac{1}{r}\ \frac{\partial^4 K}{\partial r\partial\varphi\partial r'^2} - \frac{1}{r^2}\ \frac{\partial^3 K}{\partial\varphi\partial r'^2}$$

$$cov(T_{zz}, T_{z'z'}) = \left(\frac{\partial^2}{\partial r^2}\right)\left(\frac{\partial^2 K}{\partial r'^2}\right) = \frac{\partial^4 K}{\partial r^2\partial r'^2}$$

Appendix B

B.1 Fourier Transform and Discrete Fourier Transform

The frequency domain representation of a continuous function or signal $x(t)$ given in the time domain is defined as the Fourier transform

$$X(\eta) = \mathcal{F}[x(t)] = \int_{-\infty}^{\infty} x(t)\, e^{-i2\pi\eta t}\, \mathrm{d}t\,, \tag{B.1}$$

with η denoting the frequency. In the opposite direction, the time domain equivalent of the frequency domain representation $X(\eta)$ is found by the inverse Fourier transform

$$x(t) = \mathcal{F}^{-1}[X(\eta)] = \int_{-\infty}^{\infty} X(\eta)\, e^{2\pi\eta t}\, \mathrm{d}\eta\,. \tag{B.2}$$

In practice a signal is not given in a continuous version, but is sampled with a distinct sampling interval Δt to obtain a discrete signal $x(n)$. Furthermore, only a restricted interval with a given maximum amount of samples N can be observed in reality. The corresponding equivalent to the continuous case is the discrete Fourier transform

$$X(k) = \mathcal{F}[x(n)] = \sum_{n=0}^{N-1} x(n)\, e^{-i2\pi nk/N}\,, \qquad k = 0, \ldots N-1\,, \tag{B.3}$$

and vice versa the inverse discrete Fourier transform

$$x(n) = \mathcal{F}^{-1}[X(k)] = \frac{1}{N} \sum_{k=0}^{N-1} X(k)\, e^{i2\pi nk/N}\,, \qquad n = 0, \ldots N-1\,. \tag{B.4}$$

B.2 Statistic moments of stochastic processes

We can consider a time series $x(t)$, i.e. a set of real valued numbers x in dependence of t, as a realization of a stochastic process $\mathcal{X}(t)$. It is assumed that this stochastic process is stationary, so shifting $\mathcal{X}(t)$ by an arbitrary time τ to $\mathcal{X}(t+\tau)$ does not change the statistics of the process (Koch and Schmidt, 1994). Furthermore, we assume $\mathcal{X}(t)$ to be ergodic, which means that the statistics of this process can be derived from one single realization $x(t)$. In

this way, the mean representing the first order statistic moment of this stochastic process is given by its expectation value

$$\mu_X = E\{\mathcal{X}(t)\}\,, \tag{B.5}$$

while the second order statistic moment, the autocorrelation, is defined by

$$R_{XX} = E\{\mathcal{X}(t)\,\mathcal{X}(t+\tau)\} = R_{XX}(\tau)\,, \tag{B.6}$$

which is only depending on the time shift τ. The crosscorrelation between two stochastic processes $\mathcal{X}(t)$ and $\mathcal{Y}(t)$ is given by

$$R_{XY} = E\{\mathcal{X}(t)\,\mathcal{Y}(t+\tau)\} = R_{XY}(\tau)\,. \tag{B.7}$$

The according autocovariance is found by

$$C_{XX} = E\{(\mathcal{X}(t)-\mu_x)\,(\mathcal{X}(t+\tau)-\mu_x)\} = R_{XX}(\tau) - \mu_X^2\,, \tag{B.8}$$

and the crosscovariance by

$$C_{XY} = E\{(\mathcal{X}(t)-\mu_x)\,(\mathcal{Y}(t+\tau)-\mu_Y)\} = R_{XY}(\tau) - \mu_X\mu_Y\,. \tag{B.9}$$

B.3 Power Spectral Density

For a given time series $x(t)$ the corresponding autocorrelation $R_{xx}(\tau)$ can be derived by

$$R_{xx}(\tau) = \int_{-\infty}^{\infty} x(t)\,x(t+\tau)\,\mathrm{d}\tau\,. \tag{B.10}$$

The power spectrum $S(\eta)$ is defined as the Fourier transform of the autocorrelation $R_{xx}(\tau)$

$$S(\eta) = \mathcal{F}[R_{xx}(\tau)] = \int_{-\infty}^{\infty} R_{xx}(\tau)\,e^{-i2\pi\eta\tau}\,\mathrm{d}\tau\,, \tag{B.11}$$

and thus can also be written as

$$S(\eta) = |X(\eta)|^2\,. \tag{B.12}$$

Inversely, the autocorrelation $R_{xx}(\tau)$ is the inverse Fourier transform of the power spectrum $S(\eta)$

$$R_{xx}(\tau) = \mathcal{F}^{-1}[S(\eta)]\,. \tag{B.13}$$

If the time series $x(t)$ is centered, i.e. its mean $\mu_x = 0$, the autocorrelation $R_{xx}(\tau)$ is replaced by the autocovariance $C_{xx}(\tau)$, which can be related to the power spectrum accordingly.

If we reconsider Eq. (B.10) for the case $\tau = 0$, we obtain

$$R_{xx}(0) = \int_{-\infty}^{\infty} |x(t)|^2 \, \mathrm{d}t \,, \tag{B.14}$$

which represents the total power or energy of the signal $x(t)$. This in turn can be written in terms of the Fourier transform $X(\eta)$

$$R_{xx}(0) = \int_{-\infty}^{\infty} |X(\eta)|^2 \, \mathrm{d}\eta \,, \tag{B.15}$$

which is called the Parseval theorem and states that the signal power in the time domain equals the energy in the frequency domain. Thus, the power spectrum or PSD describes the signal's energy distribution with frequency.

Since the PSD is actually defined for an infinite time series, a discrete and time limited estimate can be determined according to Oppenheim and Schafer (1975)

$$\hat{S}(k) = \frac{1}{N} \left| \sum_{n=0}^{N-1} x(n) \, e^{-i2\pi nk/N} \right|^2 \,, \tag{B.16}$$

which is called periodogram. As a matter of fact, the variance of the periodogram is increasing with an increasing number of samples N (Oppenheim and Schafer, 1975), Therefore, the use of averaged modified periodograms according to Welch (1967) for the estimation of the PSD can facilitate interpretations. This method divides the discrete time series $x(n)$ into $K = N/M$ segments with M samples per section, which may be overlapping. To each of the segments, a window function $w(n)$ is applied, so K modified periodograms

$$\hat{S}^i(k) = \frac{1}{MU} \left| \sum_{n=0}^{M-1} x^i(n) \, w(n) \, e^{-i2\pi nk/N} \right|^2 \qquad i = 1, \ldots K, \tag{B.17}$$

are generated, with

$$U = \frac{1}{M} \sum_{n=0}^{M-1} w^2(n) \,. \tag{B.18}$$

The final PSD estimate is then obtained by averaging the K modified periodograms

$$\hat{S}(k) = \frac{1}{K} \sum_{i=1}^{K} \hat{S}^i(k). \tag{B.19}$$

In this way, a smoothed PSD estimate can be achieved, which corresponds to a loss in frequency resolution due to the limitation of the sample size from N to M (Oppenheim and Schafer, 1975). In Figure B.1b the PSD estimates of a simulated GOCE time series from D/O 50 to 280 based on the periodogram and using Welch's method with different window functions, illustrated in Figure B.1a, are shown. The PSD estimated by the periodogram is given in grey and shows a high variability, which makes it difficult to discriminate the energy

content at different frequencies. The variance of the PSDs can be decreased by applying Welch's method with window functions like the Boxcar function (red), Hanning window (green) or a Kaiser window (blue). Details on the definitions of these windows can be found in Oppenheim and Schafer (1975). Depending on the weighting due to the window function, different degrees of smoothing and thus frequency resolution can be achieved. Since PSDs used in this study are primarily used for interpretation purposes, Welch's method applying a Kaiser window is used for estimating the PSDs in this thesis.

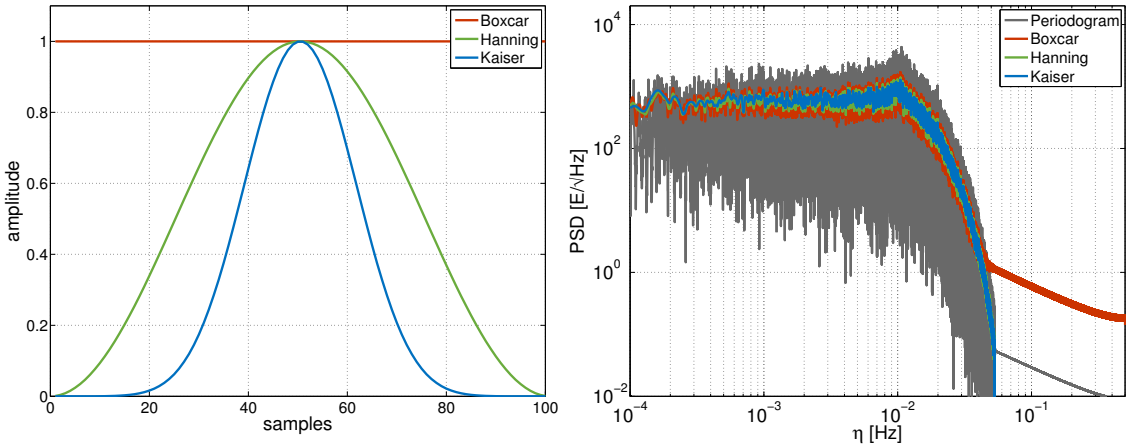

(a) Boxcar, Hanning and Kaiser Window

(b) Periodogram and PSD according to Welch's method using different windows

Figure B.1: Window functions and their application to a GOCE-type time series

Appendix C

C.1 From quaternions to rotation matrices

Quaternions are commonly used to describe frame rotations in the three-dimensional Euclidean space. The following formulations will only provide the equations how to obtain a rotation matrix from a corresponding quaternion. A detailed description on this issue can be found for instance in Gruber et al. (2010b) or Stummer (2013).

A quaternion q is defined as a hypercomplex number consisting of Euler symmetric parameters

$$q = q_4 + iq_1 + jq_2 + kq_3 \,, \tag{C.1}$$

in which the element q_4 represents the real or scalar part of the quaternion depending on the Euler angle of a three-dimensional rotation, while the complex parts q_1, q_2 and q_3 are furthermore associated with the components of the rotation axis vector, around which the frame rotation is performed. The corresponding rotation matrix R can then be derived from the quadrupel q by

$$R = \begin{pmatrix} q_1^2 - q_2^2 - q_3^2 + q_4^2 & 2(q_1q_2 + q_3q_4) & 2(q_1q_3 - q_2q_4) \\ 2(q_2q_2 - q_3q_4) & -q_1^2 + q_2^2 - q_3^2 + q_4^2 & 2(q_2q_3 + q_1q_4) \\ 2(q_1q_3 + q_2q_4) & 2(q_2q_3 - q_1q_4) & -q_1^2 - q_2^2 + q_3^2 + q_4^2 \end{pmatrix} . \tag{C.2}$$